Characterization and Morphological Analysis of Porous Electrodes for Lithium-Ion Batteries

Kumulative Dissertation

zur Erlangung des Grades eines
Doktor der Naturwissenschaften
(Dr. rer. nat.)
des Fachbereichs Chemie der Philipps-Universität Marburg

Vorgelegt von

Moritz Kroll

geboren in Berlin-Kreuzberg

Marburg an der Lahn, 2021

Abgabedatum: _____.

Vom Fachbereich Chemie der Philipps-Universität Marburg (Hochschulkennziffer 1180) als Dissertation angenommen am:_____.

Erstgutachter: Prof. Dr. Ulrich Tallarek

Zweitgutachter: Prof. Dr. Bernhard Roling

Tag der mündlichen Prüfung:_____.

Die vorliegende Arbeit wurde in der Zeit von Juni 2017 bis April 2021 am Fachbereich Chemie der Philipps-Universität Marburg unter Leitung von Herrn Prof. Dr. Ulrich Tallarek und Herrn Prof. Dr. Bernhard Roling angefertigt.

Teile der Dissertation wurden bereits in den folgenden Artikeln veröffentlicht:

1 M. Kroll, D. Hlushkou, S. Schlabach, A. Höltzel, B. Roling,* U. Tallarek*
"Reconstruction–Simulation Approach Verifies Impedance-Derived Ion Transport Tortuosity of a Graphite Battery Electrode"
J. Electrochem. Soc., **2018**, *165*, A3156–A3163. DOI: 10.1149/2.0711813jes

2 M. Cronau,[+] M. Kroll,[+] M. Szabo, F. Sälzer, B. Roling*
"Thickness-Dependent Impedance of Composite Battery Electrodes Containing Ionic Liquid-Based Electrolytes"
Batteries Supercaps, **2020**, *3*, 1–9. DOI: 10.1002/batt.202000023

3 M. Kroll, S. L. Karstens, M. Cronau, A. Höltzel, S. Schlabach, N. Nobel, C. Redenbach, B. Roling,* U. Tallarek*
"Three-Phase Reconstruction Reveals How the Microscopic Structure of the Carbon-Binder Domain Affects Ion Transport in Lithium-Ion Batteries"
Batter. Supercaps, **2021**, *accepted*. DOI: 10.1002/batt.202100057R1

4 M. Kroll,[+] M. Duchardt,[+] S. L. Karstens, S. Schlabach, F. Lange, J. Hochstrasser, B. Roling,* U. Tallarek*
"Sheet-type all-solid-state batteries with sulfidic electrolytes: Analysis of kinetic limitations based on a cathode morphology study"
J. Power Sources, **2021**, *under review*.

5 H. Reinhardt,[+] M. Kroll,[+] S. L. Karstens, S. Schlabach, N. Hampp,* U. Tallarek*
"Nanoscaled Fractal Superstructures via Laser Patterning—A Versatile Route to Metallic Hierarchical Porous Materials"
Adv. Mater. Interfaces, **2021**, *8*, 2000253. DOI: 10.1002/admi.202000253

[+] Die Beiträge dieser Autoren sind gleichwertig.

Danksagung

An dieser Stelle möchte ich gerne den Menschen danken, die mich im Rahmen meiner Promotion und darüber hinaus unterstützt haben und mir dadurch meine akademische Entwicklung ermöglicht haben.

An erster Stelle danke ich Herrn Prof. Dr. Ulrich Tallarek und Herrn Prof. Dr. Bernhard Roling für die Möglichkeit, arbeitsgruppenübergreifend an interessanten und anspruchsvollen wissenschaftlichen Fragestellungen forschen zu dürfen. Beiden danke ich für die thematische Offenheit, für die vielen hilfreichen Diskussionen, für die Bereitstellung der nötigen Ausstattung und für die insgesamte gute Zusammenarbeit, aus der viele Kooperationen mit weiteren Gruppen entstanden sind. Zudem danke ich für die Möglichkeit, dass ich unsere Forschungsergebnisse auf verschiedenen Konferenzen präsentieren durfte.

Herrn Prof. Dr. Christian Kübel danke ich für den Beisitz in der Prüfungskommission. Ihm und seiner Gruppe danke ich für die exzellente Zusammenarbeit. Ein besonderer Dank geht hierbei insbesondere an Dr. Sabine Schlabach für die Durchführung der Messungen, die zahlreichen wissenschaftlichen Diskussionen und die viele Zeit und Geduld, die sie in unsere Arbeit gesteckt hat. Der gesamten Gruppe von Herrn Prof. Dr. Christian Kübel am KIT danke ich für die freundliche Aufnahme während meiner zahlreichen Aufenthalte in Karlsruhe.

Dr. Hendrik Reinhardt, Dr. Marc Duchardt und Marvin Cronau danke ich für die enge und fruchtbare Zusammenarbeit bei der gemeinsamen Arbeit an Projekten. Die Kooperationen haben jeweils interessante Themengebiete zusammengeführt und so die Untersuchung neuer wissenschaftlicher Fragestellungen ermöglicht. Frau Dr. Alexandra Höltzel danke ich für die zielorientierte und kritische Zusammenarbeit beim wissenschaftlichen Schreiben, wodurch ich selbst viel lernen konnte. Dr. Dzmitry Hlushkou danke ich für diverse wertvolle Diskussionen. Ein besonderer Dank gilt Sally Karstens für die lange und vertrauensvolle Zusammenarbeit an unterschiedlichen Themengebiete, wodurch sich viele neuen Impulse für die Forschung ergeben haben. Herrn Prof. Dr. Hampp und Frau Prof. Dr. Redenbach gilt ebenfalls ein besonderer Dank für die erfolgreichen Kooperationen.

Den Mitgliedern der Arbeitsgruppen Tallarek und Roling danke ich für die stets angenehme und entspannte Atmosphäre, die schönen Gruppenausflüge und die gemeinsamen Kneipenabende. Besonders danke ich Nicole und Olaf für das gute Arbeitsklima im Büro. Rigo und Kirsten danke ich für die Unterstützung in bürokratischen Belangen.

Abschließend möchte ich meiner Familie und meinen Freunden für die Unterstützung und die schöne Zeit in Marburg danken.

List of abbreviations

AI	Artificial intelligence
AM	Active material
APT	Atom probe tomography
ASSB	All-solid-state battery
BSE	Backscattered electrons
CAM	Cathode active material
CBD	Carbon binder domain
CLD	Chord length distribution
CPE	Constant phase element
EDX	Energy-dispersive X-ray spectroscopy
EIS	Electrochemical impedance spectroscopy
ETD	Everhart-Thornley detector
FIB	Focused ion-beam
H-NBR	Hydrogenated nitrile butadiene rubber
HPM	Hierarchically porous material
IL	Ionic liquid
LCO	Lithium cobalt oxide, $LiCoO_2$
LIB	Lithium-ion battery
LPSI	2 Li_3PS_4·LiI
NBR	Nitrile butadiene rubber
NMC	Lithium nickel manganese cobalt oxide, $LiNi_{1-y-z}Mn_yCo_zO_2$
PE	Primary electrons
PIB	Polyisobutene
PT	Pellet-type
ROI	Region of interest
RS	Reconstruction–simulation
RWPT	Random walk particle tracking
SE	Solid electrolyte

SecE	Secondary electrons
SEI	Solid electrolyte interphase
SEM	Scanning electron microscopy
SOC	State of charge
ST	Sheet-type
STEM	Scanning transmission electron microscopy
TLM	Transmission-line model
VOI	Volume of interest
XRT	X-ray tomography
β-LPS	β-Li_3PS_4

Contents

I. Zusammenfassung

Der Klimawandel ist eine der größten Herausforderungen des Jahrhunderts. Gegenüber dem vorindustriellen Zeitalter ist die globale Durchschnittstemperatur bereits um 1 °C gestiegen (1,5 °C in Deutschland). Grund für den Temperaturanstieg ist der Ausstoß von Treibhausgasen, die in die Atmosphäre reflektiertes Sonnenlicht in Wärme umwandeln. Etwa 20% des CO_2-Austoßes in Deutschland werden dem Transportsektor zugerechnet. Die Elektromobilität stellt dabei einen möglichen Lösungsweg dar, diesen Anteil zu reduzieren. Zur mobilen Speicherung von Strom aus erneuerbaren Energien werden leistungsstarke Lithium-Ionen-Batterien (LIB) benötigt. Drei Ansätze werden im Wesentlichen verfolgt, um die Leistung von LIB zu verbessern: die Entwicklung neuer Materialien und neuer Batteriekonzepte sowie die Optimierung existierender Systeme. Diese Arbeit verfolgt den letzteren Ansatz, indem die Elektrodenmorphologie mithilfe von Tomographie abgebildet und untersucht wird. Durch eine detaillierte morphologische Analyse und Simulationen werden mikrostrukturelle kinetische Limitierungen identifiziert und mit den Ergebnissen elektrochemischer Charakterisierungsmethoden verglichen. Im Folgenden werden die Ergebnisse der fünf Kapitel dieser kumulativen Dissertation zusammengefasst. Kapitel 1–3 beziehen sich dabei auf die Untersuchung von Transportlimitierungen in Flüssigbatterien, Kapitel 4 auf Festkörperbatterien und in Kapitel 5 wird der Rekonstruktionsansatz auf ein hierarchisches poröses Material angewandt.

Im ersten Kapitel werden Transportlimitierungen in einer Elektrode komparativ durch einen Rekonstruktions-Simulations-Ansatz (RS) und mittels elektrochemischer Messungen detektiert. Ziel der Studie ist es, die ionische Tortuosität auf beiden Wegen zur Quantifizierung von Transportlimitierungen im Elektrolyt-gefüllten Porenraum einer Flüssigbatterie zu ermitteln. Als Aktivmaterial wird Graphit gewählt, das ein verbreitetes Anodenmaterial ist. Zur elektrochemischen Charakterisierung werden Graphitelektroden dickenabhängig im symmetrischen Aufbau mittels Elektrochemischer Impedanzspektroskopie (EIS) untersucht. Die resultierenden Spektren lassen sich mithilfe des Transmission Line Models (TLM) fitten, das die Impedanz poröser Elektroden beschreibt. Hieraus lässt sich eine ionische Tortuosität von $\tau_{\mathrm{EIS}} = 7{,}3$ ermitteln. Zum anderen wird eine der Graphitelektroden physikalisch mittels Elektronenmikroskopie mit fokussiertem Ionenstrahl (engl. *focused ion-beam scanning electron microscopy*, FIB-SEM) Tomographie über den gesamten Querschnitt rekonstruiert. Dazu wird der Porenraum der Elektrode mit einem Osmium-basierten Kontrastmittel gefüllt. So wird der Raum, der im Batteriebetrieb vom flüssigen Elektrolyten gefüllt ist, direkt abgebildet. Der Kontrast in den resultierenden Bildern wird so erhöht, was eine akkurate Rekonstruktion erleichtert. Es wird eine vergleichende morphologische Analyse angefertigt, die Porositätsprofile, die geometrische Tortuosität und eine Sehnenlängenverteilung (engl. *chord length distribution*, CLD) der festen Phase sowie des Porenraums beinhaltet. Alle

Analysen werden richtungsabhängig durchgeführt, wodurch gezeigt wird, dass die Plättchen-förmigen Graphitpartikel eine ausgeprägte anisotrope Mikrostruktur formen. Dies führt zu starken Transporthinderungen senkrecht zum Stromabnehmer. Eine finite-size Analyse zeigt, dass das gewählte Rekonstruktionsvolumen repräsentativ ist, und somit belastbare Ergebnisse liefert. Diffusionssimulationen basierend auf einem *random-walk*-Ansatz bringen einen Tortuositätswert von $\tau_{\mathrm{RS}} = 6{,}55$ hervor, der innerhalb des experimentellen Fehlers von τ_{EIS} liegt. Diese Studie zeigt, dass die langreichweitigen Transportsimulationen (ohne Berücksichtigung der Doppelschichtbildung) und EIS in Verbindung mit dem TLM (Ionentransport in den Poren bis zur Doppelschichtbildung) selbst für eine stark anisotrope Mikrostruktur vergleichbare Ergebnisse liefern. EIS ist im Vergleich zu FIB-SEM Tomographie in Verbindung mit numerischen Simulationen erheblich schneller, billiger und leichter durchführbar und in praktisch jedem elektrochemischen Labor verfügbar. Die mikrostrukturellen Ursachen für sterische Transporthinderungen lassen sich jedoch nur durch geeignete Tomographiemethoden analysieren. EIS-Screenings können genutzt werden, um Transportlimitierungen neu hergestellter Elektroden zu detektieren. Somit können die Ergebnisse dieser Studie zur zukünftigen Entwicklung leistungsstärkerer Elektroden beitragen.

Im zweiten Kapitel wird die Impedanz von Elektroden mit variabler Dicke für verschiedene Flüssigelektrolytsysteme untersucht. Dafür werden zunächst Batterien mit einer solvat-ionischen Flüssigkeit mit LiTFSI, einem konventionellen Carbonat-basierten Elektrolyten und einer Mischung aus ionischer Flüssigkeit (engl. *ionic liquid*, IL) und LiFSI zyklisiert. Aus den Überspannungen bei einem Ladungszustand von 50% werden die flächenspezifischen Widerstände abgeschätzt, die in der Reihenfolge Carbonat-basierter Elektrolyt < IL < Solvat-IL ansteigen. Die verschiedenen Elektrolytsysteme werden in Abhängigkeit von der Elektrodendicke mittels EIS charakterisiert. Ein besonderes Augenmerk wird dabei auf die Impedanz bei 10^{-4} Hz gelegt, da diese etwa der Zeitskala typischer Zyklisierungsraten von 1–2 C entspricht. Die Impedanzen steigen zwischen den Elektrolytsystemen in derselbe Reihenfolge an, wie es bei den Zyklisierungsexperimenten beobachtet wurde. Um die einzelnen Impedanzbeiträge für den Carbonat-basierten Elektrolyten und die Solvat-IL näher zu verstehen, wird das analytische Modell von Huang und Zhang herangezogen. Das Modell berechnet die Elektrodenimpedanz unter Berücksichtigung von Salzkonzentrationspolarisation im Elektrolyt-gefüllten Porenraum. Es ist auf Elektrolytsysteme bestehend aus jeweils einer Kationen- und einer Anionensorte in einem Lösungsmittel anwendbar. Bei 10^{-4} Hz zeigt sich für den Realteil und den Betrag der komplexen Impedanz eine nur schwache Abhängigkeit von der Elektrodendicke im Bereich von 50–100 µm. Mithilfe des generalisierten TLM werden die Impedanzbeiträge des Ionentransports und des dickenabhängigen Ladungstransfers sowie der Festphasendiffusion aufgeschlüsselt. Bei 10^{-4} Hz und bei Dicken zwischen 50–150 µm ist sowohl für die Solvat-IL als auch für den Carbonat-basierten Elektrolyten die Impedanz des Ionentransports größer als der Beitrag aus Ladungstransfer und Festphasendiffusion, woraus

sich die geringe Dickenabhängigkeit erklärt. Dies lässt den Schluss zu, dass größere Elektrodendicken als die kommerziell üblichen 80 µm möglich wären, sofern die morphologischen Eigenschaften über die gesamte Elektrode konstant gehalten werden können.

Kapitel 3 untersucht den Einfluss der Kohlenstoff-Binder-Domäne (engl. *carbon binder domain*, CBD) auf den Li^+-Transport in der Elektrolytphase anhand eines RS Ansatzes und vergleicht die Ergebnisse mit EIS-Experimenten. Die Morphologie des mit Elektrolyten gefüllten Porenraums wird in LIBs durch die Mikrostruktur der festen Komponenten beeinflusst. Hierzu zählen das Aktivmaterial (AM), der Binder und Leitkohlenstoff. Der Binder und der Leitkohlenstoff bilden eine gemeinsame nanoporöse Phase – die CBD. Während die µm-großen AM-Partikel leicht mittels 3D Tomographie rekonstruiert werden können, wird die CBD aufgrund ihrer geringen Größe dabei häufig nicht berücksichtigt. In dieser Studie wird eine $LiCoO_2$ (LCO)–Kompositkathode mittels FIB-SEM-Tomographie physikalisch rekonstruiert, um die Li^+-Transporttortuosität zu bestimmen und die CBD morphologisch zu charakterisieren. EIS-Experimente im Rahmen des TLM werden aufgenommen, um die ionische Tortuosität experimentell zu bestimmen, und mit den Ergebnissen des RS-Ansatzes verglichen. Die dreiphasige Rekonstruktion weist neben der bisher höchsten Auflösung mit einer Voxelgröße von (13,9 × 13,9 × 20,0) nm^3 ein sehr großes Volumen mit einer minimalen Kantenlänge von 20 µm auf, was eine repräsentative Beschreibung des Porenraums erlaubt. Es wird eine detaillierte morphologische Analyse zur Charakterisierung des Porenraums durchgeführt, die eine CLD, die Bestimmung der spezifischen Oberfläche, eine Konnektivitätsanalyse und die Berechnung der geometrischen Tortuosität umfasst. Die Ergebnisse zeigen, dass die mikrostrukturellen Eigenschaften der Kathode durch die Anwesenheit der CBD, die den Porenraum als verworrenes Netzwerk durchdringt, beeinflusst werden, wodurch die Li^+ Transportpfade gewundener und verengter werden. Porenskalige numerische Diffusionssimulationen ergeben bei Berücksichtigung der CBD eine deutlich höhere ionische Tortuosität von 1,9 verglichen zu 1,5 ohne CBD. Der Unterschied der Tortuositäten kann dabei nicht allein auf die Porositätsunterschiede zurückgeführt werden. Die RS-Analyse unterstreicht, dass nur porenskalige Simulationen in physikalischen Rekonstruktionen, die die CBD einschließen, dazu in der Lage sind, die durch EIS-Experimente bestimmte ionische Tortuosität zu reproduzieren.

In Kapitel 4 wird die Morphologie von zwei *sheet-type* Festkörperbatterien (engl. *sheet-type all-solid-state batteries*, ST-ASSBs) mit verschiedenen Festelektrolyten (engl. *solid electrolytes*, SEs) untersucht, um mikrostrukturelle Einflüsse zu identifizieren, die die Kinetik der Batterie limitieren. Der Slurry-basierte Herstellungsprozess ist vergleichbar mit dem konventioneller LIBs und somit relevant für eine mögliche Massenproduktion. Als schwefelbasierte SEs dienen *β*-LPS (*β*-Li_3PS_4) und LPSI (2 Li_3PS_4·LiI) mit Leitfähigkeiten von 0,2 mS cm^{-1} bzw. 0,8 mS cm^{-1}. Während *β*-LPS aus mesoporösen Nanopartikeln

zusammengesetzt ist, weisen die LPSI-Partikel Größen bis in den µm-Bereich und keine intrinsische Porosität auf. Kleine moderne NMC 85|05|10 Partikel, die mit $LiNbO_3$ beschichtet sind, werden als Kathodenmaterial (engl. *cathode active material*, CAM) eingesetzt. Dreiphasige FIB-SEM-basierte Rekonstruktionen großer Kathodenvolumina beider Proben zeigen die Mikrostruktur des SEs, der CAM-Partikel und des Porenraums in hoher Auflösung. Der Binder, der sich als dünne Schicht über alle Oberflächen verteilt, kann aufgrund seiner geringen Größe und seines schwachen Kontrasts nicht aufgelöst werden. Die in den Rekonstruktionen gefundene Volumenverteilung der einzelnen Phasen legt nahe, dass sich der Binder bei *β*-LPS aufgrund der hohen intrinsischen Oberfläche vorwiegend innerhalb der nanopartikulären SE-Phase anreichert, während er sich für LPSI auf alle Grenzflächen verteilt. Porenraum ist toter Raum in ASSBs, da er Transportpfade im SE tortuoser macht, den Ladungsdurchtritt an der SE–CAM-Grenzfläche verhindert und die volumetrische Energiedichte der Batterie herabsenkt. Für *β*-LPS kann ein Hohlraum-Anteil von 1 vol% gefunden werden, während die LPSI-Probe einen Anteil von 11 vol% aufweist. Die Hohlräume in der LPSI-basierten Kathode sind zudem größer und vor allem im SE oder an der SE–CAM-Grenzfläche zu finden. Für die *β*-LPS-basierte Kathode sind die Hohlräume vorwiegend von CAM umgeben. Dies erklärt, dass für *β*-LPS eine größere aktive Oberfläche von 87% gefunden wird, während für LPSI 62% der CAM-Oberfläche in direktem Kontakt zum SE stehen. Eine Analyse der CAM-Konnektivität zeigt, dass jeweils >99% des CAM-Volumens direkt verknüpft sind, wodurch der Elektronentransport innerhalb der Kathode ungehindert stattfinden kann. Numerische Transportsimulationen zeigen, dass die Elektrolytphase der LPSI-Probe verglichen zur *β*-LPS-Probe eine doppelt so hohe ionische Tortuosität aufweist. In Zyklisierungsexperimenten weist die LPSI-Probe hingegen eine höhere Entladekapazität (178 mAh/g vs. 150 mAh/g) und geringere Überspannungen auf. Mithilfe eines generalisierten TLM wurden die einzelnen Beiträge zur Batterieimpedanz abgeschätzt, um so Rückschlüsse auf kinetische Limitierungen in den beiden Proben ziehen zu können. Dabei kommt dem Ladungstransfer an der SE–CAM-Grenzfläche mit Abstand der größte Anteil zu, während die chemische Li-Diffusion im CAM und der ionische Transport in der SE-Phase nur einen vergleichbar geringen Anteil ausmachen. Aufgrund ihrer ähnlichen chemischen Zusammensetzung weisen beide Elektrolyte einen ähnlichen Ladungstransferwiderstand auf. Durch die höhere effektive SE–CAM-Grenzfläche der LPSI-Probe wird schließlich ein geringerer effektiver Ladungsdurchtrittswiderstand erhalten, was die geringeren Überspannungen erklärt. Insbesondere in der Absenkung der Grenzflächenimpedanz liegt folglich noch großes Potential, um die Performanz von ST-ASSB weiter zu verbessern.

Im fünften Kapitel wird die Technik der physikalischen Rekonstruktion auf hierarchische poröse Materialien (HPMs) angewandt, die ein hohes Potential für den Einsatz im Gebiet der Energiespeicherung und -konversion aufweisen. HPMs sind eine Klasse funktionaler Materialien, die sich durch eine große spezifische Oberfläche und einem verknüpften

Porenraum mit großer Zugänglichkeit auszeichnen. Die Studie präsentiert eine universelle Laser-basierte Prozedur zur Generierung metalloxidischer HPMs mit einer blumenkohlartigen Morphologie. Durch die Verwendung eines Nanosekundenlasers ist der Herstellungsprozess leicht zu implementieren, lösungsmittelfrei und skalierbar. Die resultierenden hybriden Mikro-/Nanostrukturen lassen sich auf einer Vielzahl von Metallsubstraten über einen großen Bereich von Schmelzpunkten erzeugen. Die Morphologie der Superstrukturen kann durch eine Variation der Laserparameter direkt kontrolliert werden. Mithilfe einer FIB-SEM-basierten Rekonstruktion wird der Entstehungsprozess näher untersucht. Dazu werden die blumenkohlartigen Strukturen auf Kupfermetall erzeugt, in Epoxidharz eingebettet und physikalisch rekonstruiert. Querschnitte der Superstrukturen zeigen einen ringartigen Aufbau, der an Baumringe erinnert. Diese lassen sich durch Ellipsen mit konstantem Mittelpunkt und linear ansteigenden Ellipsensehnen anpassen, was zeigt, dass die erzeugten Strukturen einem idealen Ellipsoid ähneln. Der Abstand der einzelnen Ringe ist konstant und abhängig vom Laserscanlinienabstand. Die Porosität steigt nach außen hin, was zu einer großen externen Oberfläche führt. Es entsteht ein hierarchisches Porennetzwerk mit Durchmessern vom Nanometer- bis in den Mikrometerbereich. Bei der Erzeugung rastert der Laser linienförmig über die Metalloberfläche, wodurch Material schmilzt und teilweise verdampft. Dabei oxidiert das Metall teilweise. In einem Selbstorganisationsprozess entstehen Mikrostrukturen, die, bedingt durch den gewundenen Laserpfad, durch schrittweise Rekondensation schichtweise wachsen. Es entsteht eine komplexe und über mehrere Größenordnungen selbstähnliche Morphologie. Die ermittelte fraktale Dimension entspricht interessanterweise der von natürlichem Blumenkohl. Das Konzept lässt sich auf eine Vielzahl von Materialien übertragen, insbesondere auch auf Übergangsmetalle, wie sie in Kathodenmaterialien für LIBs eingesetzt werden.

Abschließend lässt sich zusammenfassen, dass diese Arbeit neue Einblicke in die Mikrostruktur von Batterieelektroden liefert. Hierfür wird ein Protokoll zur zwei- und dreiphasigen Rekonstruktion entwickelt, und auf eine Vielzahl verschiedener Proben angewandt. Es wird gezeigt, dass nur durch eine direkte Abbildung der Morphologie sichere Rückschlüsse über den Grund von Transportlimitierungen und über morphologische Heterogenität gezogen werden können. FIB-SEM-Tomographie ist die Methode der Wahl für physikalische Rekonstruktionen von Elektroden, da zum einen eine ausreichend hohe Auflösung erzielt wird und zum anderen auch leichte Elemente, wie sie beispielsweise in der CBD zu finden sind, gut abgebildet werden. Eine Optimierung der Elektrodenmorphologie zur Reduzierung von Transportlimitierungen wird helfen, LIB in Zukunft noch leistungsfähiger zu machen.

II. Abstract

Climate change is one of the greatest challenges of the century. Compared to the pre-industrial era, the average global temperature has already risen by 1 °C (1.5 °C in Germany). The temperature increase is caused by the emission of greenhouse gases, which convert sunlight reflected into the atmosphere into heat. Around 20% of the CO_2 emissions in Germany are attributed to the transport sector. Electro mobility represents a possible solution to this problem. Powerful lithium-ion batteries (LIBs) are needed for mobile storage of electricity from renewable energy. Three main approaches are being pursued to improve the performance of LIBs: the search for new materials, the development of new battery concepts, and the optimization of existing systems. This work takes the latter approach by imaging and studying the electrode morphology using tomography. Detailed morphological analysis and simulations are used to identify microstructural kinetic limitations. The results are compared with electrochemical characterization methods. In the following, the results of the five chapters of this cumulative dissertation are summarized. Chapters 1–3 are related to the study of transport limitations in batteries using a liquid electrolyte, Chapter 4 deals with all-solid-state batteries, and Chapter 5 applies the reconstruction approach to a hierarchical porous material.

In Chapter 1, transport limitations of an electrode are detected by both reconstruction-simulation (RS) and electrochemical measurements, and the results of the two approaches are compared to each other. The aim of the study is to determine the ionic tortuosity in both ways to quantify transport limitations in the pore space, filled by a liquid electrolyte. Graphite, which is a common anode material, is chosen as the active material. First, graphite electrodes with different thicknesses are investigated by electrochemical impedance spectroscopy (EIS) in a symmetrical cell setup. The resulting spectra are fitted using the transmission line model (TLM), which describes the impedance of porous electrodes. The analysis reveals an ionic tortuosity of $\tau_{\mathrm{EIS}} = 7.3$. Second, one graphite electrode is physically reconstructed over the entire cross-section using FIB-SEM tomography. For this purpose, the pore space of the electrode is infiltrated by an osmium-based contrast agent. The space which is filled by the liquid electrolyte in normal battery operation is thus directly imaged and the contrast of the resulting image stack is enhanced, facilitating an accurate reconstruction. A comprehensive morphological analysis is conducted featuring porosity profiles, the geometric tortuosity, and a chord length distribution (CLD) of the solid phase and void space. All analyses are performed with regards to the spatial direction, showing that the flaky graphite particles form a distinct anisotropic microstructure. This leads to strong transport hindrances in the direction perpendicular to the current collector. The reconstruction volume is verified to be representative by a finite-size analysis, which is indispensable in order to obtain reliable results. Diffusion simulations based on a random-walk approach yield a similar tortuosity value of $\tau_{\mathrm{RS}} = 6.55$, which is within the experimental error of τ_{EIS}. Consequently, this study shows that long-range

transport simulations (without considering double-layer formation) and EIS combined with TLM (ion transport in the pores and double-layer formation) give comparable results even for a highly anisotropic microstructure. Compared to FIB-SEM tomography along with numerical simulations, EIS is significantly faster, cheaper, and easier to apply, and it is available in almost every electrochemical laboratory. However, the underlying microstructural features causing steric transport hindrances can only be analyzed by appropriate tomography methods. EIS screenings can be used to detect transport limitations of newly designed electrodes. Thus, the results of this study may contribute to the future development of more powerful electrodes.

In Chapter 2, the impedance of electrodes with variable thickness is examined for different liquid electrolyte systems. For this purpose, batteries are first cycled using a tetraglyme-based solvate ionic liquid (IL), a conventional carbonate-based electrolyte, and a LiFSI in IL electrolyte system. The area-specific resistances are estimated based on the overvoltages at 50% state of charge, which increase in the order; carbonate-based electrolyte < IL < solvate IL. The different electrolyte systems are characterized based on the electrode thickness by means of EIS. Special attention is paid to the impedance at 10^{-4} Hz, since this frequency corresponds approximately to the time scale of typical cyclization rates of 1–2 C. The impedances of the electrolyte systems increase in the same order as it was observed in the cycling experiments. Next, the analytical model of Huang and Zhang is used to shed light on the individual contributions to the overall electrode impedance for the carbonate-based electrolyte and the solvate IL. This model calculates the electrode impedance, taking into account salt concentration polarization in the electrolyte-filled pore space. It is applicable to electrolyte systems consisting of one type each of cation and anion in a solvent. Therefore, the LiFSI in IL electrolyte cannot be analyzed by this model. At 10^{-4} Hz, only a weak dependence on the electrode thickness is observed for the real part and the modulus of the complex impedance in the range of 50–100 µm. Using a generalized TLM, the impedance contributions of ion transport and thickness-dependent charge transfer as well as solid phase diffusion are analyzed separately. The impedance of ion transport for both the solvate IL and the carbonate-based electrolyte is higher than the contribution from charge transfer and solid phase diffusion at 10^{-4} Hz and for thicknesses between 50–150 µm. This explains the low dependence on thickness of the impedance spectra and leads to the conclusion that greater electrode thicknesses than the conventional 80 µm would be possible, given that the morphological properties can be kept constant over the entire electrode.

Chapter 3 examines the influence of the carbon-binder domain (CBD) on Li^+ charge transport in the electrolyte phase by using a RS approach and compares the results with EIS experiments. The morphology of the electrolyte-filled pore space in LIBs is influenced by the microstructure of the solid components: active material (AM) particles, binder, and conductive carbon. The binder and conductive carbon form an interpenetrating nanoporous phase, the CBD. While the

µm-scaled AM particles can be easily reconstructed by 3D tomography, the CBD is often not taken into account due to its small feature size. In this chapter, a $LiCoO_2$ (LCO) composite cathode is physically reconstructed by means of FIB-SEM tomography to determine the Li^+ transport tortuosity and to morphologically characterize the CBD. EIS experiments in the framework of the TLM are conducted to determine the ionic tortuosity experimentally and are compared with the RS approach. The three-phase reconstruction provides both the hitherto highest reported resolution down to a voxel size of $(13.9 \times 13.9 \times 20.0)\,nm^3$, and an unprecedented large volume with a minimum edge length of 20 µm. This enables a representative description of the interstitial pore space. A detailed morphological analysis is presented to characterize the morphology of the void space featuring CLD, specific surface area determination, connectivity analysis, and calculation of the geometric tortuosity. The results show that the microstructural properties of the cathode are affected by the presence of the CBD spanning the void space as a convoluted network and leading to more tortuous and constricted Li^+ transport pathways. Pore-scale numerical diffusion simulations reveal a significantly higher ionic tortuosity of 1.9 when the CBD is taken into account compared to 1.5 without CBD, which cannot be solely attributed to the lower porosity. The RS analysis underscores that only pore-scale simulations in physical reconstructions including the CBD can reproduce experimental tortuosity values derived from EIS.

In Chapter 4, the morphology of two sheet-type all-solid-state battery (ST-ASSB) cathodes with different solid electrolytes (SEs) is investigated to identify kinetic limiting features. The slurry-based manufacturing process of ST-ASSBs is comparable to that of conventional lithium-ion batteries and is thus relevant for eventual mass production. The sulfur-based SEs are *β*-LPS (*β*-Li_3PS_4) and LPSI ($2\,Li_3PS_4{\cdot}LiI$) with conductivities of $0.2\,mS\,cm^{-1}$ and $0.8\,mS\,cm^{-1}$, respectively. While *β*-LPS is composed of mesoporous nanoparticles, the LPSI particles exhibit sizes up to the µm range and no intrinsic porosity. Small state-of-the-art NMC 85|05|10 particles coated with $LiNbO_3$ are used as cathode active material (CAM). Three-phase FIB-SEM based reconstructions of large cathode volumes in high resolution reveal structurally representative and realistic models of the SE, CAM particles, and void space. The binder, which is distributed as a thin layer over all surfaces, cannot be resolved due to its small feature size and poor contrast. The volume fractions found in the reconstructions suggest that, for *β*-LPS, the binder accumulates predominantly within the nanoparticulate SE phase due to the high intrinsic surface area. For LPSI, it is distributed over all interfaces. Void space is dead space in ASSBs as it makes transport paths in SE more tortuous, prevents charge transfer at the SE–CAM interface, and reduces the volumetric energy density of the battery. For the *β*-LPS-based cathode, a small void fraction of 1 vol% can be found, while LPSI exhibits a much higher fraction of 11 vol%. The voids in the LPSI-based cathode are larger compared to *β*-LPS and mainly found at the SE or SE–CAM interface. For *β*-LPS, the voids are predominantly surrounded by CAM. This explains the larger active surface area of 87% for *β*-LPS, while 62%

of the CAM surface is in direct contact with the SE for LPSI. An analysis of CAM connectivity shows that >99% of the CAM volume is directly connected in each case, making electron transport within the cathode uncritical. Numerical transport simulations show that the ionic tortuosity of the electrolyte phase of the LPSI sample is twice that of the β-LPS sample. In contrast, cycling experiments reveal that the LPSI sample has a higher discharge capacity (178 mAh/g vs. 150 mAh/g) and lower overvoltage. Using a general TLM, the individual contributions to the battery impedance were estimated to draw conclusions about kinetic limitations in the two samples. The charge transfer at the SE–CAM interface accounts for by far the largest impedance, while Li chemical diffusion in the CAM and ionic transport in the SE phase account for only a comparably small fraction. Due to their similar chemical composition, both electrolytes exhibit a similar charge transfer resistance. However, due to the higher effective SE–CAM interface of the LPSI sample, a lower effective charge transfer resistance is obtained, which explains the lower overvoltage. Consequently, especially in lowering the interfacial impedance, there is still great potential to further improve the performance of ST-ASSB.

In the fifth Chapter, the physical reconstruction technique is applied to hierarchical porous materials (HPMs), which have a high potential for use in the field of energy storage and conversion. HPMs are a class of functional materials characterized by a large specific surface area and an interconnected pore space with high accessibility. The study presents a universal laser-based procedure for generating metal oxide HPMs with cauliflower-like morphology. Based on a facile nanosecond pulsed laser-treatment, the manufacturing process is easy to implement, solvent-free, and scalable. The resulting hybrid micro-/nanostructures can be generated on a variety of metallic substrates over a wide range of melting points. The morphology of the superstructures can be directly controlled by varying the laser parameters. The formation process is investigated in detail by means of FIB-SEM tomography. For this purpose, the cauliflower-like structures are generated on copper metal, embedded in epoxy resin, and physically reconstructed. Cross-sections of the superstructures show a ring-like pattern similar to tree rings. These rings can be fitted by ellipses with a constant center point and linearly rising elliptical axes, which makes the structures resemble an ideal ellipsoid. The distance between the single rings is constant and depends on the laser scan line distance. The porosity increases towards the outer surface, resulting in a large external surface area. A hierarchical network of pores with diameters from nanometer to micrometer is created. During generation, the laser scans the metal surface in a linear pattern, causing material to melt and partially evaporate whereby the metal partially oxidizes. In a self-organization process, microstructures are created which grow layer by layer through stepwise recondensation due to the meandering laser path. A complex and over several orders of magnitude self-similar morphology is formed. Interestingly, the determined fractal dimension corresponds to that of

natural cauliflower. The concept can be applied to a variety of materials, especially transition metals, such as those used as cathode material in LIBs.

In conclusion, this work provides new insights into the microstructure of battery electrodes. For this purpose, a protocol for two- and three-phase reconstructions is developed and applied to a variety of different samples. It is shown that only direct imaging of the morphology provides reliable conclusions about the reason for transport limitations and morphological heterogeneity. FIB-SEM tomography is the method of choice for physical reconstructions of electrodes as it achieves a sufficiently high resolution and provides a high sensitivity towards light elements, such as those found in the CBD. Optimization of the electrode morphology to reduce transport limitations will help to make LIBs even more efficient in the future.

III. Introduction

III.1 Motivation

Climate change threatens natural systems and the basis of life for millions of people.[1] Compared to the pre-industrial age, the global average temperature has already increased by 1 °C (1.5 °C in Germany). Consequences are already noticeable today, including more frequent extreme weather events, rising sea levels due to the melting of glaciers and polar ice, and an increasing loss of biodiversity. Global warming is attributed to the emissions of greenhouse gases like CO_2, methane, nitrous gases, and fluorinated gases, which convert sunlight reflected in the atmosphere into heat and thus warm it up. In the Paris Climate Convention in 2015, 197 countries committed themselves to keep global warming significantly below 2°C.[2] The emission of greenhouse gases has to be reduced significantly in order to achieve this goal and to combat climate change.

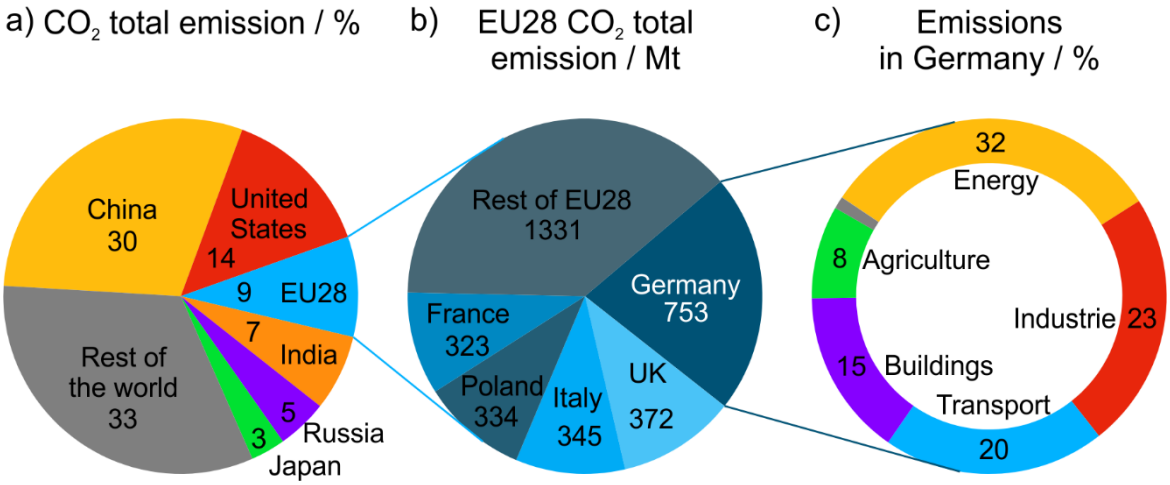

Figure III.1: a) CO_2 emissions by selected regions in 2018.[3] b) Share of the EU28 CO_2 emissions in Mt (2018).[3] c) CO_2 emissions in Germany by sector (2019).[4] 20% of Germany's CO_2 emissions are attributed to the transport sector.

Germany's CO_2 emissions of 9.2 tons per capita in 2018 are almost twice the global average.[3] Around 20% of Germany's CO_2 emissions are attributable to the transport sector (cf. Figure III.1), whose emissions have even risen by 5% compared to 1990.[2] Motorized road traffic causes 94% of the transport emissions, due to the predominance of fossil fuels.[4] There is considerable saving potential in the transport sector. Besides a significant reduction of individual traffic and a shift of freight traffic to rail, electromobility represents an important technology for reducing transport emissions. Taking into account the present German electricity

mix with 42% renewable energy, electric cars already cause around 27% less emissions than conventional cars with petrol engines (during the whole life cycle).[2] This reduction can be further improved by increasing the share of renewable energies. To achieve this goal, large-scale stationary energy storages are needed to compensate for fluctuations in power generation, and high-performance mobile energy storages to further increase the range of electric cars. The lithium-ion battery technology is key to overcome today's limitations.[5]

III.2 Lithium-ion battery

III.2.1 Principle and design

The lithium-ion battery (LIB) changed our lives. It enabled the development towards modern smartphones, laptops became lighter and thinner, and, due to its high gravimetric and volumetric energy density, it is replacing more and more combustion engines by electric motors in the transport sector.[6] Due to its low reduction potential and its small weight, lithium is an ideal candidate for batteries. LIBs usually consist of a transition metal oxide as cathode active material (CAM), graphite as anode material, and a separator soaked with a liquid electrolyte preventing direct electronic contact (and thus a short circuit) of both electrodes. The two electrodes are connected to each other via an external circuit, which provides electronic conduction. The electrolyte allows only ionic conduction of Li^+ cations. Figure III.2 schematically represents the setup of a LIB.[7]

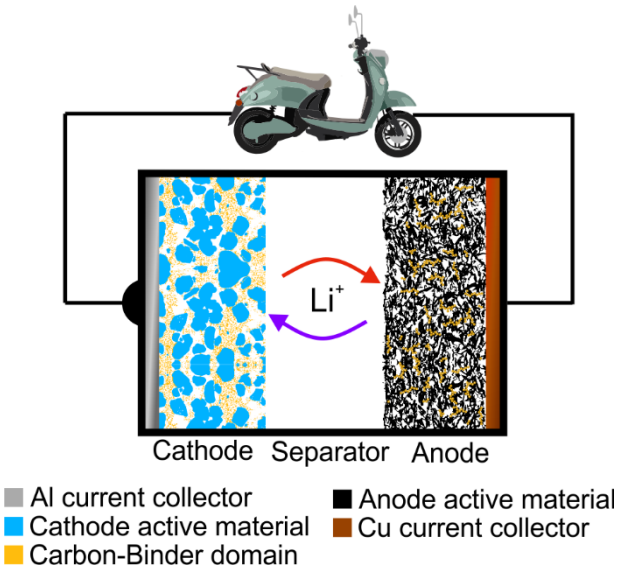

Figure III.2: Schematic representation of a lithium-ion battery. Li^+ ions intercalate the anode active material (black), e.g., graphite flakes, when the battery is charged (red arrow). Discharging the battery (purple arrow) leads to a deintercalation of Li^+ ions from the anode and transport to the cathode where Li^+ is inserted. The cathode is composed of cathode active

material (blue), e.g., $LiCoO_2$. Both electrodes are pervaded by a carbon-binder domain (orange), providing stability and electronic conduction. Al and Cu foils serve as current collectors. The stored energy can be provided for mobile applications, e.g., electric scooters.

The first rechargeable Li^+ battery was developed in the 1970s by Stanley Wittingham, who used TiS_2 as CAM and elemental lithium as anode material. Although good reversibility was achieved, the battery suffered from the comparatively low cell voltage of <2.5 V and dendrite growth.[8] Crystalline Li deposits on the anode in the form of thin needles. If the dendrites reach the cathode, a short circuit occurs, which poses enormous safety risks. Some of the cells caught fire, making a safe commercial operation impossible. Even today, modern LIBs still struggle with dendrite growth, which continues to prevent the use of elemental Li as anode material.[9] In the 1980s, John B. Goodenough's group worked on Li transition metal oxides as CAM. Goodenough used graphite as anode material, which solved the safety issues of dendrite growth. The redox potential of graphite is around 0.1 V vs. Li/Li^+ and its capacity corresponds to 372 Ah kg^{-1} for LiC_6.[6] The breakthrough of LIB technology finally came with use of layered $LiCoO_2$ (LCO) as CAM. In practice, LCO has an energy density of 140 mAh g^{-1} and cell voltages of up to 4 V can be achieved.[8] Akira Yoshino pushed the industrial production of LIBs. Finally, in 1991, Sony launched the first commercially available LIB on the market.[10] In 2019, the Nobel Prize in chemistry was jointly given to Wittingham, Goodenough, and Yoshino, highlighting the exceptional importance of this technology.[11,12]

Discharging of a battery comes with oxidation of the anode material due to deintercalation of lithium (cf. Figure III.2). At the same time, Li^+ is inserted to the cathode AM. The liquid or solid electrolyte enables ion transport. Electrons travel through the external circuit from the anode to the cathode to compensate for the positive charge of Li^+. When charging the battery, the process is reversed. In order to obtain large active surface areas, porous electrodes are used, which are composed of particles of about 1–5 µm in size. Commercial electrodes exhibit a thickness of about 80 µm and porosities of about 25%.[13] The liquid electrolyte is typically a 1 M solution of $LiPF_6$ in organic carbonates like ethylene carbonate, dimethyl carbonate, and diethyl carbonate. A thin polyethylene or polypropylene film of about 25 µm thickness is usually used as porous separator.[14,15] Furthermore, conductive carbon and binder are added to the composite electrodes. The carbon provides the electronic conduction between the AM particles and the binder mechanically stabilizes the electrode. Conductive carbon and binder form an interpenetrating phase, which is also known as the carbon binder domain (CBD).[13,16] The morphology of the CBD and its influence on ion transport will be discussed in Chapter 3.

Since cobalt is expensive and usually mined under adverse conditions,[12] in today's LIBs, Co is substituted for the most part by Mn and Ni to form $LiNi_{1-y-z}Mn_yCo_zO_2$ (NMC).[8] Depending

on the stoichiometry, capacities of about 200 mAh g^{-1} are achieved with NMC. Today gravimetric energy densities of ≲250 Wh kg^{-1} and volumetric energy densities of ≲650 Wh L^{-1} are reached.[6] Compared to 1991, modern LIBs have about four times higher capacities. However, these increases were mainly achieved by an optimized cell design.[6] Chemically, conventional LIBs are gradually reaching their limits, which is why new cell concepts such as all-solid-state batteries or, in the long term, lithium air batteries[17] are increasingly moving into focus.

III.2.2 All-solid-state batteries

In all-solid-state batteries (ASSBs), the flammable liquid electrolyte is replaced by a solid electrolyte (SE), thus providing a higher degree of safety. SEs exhibit a negligible electronic conductivity, so they also act as separator. The mechanical strength of SEs could help to inhibit dendrite growth, which would allow elemental Li to be used as anode material.[14,18,19] Especially sulfide-based SEs have high potential due to their high conductivities[20,21] of 10^{-4}–10^{-2} S cm^{-1} (approx. 10^{-2} S cm^{-1} for liquid carbonate-based electrolytes), their mechanical deformability, and the weak resistive interfaces they form to the (coated) AM.[20] Typical examples for sulfide-based SEs are amorphous 2 Li_3PS_4·LiI (LPSI, conductivity: ≈ 0.8 mS cm^{-1})[22] and crystalline β-Li_3PS_4 (β-LPS, ≈ 0.2 mS cm^{-1}),[23] $Li_{10}GeP_2S_{12}$ (LGPS, ≈ 5 mS cm^{-1}),[21,24] and argyrodite-type Li_6PS_5Cl (≈ 2 mS cm^{-1}).[25,26]

In contrast to a liquid electrolyte, which almost completely wets the AM, high mechanical pressure is required for the operation of ASSBs to establish sufficient contact between the AM and the SE. Volume expansion of the AM can also cause cracks and voids in the SE and the AM, which have a negative effect on cell performance.[18,27,28] Nevertheless, ASSBs offer great potential due to the possible use of Li anodes and the higher degree of safety, which makes them an important field of research. The morphology of ASSBs, using LPSI and β-LPS as SE, will be analyzed in detail in Chapter 4.

III.2.3 Transport in porous electrodes

When the battery is discharged, Li^+ ions travel from the anode to the cathode. The movement of charge carriers in the electric field between the two electrodes is called migration. The charge transfer reaction at the electrolyte–CAM interface can cause the formation of salt concentration gradients in the liquid electrolyte. Li^+ ion transport in liquid electrolytes is consequently also affected by diffusion (in addition to migration). Solid electrolytes are usually single-ion conductors. Due to electroneutrality constraints, concentration gradients cannot form here, so only migration is relevant for transport. The anode active material and the CAM are blocking

for anions. After intercalation, Li is transported ambipolar as Li^+ and electrons within the active material. The electrons required for charge balance are provided by the current collector and are electronically conducted through the CAM and carbon additives. The relevant transport pathways, which are investigated in this thesis, are illustrated in Figure III.3a–d.

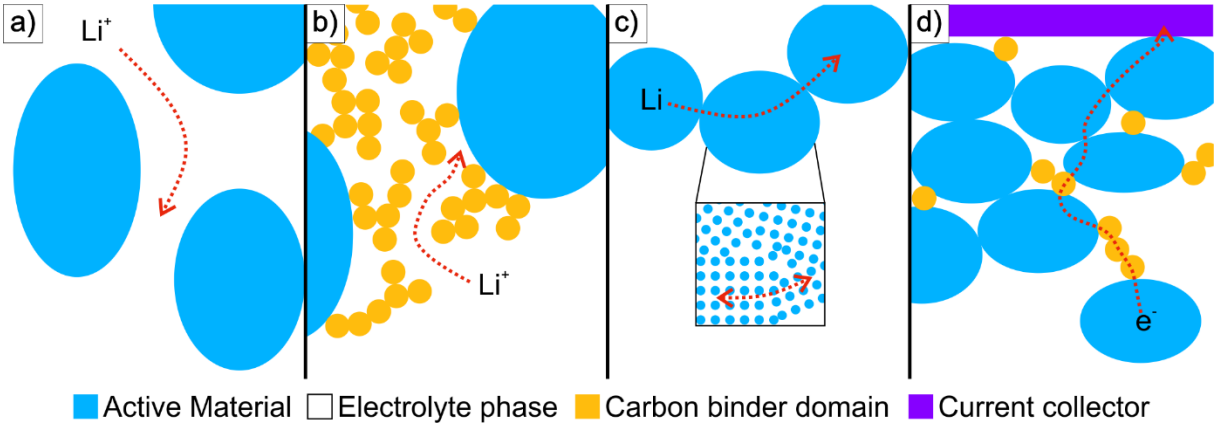

Figure III.3: Transport in porous electrodes of LIBs: a) Li^+ transport in the electrolyte phase between AM particles (length scale: <1000 nm), b) Li^+ transport in the electrolyte phase within the CBD (length scale: <100 nm), c) Ambipolar Li transport (Li^+ and electrons) in the solid state between and within primary AM particles (AM particle length scale: 1–5 µm), and d) electron transport to or from the current collector via AM particles and the CBD.

The performance of LIBs depends on thermodynamic parameters like the cell potential as well as kinetic limitations that contribute to the overpotential during charging and discharging of the battery cell. The kinetic limitations can be grouped into three categories: Ohmic polarization, activation polarization, and concentration polarization.[10] The resistances of cell components like the SE, the AM, the current collector, and the wiring contribute to the ohmic polarization. Activation polarization is caused by an inhibited charge transfer at interphases (e.g. by a limited AM–electrolyte contact area).[29] Lastly, concentration polarization describes mass transport limitations. These include diffusion hindrances of the active species in the electrolyte phase of the porous electrode.[10] In batteries using a liquid electrolyte, salt concentration gradients are formed due to charge transfer at the electrolyte–CAM interface. Interactions between the ions lead to correlated movements, which have to be taken into account.[30] The impedance increases with decreasing Li^+ transference number and decreasing ionic conductivity. The influence of kinetic limitations on battery performance will be discussed more closely in Chapters 1–4.

III.2.4 Impedance of porous electrodes

Analytical battery models can be used to describe the impedance *Z* of porous electrodes. If all relevant processes are considered by the respective model, their individual impedance contributions can be quantified, which allows the identification of kinetic limitations. The transmission line model (TLM) is an example for an 1D model, which interprets transport and electrochemical processes in terms of discrete electrical elements.[31] A general TLM is given by

$$Z = \sqrt{\frac{Z_{\mathrm{ion}} Z_{\mathrm{loc}}}{l_{\mathrm{p}} a_{\mathrm{v}}}} \cdot \coth\left(\sqrt{\frac{Z_{\mathrm{ion}} l_{\mathrm{p}} a_{\mathrm{v}}}{Z_{\mathrm{loc}}}}\right) \qquad \text{III.1}$$

Z_{ion} denotes the ion transport impedance in the electrolyte phase, Z_{loc} the local impedance including charge transfer at the electrolyte–CAM interface, double layer formation, and Li chemical diffusion in the CAM particles, l_{p} the pore length, and a_{v} corresponds to the surface of the active material particles per unit volume of the electrode. Two limiting cases can be defined depending on Z_{ion} and Z_{loc}. If $Z_{\mathrm{ion}} \gg Z_{\mathrm{loc}}/(l_{\mathrm{p}} a_{\mathrm{v}})$, the coth function becomes unity. The impedance *Z* can then be stated as

$$Z = \sqrt{\frac{Z_{\mathrm{ion}} Z_{\mathrm{loc}}}{l_{\mathrm{p}} a_{\mathrm{v}}}} \qquad \text{III.2}$$

For the case that $Z_{\mathrm{ion}} \ll Z_{\mathrm{loc}}/(l_{\mathrm{p}} a_{\mathrm{v}})$, a Taylor expansion of the coth function results in

$$Z = \frac{Z_{\mathrm{loc}}}{l_{\mathrm{p}} a_{\mathrm{v}}} + \frac{Z_{\mathrm{ion}}}{3} \qquad \text{III.3}$$

The general TLM is discussed in more detail in Chapter 2 for liquid electrolytes and in Chapter 4 for ASSBs. An alternative analytical battery model is proposed by Huang and Zhang,[32] which is based on the concentration-solution theory and explicitly includes the formation of salt concentration gradients.[33] Both models are discussed in detail in Chapter 2 . Figure III.4 shows calculated impedance spectra in the framework of both models. A LCO composite cathode with a thickness of 50 µm is assumed using 1M $LiPF_6$ in carbonates as liquid electrolyte. Both models show good agreement, especially in the high-frequency range where ion migration in the liquid electrolyte and charge transfer at the electrolyte–CAM interface take place. At lower frequencies, Li chemical diffusion in the AM and diffusion in the liquid electrolyte dominate.

At very low frequencies, the chemical capacitance of the AM becomes relevant, and the imaginary part of the impedance tends towards $-\infty$.

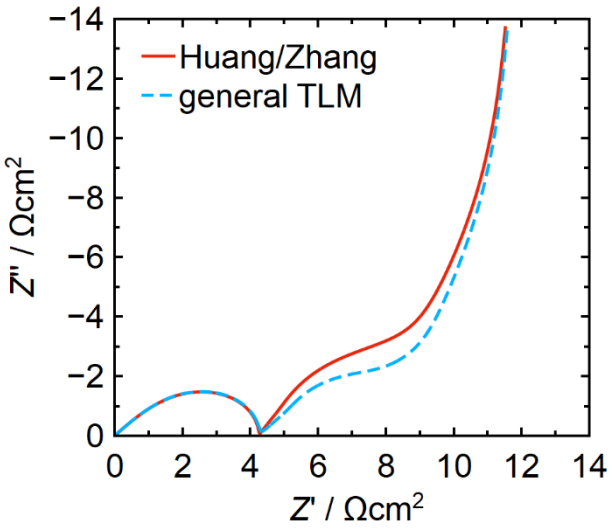

Figure III.4: Nyquist plot of calculated impedances (10^6–10^{-4} Hz) of a LCO composite cathode (thickness: 50 µm) with 1M $LiPF_6$ in carbonates as liquid electrolyte using the model by Huang and Zhang (red) and a general TLM (blue) as described in Chapter 2.

III.2.5 How to improve lithium-ion batteries?

Three different strategies are generally being pursued to improve LIBs: the search for new materials (like Ni-rich NMC or new SEs), the development of new battery concepts (like ASSBs or Li-Air batteries), and the optimization of existing systems. The latter offers considerable potential to boost battery performance by tuning the electrode microstructure to minimize kinetic limitations.[34] A detailed understanding of the Li^+ transport is essential to improve the cell design of LIBs and to reduce overpotentials. Transport in LIBs occurs on quite different length scales: mesopores in the SEI,[35] pores <100 nm within the CBD network,[36] pores <1000 nm between the AM particles, and within the AM, whose particles are 1–5 µm in size.[13] The performance of LIBs is therefore affected by many different transport processes, which extend over several orders of magnitude from the mesopore scale up to the µm range. The large range is a great challenge for an accurate description of the relevant processes in batteries if the individual microstructures are considered.

The solid components form the electrode's microstructure in a complex process during preparation. Electrodes are usually produced using a slurry coating technique. To this end, the solid components are mixed in a solvent to form a slurry and applied to the current collector as

a film. The porosity is then adjusted by calendaring. Various parameters determine the resulting microstructure.[37] These are, for example, the solvent content and composition of the solid components of the slurry, the choice of binder and conductive additives, the particle sizes of the AM (and SE), the electrode thickness, the drying time and temperature, and finally the speed, temperature, and pressure during calendaring. A variation of single parameters has a direct influence on morphological properties (such as phase distribution, porosity, pore size or electrode thickness) and thus ultimately on battery performance. This complex interplay emphasizes the need for a meaningful representation of the resulting microstructure for an accurate and detailed morphological analysis. The physical reconstruction technique directly images a porous microstructure and is introduced in the following section.

III.3 Physical reconstruction

To investigate the relationship of preparation and microstructural properties as well as the morphological interplay of the single battery components, adequate characterization methods are necessary to directly image the 3D morphology.[38] A reliable geometrical model of the battery microstructure enables to identify critical bottlenecks for ion transport, charge transfer, and electron transport. The relevant battery length scales range from atomic resolution (for characterizing charge transfer processes) up to 100 µm (for imaging electrode microstructures). Generally suitable methods for 3D imaging are atom probe microscopy (APT), scanning transmission electron microscopy (STEM), focused ion-beam scanning electron microscopy (FIB-SEM), and X-ray tomography (XRT).[39] APT and STEM are capable to image features <10 nm and are predominantly used to characterize CAM.[40,41] For imaging the interstitial pore space and the CAM particles, FIB-SEM and XRT are best suited.

XRT is a non-invasive imaging method based on the absorption of x-rays. It can image large sample volumes with edge lengths up to 1000 µm in operando. This allows large representative volumes to be imaged over the entire electrode thickness. However, the resolution in the sub-µm range is limited and materials with light atomic nuclei such as those found in the CBD can only be resolved inadequately.[39,42–44] FIB-SEM, on the other hand, offers a high resolution of 5 nm, edge lengths up to 100 µm, and can also resolve light elements with sufficient contrast. It uses focused ions (mostly Ga^+) to remove material from the sample slice-by-slice. The SEM signal is used between slicing to image the cross-sectional surface. However, the method is destructive, time-consuming, and therefore expensive. It is limited to solid materials and interactions between the ion beam and the sample can distort the image.[39,42] However, due to the very high resolution and good interpretability of the resulting SEM images, FIB-SEM is the method of choice to accurately represent the morphology of battery electrodes from the nm scale up to the µm scale. For this reason, FIB-SEM tomography was used in this work for 3D reconstructions of battery electrodes.

FIB-SEM tomography is widely used in materials science and biology to reconstruct a variety of porous media. For example, chromatographic beds of silica particles can be reconstructed for ultra-high performance liquid chromatography (UHPLC) to analyze particle packing and the influence of wall effects.[45] Silica monoliths, which are also used for separation and catalysis, can also be reconstructed well using FIB-SEM and benefit from the good contrast properties and high resolution of electron microscopy.[46,47] In electrochemistry, FIB-SEM is used for the reconstruction of LIBs and solid oxide fuel cells.[48–50] In LIBs, FIB-SEM tomography accurately images all relevant components like cathode,[13,51–54] separator,[55] and anode.[56] In addition to conventional LIBs based on the use of a liquid electrolyte, the reconstruction technique is also increasingly applied to new battery concepts like ASSBs.[57–59] In the following, the technique is presented in more detail.

III.3.1 Scanning electron microscopy

SEM benefits from small de Broglie wavelengths of electrons of <1nm, which strongly increases the resolution with a high depth of field compared to light microscopy. Besides the high resolution down to 1 nm, SEM is an ideal tool for imaging as the resulting data is comparatively easy to interpret and contains morphological as well as chemical information. SEM can easily be combined with other spectroscopic methods like energy-dispersive X-ray spectroscopy **(**EDX) or structuring methods like FIB. This makes SEM a highly versatile method that is widely used in science as well as industry and goes far beyond the mere imaging of material surfaces.[60]

Several steps are involved in creating an image. At first, primary electrons (PEs) are generated in the electron gun with an acceleration voltage of 2–30 kV. Modern SEMs usually use field emission guns as electron source. The entire setup is kept under vacuum to avoid scattering of the electron beam. Electromagnetic lenses and condenser lenses are used to bundle the electrons into a fine beam. The aperture controls the number of electrons and the convergence angle. Finally, an objective lens focuses the beam onto the sample surface as a fine spot (≈ 1 nm). The beam is scanned over the sample surface in a rectangular raster. Each point on the grid corresponds to a pixel in the resulting image. When the electron beam hits the sample, a multitude of interactions occurs which can cause the emission of backscattered electrons (BSEs), secondary electrons (SecEs), and X-rays. When the electron beam enters the sample, some PEs are elastically scattered by atomic nuclei. This deflects the electrons in a new direction without losing their kinetic energy. Some of these electrons leave the sample at its surface as BSEs, which can be detected. The larger the atomic nuclei of the sample to be examined, the more likely will be the formation of BSE. Thus, BSE create a clear material contrast in the resulting image. The second important type are SecEs. PEs can knock out weakly bound electrons from the outer shells of the sample atoms. These have much lower energies of

<50 eV compared to BSEs. For this reason, only near-surface SecEs can leave the sample. SecEs are formed close to the entry point of the electron beam and enable high-resolution imaging. Since SecEs exit near the surface, they give a strong topographic contrast.[60]

The volume, in which interactions between beam and sample occurs, is called interaction volume. It is tear-shaped and depends on the material and the selected acceleration voltage of the PEs.[61] For high-resolution images, the interaction volume should be kept small in order to obtain information as close to the surface as possible. For tomography, the interaction volume has to be smaller than the slice thickness. However, decreasing the beam energy leads to a larger spot size.[60] These opposing effects must be taken into account; hence experience is required to find optimal image settings. The investigation of multiphase samples is challenging because the electron beam interacts differently with each of the phases. The detected signal is assigned to a gray value, usually between 0 and 255, representing the brightness of the respective pixel. The resulting images can be manipulated by mathematical operations, for example for contrast optimization.[45]

III.3.2 Focused ion-beam

FIB can be used for both imaging and milling of solid materials. The ion source is usually liquid Ga, which is characterized by a low melting point (30 °C) and a low volatility. The ion beam is generated by electrospray ionization in a liquid-metal ion source. For this purpose, a tungsten needle is attached below a heated Ga reservoir. By applying a high voltage, an electric field is generated which causes the liquid metal flow to the tip forming a Taylor cone. The liquid metal is ejected from the cone tip in a thin stream. The electric field ionizes the Ga. The ions are accelerated at typically 30 kV towards electrostatic lenses that focus the beam on the sample. When entering the sample, the ions hit atomic nuclei and thus trigger collision cascades. The resulting SecEs and BSEs can be detected for imaging. If the translation energy exceeds the displacement energy of an atom, it can be knocked out of the sample. This sputtering effect can be used for micromachining, for example in FIB-SEM tomography.[60,62,63]

III.3.3 FIB-SEM tomography and physical reconstruction

Dual-beam devices combine the versatile high-resolution imaging modes of SEM with the precise micromachining of FIB. The ion beam is oriented perpendicular to the sample surface while the SEM beam is arranged at an angle of 52–54°. Both beams cross at the eucentric point on the sample. FIB-SEM tomography is based on alternating cutting and imaging of the sample's cross-section. The volume can be reconstructed afterwards from the resulting image

stack by three-dimensional interpolation.[64] Figure III.5 illustrates the reconstruction workflow from sample preparation to 3D visualization.

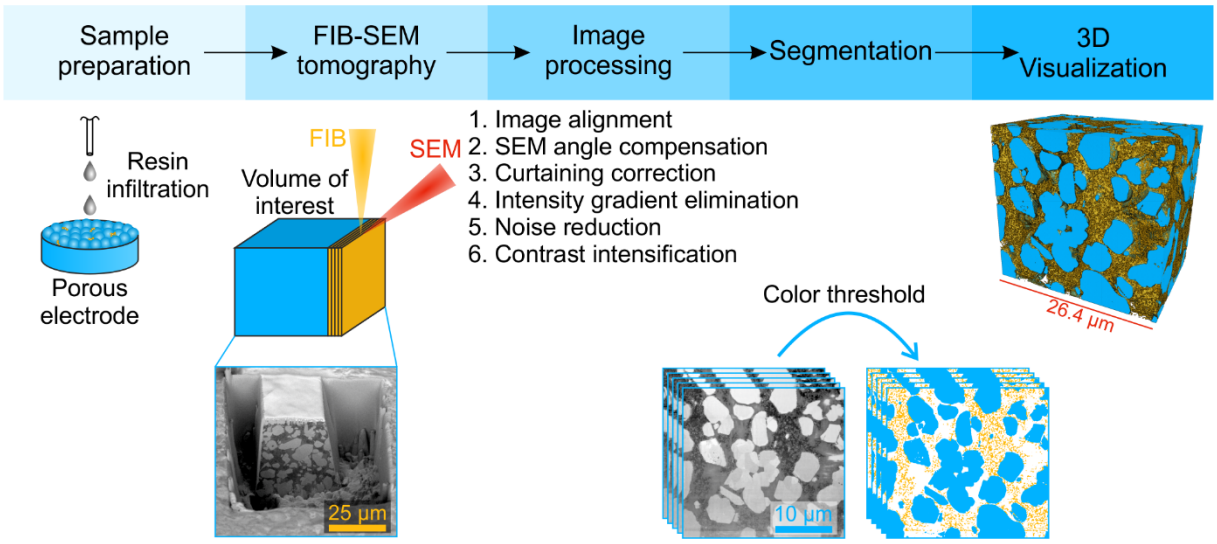

Figure III.5: Overview of the physical reconstruction workflow. First, the sample is cut and prepared for FIB-SEM tomography. A resin infiltrates the pore space to prevent charging and shine-through artifacts. In the next step, a volume of interest is defined and alternately imaged by SEM and milled by FIB. The resulting image stack is processed by eliminating artifacts. Next, a contrast-based segmentation assigns all voxels to the distinct phase. The segmented stack serves as input for the morphological analysis, pore-scale simulations, and the 3D visualization.

The definition of the volume of interest (VOI) and the image parameters is one of the most critical steps as it is always a tradeoff between acquisition time and resolution. The selected volume has to be representative. Furthermore, the size and shape of all relevant features have to be accurately characterized. Impeding finite-size effects requires reconstruction volumes with edge lengths on the order of ~25 times the morphological feature size.[65] The smallest features have to be imaged with sufficient resolution (8–10 slices per feature).[66] These prerequisites usually produce large amounts of data that have to be processed in the later image processing step.

A few preparation steps are necessary prior to the automated slice-and-view procedure. It is recommended to infiltrate the pore space with a resin. This way, the resin prevents charging at the edges of the voids and shine-through artifacts[67] of deeper layers. Moreover, the contrast to other phases can be improved (by active staining)[55] which facilitates the segmentation in the

reconstruction procedure. The VOI should be protected against unwanted sputtering by depositing a Pt or C protective layer on its surface. A smooth edge furthermore reduces the formation of curtaining artifacts, which are often caused by an uneven cross-section.[63] Curtaining occurs in the form of stripes on the resulting SEM images, which impairs subsequent image interpretation. A U-shaped trench is cut around the VOI and its cross-section is polished. The trench reduces shadows (intensity gradients) on the cross-sectional surface and collects sputtered material, thus avoiding redeposition on the sample.

A large stack of images is obtained from the automated slice-and-view process (up to >1000 images). Each voxel represents a color value and 3D coordinates. Height and width of the voxel are defined by the SEM image resolution while its depth corresponds to the FIB slice thickness. The goal of the subsequent image restoration is to remove image artifacts by voxel-based mathematical operations in order to enable the subsequent segmentation of the different phases. This typically includes image alignment, correction of the SEM incident angle, removal of curtaining effects as well as intensity gradients, noise reduction, and contrast enhancement (see Figure III.5).[45] Afterwards, a color value range is assigned to each material phase, whereby the grayscale images are segmented. Besides this simple contrast-based segmentation, more advanced approaches also include the respective voxel environment.[68] Modern machine learning approaches use neural networks, which are trained by means of supervised learning to distinguish between individual phases.[69]

The reconstructed microstructure allows for a detailed morphological analysis to characterize its morphology. This includes the recording of chord length distributions (CLD),[70,71] the determination of volume fractions, surfaces,[72] contact areas,[13] the calculation of the geometric/geodetic tortuosity,[70] the fractal dimension[73] as well as the connectivity,[70] and distribution of the individual phases. Furthermore, the reconstruction serves as input for realistic pore-scale simulations.[59,74–78] The reconstruction–simulation (RS) approach enables to quantify rate capability limitations of LIBs and to link the results of electrochemical measurements with microstructural features. Chapters 1 and 3–5 feature physical reconstructions and provide more details on morphological analysis and the RS approach.

III.4 References

[1] M.R. Allen, O.P. Dube, W. Solecki, F. Aragón-Durand, W. Cramer, S. Humphreys, M. Kainuma, J. Kala, N. Mahowald, Y. Mulugetta, R. Perez, M. Wairiu, K. Zickfeld in *Global Warming of 1.5 ºC*. Special Report (Ed.: Intergovernmental Panel on Climate Change), **2018**.

[2] M. Welke, M. Beck, *Climate Action in Figures*. *Facts, Trends and Incentives for German Climate Policy 2020 edition*, **2020**.

[3] M. Crippa, G. Oreggioni, D. Guizzardi, M. Muntean, E. Schaaf, E. Lo Vullo, E. Solazzo, F. Monforti-Ferrario, J. Olivier, E. Vignati, *Fossil CO2 and GHG emissions of all world countries*. *2019 report*, Publications Office of the European Union, Luxembourg, **2019**.

[4] P. Gniffke, *National trend tables for greenhouse gas emissions by sectors of the German Climate Protection Act*. *1990 - 2018*, Dessau, **2020**.

[5] M. M. Thackeray, C. Wolverton, E. D. Isaacs, *Energy Environ. Sci.* **2012**, *5*, 7854.

[6] A. Manthiram, *ACS Cent. Sci.* **2017**, *3*, 1063.

[7] J. B. Goodenough, K.-S. Park, *J. Am. Chem. Soc.* **2013**, *135*, 1167.

[8] A. Manthiram, *Nat. Commun.* **2020**, *11*, 1550.

[9] H. Liu, X.-B. Cheng, J.-Q. Huang, H. Yuan, Y. Lu, C. Yan, G.-L. Zhu, R. Xu, C.-Z. Zhao, L.-P. Hou et al., *ACS Energy Lett.* **2020**, *5*, 833.

[10] M. Winter, R. J. Brodd, *Chem. Rev.* **2004**, *104*, 4245.

[11] P. V. Kamat, *ACS Energy Lett.* **2019**, *4*, 2757.

[12] R. F. Service, *Science* **2019**, *366*, 292.

[13] L. Almar, J. Joos, A. Weber, E. Ivers-Tiffée, *J. Power Sources* **2019**, *427*, 1.

[14] K. M. Abraham, *J. Phys. Chem. Lett.* **2015**, *6*, 830.

[15] M. F. Lagadec, R. Zahn, V. Wood, *Nat. Energy* **2019**, *4*, 16.

[16] G. Liu, H. Zheng, S. Kim, Y. Deng, A. M. Minor, X. Song, V. S. Battaglia, *J. Electrochem. Soc.* **2008**, *155*, A887.

[17] P. G. Bruce, S. A. Freunberger, L. J. Hardwick, J.-M. Tarascon, *Nat. Mater.* **2011**, 19.

[18] J. Janek, W. G. Zeier, *Nat. Energy* **2016**, *1*, 16141.

[19] C. Sun, J. Liu, Y. Gong, D. P. Wilkinson, J. Zhang, *Nano Energy* **2017**, *33*, 363.

[20] A. Miura, N. C. Rosero-Navarro, A. Sakuda, K. Tadanaga, N. H. H. Phuc, A. Matsuda, N. Machida, A. Hayashi, M. Tatsumisago, *Nat. Rev. Chem.* **2019**, *3*, 189.

[21] N. Kamaya, K. Homma, Y. Yamakawa, M. Hirayama, R. Kanno, M. Yonemura, T. Kamiyama, Y. Kato, S. Hama, K. Kawamoto et al., *Nat. Mater.* **2011**, *10*, 682.

[22] S. Spannenberger, V. Miß, E. Klotz, J. Kettner, M. Cronau, A. Ramanayagam, F. Di Capua, M. Elsayed, R. Krause-Rehberg, M. Vogel et al., *Solid State Ionics* **2019**, *341*, 115040.

[23] M. Duchardt, M. Diels, B. Roling, S. Dehnen, *ACS Appl. Energy Mater.* **2020**, *3*, 6937.

[24] S. Wenzel, S. Randau, T. Leichtweiß, D. A. Weber, J. Sann, W. G. Zeier, J. Janek, *Chem. Mater.* **2016**, *28*, 2400.

[25] R. P. Rao, S. Adams, *Phys. Status Solidi A* **2011**, *208*, 1804.

[26] S. Wenzel, S. J. Sedlmaier, C. Dietrich, W. G. Zeier, J. Janek, *Solid State Ionics* **2018**, *318*, 102.

[27] X. Wu, J. Billaud, I. Jerjen, F. Marone, Y. Ishihara, M. Adachi, Y. Adachi, C. Villevieille, Y. Kato, *Adv. Energy Mater.* **2019**, *9*, 1901547.

[28] R. Ruess, S. Schweidler, H. Hemmelmann, G. Conforto, A. Bielefeld, D. A. Weber, J. Sann, M. T. Elm, J. Janek, *J. Electrochem. Soc.* **2020**, *167*, 100532.

[29] C. H. Hamann, W. Vielstich, *Elektrochemie*, Wiley-VCH-Verlag GmbJ &Co. KGaA, Weinheim, **2005**.

[30] N. M. Vargas-Barbosa, B. Roling, *ChemElectroChem* **2020**, *7*, 367.

[31] Z. Siroma, N. Fujiwara, S. Yamazaki, M. Asahi, T. Nagai, T. Ioroi, *Electrochim. Acta* **2015**, *160*, 313.

[32] J. Huang, J. Zhang, *J. Electrochem. Soc.* **2016**, *163*, A1983.

[33] F. Sälzer, L. Pateras Pescara, F. Franke, C. Müller, J. Winkler, M. Schwalm, B. Roling, *Batteries Supercaps* **2020**, *3*, 117.

[34] H. Sun, J. Zhu, D. Baumann, L. Peng, Y. Xu, I. Shakir, Y. Huang, X. Duan, *Nat. Rev. Mater.* **2019**, *4*, 45.

[35] S. Kranz, T. Kranz, T. Graubner, Y. Yusim, L. Hellweg, B. Roling, *Batteries Supercaps* **2019**, *2*, 1026.

[36] L. Zielke, T. Hutzenlaub, D. R. Wheeler, C.-W. Chao, I. Manke, A. Hilger, N. Paust, R. Zengerle, S. Thiele, *Adv. Energy Mater.* **2015**, *5*, 1401612.

[37] H. Bockholt, M. Indrikova, A. Netz, F. Golks, A. Kwade, *J. Power Sources* **2016**, *325*, 140.

[38] K. Shah, N. Balsara, S. Banerjee, M. Chintapalli, A. P. Cocco, W. K. S. Chiu, I. Lahiri, S. Martha, A. Mistry, P. P. Mukherjee et al., *J. Electrochem. Energy Convers. Storage* **2017**, *14*.

[39] A. P. Cocco, G. J. Nelson, W. M. Harris, A. Nakajo, T. D. Myles, A. M. Kiss, J. J. Lombardo, W. K. S. Chiu, *Phys. Chem. Chem. Phys.* **2013**, *15*, 16377.

[40] R. Huang, Y. Ikuhara, *Curr. Opin. Solid State Mater. Sci.* **2012**, *16*, 31.

[41] A. Devaraj, M. Gu, R. Colby, P. Yan, C. M. Wang, J. M. Zheng, J. Xiao, A. Genc, J. G. Zhang, I. Belharouak et al., *Nat. Commun.* **2015**, *6*, 8014.

[42] J. Conder, C. Marino, P. Novák, C. Villevieille, *J. Mater. Chem. A* **2018**, *6*, 3304.

[43] P. Pietsch, M. Hess, W. Ludwig, J. Eller, V. Wood, *Sci. Rep.* **2016**, *6*, 27994.

[44] J. Landesfeind, M. Ebner, A. Eldiven, V. Wood, H. A. Gasteiger, *J. Electrochem. Soc.* **2018**, *165*, A469.

[45] A. E. Reising, S. Schlabach, V. Baranau, D. Stoeckel, U. Tallarek, *J. Chromatogr. A* **2017**, *1513*, 172.

[46] D. Stoeckel, C. Kübel, M. O. Loeh, B. M. Smarsly, U. Tallarek, *Langmuir* **2015**, *31*, 7391.

[47] D. Stoeckel, C. Kübel, K. Hormann, A. Höltzel, B. M. Smarsly, U. Tallarek, *Langmuir* **2014**, *30*, 9022.

[48] J. Joos, T. Carraro, A. Weber, E. Ivers-Tiffée, *J. Power Sources* **2011**, *196*, 7302.

[49] H. Iwai, N. Shikazono, T. Matsui, H. Teshima, M. Kishimoto, R. Kishida, D. Hayashi, K. Matsuzaki, D. Kanno, M. Saito et al., *J. Power Sources* **2010**, *195*, 955.

[50] J. R. Wilson, A. T. Duong, M. Gameiro, H.-Y. Chen, K. Thornton, D. R. Mumm, S. A. Barnett, *Electrochem. Commun.* **2009**, *11*, 1052.

[51] Z. Liu, T. W. Verhallen, D. P. Singh, H. Wang, M. Wagemaker, S. Barnett, *J. Power Sources* **2016**, *324*, 358.

[52] A. H. Wiedemann, G. M. Goldin, S. A. Barnett, H. Zhu, R. J. Kee, *Electrochim. Acta* **2013**, *88*, 580.

[53] M. Ender, J. Joos, T. Carraro, E. Ivers-Tiffée, *J. Electrochem. Soc.* **2012**, *159*, A972.

[54] M. Ender, J. Joos, T. Carraro, E. Ivers-Tiffée, *Electrochem. Commun.* **2011**, *13*, 166.

[55] M. F. Lagadec, M. Ebner, R. Zahn, V. Wood, *J. Electrochem. Soc.* **2016**, *163*, A992.

[56] R. Scipioni, P. S. Jørgensen, C. Graves, J. Hjelm, S. H. Jensen, *J. Electrochem. Soc.* **2017**, *164*, A2017.

[57] T. Shi, Y.-Q. Zhang, Q. Tu, Y. Wang, M. C. Scott, G. Ceder, *J. Mater. Chem. A* **2020**, *8*, 17399.

[58] S. Choi, M. Jeon, J. Ahn, W. D. Jung, S. M. Choi, J.-S. Kim, J. Lim, Y.-J. Jang, H.-G. Jung, J.-H. Lee et al., *ACS Appl. Mater. Interfaces* **2018**, *10*, 23740.

[59] D. Hlushkou, A. E. Reising, N. Kaiser, S. Spannenberger, S. Schlabach, Y. Kato, B. Roling, U. Tallarek, *J. Power Sources* **2018**, *396*, 363.

[60] A. Ul-Hamid, *A Beginners' Guide to Scanning Electron Microscopy*, Springer International Publishing, Cham, **2018**.

[61] P. Hovington, D. Drouin, R. Gauvin, *Scanning* **1997**, *19*, 1.

[62] C. A. Volkert, A. M. Minor, *MRS Bull.* **2007**, *32*, 389.

[63] P. R. Munroe, *Mater. Charact.* **2009**, *60*, 2.

[64] G. Möbus, B. J. Inkson, *Mater. Today* **2007**, *10*, 18.

[65] T. Müllner, A. Zankel, F. Svec, U. Tallarek, *Mater. Today* **2014**, *17*, 404.

[66] M. D. Uchic, L. Holzer, B. J. Inkson, E. L. Principe, P. Munroe, *MRS Bull.* **2007**, *32*, 408.

[67] T. Prill, K. Schladitz, *Scanning* **2013**, *35*, 189.

[68] P. Pietsch, M. Ebner, F. Marone, M. Stampanoni, V. Wood, *Sustainable Energy Fuels* **2018**, *2*, 598.

[69] I. Arganda-Carreras, V. Kaynig, C. Rueden, K. W. Eliceiri, J. Schindelin, A. Cardona, H. Sebastian Seung, *Bioinformatics* **2017**, *33*, 2424.

[70] K. Hormann, V. Baranau, D. Hlushkou, A. Höltzel, U. Tallarek, *New J. Chem.* **2016**, *40*, 4187.

[71] Torquato, Lu, *Phys. Rev. E* **1993**, *47*, 2950.

[72] J. Joos, T. Carraro, M. Ender, B. Rüger, A. Weber, E. Ivers-Tiffée, *ECS Trans.* **2011**, *35*, 2357.

[73] R. Zahn, M. F. Lagadec, V. Wood, *ACS Energy Lett.* **2017**, *2*, 2452.

[74] J. Hochstrasser, A. Svidrytski, A. Höltzel, T. Priamushko, F. Kleitz, W. Wang, C. Kübel, U. Tallarek, *Phys. Chem. Chem. Phys.* **2020**, *22*, 11314.

[75] F. Gritti, J. Hochstrasser, A. Svidrytski, D. Hlushkou, U. Tallarek, *J. Chromatogr. A* **2020**, *1620*, 460991.

[76] S.-J. Reich, A. Svidrytski, A. Höltzel, W. Wang, C. Kübel, D. Hlushkou, U. Tallarek, *Microporous Mesoporous Mater.* **2019**, *282*, 188.

[77] S.-J. Reich, A. Svidrytski, A. Höltzel, J. Florek, F. Kleitz, W. Wang, C. Kübel, D. Hlushkou, U. Tallarek, *J. Phys. Chem. C* **2018**, *122*, 12350.

[78] S.-J. Reich, A. Svidrytski, D. Hlushkou, D. Stoeckel, C. Kübel, A. Höltzel, U. Tallarek, *Ind. Eng. Chem. Res.* **2018**, *57*, 3031.

Chapter 1: Reconstruction–Simulation Approach Verifies Impedance-Derived Ion Transport Tortuosity of a Graphite Battery Electrode

Authors

Moritz Kroll, Dzmitry Hlushkou, Sabine Schlabach, Alexandra Höltzel, Bernhard Roling*, and Ulrich Tallarek*

State of publication

Published 05 October 2018 in *Journal of the Electrochemical Society*, Vol. 165, pp. A3156–A3163.
DOI: 10.1149/2.0711813jes

Abstract

The performance of a composite battery electrode depends strongly on the morphology of its liquid electrolyte-filled pore space, where ion transport takes place. Ion transport limitations within the pore space are quantified by the tortuosity, which can be determined from diffusion simulations in the reconstructed pore space or through electrochemical impedance spectroscopy (EIS) using, for example, the transmission line model. Although rarely directly compared, the tortuosities determined by the two approaches have so far been lacking in agreement, raising doubts about the validity of each method. In this study, we use a graphite composite electrode to demonstrate that the two methods deliver comparable tortuosity values under two conditions: (i) The pore space is reconstructed by focused ion-beam scanning electron microscopy using an osmium-based contrast agent for positive staining. (ii) The dimensions of the reconstructed volume are sufficient to represent the electrode microstructure and to prevent finite-size effects in the diffusion simulations. Fulfillment of these conditions is proven by a comprehensive morphological analysis, comprising porosity profiles, chord length distributions of solid phase and pore space, and the geometrical tortuosity. Our results confirm EIS as a reliable method for assessing the ion transport tortuosity of battery electrodes.

1.1 Introduction

Lithium ion batteries (LIBs) have become the most important storage medium for electrical energy in mobile devices. The growing importance of electromobility raises the demand for LIBs with high energy density, which are characterized by small internal resistances at high charge/discharge rates.[1,2] Apart from evaluating new battery materials, improving the existing components is worthwhile to get to more efficient LIBs. The porous electrodes in particular have considerable optimization potential. Composite battery electrodes contain active material particles for Li^+ storage, binders, and conductive additives; the solid components define a porous microstructure that is filled by the liquid electrolyte. The pore space morphology determines the Li^+ ion transport pathways and thus the ion transport resistance of the electrode.[3] The effective ionic resistance, in turn, contributes to the overall internal impedance of the battery and thus influences its power density.[4] The electrode microstructure depends on properties of the active material particles, principally their shape and size distribution. Commercial battery electrodes are generally fabricated from irregularly shaped particles, including those with a decided anisotropy.[5-7] This carries the risk of transferring the particle anisotropy to the formed microstructure and engendering a pore space with long and tortuous pathways, which is even observed for virtually spherical particles.[8] The formed anisotropic microstructures usually result in high ion transport resistances and the diffusive ion transport tortuosity is a global measure to assess morphological transport limitations in battery electrodes.

Two approaches are currently used to determine the ion transport tortuosity of battery electrodes: electrochemical impedance spectroscopy (EIS) and direct numerical simulations in the reconstructed pore space of an electrode (reconstruction–simulation, RS). Although both methods work under ion-blocking conditions at the electrolyte / active material interface, there are often discrepancies between the obtained tortuosity values.[9-11] Electrochemical impedance spectra are analyzed in the framework of the transmission line model (TLM) to derive the effective ion transport resistance of the composite electrode, R_{ion}.[12-14] The TLM describes the impedance of straight, cylindrical pores filled with liquid electrolyte. The electronic resistance of the active material particles is assumed as zero. The effective ion transport resistance is then used to calculate the EIS-derived tortuosity according to[9,10]

$$\tau_{\mathrm{EIS}} = \frac{\sigma_{\mathrm{bulk}}}{\sigma_{\mathrm{eff}}} \cdot \varepsilon = \frac{\sigma_{\mathrm{bulk}}}{\frac{1}{R_{\mathrm{ion}}} \cdot \frac{d}{A}} \cdot \varepsilon \tag{1.1}$$

Here, σ_{bulk} and σ_{eff} denote the bulk ionic conductivity of the pure electrolyte and the effective ionic conductivity of the electrolyte in the composite electrolyte, respectively, while ε, d, and

A are the volume fraction of the electrolyte in the composite electrode, the thickness of the electrode, and the area of the electrode, respectively. EIS is a fast way to determine the ion transport tortuosity with a simple experimental setup available in many industrial and academic laboratories. An increasing number of studies[9-11,15] reports EIS-derived tortuosity values, although the TLM has not yet been validated by an independent microscopic method employing a realistic morphology of the pore space.

The reconstruction–simulation (RS) approach has been around longer than EIS for tortuosity determinations, but requires considerably more time and specialized equipment to obtain the required 3D reconstruction of the electrode microstructure.[7,16] The diffusion process in the pores can be simulated by a random walk method, where point-like, inert tracers are randomly distributed in the void space. A random displacement is determined for all tracers at each time step. From the tracer displacements, a time-dependent diffusion coefficient is calculated, which gives the effective diffusion coefficient D_{eff} in the asymptotic (long-time) limit. The diffusive tortuosity τ_{RS} is the ratio of bulk diffusion coefficient D_{bulk} and D_{eff}:

$$\tau_{\mathrm{RS}} = \frac{D_{\mathrm{bulk}}}{D_{\mathrm{eff}}} \tag{1.2}$$

The accuracy of the diffusion simulations and thus of the obtained τ_{RS} value depends entirely on the quality of the reconstruction, that is, its resolution and volume. For battery electrodes, focused ion-beam scanning electron microscopy (FIB-SEM) and X-ray tomography are the two reconstruction methods-of-choice. Both techniques resolve the void space between micrometer-sized particles with a resolution down to 10 nm.[17] Unlike X-ray tomography, FIB-SEM serial sectioning requires filled pores to enhance the contrast and to prevent shine-through artefacts. X-ray tomography detects the solid phase, whereas FIB-SEM offers the possibility of staining the solid phase or the void space. Irrespective of the technique used, the reconstruction has to be large enough to be representative of the entire electrode microstructure and to prevent finite-size effects in the diffusion simulations.

Although both approaches should come to the same result, this corroboration has so far not been observed in practice.[9,10] Landesfeind et al.[11] compared EIS- and RS-derived ion transport tortuosity values of battery electrodes whose microstructure was reconstructed by X-ray tomography. They found about twofold lower values for the RS-derived tortuosities and attributed this discrepancy to an inadequate reconstruction of the pore space. X-ray tomography did not recognize the binder as part of the solid phase, so that in simulations diffusion extended into parts of the electrode that are effectively blocked by the binder in the real sample. Thereby,

the diffusion paths became less obstructed and the porosity increased, leading to underestimated tortuosity values in the simulations. The equality of EIS and the RS approach for the tortuosity determination of battery electrodes remains to be shown.

In this work, we attempt to validate the EIS-based tortuosity determination of porous battery electrodes through the RS approach. To this end, we used graphite as the most widespread anode material for LIBs.[18] The chosen graphite flakes, which have also been used already in other studies[9,19,20], form an anisotropic microstructure, which poses a particular challenge with regard to the reconstruction and the choice of adequate analysis methods. We intentionally selected FIB-SEM as the tomography technique, since it allows a direct staining of the pore space. An osmium-based contrast agent has access to the entire pore space including the cusp regions between graphite flakes and small pores. Thus, we image the same space that the liquid electrolyte penetrates under conventional operating conditions of the battery. The electrode is reconstructed over the entire cross-section, i.e., from current collector to the top, to monitor possible porosity variations introduced by the doctor-blade manufacturing process. Prior to simulations of diffusion in the reconstructed pore space, the reconstruction is critically evaluated to ensure the absence of finite-size effects[21] and extract important morphological information in the form of porosity profiles, chord length distributions (CLDs) of solid phase and void space, and geometrical tortuosity values.

1.2 Experimental

1.2.1 Electrode preparation

The nonporous graphite flakes used for electrode preparation had a mean length (long side) of 4.73 ± 1.81 µm, a mean height (perpendicular to the long side) of 2.73 ± 1.16 µm, and a mean thickness of 0.473 ± 0.156 µm. Graphite electrodes with varied thickness were prepared from an aqueous slurry of 90 wt% of C-NERGY KS6 L synthetic graphite (Timcal, Bodio, Switzerland), 5 wt% of C-NERGY SUPER C 65 carbon black (Timcal), and 5 wt% Walocel CRT 2000 PA sodium carboxymethyl-cellulose (Biogrund, Hünstetten, Germany), following a similar procedure as reported in Balabajew et al.[22] Briefly, the slurry was applied to an aluminum foil, whereby the thickness of the slurry application was adjusted using a ZAA 2300 automatic film applicator (Zehntner, Sissach, Switzerland), and dried overnight at room temperature. From the dried slurries, discs with a radius of 0.6 cm were cut out. No pressure was applied for secondary consolidation so that all electrodes should have similar porosity. To determine the mass of the electrodes, the discs were weighed on an analytical balance and the mean weight of the aluminum current collector was subtracted.

1.2.2 Electrochemical impedance spectroscopy (EIS) measurements

EIS was performed in a TSC battery cell (rhd instruments, Darmstadt, Germany) using a symmetrical two-electrode setup. The cells were assembled in an argon-filled glove box. Two graphite electrodes with minimal weight difference (< 0.08 mg) were separated by four layers of Whatman GF/A glass microfiber filters (GE Healthcare, Buckinghamshire, United Kingdom). The separators were soaked with 120 µl of liquid LP30 electrolyte (Merck, Darmstadt, Germany) consisting of a 1/1 (v/v) mixture of ethylene carbonate and dimethyl carbonate containing 1 mol l^{-1} $LiPF_6$. Cells were equilibrated over night at room temperature. Impedance measurements were performed between 1 MHz and 0.1 Hz with an AC amplitude of 12.5 mV at the open circuit potential using a Zennium electrochemical workstation (Zahner-Schiller, Kronach-Gundelsdorf, Germany). Impedance spectra were analyzed using the software RelaxIS 3 (rhd instruments).

1.2.3 Determination of the electrode thickness

The precise determination of the electrode thickness is critical, as the parameter affects the accuracy of the calculated τ_{EIS} (Eq. 1.1). After the EIS experiments, the electrodes were embedded in epoxy resin. To this end, a 5/2 (w/w) mixture of SpeciFix Resin and SpeciFix-40 Curing Agent (Struers, Ballerup, Denmark) was used. After curing for 24 h at room temperature, the embedded electrodes were cut and the cross-section was examined with a DM2700 M optical microscope (Leica Microsystems, Wetzlar, Germany) equipped with an N PLAN EPI 50x/0.75 BD objective (Leica) and a MC190 HD camera (Leica). The electrode thickness was determined with the help of Fiji[23] ImageJ image processing software from 100 values estimated along the entire cross-section.

1.2.4 Focused ion-beam scanning electron microscopy (FIB-SEM) serial sectioning

For positive staining with OsO_4,[24,25] one of the prepared electrodes was placed on top of an upturned snap-cap vial in a round-bottomed flask filled with 1.5 ml of 4% aqueous OsO_4. The electrode was moistened with one drop of 1-dodecene (Sigma Aldrich, St. Louis, MO) to fill the pore space. The flask was then closed and kept in darkness for six weeks. During this resting time, the OsO_4 solution partially evaporated and penetrated the pore space of the electrode, where formation of solid osmic esters with the alkene took place. The sample was then embedded in epoxy resin, using a 5/2 (w/w) mixture of SpeciFix Resin and SpeciFix-40 Curing Agent (Struers), and cured for 24 hours at room temperature.

FIB-SEM serial sectioning was performed on a Strata 400S dual-beam-FIB system (FEI, Hillsboro, OR) at the Karlsruhe Nano Micro Facility, Karlsruhe Institute of Technology (Karlsruhe, Germany). The SEM unit was operated at an acceleration voltage of 5 kV. A protective Pt layer (~1 µm) was deposited at the region of interest (ROI) to reduce curtaining effects. A focused Ga^+ beam (30 kV, 6.5 nA) served to create a trench around the ROI to prevent re-deposition onto the surface and to expose the sample volume for slicing. A 30 kV Ga^+ ion beam with a current of 6.5 nA was then used to create an image stack from the ROI using the Slice&View package of the instrument software. The FIB slicing direction defines the *y*-direction. The final image stack contained 1065 images of 3712 pixels × 1852 pixels with $(14.2\ \text{nm})^2$ pixel size and 30.0 nm spacing in milling direction (*y*-direction). This yields a reconstructed electrode volume of 52.8 × 32.0 × 26.3 μm^3 ($x \times y \times z$).

1.2.5 Physical reconstruction

Image restoration and processing was realized with Fiji[23] ImageJ image processing software and Visual C# scripts using Visual Studio Community 2017 (Microsoft Corporation, Redmond, WA). Images were contaminated by waterfall effects from re-deposition of sputtered material. The artifacts were removed using the Stripe Filter of the Xlib Fiji plugin.[26] Drifts between images were corrected by an in-house script written in Matlab R2014b (The MathWorks, Inc., Natick, MA). The FIB cutting procedure causes small stage drifts between the SEM images that are not fully corrected by the Slice&View software. Hence, the algorithm displaces the subsequent image relative to the previous one. For each shift between successive images the algorithm takes overlapping parts of both images and computes a normalized cross-correlation, which is essentially the correlation coefficient if pixel values are treated as random data. Finally, the subsequent image is shifted so that maximum cross-correlation between the two images is achieved. This procedure is repeated for the entire image stack. The inclined viewing angle of the SEM detector was corrected by scaling along the *z*-axis using Fiji. The slight tilt of the sample was corrected using the TransformJ plugin.[27] Intensity gradients within and between images were normalized to avoid errors in the thresholding step. A Gaussian filter ($\sigma = 2$) was applied to remove noise. The image contrast was enhanced and a global threshold was defined to binarize the images. Binary and raw images were visually compared to find an optimal threshold. The binder and carbon black are actually not distinguishable from the graphite flakes in the final reconstruction. In evaluating the reconstruction, we noted that some parts of the pore space were not completely filled with contrast agent and were thus incorrectly assigned as solid phase. These parts were semi-manually corrected using the 3D watershed segmentation of the MorphoLibJ plugin[28] to identify these holes. The resulting 8-bit binary image stack was

used as input for further analysis. Figure 1.1 provides a brief overview of the reconstruction steps and shows a 3D visualization of the reconstructed microstructure of the graphite electrode.

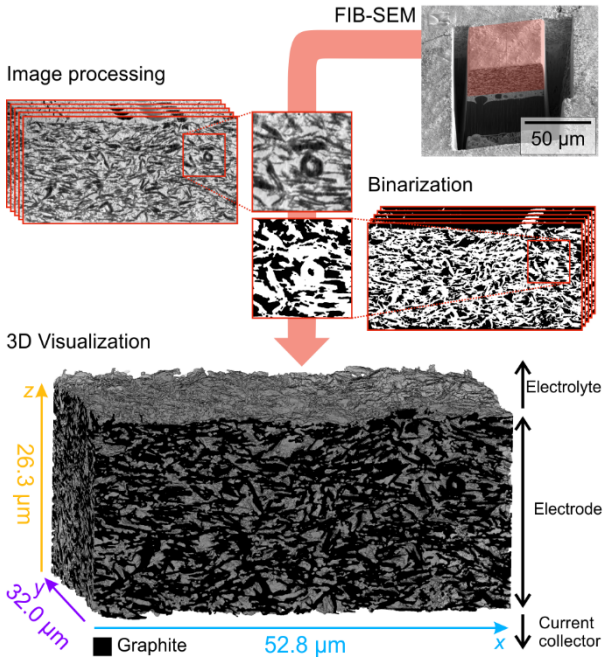

Figure 1.1: Reconstruction procedure spanning from the prepared volume-of-interest (red) for FIB-SEM serial sectioning analysis to the 3D visualization of the reconstructed volume. The image stack, acquired via Slice&View tomography, was processed and binarized into solid phase (white) and void space (black). In the final visualization, the graphite flakes are displayed in black.

1.2.6 Chord length distribution (CLD) analysis

A simple and widely applicable approach to characterize the shape and size of arbitrary geometrical structures is the use of CLDs. Since CLD analysis does not require any assumptions about the size and shape of a solid, liquid, or void phase, it is virtually applicable to all multiphase materials and has been used to describe packed beds of micrometer-sized particles, the macropore space, skeleton, and mesopore space of silica monoliths, the formation of porous glasses, to study crystallisation, etc.[29] In general, chords are used to scan a geometry by measuring the distances between two interfaces, which are set apart by a homogenous phase.[30,31] The recorded CLD is abstract but accurate in describing the phase distribution, eliminating the need to define limits for individual pores or their geometric form (as required,

for example, in a porometric characterization to derive a pore size distribution[32]). CLD analysis for the solid phase and void space of the reconstructed electrode microstructure proceeds along the following steps: (i) 10^5 seed points are randomly distributed within each phase; (ii) from each seed point, six vectors in total are projected along $\pm x$, $\pm y$, and $\pm z$ until they hit the solid–void interface (the three spatial directions are orthogonal axes according to the designation in Figure 1.1); (iii) chord lengths are extracted as the sum of the absolute lengths of a pair of opposed vectors (spanning the distance between two interfaces while traversing the material) and stored unless a vector projects out of the reconstruction boundaries, in which case the chord is discarded. The resulting histogram (the CLD) and its analysis are valuable to describe the solid phase and void space inside the battery electrode prepared from the flaky shaped particles, where defining individual pore limits would be difficult and possibly arbitrary. This approach is furthermore applied in a straightforward manner to other electrode morphologies, thereby aiding in the establishment and comparison of quantitative morphology–performance relationships.

1.2.7 Calculation of the geometric tortuosity

The geometric tortuosity was determined from the topological skeleton of the reconstructed pore space. For this purpose, the Fiji Skeletonize3D plugin was applied to the binary image stack to obtain a representation of the void space where pores are reduced to centerlines of one voxel thickness (branch–node network). This skeletonization procedure reduces the pore space to a medial axis under conservation of the topological and geometrical information. To calculate the geometric tortuosity τ_{geom} in *x*-, *y*-, and *z*-direction (the three spatial directions are again the orthogonal axes according to the designation in Figure 1.1), a cuboid with a surface of 1000 × 1000 voxels and maximum depth in the respective direction (that is, along *x*, *y*, or *z*) was cut from the topological skeleton to reduce calculation times. For example, to calculate τ_{geom} in the *z*-direction the cuboid had dimensions of 14.2 × 14.2 × 26.3 µm^3 ($x \times y \times z$). The branch–node network covered by the cuboid was then examined using the AnalyzeSkeleton[33] plugin in Fiji and the corresponding "branch information" output (node positions, branch lengths) was used as input for the subsequent calculations of τ_{geom}. The geometric tortuosity represents the shortest possible distance (along the branches of the branch–node network) between two nodes with respect to the Euclidean distance between these points. To arrive at global τ_{geom}-values for the pore space in *x*-, *y*-, and *z*-direction of the reconstruction the Euclidean distances between point pairs (in the respective direction) were increased and the corresponding shortest distances along the topological skeleton recorded. In particular, about 200 nodes lying on one of the faces of a cuboid were defined as start points to project straight lines (representing Euclidean distances) along the monitored *x*-, *y*-, or *z*-direction. The nearest node from each end of a line was assigned

as end point. The ratio of the shortest distance between start and end point along the branch–node network and the Euclidean distance corresponds to the geometric tortuosity. By step-wise increasing the length of the 200 lines (shifting their end points) an asymptotic value is attained for τ_{geom}. This value is the global (asymptotic) geometric tortuosity in a particular direction of the electrode reconstruction. A Visual C# application was written to calculate the shortest distances along the skeleton branches between corresponding (start-end) point pairs using Dijkstra's algorithm.[34,35]

1.2.8 Pore-scale diffusion simulations

Diffusion in the void space of the reconstructed electrode was simulated by a random-walk particle-tracking technique.[36] A large number $N = 10^7$ of passive, point-like tracer particles were randomly distributed in the reconstructed void space. During each time step Δt of the simulation, the random displacement $\Delta\mathbf{r}$ of every tracer due to molecular diffusion was calculated as

$$\Delta\mathbf{r} = \boldsymbol{\gamma}\sqrt{6D_{\mathrm{bulk}}\Delta t} \tag{1.3}$$

where D_{bulk} is the tracer diffusion coefficient in the open space and is a vector with random orientation in space and a length governed by a Gaussian distribution with zero mean and unity standard deviation. The value of Δt was adjusted such that the mean diffusive displacement did not exceed $\Delta h/10$ (where Δh = 14.2 nm is the pixel size of the FIB-SEM images used for the electrode reconstruction). To restrict diffusion to the void space, a multiple-rejection boundary condition[37] was implemented at the solid–void interface: If at the current time iteration a tracer crossed the solid–void interface, this displacement was rejected and recalculated until the tracer position was in the void space. At the external faces of the reconstructed domain, a mirror boundary condition was imposed, that is, if at the current iteration a tracer hit an external face, it was mirror-reflected from that face, but the total length of the displacement (with reflection) was equal to $\Delta\boldsymbol{r}$. During the simulation, the displacements of every tracer along *x*-, *y*-, and *z*-direction were monitored, which allowed us to determine time-dependent diffusion coefficients along each direction *j* according to[38]

$$D_j(t) = \frac{1}{2N}\frac{d}{dt}\sum_{i=1}^{N}\left[\Delta r_{ij}(t)\right]^2 \tag{1.4}$$

where j denotes x, y, or z, and $\Delta r_{ij}(t)$ is the accumulated displacement of the ith tracer along direction j after time t.

A decrease of $D_j(t)/D_{\text{bulk}}$ with time (i.e., the number of iterations) from the initial value of 1 results from interactions of tracers with the solid phase. At short times, only a small fraction of the tracers experiences geometric confinement during their random walk. At long times, the transient diffusion coefficients approach asymptotic values, with superimposed stochastic noise inherent to random processes. These long-time asymptotic values correspond to effective diffusion coefficients $D_{\text{eff},j}$, which characterize steady-state anisotropic diffusion in the void space of the reconstructed electrode in the specified direction. Then, the corresponding value of the diffusive tortuosity $\tau_{\text{RS},j}$ can be determined according to Eq. 1.2.

1.3 Results and discussion

1.3.1 Tortuosity determination by the electrochemical impedance spectroscopy (EIS) approach

EIS measurements were performed using a symmetrical cell setup (graphite electrode | electrolyte | graphite electrode) assembled from two electrodes of similar weight (weight difference < 0.08 mg).[14,39] Using a conventional battery cell with a cathode and an anode in a two-electrode setup would result in a mixed impedance to which both electrodes contribute. A three-electrode setup has challenging demands concerning the correct position of the reference electrode to prevent artifacts.[40] The symmetrical cell setup was chosen to ensure that the received structural information only refers to the investigated sort of electrode. Because the electrode contains conductive carbon, the electronic resistance is negligibly small and not taken into account in formulating the TLM. Under blocking-electrode conditions, only double layer formation but no charge transfer reaction takes place at the interface between liquid electrolyte and graphite flakes. In the following, the interfacial double layer capacitance is denoted by C_{DL}. Microscopic roughness of the pore walls and deviations from cylindrical pore geometry could influence the shape of the impedance spectra.[41,42] A constant phase element (CPE) was introduced to account for deviations from ideal capacitive behavior.[9,43] The impedance Z for the TLM under blocking conditions (0% state-of-charge) can be expressed as

$$Z = \sqrt{\frac{R_{\text{ion}}}{Q_{\text{DL}}(j\omega)^{\alpha}}} \cdot \coth\left(\sqrt{R_{\text{ion}} \cdot Q_{\text{DL}}(j\omega)^{\alpha}}\right) \tag{1.5}$$

with the effective ion transport resistance R_{ion}, the CPE coefficient Q_{DL} and its exponent α, the imaginary number j, and the angular frequency ω.[9]

To determine R_{ion}, impedance spectra of four electrode pairs with varying thickness d were collected and fitted to Eq. 1.5. Figure 1.2a shows Nyquist plots of the spectra and the fits to the TLM; the values received from the fits for the parameters R_{ion}, Q_{DL}, and α for each electrode pair are listed in Table 1.1. The slope of the Nyquist plots is 42°–44° at high frequencies and 85°–87° at low frequencies, which corresponds to α-values that deviate only slightly from unity (α = 0.94–0.97).

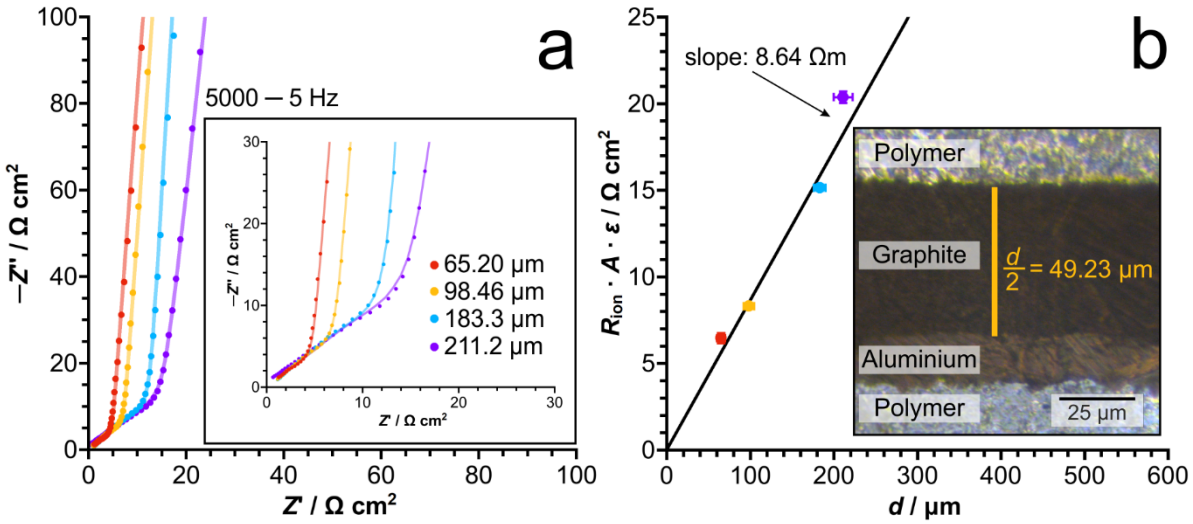

Figure 1.2: (a) Nyquist plot of the impedance acquired for symmetrical graphite cells with varying electrode thickness (symbols), together with fits according to Eq. 1.5 (solid lines). EIS experiments were performed in a two-electrode setup under ion-blocking conditions at the active material particle / electrolyte interface. For a better comparison of the ion transport resistance in the composite electrodes, the resistance of the liquid electrolyte in the separator was subtracted. The fitting results for the parameters R_{ion}, Q_{DL}, and α are listed in Table I. (b) Tortuosity determination from plots of ($R_{\text{ion}} \cdot A \cdot \varepsilon$) vs. the electrode pair thickness d. The thickness of one electrode, d/2, was determined using an optical microscope, after electrodes had been resin-embedded and cut. τ_{EIS} was calculated from the slope of the linear fit to the data and the electrolyte bulk conductivity (cf. Eq. 1.1).

Table 1.1: Parameters derived from fitting the EIS data to the TLM (Eq. 1.5).[a]

$R_{ion} \cdot A$ / Ω cm^2	$Q_{DL} \cdot A^{-1}$ / µF s$^{\alpha-1}$ cm^{-2}	α / —
13.89 ± 0.22	252.3 ± 0.37	0.959
20.90 ± 0.09	416.8 ± 0.56	0.961
36.19 ± 0.13	727.6 ± 3.74	0.968
43.93 ± 0.27	1013 ± 1.04	0.941

[a] The effective ion transport resistance R_{ion} and the constant-phase element coefficient Q_{DL} have been normalized by the electrode area A.

The calculation of τ_{EIS} according to Eq. 1.1 requires knowledge of the electrode porosity ε. The porosity was determined from the mass m, the area A, and the thickness d of the electrode pairs and the mass density ρ of graphite, the main component of the solid phase, as $(1-\varepsilon) = m/(A \cdot d \cdot \rho)$. Mass and thickness of the electrode pairs are listed in Table 1.2; for convenience, the mass is given normalized by the area of two circular electrodes with a radius of 0.6 cm (A = 2.26 cm^2). For the graphite density, we assumed a value of ρ = (2.1 ± 0.2) g cm^{-3} based on the range of data given in the literature.[44] The resulting porosities of the electrode pairs were between 39.7% and 46.5% (Table 1.2), yielding an average porosity of ε = (43.6 ± 2.6)%. The stated errors of the porosity values in Table 1.2 result mainly from uncertainties in the density of graphite. For the tortuosity determination according to Eq. 1.1, we plot ($R_{ion} \cdot A \cdot \varepsilon$) vs. electrode thickness $\boldsymbol{d}$. A linear fit to the data (Figure 1.2b) returned a slope of 8.64 Ωm. Multiplying this slope with the measured bulk conductivity of the used electrolyte (σ_{bulk} = 0.85 (Ωm)$^{-1}$ at 25 °C) resulted in a EIS-derived tortuosity of τ_{EIS} = 7.3 ± 0.9.

Table 1.2: Mass m (normalized by area A), thickness d, and porosity ε of the electrode pairs.

$m \cdot A^{-1}$ / mg cm^{-2}	d / µm	ε / —
7.329 ± 0.01	65.20 ± 4.84	0.465 ± 0.056
12.46 ± 0.01	98.46 ± 6.26	0.397 ± 0.045
22.39 ± 0.01	183.3 ± 7.14	0.418 ± 0.043
23.80 ± 0.01	211.2 ± 11.3	0.464 ± 0.051

The calculated τ_{EIS} value reflects highly tortuous ion transport pathways. The tortuosity–porosity ratio corresponds to a McMullin number of $N_M = \tau/\varepsilon = 16.8$. Landesfeind et al.[9] reported very similar McMullin numbers of 18–19 for electrodes manufactured from the same type of graphite flakes as used in this study.

1.3.2 Tortuosity determination by the reconstruction–simulation (RS) approach

The RS approach for tortuosity determination relies on the accurate reconstruction of a representative volume of the electrode pore space. Thus, the reconstructed volume was first critically evaluated (i) to extract valuable morphological information about the microstructure of the porous electrode, and (ii) to ensure that the reconstructed volume satisfied the criteria for obtaining statistically relevant information from the diffusion simulations.

Morphological analysis

First, the porosity was determined as the fraction of void voxels in the reconstruction (the ratio between black (void) voxels and the sum of white (solid) and black voxels in the binarized image stack). This was done for the entire reconstructed volume to determine the global porosity and then along each of the three spatial planes to monitor porosity fluctuations in *x*-, *y*- and *z*-direction (Figure 1.3). For example, the porosity plot for the *x*-direction (blue curve) summarizes the slice-by-slice mean porosity in the *yz*-plane of the reconstruction. The global porosity was determined as ε = 42.6%, which is in excellent agreement with the average porosity value of (43.6 ± 2.6)% estimated from mass and dimension for the four electrode pairs (Table 1.2). In each spatial direction, the porosity fluctuates randomly around the global value, without indication of a trend, reflecting a microstructure with a uniform and isotropic porosity distribution.

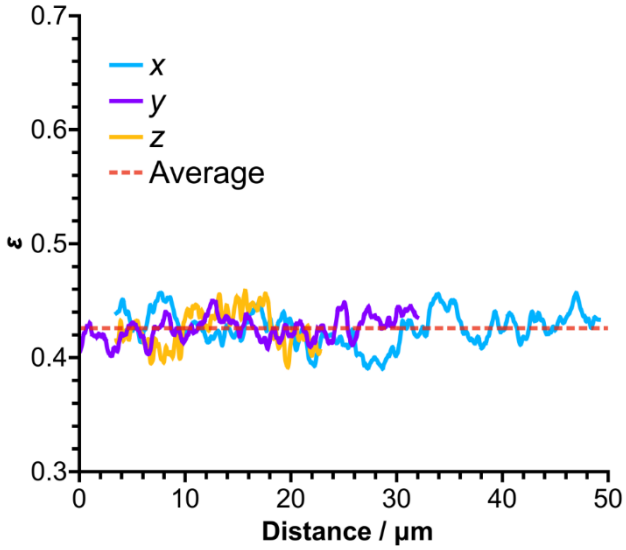

Figure 1.3: Direction-dependent porosity profiles determined in the reconstruction. The porosity fluctuates around the global average of $\varepsilon = (0.426 \pm 0.03)\%$.

Next, the reconstructed volume was subjected to CLD analysis to determine the geometric properties of void space and solid phase.[45-48] In CLD analysis, the investigated space is probed by chords of variable length, eliminating the need to assume a specific geometric shape for the investigated space, e.g., a cylindrical pore model conveniently applied in the derivation of a pore size distribution based on porometric data.[32] Once a statistically significant number of chords has been collected, they are displayed in a histogram. For highly ordered, crystalline structures the CLD exhibits a multi-modal pattern, whereas materials with Debye randomness (e.g., Vycor glass, cement, sand) show a CLD that follows an exponential decay function.[29] Most interesting is the occurrence of correlated disorder, as found in randomly packed particulate beds or hard and soft matter-type monoliths. For those materials it has been shown that the CLD is well described by the *k*-Gamma function[29] (which can be also motivated from a statistical mechanics approach[49])

$$f(l_c) = S \cdot \frac{k^k}{\Gamma(k)} \frac{{l_c}^{k-1}}{\mu^k} \exp\left(-k \frac{l_c}{\mu}\right) \tag{1.6}$$

with the scaling parameter S, the chord length l_c, the form parameter k, the gamma function Γ, and the mean chord length μ. The chord lengths analyse microstructure on a local scale, i.e.,

the majority of the chords probe a single pore, with some chords also exploring adjacent pores. The CLDs therefore reveal information about the local (pore level) and short-range (few pores) heterogeneity.[50] In this regard, the first-moment parameter μ in Eq. 1.6 is a measure of the average feature size (e.g., the lateral pore extension or solid thickness, represented by the mean chord length), whereas the second-moment parameter $k = \mu^2/\sigma^2$ is a measure of microstructural homogeneity (σ is the standard deviation of the CLD). Higher k values (narrower CLDs with respect to μ) indicate a higher degree of homogeneity, i.e., a more homogeneous morphology over a length scale of a few pores.[51,52] One of the strengths of the CLD approach is the ability to compare fundamentally different morphologies (e.g., with continuous or discontinuous solid phase), regardless of material preparation history, in a simple, accurate, and quantitative manner.[29]

To honor the anisotropic microstructure of the graphite electrode, CLD analysis was performed for each spatial direction individually. Figure 1.4 shows a schematic illustration of chord generation in the void space of the electrode and the CLDs obtained for void space and solid phase including the respective fits to Eq. 1.6. The parameters derived from fits of the CLDs to Eq. 1.6 are listed in Table 1.3. The CLDs reflect the arrangement of the graphite flakes in the electrode and the consequences for the pore space. For void space and solid phase, the average feature size μ in *z*-direction is about half of the average feature size in *x*- and *y*-direction. For the solid phase, this indicates that most of the graphite flakes are layered in the *xy*-plane. This arrangement has been attributed to gravitational forces during the drying of the slurry.[53] Compared to the graphite flake dimensions, μ is smaller in *x*- and *y*-direction and larger in *z*-direction. This could reflect a tilted orientation of the flakes, which is supported by visual inspection of the reconstructed volume (Figure 1.1). On the other hand, the graphite flakes are not isolated entities in the reconstruction. The reconstructed solid phase encompasses also binder and conductive carbon, so that flakes can appear connected. Chords spanning over several flakes would increase μ in *z*-direction compared with the flake thickness. The layered arrangement of the graphite flakes shapes the pore space into a similar arrangement; as the mean feature sizes in the three spatial directions indicate, the free diffusion path of an ion is about twice longer in the *xy*-plane than perpendicular to it. Thus, the path in *z*-direction, that is, perpendicular to the current collector, is highly obstructed, which explains the high tortuosity value of $\tau_{EIS} = 7.3 \pm 0.9$ determined by EIS.

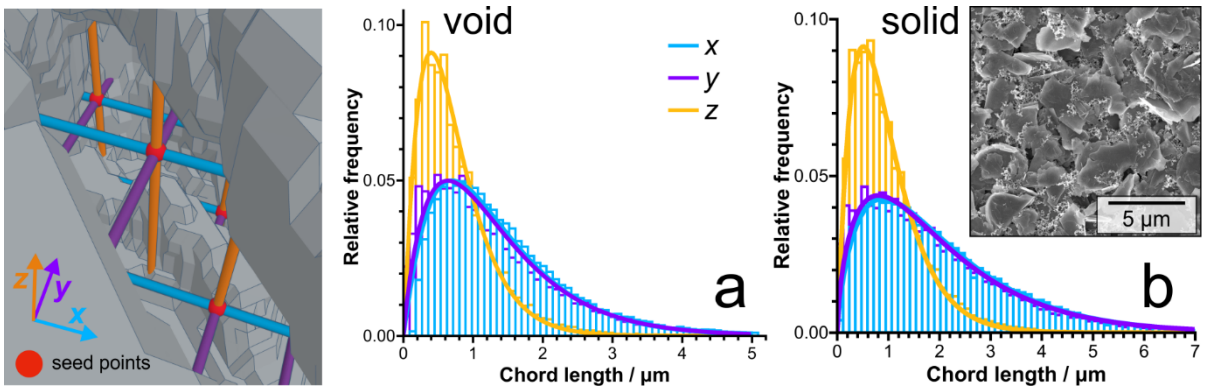

Figure 1.4: Schematic 3D illustration of chord generation for direction-dependent CLD analysis in the void space of the reconstruction (left panel). Direction-dependent CLDs obtained for (a) void space and (b) solid phase along with the respective fits to the *k*-Gamma function (Eq. 1.6). The CLDs reflect the anisotropy of the microstructure in *z*-direction, caused by the preferential layering of graphite flakes in the *xy*-plane, an arrangement visible in the SEM image (see inset in panel b).

Table 1.3: Parameters derived from fitting the CLDs to the *k*-Gamma function (Eq. 1.6).[a]

	Void space		Solid phase	
Direction	μ / µm	k / —	μ / µm	k / —
x	1.314	1.942	1.997	1.678
y	1.326	2.117	2.044	1.788
z	0.722	2.235	0.954	2.160

[a] The coefficient of determination was $R2 > 0.99$ for all fits; the scaling parameter S in Eq. 1.6 was 0.09 for the void space and 0.12 for the solid phase.

Analysis of finite-size effects

To ensure the absence of finite-size effects, the reconstructed volume was stepwise reduced by decreasing its edge lengths. CLD analysis was performed for each subvolume in all three spatial directions. Figure 1.5 shows the μ and k values obtained from the void space of the subvolumes

for the *x*- and *z*-direction. (Values obtained for the *y*-direction were highly similar to those for the *x*-direction and thus omitted from the figure for clarity.) If the volume is too small, long chords are underrepresented, resulting in too small μ values and compromised *k* values.[21] The form parameter *k* and the mean chord length μ tend to constant values at ~60% of the full edge lengths, which corresponds to 31.7 µm in *x*-direction and 15.8 µm in *z*-direction. The mean chord length is μ = 1.31 µm in *x*-direction and μ = 0.722 µm in *z*-direction, that is, representative values for the morphological parameters are reached at edge lengths corresponding to 24μ in *x*-direction and to 22μ in *z*-direction. The findings confirm the results of a former study,[21] which investigated finite-size effects in the reconstruction of an organic-polymer monolith and gave the minimum edge length to extract representative morphological data from the reconstruction as 20–25 times the average feature size.

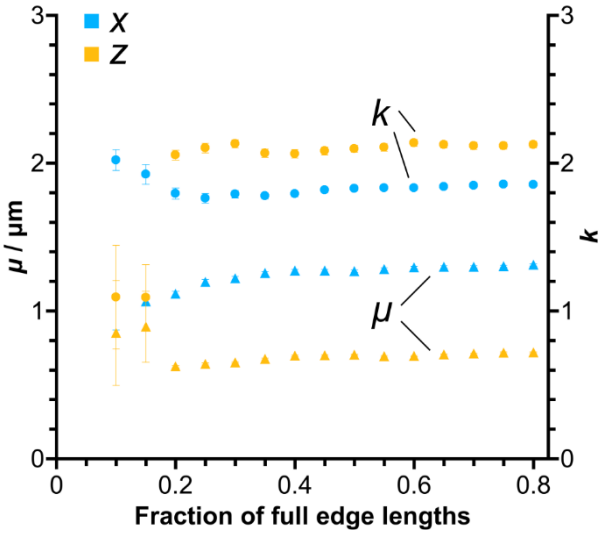

Figure 1.5: CLD analysis of the void space in *x*- and *z*-direction (blue and yellow, respectively) for subvolumes of the entire reconstruction. Subvolumes were generated by decreasing the edge lengths of the reconstructed volume (Figure 1.1) in each spatial direction by the same factor. Finite-size effects disappear at 60% of the full edge lengths.

Analysis of geometric tortuosity

The geometric tortuosity τ_{geom} was determined to check if the assumed voxel depth in *y*-direction is correct. The voxel depth in *y*-direction corresponds to the spacing between the SEM images, which is determined by the cutting width of the ion beam and is thus an input parameter for serial sectioning. Because the graphite flakes are randomly oriented in *x*- and *y*-direction,

the geometric tortuosity should lead to very similar values in the *xy*-plane, if the cutting width of the ion beam was chosen correctly. In the literature, the geometric tortuosity is often determined to characterize porous media,[16] although its significance is limited. It is defined as the shortest possible path between two points in a porous medium divided by the Euclidean distance between these points. The shortest possible path is not necessarily the path with the smallest transport resistance. Bottlenecks or other constrictions have no influence on τ_{geom}, whereas diffusing species deviate from the ideal route, as the direction of Brownian motion is random and, more importantly, solutes are sensitive to constrictions in their diffusion path. Hence, the geometry-based tortuosity is always lower than the actual mass transport-based tortuosity.[16,47,54]

For calculation of τ_{geom}, the distances were determined along the branches of the 3D topological skeleton (branch–node network; red lines in the 2D representation of the skeleton in Figure 1.6). The topological skeleton represents the pores as centerlines while retaining the topology of the pore space.[55] Figure 1.6 shows the evolution of the geometric tortuosity value with increasing Euclidean distance in the three directions. The error decreases for longer Euclidean distances and τ_{geom} approaches constant values. The asymptotic values of the geometric tortuosity are $\tau_{geom,x} = 1.62 \pm 0.06$, $\tau_{geom,y} = 1.57 \pm 0.09$, and $\tau_{geom,z} = 2.67 \pm 0.12$. The results reflect the anisotropic microstructure of the graphite electrode and confirm the assumed voxel depth in *y*-direction as correct.

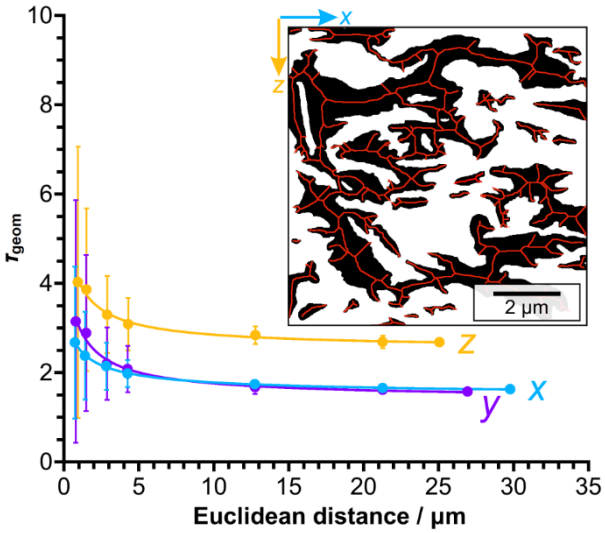

Figure 1.6: Evolution of the direction-dependent geometric tortuosity with increasing Euclidean distance. Tortuosity values were determined from the 3D topological skeleton

(branch–node network) of the reconstructed pore space. One point in the graph represents contributions from more than 200 node pairs with similar Euclidean distance. The inset shows a schematic 2D representation of the topological skeleton (solid phase: white, void space: black, skeleton: red).

Diffusion simulations

Figure 1.7 shows the evolution of the simulated transient diffusion coefficients $D_j(t)$, normalized by D_{bulk}, with increasing number of iterations. For all three directions asymptotic values were reached, yielding tortuosities of $\tau_{RS,x} = 2.62$, $\tau_{RS,y} = 2.48$, and $\tau_{RS,z} = 6.55$ (Table 1.4). The most important result is the good agreement between the simulated tortuosity value for the z-direction and the EIS-based tortuosity value (which measures the tortuosity perpendicular to the current collector, that is, in z-direction). The values determined for $\tau_{RS,z}$ and τ_{EIS} agree within the experimental error in the determination of τ_{EIS}, validating the EIS approach for the tortuosity determination of the porous graphite electrodes.

Table 1.4: Synopsis of the determined tortuosity values.

Direction	τ_{EIS}[a] / —	τ_{RS}[b] / —	τ_{geom}[c] / —
x	—	2.62	1.62 ± 0.06
y	—	2.48	1.57 ± 0.09
z	7.3 ± 0.9	6.55	2.67 ± 0.12

[a] Determined from electrochemical impedance spectroscopy measurements; [b] from diffusion simulations in the reconstructed pore space; [c] from the topological skeleton of the reconstructed pore space.

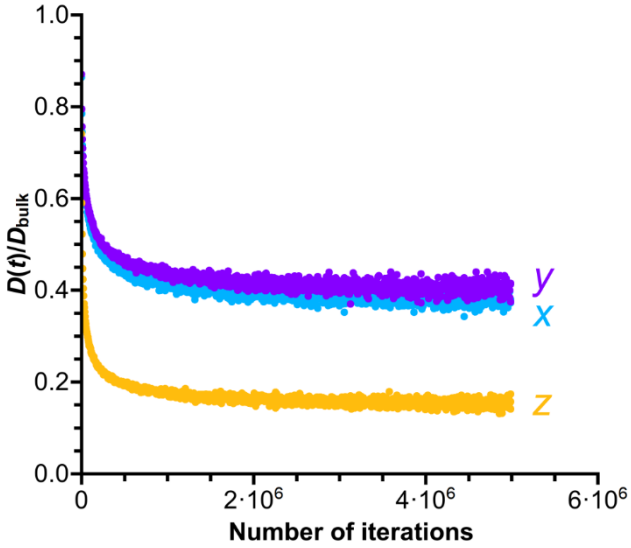

Figure 1.7: Evolution of the direction-dependent transient diffusion coefficients $D_j(t)$, normalized by the diffusivity in the bulk liquid (D_{bulk}), with the number of iterations. $D_j(t)$ values were obtained from diffusion simulations in the reconstructed pore space. The direction-dependent tortuosity $\tau_{RS,j}$ is determined from $D_{eff,j}$, the asymptotic value of $D_j(t)$ in the long-time limit (cf. Eq. 1.2).

Finally, we revisit the relation between microstructure and tortuosity. The anisotropy in the electrode microstructure introduced by the *xy*-layered arrangement of the graphite flakes is reflected in the CLDs (Figure 1.4) and in the direction-dependent geometric and diffusive tortuosity values (Figures 1.6 and 1.7, respectively). The geometric tortuosity is 1.7-times larger in *z*-direction than in *x*- and *y*-direction, but the diffusion-simulation based tortuosity is already 2.7-times larger in *z*-direction than in *x*- and *y*-direction (Table 1.4). This synopsis shows that from structure to ideal (geometric) pathways to real (mass-transport relevant) pathways, the anisotropy is amplified. Isotropic structures should therefore be an immediate goal for the design of composite battery electrodes. But even aside from the anisotropy, the microstructure of graphite electrodes leaves much room for improvement, as the comparison with computer-generated packings shows. With $\tau_{RS,xy} \approx 2.55$, the tortuosity of the graphite electrode in the less obstructed directions is still 1.8-times higher than the tortuosity of ~1.4 found for computer-generated sphere packings with similar porosity as the investigated electrodes.[56-58]

1.4 Conclusions

In this study, we have shown that EIS measurements of porous graphite electrodes and numerical simulations of diffusion in the reconstructed pore space of such a graphite electrode lead to similar tortuosity values. The value of $\tau_{RS,z} = 6.55$ determined by the RS approach was within the experimental error of the EIS-determined tortuosity ($\tau_{EIS} = 7.3 \pm 0.9$). The experimental error of τ_{EIS} is mainly caused by the uncertainty in the porosity estimation. Apart from uncertainties in the determination of experimental parameters, differences between $\tau_{RS,z}$ and τ_{EIS} can originate in deviations of the real pore space from the idealized cylindrical pore of the TLM. As more reconstructions of porous electrodes become available, the TLM could be refined in the future to consider the actual shape, connectivity, and surface roughness of the pores rather than a generic pore model.

To make progress in this direction, accurate and representative reconstructions of porous electrodes are required. We have shown several criteria for obtaining such a reconstruction: 1. Using FIB-SEM as imaging method together with positive staining of the pore space allows to reconstruct directly the space that is penetrated by the electrolyte in the battery electrode. 2. The porosity of the reconstructed volume must meet the experimentally determined porosity of the electrodes to be representative. 3. The reconstructed volume must be sufficiently large to prevent finite-size effects and deliver statistically meaningful results in the diffusion simulations. This criterion is met when for each spatial direction the edge length of the reconstruction covers 20–25 times the average feature size of the pore space in this direction.

FIB-SEM reconstructions and numerical simulations are invaluable to understand the consequences of a given microstructure for the transport properties of battery electrodes, as we have shown here. As a routine method for the tortuosity determination of battery electrodes, the RS approach is too complex, expensive, and time-consuming, whereas EIS is fast and easily applicable. By demonstrating through the RS approach that EIS measurements and the TLM yield reliable tortuosity values even for an anisotropic microstructure with highly tortuous diffusion pathways, this study contributes to the validation of EIS as a routine method for the tortuosity determination of porous battery electrodes. Thus, an EIS-screening of newly designed LIB electrodes for morphology-caused ion transport limitations could help towards improving battery performance in the future.

1.5 References

1. S. Passerini and B. Scrosati, *Interface,* **25,** 85 (2016).
2. A. Manthiram, *ACS Cent. Sci.,* **3,** 1063 (2017).
3. D. R. Rolison, J. W. Long, J. C. Lytle, A. E. Fischer, C. P. Rhodes, T. M. McEvoy, M. E. Bourg, and A. M. Lubers, *Chem. Soc. Rev.,* **38,** 226 (2009).
4. D. Pritzl, J. Landesfeind, S. Solchenbach, and H. A. Gasteiger, *J. Electrochem. Soc.*, **165**, A2145 (2018).
5. M. Ender, J. Joos, T. Carraro, and E. Ivers-Tiffée, *J. Electrochem. Soc.,* **159,** A972 (2012).
6. Z. Liu, Y.-C. K. Chen-Wiegart, J. Wang, S. A. Barnett, and K. T. Faber, *Microsc. Microanal.,* **22,** 140 (2016).
7. J. Gelb, D. P. Finegan, D. J. L. Brett, and P. R. Shearing, *J. Power Sources,* **357,** 77 (2017).
8. M. Ebner, D.-W. Chung, R. E. García, and V. Wood, *Adv. Energy Mater.,* **4,** 1301278 (2014).
9. J. Landesfeind, J. Hattendorff, A. Ehrl, W. A. Wall, and H. A. Gasteiger, *J. Electrochem. Soc.,* **163,** A1373 (2016).
10. G. Inoue and M. Kawase, *J. Power Sources,* **342,** 476 (2017).
11. J. Landesfeind, M. Ebner, A. Eldiven, V. Wood, and H. A. Gasteiger, *J. Electrochem. Soc.,* **165,** A469 (2018).
12. R. de Levie, in *Advances in Electrochemistry and Electrochemical Engineering*, P. Delahay, Editor, p. 329, Interscience, New York (1967).
13. N. Ogihara, S. Kawauchi, C. Okuda, Y. Itou, Y. Takeuchi, and Y. Ukyo, *J. Electrochem. Soc.,* **159,** A1034 (2012).
14. N. Ogihara, Y. Itou, T. Sasaki, and Y. Takeuchi, *J. Phys. Chem. C,* **119,** 4612 (2015).
15. D. Cericola and M. E. Spahr, *Electrochim. Acta,* **191,** 558 (2016).
16. B. Tjaden, D. J. L. Brett, and P. R. Shearing, *Int. Mat. Rev.,* **63,** 47 (2018).

17. A. P. Cocco, G. J. Nelson, W. M. Harris, A. Nakajo, T. D. Myles, A. M. Kiss, J. J. Lombardo, and W. K. S. Chiu, *Phys. Chem. Chem. Phys.,* **15,** 16377 (2013).

18. M. Yoshio, *Lithium-Ion Batteries: Science and Technologies,* Springer, New York (2009).

19. T. Placke, O. Fromm, S. F. Lux, P. Bieker, S. Rothermel, H.-W. Meyer, S. Passerini, and M. Winter, *J. Electrochem. Soc.,* **159,** A1755 (2012).

20. M. Ebner and V. Wood, *J. Electrochem. Soc.*, **162**, A3064 (2015).

21. T. Müllner, A. Zankel, F. Svec, and U. Tallarek, *Mater. Today,* **17,** 404 (2014).

22. M. Balabajew, T. Kranz, and B. Roling, *ChemElectroChem,* **2,** 1991 (2015).

23. J. Schindelin, I. Arganda-Carreras, E. Frise, V. Kaynig, M. Longair, T. Pietzsch, S. Preibisch, C. Rueden, S. Saalfeld, B. Schmid, J.-Y. Tinevez, D. J. White, V. Hartenstein, K. Eliceiri, P. Tomancak, and A. Cardona, *Nat. Methods,* **9,** 676 (2012).

24. K. N. Dalby, R. P. Harti, H. O. Sørensen, and S. L. S. Stipp, *Microsc. Microanal.,* **21,** 631 (2015).

25. M. F. Lagadec, M. Ebner, R. Zahn, and V. Wood, *J. Electrochem. Soc.,* **163,** A992 (2016).

26. B. Münch, P. Trtik, F. Marone, and M. Stampanoni, *Opt. Express,* **17,** 8567 (2009).

27. E. H.W. Meijering, W. J. Niessen, and M. A. Viergever, *Med. Image Anal.,* **5,** 111 (2001).

28. D. Legland, I. Arganda-Carreras, and P. Andrey, *Bioinformatics,* **32,** 3532 (2016).

29. T. Müllner, K. K. Unger, and U. Tallarek, *New J. Chem.,* **40,** 3993 (2016).

30. S. Torquato and B. Lu, *Phys. Rev. E,* **47,** 2950 (1993).

31. B. Lu and S. Torquato, *J. Chem. Phys.,* **98,** 6472 (1993).

32. K. A. Cychosz, R. Guillet-Nicolas, J. García-Martínez, and M. Thommes, *Chem. Soc. Rev.,* **46,** 389 (2017).

33. I. Arganda-Carreras, R. Fernández-González, A. Muñoz-Barrutia, and C. Ortiz-De-Solorzano, *Microsc. Res. Tech.,* **73,** 1019 (2010).

34. M. Burstein, *Dijkstra's algorithm,* https://github.com/mburst/dijkstras-algorithm (2013).

35. E. W. Dijkstra, *Numer. Math.,* **1,** 269 (1959).

36. F. Delay, P. Ackerer, and C. Danquigny, *Vadose Zone J.,* **4,** 360 (2005).

37. P. Szymczak and A. J. C. Ladd, *Phys. Rev. E,* **68,** 036704 (2003).

38. H. Brenner, *Phil. Trans. R. Soc. Lond. A,* **297,** 81 (1980).

39. C. H. Chen, J. Liu, and K. Amine, *J. Power Sources,* **96,** 321 (2001).

40. M. Balabajew and B. Roling, *Electrochim. Acta,* **176,** 907 (2015).

41. S. J. Cooper, A. Bertei, D. P. Finegan, and N. P. Brandon, *Electrochim. Acta,* **251,** 681 (2017).

42. H. Keiser, K. D. Beccu, and M. A. Gutjahr, *Electrochim. Acta,* **21,** 539 (1976).

43. V. F. Lvovich, *Impedance Spectroscopy: Applications to Electrochemical and Dielectric Phenomena,* Wiley, Hoboken (2012).

44. D. R. Lide, *CRC Handbook of Chemistry and Physics,* CRC Press, Boca Raton (2003).

45. A. Çeçen, E. A. Wargo, A. C. Hanna, D. M. Turner, S. R. Kalidindi, and E. C. Kumbur, *J. Electrochem. Soc.,* **159,** B299 (2012).

46. T. Müllner, A. Zankel, Y. Lv, F. Svec, A. Höltzel, and U. Tallarek, *Adv. Mater.,* **27,** 6009 (2015).

47. K. Hormann, V. Baranau, D. Hlushkou, A. Höltzel, and U. Tallarek, *New J. Chem.,* **40,** 4187 (2016).

48. D. Hlushkou, A. E. Reising, N. Kaiser, S. Spannenberger, S. Schlabach, Y. Kato, B. Roling, and U. Tallarek, *J. Power Sources,* **396,** 363 (2018).

49. T. Aste and T. Di Matteo, *Phys. Rev. E,* **77,** 021309 (2008).

50. S. Bruns, T. Hara, B. M. Smarsly, and U. Tallarek, *J. Chromatogr. A,* **1218,** 5187 (2011).

51. K. Hormann, T. Müllner, S. Bruns, A. Höltzel, and U. Tallarek, *J. Chromatogr. A,* **1222,** 46 (2012).

52. D. Stoeckel, C. Kübel, M. O. Loeh, B. M. Smarsly, and U. Tallarek, *Langmuir,* **31,** 7391 (2015).

53. M. Ebner, D.-W. Chung, R. E. García, and V. Wood, *Adv. Energy Mater.,* **4,** 1301278 (2014).

54. S.-J. Reich, A. Svidrytski, D. Hlushkou, D. Stoeckel, C. Kübel, A. Höltzel, and U. Tallarek, *Ind. Eng. Chem. Res.,* **57,** 3031 (2018).

55. T. C. Lee, R. L. Kashyap, and C.-N. Chu, *CVGIP: Graphical Models Image Process.,* **56,** 462 (1994).

56. S. Khirevich, A. Höltzel, A. Daneyko, A. Seidel-Morgenstern, and U. Tallarek, *J. Chromatogr. A,* **1218,** 6489 (2011).

57. H. Liasneuski, D. Hlushkou, S. Khirevich, A. Höltzel, U. Tallarek, and S. Torquato, *J. Appl. Phys.,* **116,** 034904 (2014).

58. D. Hlushkou, H. Liasneuski, U. Tallarek, and S. Torquato, *J. Appl. Phys.,* **118,** 124901 (2015).

Chapter 2: Thickness-dependent Impedance of Composite Battery Electrodes containing Ionic Liquid-based Electrolytes

Authors

Marvin Cronau,[+] Moritz Kroll,[+] Marvin Szabo, Fabian Sälzer, and Bernhard Roling*

[+]These authors contributed equally to this work.

State of publication

Published 02 March 2020 in *Batteries & Supercaps*, Vol. 3, pp. 1–9.
DOI: 10.1002/batt.202000023

Abstract

Lithium-ion battery models often neglect the salt concentration polarization inside the electrolyte-filled pores of the composite electrodes. However, this concentration polarization causes a significant impedance, in particular in the case of electrolytes with low Li^+ transference numbers. Here, we analyze in detail measured and calculated impedance spectra of composite electrodes containing a solvate ionic liquid-based electrolyte and an ionic liquid-based electrolyte, respectively, in comparison to a conventional carbonate-based electrolyte. For calculating spectra, we use a recently published model by Huang and Zhang. We find that the impedance at 10^{-4} Hz, which is relevant for battery cycling rates around 1 C to 2 C, increases in the order carbonate-based electrolyte < ionic liquid-based electrolyte < solvate ionic liquid-based electrolytes, but exhibits a remarkably weak thickness dependence, when the electrode thickness exceeds 50-100 µm. This suggests that electrodes considerably thicker than the conventional 80 µm can be used in batteries without significantly deteriorating battery power.

2.1 Introduction

In state-of-the-art lithium-ion batteries (LIBs), the liquid electrolyte is based on volatile organic carbonates. Due to the high vapor pressure, the electrolyte is flammable, leading to serious safety concerns.[1,2] Consequently, a lot of current research is devoted to the study of alternative electrolytes with low vapor pressure and high thermal and electrochemical stability. These are e.g. solvate ionic liquids,[3-6] solvent-in-salt electrolytes,[7-10] and ionic liquid/Li salt mixtures.[11-13] The Li^+ ion transport in these alternative electrolytes is, however, slower than in the carbonate-based electrolytes. Therefore, it is important to carry out comprehensive studies of the ion transport properties of these electrolytes and to use the results for assessing the influence of the electrolyte on the battery impedance. Here, the impedance of the composite electrodes is particularly relevant, since the electrodes are considerably thicker (typically around 80 µm) than the electrolyte-filled separator (typically around 20 µm). During stationary battery cycling, a salt concentration gradient is formed inside the electrolyte-filled pores of the composite electrode leading to anion blocking and stationary Li^+ ion transport. The impedance due to this salt concentration polarization increases with decreasing ionic conductivity and decreasing Li^+ transference number of the electrolyte.[14] Consequently, the salt concentration polarization impedance in the case of solvate ionic liquid-based electrolytes, solvent-in-salt electrolytes, and ionic liquid-based electrolytes is expected to be higher than in the case of carbonate-based electrolytes. However, this concentration polarization impedance is often not explicitly taken into account in battery impedance models, see e.g. Ref. [15], which may be acceptable for carbonate-based electrolytes, but is problematic for alternative electrolytes with slower Li^+ ion transport. Recently, Huang and Zhang published an analytical model for the impedance of composite electrodes explicitly taking into account the salt concentration polarization inside the electrolyte-filled pores of the composite electrodes.[16]

In this paper, we analyze in detail measured and calculated impedance spectra of composite cathodes containing three different classes of electrolytes: (i) A solvate ionic liquid consisting of a 50:50 molar ratio of tetraglyme (G4) with LiTFSI; (ii) a conventional carbonate-based electrolyte, 1 M $LiPF_6$ in EC/EMC 50:50; (iii) a mixture of the ionic liquid *N*-methyl-*N*-propyl-pyrrolidinium bis(fluorosulfonyl)imide ($Pyrr_{13}FSI$) with the Li salt LiFSI in a molar ratio of 60:40. This molar ratio was chosen, since this mixture exhibits the best ion transport properties.[17] The chemical structures of these electrolytes is illustrated in Figure 2.1. For calculating the impedance spectra, we use the model by Huang et al.[16] We compare experimental and model spectra of composite electrodes with variable thickness, but constant porosity, and we analyze in detail the different contributions to the electrode impedance in dependence of the thickness. We note that the impedance spectra of composite electrodes up to 50 µm thickness containing a standard carbonate-based electrolyte have been analyzed recently

by Gruet et al.[18] Here, we consider also thicker electrodes up to about 150-200 µm, and we pay special attention to the electrode impedance at a frequency of 10^{-4} Hz, which is relevant for battery cycling with rates around 1 C to 2 C. We find that this impedance depends on the type of electrolyte, but exhibits a remarkably weak thickness dependence, when the electrode thickness exceeds 50-100 µm. To our knowledge, this weak thickness dependence has not yet been reported and discussed in the literature.

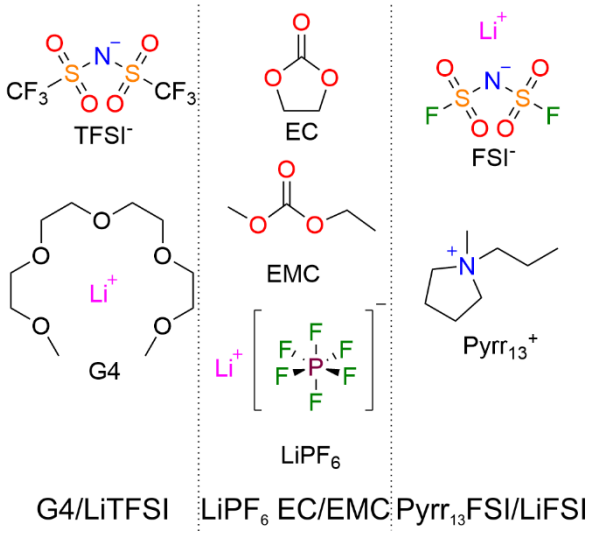

Figure 2.1: Chemical structures of the studied solvate ionic liquid-based electrolyte, carbonate-based electrolyte, and ionic liquid-based electrolyte.

2.2 Experimental

2.2.1 Preparation of electrolytes

The conventional carbonate-based electrolyte was purchased from Sigma Aldrich (Steinheim, Germany). The solvate ionic liquids were prepared by dissolving LiTFSI (Sigma Aldrich, Steinheim, Germany, 99.95%) in tetraglyme (Sigma Aldrich, Steinheim, Germany, >99%) at room temperature. The ionic liquid / lithium salt mixtures were prepared by dissolving LiFSI (TCI GmbH, Zwijndrecht, Belgium, 98.00%) in $Pyrr_{13}FSI$ (Fluorochem Ltd., Derbyshire, United Kingdom, battery grade) at room temperature.

2.2.2 Electrode preparation

$LiCoO_2$ (LCO) composite electrodes with variable thickness were prepared from an *N*-Methyl-2-pyrrolidone-based (NMP 99.5%, Alfa Aesar, Thermo Fischer GmbH, Kandel, Germany)

slurry of 90 wt% LCO (97%, Alfa Aesar), 5 wt% C-NERGY SUPER C 65 carbon black (Timcal, Bodio, Switzerland), and 5 wt% polyvinylidene fluoride (PVDF, Solvay GmbH, Hannover). To this end, the binder was dissolved in NMP at 40 °C, and LCO particles and carbon black were added gradually. The slurry was mixed by means of a T 25 disperser (IKA, Staufen, Germany) and then casted onto an aluminum foil, whereby the thickness of the resulting films was adjusted by means of a ZAA 2300 automatic film applicator (Zehntner, Sissach, Switzerland). The foils were dried for 24 hours at 80 °C under air atmosphere and then transferred into an argon-filled glovebox (UniLab, MBraun, Germany; $x_{H2O} < 1$ ppm, $x_{O2} < 1$ ppm). The porosity of the composite electrodes was determined from the mass, the area and the thickness of the electrodes, taking into account the densities of the electrode components. In order to adjust the porosity of the electrodes to a value of 35%, the films were compacted by using a hot rolling press (MSK-HRP-01, MTI Corporation, Richmond, USA). Discs with a diameter of 12 mm were then cut out of the resulting films. The thickness and weight of each disc electrode including the current collector was determined to calculate the porosity. To this end, a micrometer screw (IP65, Mitutoyo Deutschland GmbH, Neuss) with an error of ±1 µm was used. To determine the weight, we used an analytical balance inside an argon-filled glovebox. To calculate the porosity of each electrode, the mean weight and height of the aluminum current collector was subtracted. To this end, the weight and thickness of 50 aluminum discs with the same diameter were measured. This leads to a mean weight of 9.3 ± 0.1 mg and a mean thickness of 32.8 ± 1.3 µm.

2.2.3 Battery cycling

Battery cycling was performed in a TSC battery cell (rhd instruments, Darmstadt, Germany), using a Multi Autolab/M101 (Metrohm Autolab BV, Utrecht, Netherlands). The cells were assembled in an argon-filled glovebox (UniLab, MBraun, Germany; $x_{H2O} < 1$ ppm, $x_{O2} < 1$ ppm). The battery cycling was carried out in a three-electrode setup with the LCO composite electrode as working electrode and Li metal foil (Albemarle, Germany) as counter and quasi-reference electrode. Working and counter electrodes were separated by 8 layers of Whatman GF/A glass microfiber filters (GE Healthcare, Buckinghamshire, United Kingdom). The separators were soaked with 240 µl of the respective electrolyte. The cells were equilibrated over night at room temperature before starting the cycling.

2.2.4 Electrochemical impedance spectroscopy

The electrochemical impedance measurements were carried out by means of a Multi Autolab/M101 equipped with a FRA32 M impedance modul (Metrohm Autolab BV, Utrecht,

Netherlands) in a three-electrode setup. The spectra were taken at 50% of the maximum discharge capacity achieved with the respective electrolyte. The frequency range extended from 1 MHz to 10^{-4} Hz with an applied AC voltage amplitude of 10 mV at the open-circuit potential of the respective charge state. Impedance spectra were analyzed using the software RelaxIS 3 (rhd instruments, Darmstadt, Germany).

2.2.5 Calculation of impedance spectra

The complex impedance of the composite LCO cathodes was calculated using the model published by Huang and Zhang[16] To this end, the model was implemented as a Visual C# plugin to the RelaxIS Circuit Simulator (rhd instruments, Darmstadt, Germany). The input parameters are listed in Table 2.1. The mean radius of the active material particles R_{ap} was determined from an SEM image (Figure 2.S1). The surface of the active material particles was then estimated by assuming spherical particles with the mean radius. The ion transport tortuosity τ_{ion} was determined from EIS measurements under ion-blocking conditions at the electrolyte / LCO particle interface based on the conventional transmission line model (see Supporting Information for more details).[C,D] In order to assess the dependence of the electrode potential on the Li concentration in the active material particles, the charge/discharge potentials of a thin electrode with high porosity (resulting in low overpotentials) was plotted vs. the Li concentration (Figure 2.S3). At the end of the charging process, the stoichiometry of LCO is $Li_{0.5}CoO_2$. The derivative dU/dc_s was determined from the slope at 50% state of charge ($Li_{0.75}CoO_2$). The electronic resistance was assumed to be negligible due to the usage of a conductive carbon additive.

Table 2.1: Parameters for the calculation of impedance spectra using the model of Huang and Zhang[16] for LCO composite cathodes containing G4/LiTFSI 50:50 or 1 M $LiPF_6$ in a carbonate mixture as electrolyte.

Parameter	Physical meaning	Value	
		G4/LiTFSI 50 : 50	**1 M $LiPF_6$ in carbonates**
σ_{ion}	Ionic conductivity	0.152 S m^{-1} [21]	1 S m^{-1} [22]
D_{salt}	Salt diffusion coefficient	$6.96 \cdot 10^{-12}$ m^2 s^{-1} [22]	$3 \cdot 10^{-10}$ m^2 s^{-1} [22]
$\frac{d\ln(a_{+-})}{d\ln(c_{salt})}$	Thermodynamic factor	30 [23]	2 [24]
t_+^{μ}	Mobility-based Li^+ transference number of the electrolyte	0.45 [17]	0.35 [22]
c_{salt}	Salt concentration	2640 mol m^{-3} [23]	1000 mol m^{-3}
j_0	Exchange current density for cathode active material particles	1 A m^{-2}	0.124 A m^{-2}
T	Temperature	303.15 K	
m_{ap}	Active material weight per electrode thickness	0.3115 kg m^{-1}	
R_{ap}	Radius of the active material particles	$1.7 \cdot 10^{-6}$ m	
ρ_{ap}	Active material mass density	5060 kg m^{-3}	
ε_e	Electrode porosity	0.35	
τ_{ion}	Ionic tortuosity	2.7	
dU/dc_s	Dependence of electrode potential on Li^+ concentration in the active material particles	$-6.68 \cdot 10^{-6}$ V m^3 mol^{-1}	
C_{DL}	Double layer capacitance	$5 \cdot 10^{-2}$ F m^{-2}	

D_s	Li chemical diffusion coefficient in active material particle	$1 \cdot 10^{-15}$ m^2 s^{-1} [25]

2.3 Results and discussion

In Fig. 2.2, we compare the galvanostatic charge/discharge curves of LCO composite cathodes with a thickness of 66-67 µm containing one of the three electrolytes. The discharge capacity of commercial LCO is typically in the range of 160-170 mAh g^{-1}.[26] In the case of the carbonate-based electrolyte 1 M $LiPF_6$ in EC/EMC 50:50, this typical discharge capacity is achieved. In contrast, with the two alternative electrolytes, lower discharge capacities are observed, namely about 30 mAh g^{-1} in the case of the G4/LiTFSI 50:50 and about 85 mAh g^{-1} in the case of $Pyrr_{13}FSI$/LiFSI 60:40. In order to estimate the area-specific effective resistances during galvanostatic cycling, the charge and discharge overpotential at SOC50 was taken, since the impedance spectra were also taken at this SOC. The difference between the charge and discharge potential at SOC50 was identified with the sum of the charge and the discharge overpotential. By taking into account the current density, the following area-specific effective resistances were estimated: (i) about 130 Ω cm^2 in the case of G4/LiTFSI 50:50; (ii) about 30 Ω cm^2 in the case of 1 M $LiPF_6$ in EC/EMC 50:50; (iii) about 95 Ω cm^2 in the case of $Pyrr_{13}FSI$/LiFSI 60:40.

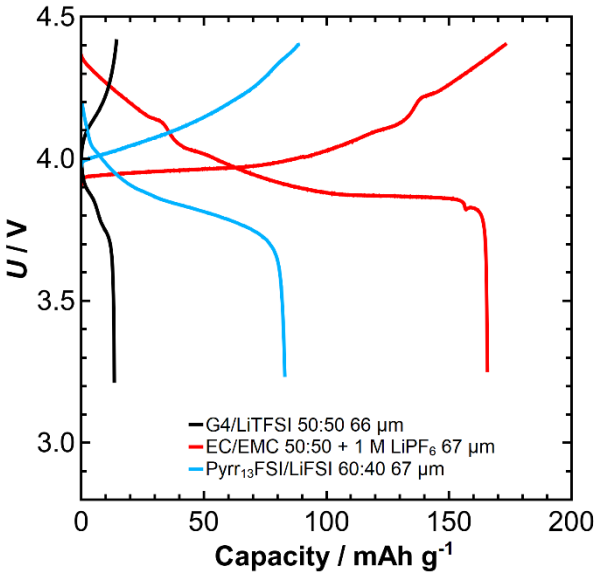

Figure 2.2: First galvanostatic cycle of LCO composite electrodes with a thickness of 66-67 µm containing different electrolytes. The electrodes were cycled with a C rate of 0.26 C (44 mA g^{-1}).

In Fig. 2.3 (a)-(c) we show measured impedance spectra taken for composite electrodes of variable thickness containing one of the three electrolytes. The insets show zooms into the high-frequency regime of the spectra. We note that all spectra exhibit a high-frequency resistance, which is caused by the electrolyte-filled separator between the composite LCO working electrode and the quasi-reference electrode. In Fig. 2.3, this high-frequency resistance is subtracted in order to show exclusively the impedance of the LCO composite electrode. The high-frequency impedance of this composite electrode down to about 1 Hz is characterized by a transmission-line-type impedance caused by the ion migration resistance of the composite electrodes, R_{ion}, and the charge transfer resistance R_{ct} for Li^+ ions at the electrolyte/active material interface.[27] At frequencies below 1 Hz, a Warburg-type impedance is detected. In all spectra, the impedance measured at the lowest frequency of 10^{-4} Hz is indicated, since this impedance is relevant for typical battery cycling rates around 1 C - 2 C. This cycling rate implies a cycling time scale of τ = 1 hour = 3600 s, corresponding to a frequency of $1/(2\pi\tau) \approx 4 \cdot 10^{-5}$Hz. Since our lowest measurement frequency of 10^{-4} Hz is close to $1/(2\pi\tau)$, the impedance at this frequency should be similar to the effective resistance of the composite electrode during 1 C - 2 C cycling. For the electrode thicknesses in the range of 66-67 µm, we obtain the following order of $Z'(10^{-4}$ Hz) values: G4/LiTFFSI 50:50 > $Pyrr_{13}$FSI/LiFSI 60:40

> 1 M $LiPF_6$ in EC/EMC 50:50. This is the same order as obtained for the effective resistances from the galvanostatic charge/discharge curves shown in Fig. 2.2.

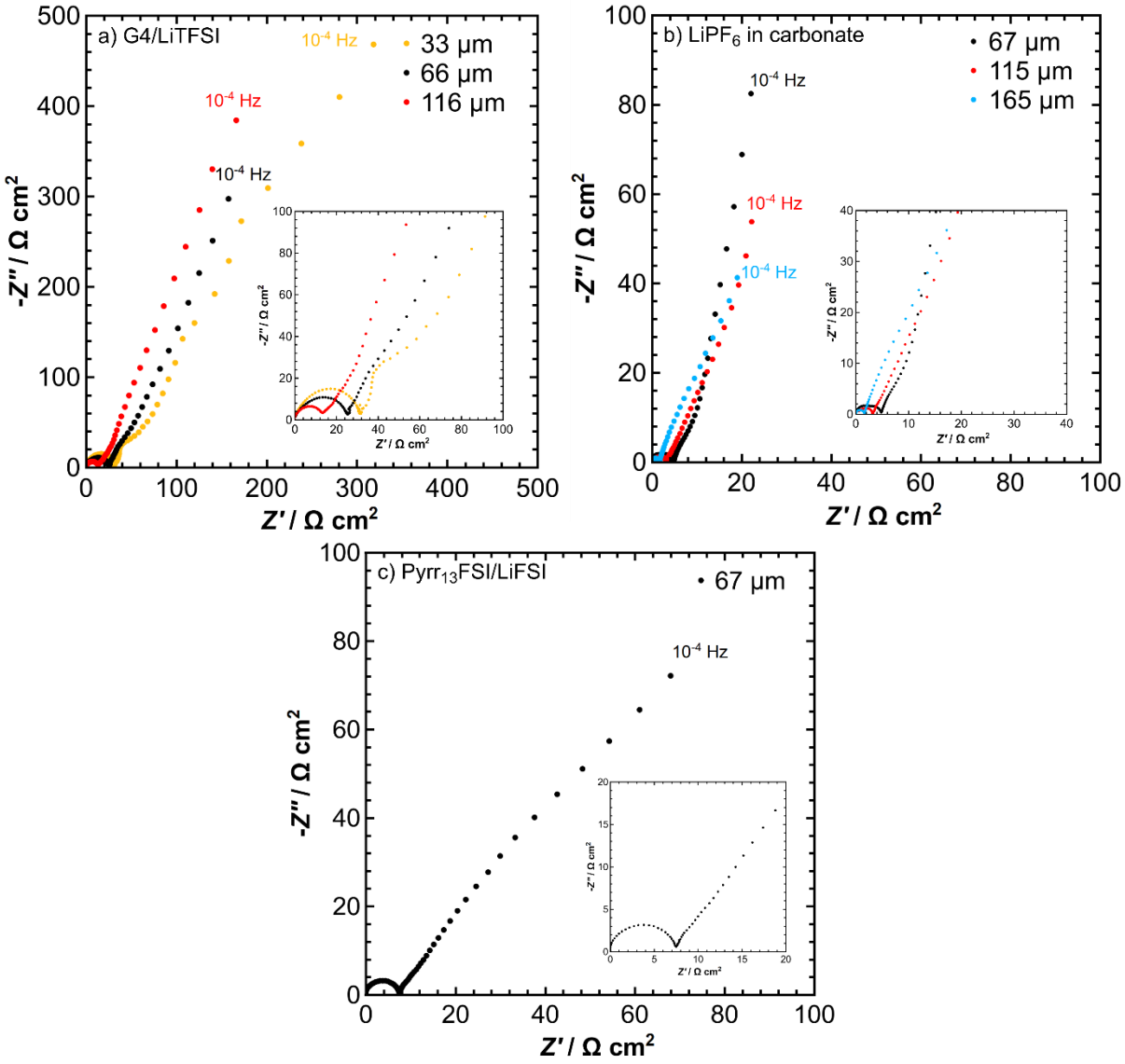

Figure 2.3: Impedance spectra (Frequency range: 10^3 Hz to 10^{-4} Hz) of LCO composite electrodes with varying thicknesses. a) G4/LiTFSI 50:50, thicknesses between 33 µm and 116 µm. b) 1 M $LiPF_6$ in EC/EMC 50:50, thicknesses between 67 µm and 165 µm. c) $Pyrr_{13}FSI$/LiFSI 60:40, thickness of 67 µm. The insets show zooms into the high-frequency range.

In Fig. 2.4 a) and b) we show in comparison calculated impedance spectra for composite electrodes containing the two electrolytes G4/LiTFSI 50:50 and 1 M $LiPF_6$ in a carbonate mixture. The very-low-frequency spikes due to the chemical capacitance of the active material particles are shown in Fig. 2.S4. The spectra were calculated by means of the impedance model by Huang and Zhang[16], which is only applicable to electrolytes containing a single type of cations and a single type of anions. Consequently, it cannot be used for calculating impedance spectra of the ionic liquid-based electrolyte $Pyrr_{13}FSI$/LiFSI containing three types of ions. The high-frequency semicircle is due to ion migration resistance and the charge transfer resistance, while the low-frequency semicircle is caused by the salt concentration polarization impedance (see Figure 2.S5). The model spectra are similar to the measured spectra, not only with regard to the spectral shape, which will be discussed later in more detail, but also regarding the dependence of the impedance on the electrode thickness. In the case of G4/LiTFSI 50:50, we observe a decrease of $Z'(10^{-4}\ \mathrm{Hz})$ with increasing thickness of the electrode, see Fig. 2.3 a) and Fig. 2.4 a). In the case of 1 M $LiPF_6$ in EC/EMC/PC, the real part of the impedance at 10^{-4} Hz, $Z'(10^{-4}\ \mathrm{Hz})$, depends only weakly on the thickness of the composite electrode, see Fig. 2.4 (b). This weak dependence is also observed in the experimental spectra in Fig. 2.3 b).

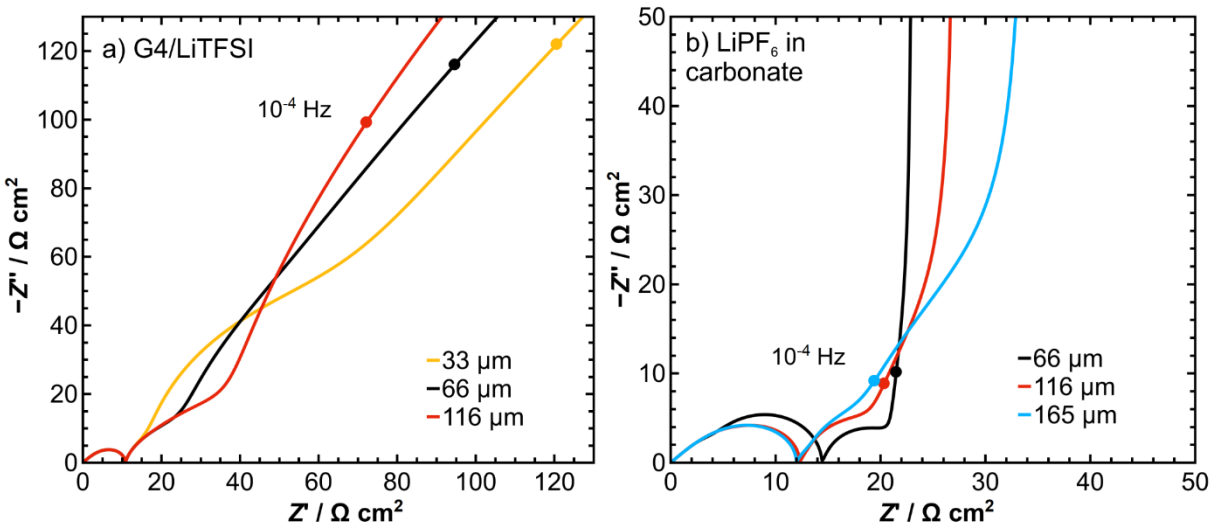

Figure 2.4: a) Calculated impedance spectra of a LCO composite cathode with a) G4/LiTFSI 50:50 and b) $LiPF_6$ in carbonate as electrolyte.

In Fig. 2.5, we consider the thickness dependence of the calculated electrode resistances in more detail. We compare the electrode resistance in the limit of zero frequency $R_{zf} = Z'(\nu \to 0)$ with the real part and the modulus of the impedance at 10^{-4} Hz, $Z'(10^{-4}\ \mathrm{Hz})$ and $|Z|(10^{-4}\ \mathrm{Hz})$. At

low electrode thicknesses, R_{zf} decreases with increasing thickness. With further increasing thickness R_{zf} goes through a minimum and then increases. In contrast, $Z'(10^{-4}\ \text{Hz})$ and $|Z|(10^{-4}\ \text{Hz})$ decrease essentially with increasing thickness, but beyond 100 µm, $Z'(10^{-4}\ \text{Hz})$ and $|Z|(10^{-4}\ \text{Hz})$ exhibit only a very weak thickness dependence.

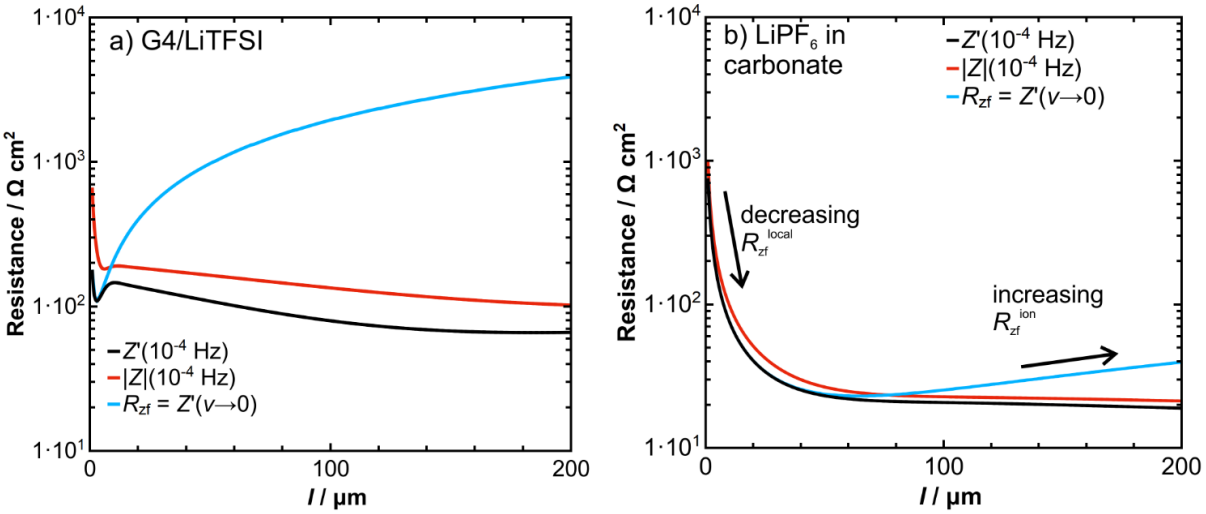

Figure 2.5: Dependence of the zero-frequency electrode resistance R_{zf} and of the real part and the modulus of the impedance at 10^{-4} Hz, Z' (10^{-4} Hz), and $|Z|(10^{-4}\ \text{Hz})$ on electrode thickness when using a) G4/LiTFSI 50:50 and b) $LiPF_6$ in carbonate as electrolyte.

In the following, we discuss the origin of these thickness dependences. In a recent paper, we showed that low-frequency impedance spectra of a porous electrode in the framework of the Huang and Zhang model can be approximated by a modified transmission-line model expression:[17]

$$Z_{\text{pe}}^{\text{lf-TLM}} = \sqrt{\frac{Z_{\text{loc}}}{a_{\text{v}} \cdot \sigma_{\text{Li}^+}^{\text{ABC,eff}}}} \cdot \coth\left(\sqrt{\frac{a_{\text{v}} \cdot l_{\text{p}}^2}{\sigma_{\text{Li}^+}^{\text{ABC,eff}} \cdot Z_{\text{loc}}}}\right) \tag{2.1}$$

Here, $\sigma_{\text{Li}^+}^{\text{ABC,eff}} = t_{\text{Li}^+}^{\text{ABC}} \cdot \sigma_{\text{ion}}^{\text{eff}}$ is the effective ionic conductivity of the composite electrode under anion-blocking conditions. $\sigma_{\text{ion}}^{\text{eff}} = \frac{\sigma_{\text{ion}}\,\varepsilon_{\text{e}}}{\tau_{\text{ion}}}$ is the effective ionic conductivity of the composite electrode without salt concentration polarization, and $t_{\text{Li}^+}^{\text{ABC}}$ is the Li^+ ion transference number

under anion-blocking conditions. The pore length is denoted by $l_\mathrm{p} = l \cdot \tau_\mathrm{ion}$, and $a_\mathrm{v} = \frac{3(1-\varepsilon_\mathrm{e})}{R_\mathrm{ap}}$ corresponds to the surface of the active material particles per unit volume of the electrode. The local impedance Z_loc is given by:

$$Z_\mathrm{loc} = \left(\left(R_\mathrm{CT} + \frac{\mathrm{d}U}{\mathrm{d}c_\mathrm{s}} Y_\mathrm{s}\right)^{-1} + i\omega C_\mathrm{DL}\right)^{-1} \tag{2.2}$$

with

$$Y_s = \frac{R_\mathrm{ap}}{F D_\mathrm{s}} \cdot \frac{\tanh(\Omega_\mathrm{s})}{\tanh(\Omega_\mathrm{s}) - \Omega_\mathrm{s}} \tag{2.3}$$

and

$$\Omega_\mathrm{s} = \sqrt{\frac{i\omega R_\mathrm{ap}^2}{D_\mathrm{s}}} \tag{2.4}$$

$R_\mathrm{CT} = \frac{RT}{F j_0}$ is the area-specific charge transfer resistance at the electrode / active material particle interface. The other parameters are explained in Tab. 1. Eq. (1) describes the impedance under the assumption that the salt concentration polarization in the electrolyte-filled pores of the electrode is complete (complete anion blocking), but the Li^+ chemical diffusion inside the active material particles still takes place. A zero-frequency Taylor expansion of Eq. (1) results in the following expression for the real part of the electrode impedance in the zero-frequency limit, R_zf:

$$R_\mathrm{zf} = \underbrace{\frac{l_\mathrm{p}}{3\sigma_\mathrm{ion}^\mathrm{ABC,eff}}}_{R_\mathrm{zf}^\mathrm{ion}} + \underbrace{\frac{R_\mathrm{CT}}{a_\mathrm{v} l_\mathrm{p}} - \frac{R_\mathrm{ap}}{5 F D_\mathrm{s} a_\mathrm{v} l_\mathrm{p}} \cdot \frac{\mathrm{d}U}{\mathrm{d}c_\mathrm{s}}}_{R_\mathrm{zf}^\mathrm{local}} \tag{2.5}$$

The first term in the middle part of Eq. (5) describes the Li^+ ion transport limitations due to concentration polarization and anion-blocking and is in the following denoted by R_{zf}^{ion}. The second term accounts for the charge transfer at the electrolyte / LCO interface and the third term for the resistance due to Li chemical diffusion into the active material particles. The second and the third term arise from the local impedance given in Eqs. (2)-(4). Therefore, the sum of the second and of the third term is denoted in the following by R_{zf}^{local}. While the ion transport resistance R_{zf}^{ion} increases with the electrode thickness $\boldsymbol{l}$, the local resistance R_{zf}^{local} decreases with l. For thin electrodes, R_{zf}^{local} dominates and leads to a decrease of R_{zf} with increasing l. At thick electrodes, R_{zf}^{ion} dominates and leads to an increase of R_{zf} with increasing l, see Fig. 2.5.

In order to elucidate the origin of the weak thickness dependence of $Z'(10^{-4}\,\mathrm{Hz})$ and $|Z|(10^{-4}\,Hz)$, we approximate the impedance by a more general transmission-line type equation:

$$Z_{\mathrm{pe}}^{\text{general TLM}} = \sqrt{\frac{Z_{\mathrm{ion}} \cdot Z_{\mathrm{loc}}}{l_{\mathrm{p}} \cdot a_{\mathrm{v}}}} \cdot \coth\left(\sqrt{\frac{Z_{\mathrm{ion}} \cdot l_{\mathrm{p}} \cdot a_{\mathrm{v}}}{Z_{\mathrm{loc}}}}\right) \tag{2.6}$$

with

$$Z_{\mathrm{ion}} = \frac{l_{\mathrm{p}}}{\sigma_{\mathrm{ion}}^{\mathrm{eff}}} + \left(\frac{l_{\mathrm{p}}}{\sigma_{\mathrm{ion}}^{\mathrm{ABC,eff}}} - \frac{l_{\mathrm{p}}}{\sigma_{\mathrm{ion}}^{\mathrm{eff}}}\right)\frac{\tanh(\Omega_{\mathrm{ion}})}{\Omega_{\mathrm{ion}}} \tag{2.7}$$

and

$$\Omega_{\mathrm{ion}} = \sqrt{\frac{i\omega {l_{\mathrm{p}}}^2}{D_{\mathrm{salt}}}} \tag{2.8}$$

Eq. (6) takes into account the frequency dependence of Z_{ion}, as described by Eqs. (7) and (8), while Eq. (1) contains only the zero-frequency limit of Z_{ion}. These equations are based on a generalized transmission line model (TLM). TLMs are widely used in the literature to describe

the response of porous electrodes.[28] In Ref. [28], the TLM with open-open condition and with $Z_C = 0$ leads to Eq. (6). Eq. (7) is derived from the equations for the ion transport impedance between planar electrodes under anion-blocking conditions,[21] and is only modified for porous electrodes by replacing the ionic conductivities by effective ionic conductivities according to the porosity and tortuosity of the electrode.

Two limiting cases of Eq. (6) can be considered: (i) If $Z_{ion} \gg Z_{loc}/(l_p \cdot a_v)$, the coth function becomes unity and the impedance is given by $Z_{pe}^{general\ TLM} = \sqrt{\frac{Z_{ion} \cdot Z_{loc}}{l_p \cdot a_v}}$. This impedance is independent of electrode thickness. (ii) If $Z_{loc}/(l_p \cdot a_v) \gg Z_{ion}$, the coth(x) function can be Taylor expanded $1/x + x/3$. This results in $Z_{pe}^{general\ TLM} = Z_{\mathrm{loc}}/(l_{\mathrm{p}} \cdot a_{\mathrm{v}}) + Z_{\mathrm{ion}}/3$. In this case, the impedance does depend on thickness. Since $Z_{\mathrm{loc}}/(l_{\mathrm{p}} \cdot a_{\mathrm{v}})$ and Z_{ion} exhibit distinct frequency dependences, the ratio of these two impedance is frequency-dependent.

In Fig. 2.6, we plot the modulus of $Z_{\mathrm{loc}}/(l_{\mathrm{p}} \cdot a_{\mathrm{v}})$ and of Z_{ion} versus the frequency for a composite electrode containing the electrolytes G4/LiTFSI 50:50 and 1 M $LiPF_6$ in a carbonate mixture, respectively. Three different electrode thicknesses, 50 µm, 100 µm, and 150 µm are considered. In the case of the electrolyte G4/LiTFSI 50:50, we find that $Z_{\mathrm{ion}} \gg Z_{\mathrm{loc}}/(l_{\mathrm{p}} \cdot a_{\mathrm{v}})$ for all thicknesses and over the entire frequency range, see Fig. 2.6 a). Consequently, the impedance can be well approximated by $Z_{\mathrm{pe}}^{\mathrm{general\ TLM}} = \sqrt{\frac{Z_{\mathrm{ion}} \cdot Z_{\mathrm{loc}}}{l_{\mathrm{p}} \cdot a_{\mathrm{v}}}}$. At a frequency of 10^{-4} Hz, the modulus of Z_{ion} is in the range of 10^3 Ω cm^2 and depends only weakly on thickness, while the modulus of $Z_{\mathrm{loc}}/(l_{\mathrm{p}} \cdot a_{\mathrm{v}})$ is in the range of 4-12 Ω cm^2 and decreases with increasing thickness. Since in this case $Z_{\mathrm{pe}}^{\mathrm{general\ TLM}}$ is the geometrical average of Z_{ion} and $Z_{\mathrm{loc}}/(l_{\mathrm{p}} \cdot a_{\mathrm{v}})$, its modulus should be in the range of 100-200 Ωcm^2 and should decrease slightly with increasing thickness. As shown in Fig. 2.5 a), $|Z|(10^{-4}$ Hz) is indeed in the range of 160 Ωcm^2 and decreases slightly with increasing thickness. Thus, the origin of this slight decrease is the decreasing $Z_{\mathrm{loc}}/(l_{\mathrm{p}} \cdot a_{\mathrm{v}})$ due to an increasing interfacial area between electrolyte and LCO particles. In the case of the electrolyte 1 M $LiPF_6$ in a carbonate mixture, the modulus of $Z_{\mathrm{loc}}/(l_{\mathrm{p}} \cdot a_{\mathrm{v}})$ is in a similar range, see Fig. 2.6 b). At 10^{-4} Hz we also have $Z_{\mathrm{ion}} > Z_{\mathrm{loc}}/(l_{\mathrm{p}} \cdot a_{\mathrm{v}})$ and consequently the impedance $Z_{\mathrm{pe}}^{\mathrm{general\ TLM}}$ should become virtually independent of thickness at 10^{-4} Hz. As shown in Fig. 2.5 b), Z' (10^{-4} Hz) and $|Z|(10^{-4}$ Hz) for the electrolyte 1 M $LiPF_6$ in a carbonate mixture depend indeed very weakly on thickness, when the thickness exceeds about 50 µm.

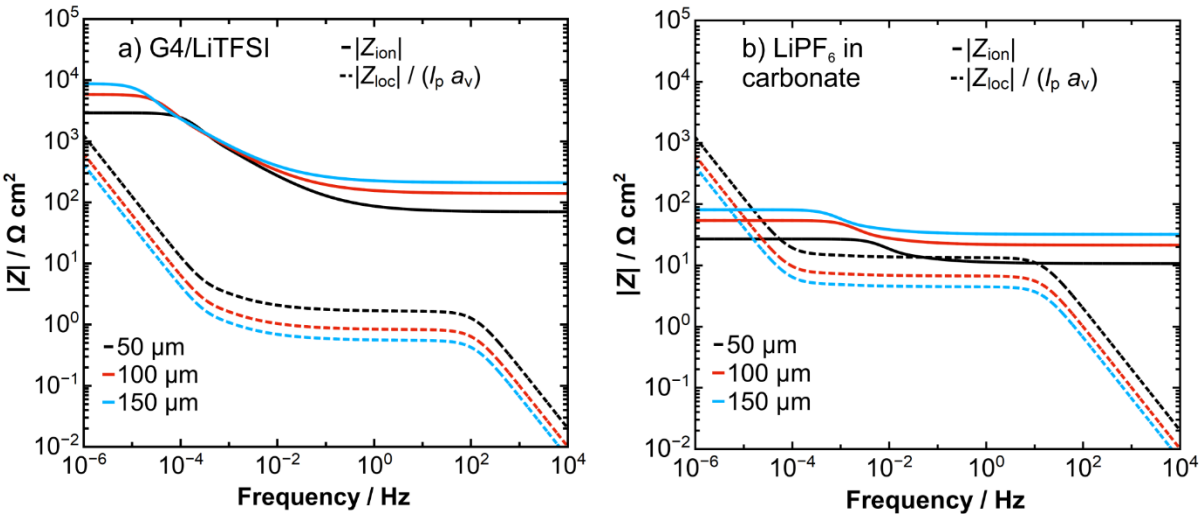

Figure 2.6: Frequency dependence of the ion transport impedance Z_{ion} and of the local impedance $Z_{\mathrm{loc}}/(l_{\mathrm{p}} \cdot a_{\mathrm{v}})$ for different electrode thicknesses when using a) G4/LiTFSI 50:50 and b) 1 M $LiPF_6$ in carbonate as electrolyte.

Thus, we can state that for both electrolytes, the thickness dependence of Z' (10^{-4} Hz) and of $|Z|(10^{-4}\ \mathrm{Hz})$ is much weaker than the thickness dependence of the zero-frequency limit R_{zf} given in Eq. (5). This suggests that it should be possible to use battery electrodes considerably thicker than the conventional 80 µm without significantly deteriorating battery power at cycling rates around 1C – 2C. A prerequisite is, however, that the composite electrode morphology can be held constant over the entire thickness range. In this context, it is worth noting that recently Gao et al. reported an increasingly sluggish Li^+ ion transport when increasing the thickness of Ni-Mn-Co oxide (NMC) composite electrodes above 200 µm.[29] Our results suggest that this sluggish Li^+ transport is caused by morphological changes when increasing electrode thickness and is *not* an intrinsic feature of thick electrodes.

2.4 Conclusions

We have analyzed experimental and simulated impedance spectra of composite LCO electrodes containing the electrolytes G4/LiTFSI 50:50 and $Pyrr_{13}FSI$/LiFSI 60:40 in comparison to electrodes containing the conventional electrolyte 1 M $LiPF_6$ in EC/EMC 50:50. The results

show that the electrode impedance increases in the order 1 M $LiPF_6$ in EC/EMC 50:50 < $Pyrr_{13}FSI$/LiFSI 60:40 < G4/LiTFSI 50:50. This is due to the lower ionic conductivity and lower Li^+ ion transference number of the ionic liquid-based and the solvate ionic liquid-based electrolytes. We focused in particular on the impedance at 10^{-4} Hz , since this frequency is relevant for battery cycling at 1 C - 2 C. Remarkably, the real and modulus of this impedance, Z' (10^{-4} Hz) and $|Z|(10^{-4}$ Hz) , depend much more weakly on the electrode thickness than the zero-frequency limit of the electrode impedance, $R_{\mathrm{lf}} = Z'(\nu \to 0)$. In the framework of a transmission-line approach, we showed that for thick electrodes $\geq$ 100 µm and at a frequency of 10^{-4} Hz, the ion transport resistance Z_{ion} becomes larger than the local impedance $Z_{\mathrm{loc}}/(l_{\mathrm{p}} \cdot a_{\mathrm{v}})$ for charge transfer and solid-state diffusion. In this case, the composite electrode impedance is given, to a good approximation, by the geometrical average of Z_{ion} and $Z_{\mathrm{loc}}/(l_{\mathrm{p}} \cdot a_{\mathrm{v}})$ and therefore depends only weakly on thickness. This geometrical impedance averaging results also in an electrode impedance at 10^{-4} Hz when using the alternative electrolytes, which is only a factor of 3-5 higher than for the conventional carbonate-based electrolyte. Thus, battery cycling with the alternative electrolytes should be considerably faster than expected from the zero-frequency limit $R_{\mathrm{zf}} = Z'(\nu \to 0)$. Furthermore, the weak thickness dependence of Z' (10^{-4} Hz) and $|Z|(10^{-4}$ Hz) suggests that it should be possible to use battery electrodes considerably thicker than the conventional 80 µm, provided that the morphological features of the electrodes can be held constant over the entire thickness range.

2.5 Supporting Information

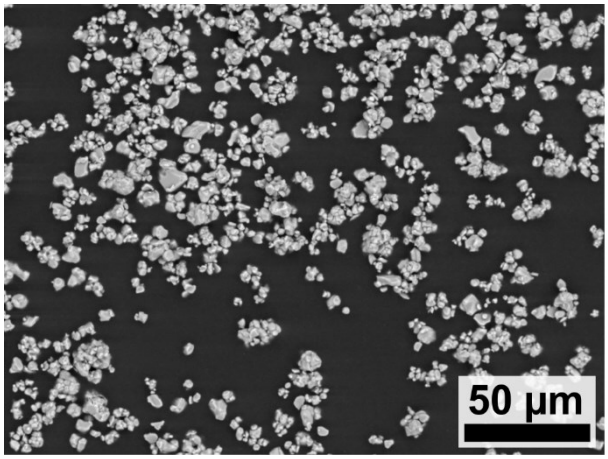

Figure 2.S1: Scanning electron microscopy image of the $LiCoO_2$ particles. The mean particle diameter was determined to be (3.4 ± 1.6) µm.

2.5.1 Determination of ion transport tortuosity

The ion transport tortuosity of the composite electrodes was determined using electrochemical impedance spectroscopy on symmetrical cells at 0% state of charge (SOC). The obtained spectra were analyzed in the framework of a transmission line model (TLM) describing ion migration in the electrolyte-filled pores and double layer formation at the active material / electrolyte interface.[19,20] The electronic resistance of the active material was assumed to be negligible due to the presence of conductive carbon, and the charge transfer resistance was assumed to be infinity at 0% SOC.

The TLM measurements were performed in a TSC battery cell (rhd instruments, Darmstadt, Germany) using a symmetrical two-electrode setup. The cells were assembled in an argon-filled glove box. Two LCO composite electrodes with a maximum porosity difference of < 1% and thicknesses between 145 µm and 180 µm were separated by three layers of Whatman GF/A glass microfiber filters (GE Healthcare, Buckinghamshire, United Kingdom). The separators were soaked with 120 µl of a commercial battery grade 50:50 mixture of ethylene carbonate (EC), ethyl-methyl carbonate (EMC) containing 1 mol l^{-1} $LiPF_6$ (Sigma Aldrich, Merck, Darmstadt, Germany). The cells were equilibrated over night at room temperature. Impedance measurements were performed in a range from 1 MHz to 0.1 mHz with an AC amplitude of 10 mV at the open circuit potential using a Multi Autolab/M101 equipped with a FRA32 M

impedance module (Metrohm Autolab BV, Utrecht, Netherlands). Impedance spectra were analyzed using the software RelaxIS 3 (rhd instruments, Darmstadt, Germany).

Figure 2.S1a shows the resulting impedance spectra for different porosities. The spectra were fitted by the following TLM expression: [19,20]

$$Z = \sqrt{\frac{R_{\mathrm{ion}}}{Q_{\mathrm{DL}}(i\omega)^{\alpha}}} \cdot \coth\left(\sqrt{R_{\mathrm{ion}} \cdot Q_{\mathrm{DL}}(i\omega)^{\alpha}}\right) \tag{2.S1}$$

with the effective ion transport resistance R_{ion}, the constant-phase element coefficient Q_{DL}, the exponent α, the imaginary number i, and the angular frequency ω. The constant-phase element describes non-ideal double layer formation.

The ion transport tortuosity is then given by:[19]

$$\tau_{\mathrm{ion}} = \frac{\sigma_{\mathrm{bulk}} R_{\mathrm{ion}} A \varepsilon_{\mathrm{e}}}{2l} \tag{2.S2}$$

Here, σ_{bulk} is bulk conductivity of the electrolyte, A is the area of the electrode, ε_{e} stands for the porosity, and l is the electrode thickness.

A tortuosity vs. porosity plot is shown in Figure 2.S2 b). The data were fitted by a power law, leading to a Bruggeman exponent of $\alpha = 0.49$. For a porosity of $\varepsilon = 0.35$, a tortuosity value of $\tau_{\mathrm{ion}} = 2.7$ was obtained.

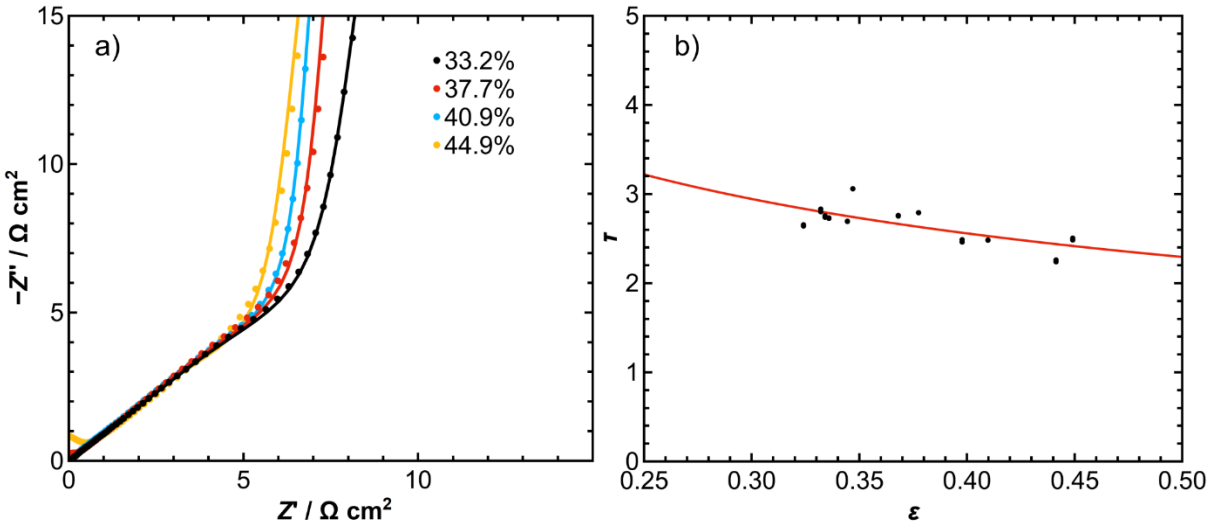

Figure 2.S2: Tortuosity determination by means of electrochemical impedance spectroscopy in a symmetrical two-electrode setup using two identical LCO composite electrodes at 0% SOC. a) Nyquist plot of the impedance spectra for electrodes with different porosities. The spectra were fitted to Eq. (S1) to determine the ionic resistance R_{ion}. b) Tortuosity vs. porosity plot for LCO composite electrodes. The data were fitted to the Bruggeman relation.

2.5.2 Dependence of the electrode potential on the Li^+ concentration

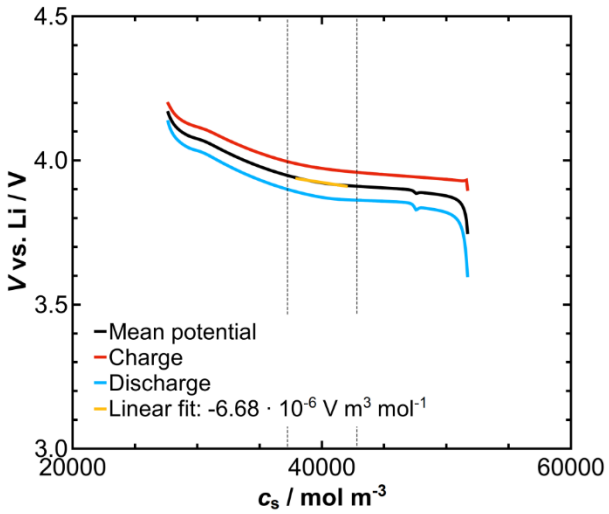

Figure 2.S3: Estimation of the equilibrium cathode potential vs. on the Li^+ concentration in the LCO particles from a charge/discharge curve of a thin (34 µm) and highly porous (48 %)

electrode (resulting in low overpotentials). The equilibrium potential was approximated by the mean potential of charging and discharging.

2.5.3 Calculated impedance spectra of composite electrodes

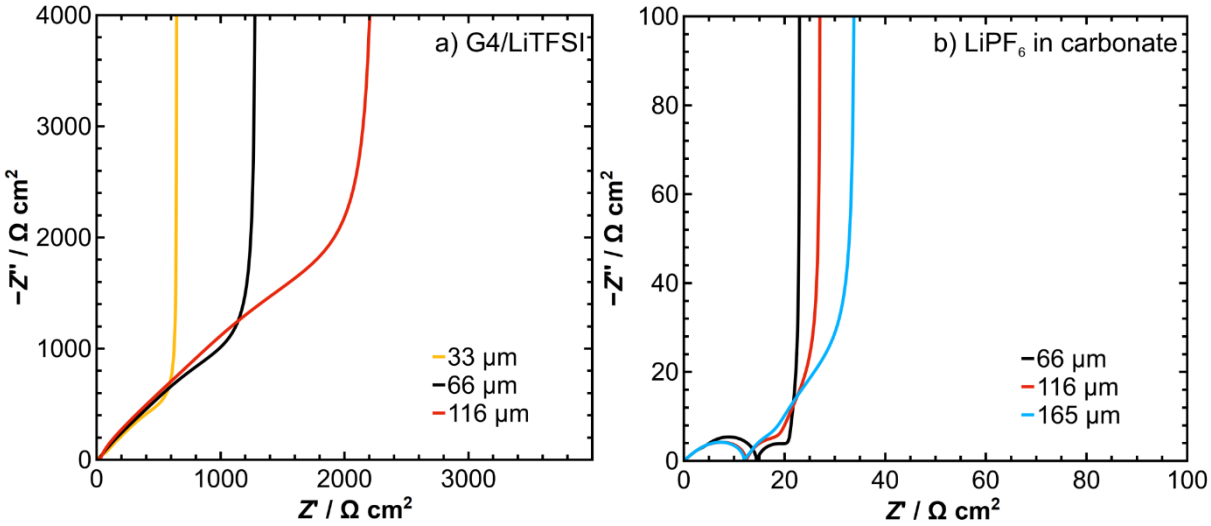

Figure 2.S4: a) Calculated impedance spectra of LCO composite cathodes with G4/LiTFSI 50:50 as electrolyte. b) Calculated impedance spectra of a LCO composite cathode with $LiPF_6$ in carbonate as electrolyte. Both spectra show very-low-frequency spikes due to the chemical capacitance of the active material particles.

In order to illustrate that the model by Huang et al. takes into account salt concentration polarization, we calculated model impedance spectra for the carbonate-based electrolyte (1 M $LiPF_6$ in carbonates). The electrode thickness was set to l = 100 µm. The simulation parameters were taken from Tab. 1, expect for the Li diffusion coefficient in the active material particles D_s, which was increased by 10 orders of magnitude, and for dU/dc_s, which was set to zero (infinite chemical capacitance of the active material particles). In this case, the impedance due to Li chemical diffusion in the active material particles is negligible, and the impedance spectra are governed by ion transport in the electrolyte-filled pores, see Fig. 2.S5. The high-frequency semicircle is due to ion migration resistance and the charge transfer resistance, while the low-frequency semicircle represents the concentration polarization impedance, which depends on the Li^+ transference number.

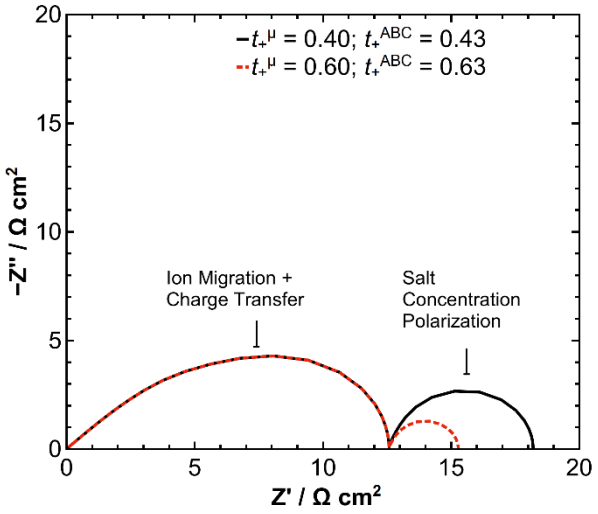

Figure 2.S5: Calculated impedance spectra of LCO composite cathode with G4/LiTFSI 50:50 as electrolyte from 1 MHz to 1 µHz. D_s was set to 10^{-5} m^2 s^{-1}, dU/dc_s to zero, the electrode thickness to 100 µm, while the other parameters were taken from Tab. 1.

2.6 References

[1] J. B. Goodenough, Y. Kim, *Chem. Mater.* **2010**, *22*, 587.

[2] P. G. Balakrishnan, R. Ramesh, T. Prem Kumar, *J. Power Sources* **2006**, *155*, 401.

[3] T. M. Pappenfus, W. A. Henderson, B. B. Owens, K. R. Mann, W. H. Smyrl, *J. Electrochem. Soc.* **2004**, *151*, A209.

[4] K. Ueno, K. Yoshida, M. Tsuchiya, N. Tachikawa, K. Dokko, M. Watanabe, *J. Phys. Chem. B* **2012**, *116*, 11323.

[5] K. Ueno, R. Tatara, S. Tsuziki, S. Saito, H. Doi, K. Yoshida, T. Mandai, M. Matsugami, Y. Umebayashi, K. Dokko, M. Watanabe, *Phys. Chem. Chem. Phys.* **2015**, *17*, 8248.

[6] K. Yoshida, M. Tsuchiya, N. Tachikawa, K. Dokko, M. Watanabe, *J. Phys. Chem. C* **2011**, *115*, 18384.

[7] H. Lundgren, J. Scheers, M. Behm, G. Lindbergh, *J. Electrochem. Soc.* **2015**, *162*, A1334.

[8] Y. Yamada, K. Furukawa, K. Sodeyama, K. Kikuchi, M. Yaegashi, Y. Tateyama, A. Yamada, *J. Am. Chem. Soc.* **2014**, *136*, 5039.

[9] J. Zheng, J. A. Lochala, A. Kwok, Z. D. Deng, J. Xiao, *Adv. Sci.* **2017**, *4*, 1700032.

[10] Y. Hu, H. Li, X. Huang, L. Chen, *Electrochem. Commun.* **2004**, *6*, 28.

[11] A. Balducci, *Top. Curr. Chem. (Z)* **2017**, *375,*20.

[12] K. Xu, *Chem. Rev.* **2014**, *114*, 11503.

[13] C. Liu, X. Ma, F. Xu, L. Zheng, H. Zheng, H. Zhang, W. Feng, X. Huang, M. Armand, J. Nie, H. Chen, Z. Zhou, *Electrochim. Acta* **2014**, *149*, 370.

[14] M. Doyle, J. Newman, *J. Electrochem. Soc.* **1995**, *142*, 3465.

[15] J. Newman, K. E. Thomas-Alyea, *Electrochemical Systems*, John Wiley & Sons., **2004**.

[16] J. Huang, J. Zhang, *J. Electrochem. Soc.* **2016**, *163*, A1983.

[17] F. Sälzer, L. Pateras Pescara, F. Franke, C. Müller, J. Winkler, M. Schwalm, B. Roling, *Batteries & Supercaps* **2019**, *22*, 587.

[18] D. Gruet, B. Delobel, D. Sicsic, I. T. Lucas, V. Vivier, *Electrochimica Acta* **2019***, 295, 787.*

[19] J. Landesfeind, A. Ehrl, M. Graf, W. A. Wall, H. A. Gasteiger, *J. Electrochem. Soc.*, **2016**, *163*, A1254.

[20] M. Kroll, D. Hlushkou, S. Schlabach, A. Höltzel, B. Roling, U. Tallarek, *J. Electrochem. Soc.*, **2018**, *165*, A3156.

[21] F. Wohde, M. Balabajew, B. Roling, *J. Electrochem. Soc.* **2016**, *163*, A714.

[22] L. O. Valøen, J. N. Reimers, *J. Electrochem. Soc.* **2005**, *152*, A882.

[23] D. Dong, F. Sälzer, B. Roling, D. Bedrov, *Phys. Chem. Chem. Phys.* **2018**, *20*, 29174.

[24] A. Nyman, M. Behm, G. Lindbergh, *Electrochimica Acta* **2008**, *53*, 6356.

[25] J. Xie, N. Imanishi, T. Matsumura, A. Hirano, Y. Takeda, O. Yamamoto, *Solid State Ionics* **2008**, *179*, 362.

[26] Q. Liu, X. Su, D. Lei, Y. Qin, J. Wen, F. Guo, Y. A. Wu, Y. Rong, R. Kou, X. Xiao, F. Aguesse, J. Bareño, Y. Ren, W. Lu, Y. Li, *Nat. Energy* **2015**, *3*, 936.
[27] N. Ogihara, Y. Itou, T. Sasaki, Y. Takeuchi, *J. Phys. Chem. C* **2015**, 119, *9*, 4612.
[28] Z. Siroma, N. Fujiwara, S.-i. Yamazaki, M. Asahi, T. Nagai, T. Ioroi, *Electrochimica Acta* **2015**, *160*, 313.
[29] H. Gao, Q. Wu, Y. Hu, J. P. Zheng, K. Amine, Z. Chen, *J. Phys. Chem. Lett* **2018**, *9*, 5100.

Chapter 3: Three-Phase Reconstruction Reveals How the Microscopic Structure of the Carbon-Binder Domain Affects Ion Transport in Lithium-Ion Batteries

Authors

Moritz Kroll, Sarah L. Karstens, Marvin Cronau, Sabine Schlabach, Alexandra Höltzel, Nikita Nobel, Claudia Redenbach, Bernhard Roling,* and Ulrich Tallarek*

State of publication

Accepted 09 April 2021 by *Batteries & Supercaps*.
DOI: 10.1002/batt.202100057R1

Abstract

The morphology of the electrolyte-filled pore space in lithium-ion batteries is determined by the solid microstructure formed by µm-sized active material particles and the smaller-featured carbon binder domain (CBD). Tomographic reconstructions have largely neglected the CBD, resulting in inadequately defined pore space morphologies at odds with experimental ionic tortuosity values. We present a three-phase reconstruction of a $LiCoO_2$ composite cathode by focused ion-beam scanning electron microscopy tomography. Morphological analysis proves that the reconstruction, which combines an unprecedented volume (20 µm minimum edge length) with the hitherto highest resolution ($13.9 \times 13.9 \times 20$ nm^3 voxel size), represents the cathode's pore space morphology. Pore-scale diffusion simulations show consideration of the resolved CBD as indispensable to reproduce ionic tortuosity values from electrochemical impedance spectroscopy. Our results reveal the CBD as a convoluted network that dominates the pore space morphology and limits Li^+ transport through tortuous and constricted diffusion pathways.

3.1 Introduction

Against the rising demand for more efficient and cost-effective lithium-ion batteries (LIBs), the research and development of new materials and battery systems has led to significant progress in recent years.[1,2] Additionally, the established battery systems offer considerable optimization potential, particularly regarding the morphology of the porous electrodes, which should combine high capacity for Li^+ storage in the active material (AM) with fast Li^+ transport kinetics in the electrolyte-filled pore space.[3]

Conventional composite electrodes of LIBs are composed of an AM such as $LiCoO_2$ (LCO), a carbonate-based liquid electrolyte, and electrochemically inactive carbon binder additives. The carbon's task is to guarantee electronic conduction between the AM particles, including those disconnected from the rest of the network due to volume changes during charge/discharge, and between AM particles and the current collector.[4] The binder connects the different components and mechanically stabilizes the electrode.[5] Electrodes typically contain 90–95 wt% AM and 5–10 wt% carbon binder[6,7] and are obtained from a slurry-coating procedure. A thin slurry film of AM and carbon particles added to a solution of the binder in an organic solvent is applied to the current collector by doctor blading. When the slurry dries, the binder adheres to the surface of the conductive carbon,[8] forming an interpenetrating porous phase, the carbon-binder domain (CBD). Cross-sectional scanning electron microscopy (SEM) images revealed that the CBD partially fills the interstitial space between the AM particles and spreads over the entire electrode.[4,9,10] Electrochemical investigations have qualitatively shown that chemical composition and volume fraction of the CBD directly influence charge transport in the porous electrode and the cycling performance of the battery.[11–15] However, detailed quantitative descriptions of CBD morphology and spatial CBD distribution in electrodes as well as the expected impact on ionic transport and overall battery performance are still rare.[6,7,16–24]

The microstructure formed by the solid components is the negative of the liquid electrolyte-filled pore space, in which Li^+ transport takes place. AM particles are usually 3–6 µm sized, whereas the size of the conductive carbon particles is up to two orders of magnitude smaller, at 80–100 nm. Consequently, the distance between the AM particles is in the µm-range, but the pore space becomes much smaller in regions pervaded by the CBD. The tortuous nature of the pathways for ion transport is described by the ionic tortuosity τ_{ion}, which is primarily dependent on the porosity ε, but also influenced by constrictivities such as bottlenecks and dead-ends.[25,26] The ionic tortuosity τ_{ion} quantifies the dependence of the ion transport on the pore space morphology and can be determined electrochemically or through a reconstruction–simulation (RS) approach, where pore-scale diffusion simulations are performed in physically reconstructed electrode structures.[27,28]

The accuracy of an RS-derived tortuosity value depends critically on the quality and resolution of the reconstruction, which should cover a representative volume of the electrode and resolve each phase adequately. Reconstructions of electrode structures can be obtained from X-ray tomography (XRT) or focused ion-beam scanning electron microscopy (FIB-SEM) tomography. In XRT, large sample volumes (>10,000 μm^3) can be imaged non-destructively in a short time, but the resolution remains in the hundreds-of-nanometers range. As XRT is based on the absorption of X-rays, the method is suited for heavy elements, such as found in the AM particles, but insensitive to light elements, such as present in the CBD.[29,30] FIB-SEM tomography uses ions (mostly Ga^+) to remove material from the sample slice-by-slice (milling). Between slicing the SEM signal is used to image the cross-sectional surface. Alternate milling and imaging steps are repeated hundreds of times to produce an image stack, from which a representation of the microstructure of the investigated volume can be obtained by 3D interpolation.[31,32] Volumes with edge lengths of up to 100 µm can be reconstructed by FIB-SEM tomography, but the slicing becomes very time consuming for edge lengths >10 µm. The main advantages of FIB-SEM tomography are its high resolution, down to <1 nm[33], and the availability of all imaging modes of modern electron microscopy.

Studies that compared RS-derived tortuosity values with those obtained from electrochemical impedance spectroscopy (EIS) experiments often found the RS approach to underestimate the ionic tortuosity.[28,34] The difference between experimental and simulated tortuosity values was particularly large for XRT reconstructions, although the AM phase was accurately represented, which lead to the conclusion that the deviation was due to the insufficiently resolved CBD.[34]

The size difference between the finer-featured CBD and the AM phase poses a particular challenge to three-phase reconstructions of electrodes, which have been pursued by FIB-SEM tomography[7,17,18,20] and by a combination of tomography and stochastic modelling.[6,19,35–38] The latter approach requires numerous assumptions and is thus subject to uncertainties, which explains why the assumed microstructure and porosity of the CBD differ significantly between the studies.[19,37] Direct imaging by FIB-SEM tomography is the best approach to obtain an accurate description of the CBD, because the method provides the necessary resolution and allows the straightforward, contrast-based interpretation of SEM images that enables a robust segmentation of the different phases. But imaging large volumes at high resolution by FIB-SEM tomography requires long measurement times and produces correspondingly large amounts of raw data that have to be processed and analyzed. Hutzenlaub et al.[16,39] presented a three-phase, FIB-SEM tomography-based reconstruction including the CBD and compared the calculated ionic tortuosity values with electrochemical experiments. The resolution of their reconstruction was, however, too low to resolve CBD porosity, so that the (negative) impact of the CBD on Li^+ transport was overestimated. Liu et al.[17] filled the electrode's pore space with

a silicone-based resin and obtained good contrast between the individual phases (without resolving the CBD microstructure and its porosity). Almar et al.[7] succeeded in direct imaging of all three phases by FIB-SEM tomography over a large volume, but the resolution (30–50 nm) was too close to the feature size of the CBD branches to fully capture the microstructural information.

In this study we attempt a three-phase reconstruction that combines a sufficiently large volume with sufficiently high resolution to obtain an adequate representation of the pore space morphology of an LCO cathode. Assuming the preparation conditions to control the pore space morphology, we prepare a set of LCO cathodes samples using the slurry-coating technique. One sample is investigated by the RS approach, the other samples by EIS. We present our strategy for FIB-SEM tomography and a procedure to obtain a multiscale, multiphase reconstruction of the cathode sample from the image data. A detailed morphological analysis of the void space is carried out to ascertain that the reconstructed volume is representative of the electrode structure and to obtain a quantitative description of the pore space morphology. Pore-scale diffusion simulations performed in the reconstructed volume deliver a tortuosity value for comparison with the ionic tortuosity determined by EIS from the other cathode samples. The goal of the study is to shed light on the influence of the CBD microstructure on Li^+ transport in LIBs.

3.2 Results

3.2.1 Cathode preparation and electrochemical characterization

Using the slurry-coating technique we prepared LCO cathode samples at a typical composition of 90 wt% AM, 5 wt% carbon, and 5 wt% binder. Disc electrodes were cut from the calendared film whose porosity had been adjusted to $\varepsilon \approx 40\%$. A porosity of about 40% was confirmed for all punched electrodes from their respective weight and thickness, which shows that cathodes with reproducible properties were obtained from the film. One cathode sample was cycled using lithium metal as counter electrode to demonstrate that the electrode works properly (Figure 3.S1). After 3.25 cycles, the cathode was removed and prepared for FIB-SEM tomography (see section 3.2.2). The other samples were used to determine the ionic tortuosity τ_{EIS} of the electrolyte-filled void space by EIS within the framework of the transmission line model (TLM).

The TLM describes the impedance of a straight, cylindrical pore considering ion migration in the electrolyte-filled pore space and double layer formation at the AM–liquid interface.[40–42] Previous studies have shown the applicability of the TLM to porous electrodes.[28,43] Through the use of a relatively large amount of conductive carbon (5 wt%) the electronic resistance of

the cathode can be assumed as negligible. For 0% or 100% state-of-charge (ion-blocking conditions), the charge transfer resistance is approximately infinite. The impedance Z for the TLM can then be stated as[43]

$$Z = \sqrt{\frac{R_{\mathrm{ion}}}{Q_{\mathrm{DL}}(j\omega)^{\beta}}}\ \coth\left(\sqrt{R_{\mathrm{ion}}Q_{\mathrm{DL}}(j\omega)^{\beta}}\right) \tag{3.1}$$

where R_{ion} is the effective ion transport resistance, Q_{DL} is the constant phase element (CPE) coefficient with its exponent β (to account for deviations from ideal capacitive behavior), j is the imaginary number and ω the angular frequency. From R_{ion}, an effective conductivity for the electrode's pore space σ_{eff} can be calculated. The ionic tortuosity τ_{EIS} then results from the ratio of the electrolyte's bulk conductivity (σ_{bulk} = 7.93 mS cm^{-1} for the liquid electrolyte used) and σ_{eff} multiplied with the porosity ε. Using a symmetrical cell setup to acquire EIS spectra ensures that the obtained σ_{eff} values refer only to the pore space of the investigated LCO electrodes.[44] For a symmetrical cell setup, τ_{EIS} can be calculated according to[43]

$$\tau_{\mathrm{EIS}} = \frac{\sigma_{\mathrm{bulk}}}{\sigma_{\mathrm{eff}}}\ \varepsilon = \frac{\sigma_{\mathrm{bulk}}R_{\mathrm{ion}}A}{2d}\ \varepsilon \tag{3.2}$$

where A and d denote the mean area and thickness of the electrodes, respectively.

For EIS measurements, six LCO electrodes were combined into three pairs (for the symmetrical cell setup). Figure 3.1 shows the Nyquist plot acquired for the three electrode pairs. As intended by the preparation protocol, the three electrode pairs showed very similar impedance behavior. Equation 3.1 was fitted to the spectra to derive R_{ion}values. τ_{EIS} values (Table 3.1) were then calculated using equation 2 from the R_{ion} values and the values for area, thickness, and porosity determined for the electrodes (Table 3.1). Averaging over the individual τ_{EIS} values yielded a mean ionic tortuosity of τ_{EIS} = 2.31 ± 0.20 (standard deviation). The high standard deviation of τ_{EIS} reflects uncertainties in the experimental determination of the parameters from which τ_{EIS} is calculated, but also hidden variations between the samples, such as small fluctuations in electrode or current collector thickness or slight deteriorations sustained during cell assembly.

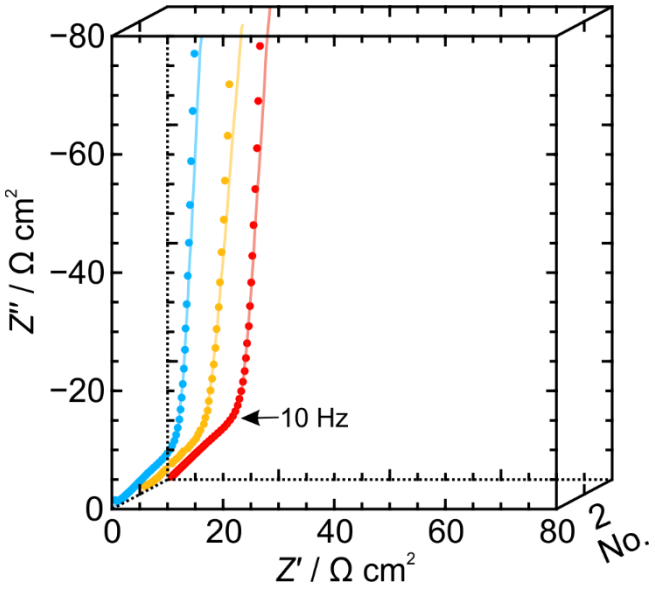

Figure 3.1: Nyquist plot acquired for symmetrical cells under ion-blocking conditions. The data for the three LCO cathode pairs (no. 1–3) are plotted in the third dimension for better visibility. The resistance of the liquid electrolyte in the separator was subtracted for better comparability of the impedance spectra. As intended, the EIS spectra of all samples show very similar impedances. The TLM (lines) was fitted to the spectra to determine R_{ion}.

Table 3.1: Experimental data for the three electrode pairs[a] used for calculation of τ_{EIS}.

No.	Porosity ε[b]	Thickness d / µm	$R_{\mathrm{ion}}A$ / Ω cm²	τ_{EIS}
1	40.5%	288	36.5	2.03
2	41.3%	250	36.6	2.39
3	39.5%	238	38.1	2.50

[a] Data reflect the average value from the two electrodes of a pair.

[b] Porosities ε were determined from the weight of the electrodes and densities of the solid components (4.79 g cm^{-3} for LCO,[45] 1.88 g cm^{-3} for PVDF,[46] and 1.60 g cm^{-3} for carbon black).

3.2.2 Tomography and physical reconstruction

Figure 3.2 illustrates the workflow from cycling to phase segmentation for the cathode sample selected for the RS approach. After cycling, the cathode sample was prepared for FIB-SEM tomography by filling the pore space with a low-viscosity silicone resin, whose SEM contrast lies between the high-contrast AM particles and the low-contrast CBD branches. The resin-filling performs two important tasks: it increases the contrast between the different phases[7] and prevents shine-through artifacts from deeper layers.[47] Vacuum was applied to completely fill even narrow pores within the CBD; unfilled pores were not observed in the tomographic images afterwards. After curing, the sample was embedded in epoxy resin and cut orthogonal to the current collector. The sample was mounted so that the electrode's cross-section was facing upwards. A bulk section from the center of the electrode was selected as the volume-of-interest.

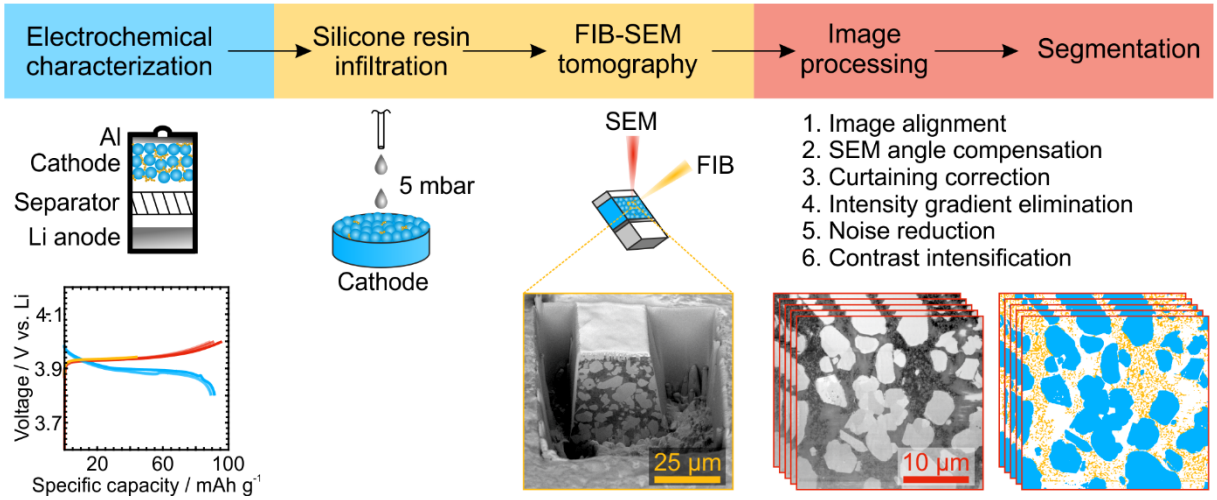

Figure 3.2: Overview of the workflow from cycling to phase segmentation. One cathode sample was integrated into a battery, using Li metal as anode, and subjected to cycling experiments. After disassembly of the battery, the cathode sample was infiltrated by a low-viscosity silicone resin to enhance the SEM contrast between the different phases, embedded in epoxy resin, and cut to probe the cross-section by FIB-SEM tomography. The resulting image stack was processed following a multi-step routine and segmented into the three different phases: solid AM, solid CBD, and void space.

The volume-of-interest and the resolution (slice thickness) are critical to the success of the RS approach in terms of delivering reliable and representative tortuosity values. The edge length of a reconstructed volume must be 20–25 times the average feature size of the phase-of-interest (here the electrolyte-soaked pore space or void phase) to guarantee the absence of finite-size

effects.[48] At the same time, the smallest feature (pores within the CBD) has to be covered by at least 8–10 voxels in each direction to capture its morphology.[49] From SEM images, the AM particle size was estimated as ~3.5 µm and the carbon particle size as 80–120 nm (cf. Figure 3.S2). Due to the adhering binder, the solid CBD branches are thicker than the carbon particles. Based on these discriminative feature sizes for the solid components, we estimated an average feature size of ~1 µm for the pore space. Therefore, edge lengths of 20–25 µm were targeted for the volume-of-interest, and a slice thickness of 20 nm was chosen for the resolution.

High-resolution imaging was achieved by using the through-the-lens detector (TLD) of the FIB-SEM instrument. This detector was used in backscatter electron mode (TLD-BSE) as the backscattered electrons carry chemical information that can be used to further enhance the contrast (Z or compositional contrast) between the different phases.[33] A low voltage of 2 kV was applied for a small interaction volume between electron beam and the sample. The information depth of the electron beam was kept small compared to the slice thickness to achieve the highest possible resolution.

After image acquisition, the subsequent image restoration removed artifacts to enable the contrast-based segmentation of the individual phases. Image reconstruction relied heavily on software-supported automation, as the data amount was much too large for an individual post-processing of single images. Typical corrections included in the restoration process were the alignment of the image stack (985 slices) and the compensation of brightness gradients, local charging, and noise. Curtaining artifacts, which are caused by unevenness on the cross-sectional surface,[31] were a major issue. Each material interacts differently with the ion beam leading to individual sputter rates. The examined composite electrode exhibits numerous material interfaces between solid AM, solid CBD, and silicone resin, thus leading to local changes of beam milling. Curtaining produces stripes that run like a waterfall from top to bottom of an image, becoming more pronounced towards the bottom. The stripes had to be carefully corrected to prevent a considerable loss of resolution. The results of FIB-SEM tomography and image restoration are shown in Figure 3a for the complete reconstructed volume of 26.4 × 24.5 × 19.7 μm^3.

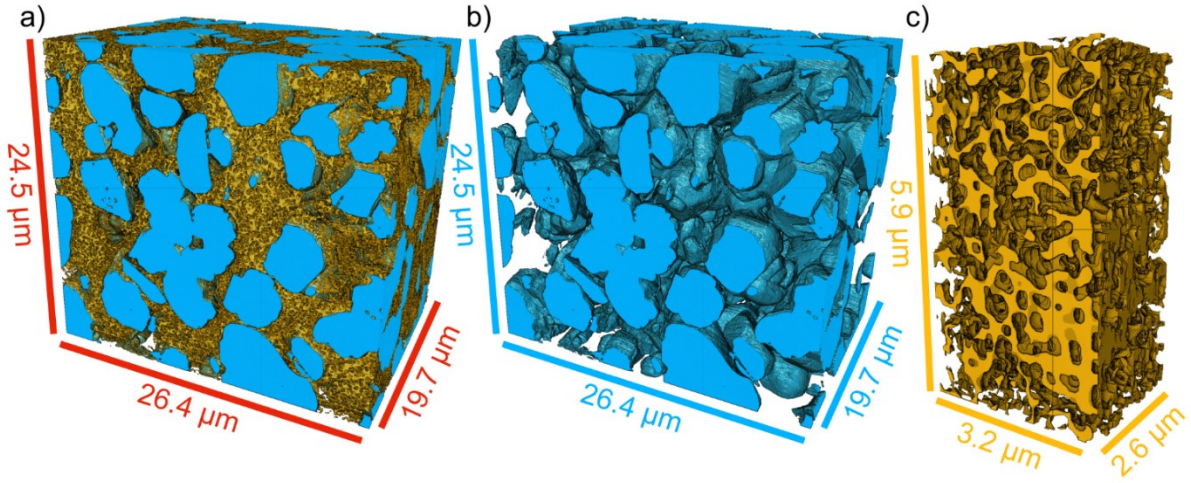

Figure 3.3: a) 3D representation of the total reconstructed volume of a bulk section of the LCO cathode (solid AM, solid CBD, and void phase in blue, orange, and transparent, respectively). For morphological analysis, this representation is referred to as case I. b) Representation of the reconstructed volume in which solid CBD voxels were replaced by void voxels to simulate the results of imaging without resolution of the CBD (case II). c) Extracted section from the reconstructed volume completely filled by the porous CBD (case III).

3.2.3 Morphological Analysis

The three-phase physical reconstruction of the LCO cathode sample shown in Figure 3a is a direct image of the cathode's morphology within the limits of the achieved resolution. The microstructural properties of the electrolyte-filled pore space (void space) correspond to real bulk conditions (as probed by EIS) insofar as the reconstruction is accurate and representative. In the following morphological analysis, this representation is referred to as case I. Although the reconstruction process itself is quite complex, the results can be easily manipulated afterwards to create or isolate structures inaccessible to experiments. Taking advantage of this possibility, we reassigned voxels belonging to the solid CBD as void voxels to simulate the results of a two-phase reconstruction where the CBD was not taken into account (Figure 3b, case II). This representation serves as reference to evaluate the contribution of the CBD to the overall morphology and transport properties of the electrode. The sub-volume shown in Figure 3c corresponds to the largest section occupied by the porous CBD in the reconstructed volume. Analysis of this sub-volume (case III) focuses on the morphology of the CBD. The selected sub-volume represents CBD porosity and feature size, as ascertained by probing the (smaller) porous CBD subsections in the reconstructed volume.

3.2.3.1 Evaluation of Phase Fractions

Prior to deriving values for morphological descriptors, we assess whether the three-phase reconstruction (case I) recovers the composition of the cathode sample. Table 3.2 lists the different volume fractions in the reconstruction, determined as the ratio between the number of voxels assigned to a particular phase or feature and the total number of voxels in the reconstruction. Multiplication with the respective density converts the volume fractions of the solid components into weight fractions. The reconstruction-derived weight fractions for the solid AM and CBD phases closely approach the respective weight fractions of the solid components used in cathode preparation. The porosity of the cathode sample of $\varepsilon = 40.8\%$, experimentally determined as for the cathode samples used for EIS (Table 3.1), is also recovered by the void voxel fraction of the reconstructed volume (40.0%).

Table 3.2: Reconstruction-derived volume fractions vs cathode sample composition.

Phase	Reconstruction	Cathode sample
Solid AM	48.5 vol% (92.0 wt%)[a]	90.0 wt%
Solid CBD	11.5 vol% (8.0 wt%)[a]	10.0 wt%
Total void	40.0 vol%	40.8%
Void inside CBD	17.5 vol%	–
Void outside CDB	22.5 vol%	–
Porous CBD (solid and void)	29.0 vol%	–

[a] Wt% calculated from vol% by multiplication with the respective densities (4.79 g cm^{-3} for LCO,[45] 1.88 g cm^{-3} for PVDF,[46] and 1.60 g cm^{-3} for carbon black).

Having ascertained that case I recovers the phase fractions of the cathode sample, we next look at case III. The CBD-pervaded sub-volume consists of 39.7 vol% solid phase and 60.3 vol% void space. Assuming case III as representative of the CBD porosity, the space occupied by the porous CBD in case I must have the same ratio of solid to void space as case III. From this ratio the void space within the CBD calculates to 17.5 vol% of the reconstruction, which leaves 22.5

vol% of the reconstructed volume to the void space outside the CBD. The porous CBD (solid and void voxels together) then occupies 29.0 vol% of the reconstructed volume. That nearly half of the total pore space (43.8%) is confined within the CBD underscores the high impact of the CBD microstructure on the pore space morphology.

With 60.3% the CBD porosity is considerably above the 47% estimated by Zielke et al.[19] for the CBD porosity in an LCO cathode. To which extent this divergence reflects differences in electrode preparation conditions that could affect the CBD porosity or advances in the reconstruction process that improve the accuracy of the results (enhanced SEM image quality from resin-filling of the pore space, larger sample volume), is impossible to tell at this point.

3.2.3.2 Void Space Distribution

The void space distribution in the electrode is determined by the distribution of the two solid components, which differ considerably in morphology. The high degree of connectivity and the complex geometry of the void space preclude a division into individual pores. We describe the void space distribution through chord length distributions (CLDs), which is an automatable method that does not rely on assumptions about the void space geometry and can in principle be applied to any porous medium.[50–52] The void space is scanned up to the solid–void interface by chords of variable length; collecting and sorting the chords according to their length in a histogram yields the CLD. The mean chord length $\overline{l_c}$ of the CLD is a measure of the average pore size. Figure 3.4 shows the void space CLDs obtained for cases I–III. The mean chord length $\overline{l_c}$ derived from each CLD is listed in Table 3.3.

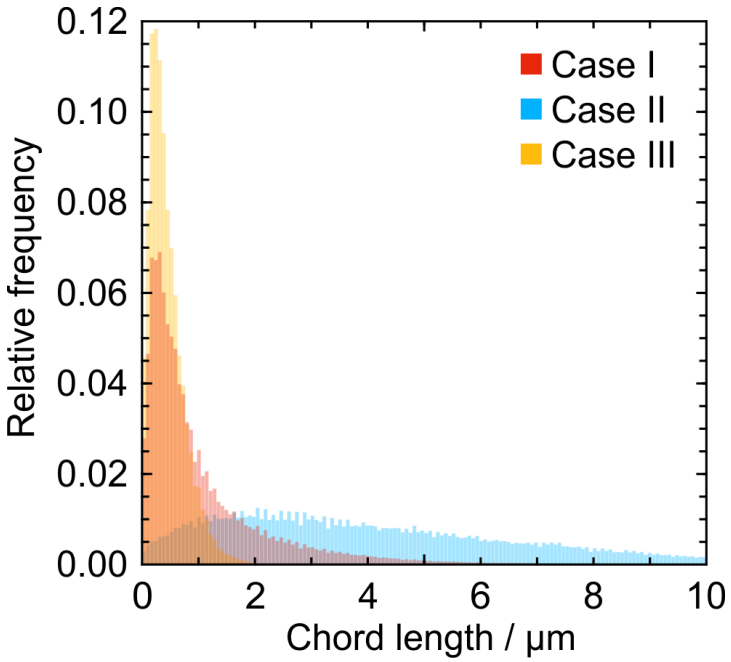

Figure 3.4: CLDs obtained from different representations of the physical reconstruction describe the void space distribution as defined by solid AM and CBD phases (case I), solid AM phase (case II), and solid CBD phase (case III).

Table 3.3: Morphological parameters obtained by the RS approach.

	Case I	Case II	Case
Porosity ε	40.0%	51.5%	60.3
CLD mean chord length $\overline{l_c}$ / µm	1.04	4.46	0.44
CLD median / µm	0.64	3.73	0.37
CLD mode / µm	0.28	2.02	0.28
Fraction of three-branch connections	74.0%	91.0%	77.5
Fraction of four-branch connections	16.1%	7.2%	15.6
Fraction of higher-branch connections	9.8%	1.8%	7.0%
Average connectivity Z	3.36	3.11	3.30
τ_{RS}	1.89	1.47	1.96

The CLDs are used first to check whether the resolution limits of the reconstruction were chosen correctly at both boundaries. According to the CLD for case I, the average pore size in the

cathode is $\overline{l_c}$ = 1.04 µm, which agrees with our estimate of 1.0 µm for the discriminate feature size in the void phase on which the edge lengths for the reconstructed volume had been based. According to the CLD for case III, the average pore size within the CBD is $\overline{l_c}$ = 0.44 µm and thus 22-times the tomographic slice thickness of 20 nm. The reconstruction's resolution limits thus conform to the requisites for an accurate representation of the electrode's pore space.

The void space CLDs for the three cases are very different from each other. Close inspection of the void space CLD for case I reveals a shoulder to the right (at l_c = 0.6 µm), congruent with a bimodal distribution caused by the size difference between pores within and pores outside the CBD. The void space CLD for case II covers, as expected, much larger chord lengths than the CLD for case I, which is also reflected in a mean chord length of $\overline{l_c}$ = 4.46 µm, about four-times the average pore size of $\overline{l_c}$ = 1.04 µm in the three-phase reconstruction. Comparison of the void space CLDs for cases I and II visualizes that the presence of the CBD reduces the global average pore size significantly. The void space CLD for case III contains chord lengths up to 1.5 µm and exhibits a mode of 0.28 µm and a median of 0.37 µm. Interestingly, the void space CLDs for cases I and III share the same mode (i.e., the most frequent chord length); the void space CLD for case III, however, contains a considerably larger amount of short chords and features a decidedly smaller mean chord length ($\overline{l_c}$ = 0.44 and 1.04 µm for cases III and I, respectively). This comparison shows that smaller pores are found mostly within the CBD, where the average pore size is less than half of the global average pore size.

3.2.3.3 Surface Area of and Contact Area between AM and CBD Phase

The CBD's role in the electrode is to stabilize the AM particle network and provide electronic conduction between the AM particles. Contact between AM particles and the CBD is therefore necessary, but also reduces the active surface area of the AM particles, where Li^+ charge transfer takes place. The three-phase reconstruction allows a precise calculation of the surface area of the solid phases as well as of the contact area between them. The surface areas of solid AM, solid CBD, and both solid phases together were calculated from the full reconstruction volume using the marching cube algorithm[53] (see ref. 54 and the Computational Methods section for more details). Calculation directly from the cuboid voxels overestimates the surface area of curved objects.[54] The marching cube algorithm approximates the curved surface area by using triangles to interpolate the cuboid-voxel based surface area. The volume-specific surface area was obtained by normalizing all received values to the reconstructed volume. The calculation yielded surface areas of A_{AM} = 1.02 µm^{-1}, A_{CBD} = 3.96 µm^{-1}, and $A_{AM,CBD}$ = 4.78 µm^{-1}. These data show that most of the solid-phase surface area in the electrode stems from the CBD.

The AM–void interface, where Li^+ charge transfer takes place, is defined as the active surface whose area A_{active} is calculated from the volume-specific surface areas of solid AM, solid CBD, and both solid phases together:[7]

$$A_{\mathrm{active}} = A_{\mathrm{AM}} - \frac{1}{2}\left(A_{\mathrm{AM}} + A_{\mathrm{CBD}} - A_{\mathrm{AM,CBD}}\right) \tag{3.3}$$

A_{active} is 0.92 μm^{-1}, which corresponds to 90.2% of A_{AM}. Consequently, the contact area between AM and solid CBD is 0.10 μm^{-1} (10% of the AM surface area). The 10% blockage of the AM surface area by the solid CBD apparently suffices for mechanical stability of the electrode. This leaves 90% of the AM surface in contact with the liquid electrolyte and thus available for charge transfer reactions, which excludes poor accessibility of the electrolyte–AM interface as a limiting factor to battery operation.

3.2.3.4 Void Space Connectivity

The connectivity of the pore space[55] was analyzed through skeletonization.[56] Figure 3.S3 shows a 2D representation of the skeleton lines in the void space. The analysis was performed in 3D. Skeletonization reduces the amount of data, but conserves topological properties of the pore space, such as branch lengths, curvature, connectivity, and dead-ends. The nodes in the skeleton are sorted according to how many branches (three, four, or more than four) converge there, whereby a three-branch node represents the minimum degree of connectivity. The connectivity of the pore space is then described by the fraction of three-, four-, and higher-branch nodes and by the average connectivity Z calculated from these fractions.

The connectivity analysis for the three-phase reconstruction (case I) yields a surprisingly high fraction of four-branch and higher nodes (~25%), resulting in an average connectivity of Z = 3.36 (Table 3.3). Similar connectivity values have been found for the macropore space of silica monoliths, whose pore space interconnectivity is one of their main advantages as support structures for chromatographic separations and heterogeneous catalysis.[55,56] Comparison with the results of the connectivity analysis for cases II and III clearly shows that the high connectivity of the electrode's pore space is owed mainly to the CBD. The irregularly shaped AM particles form large pores with few interconnections. The void space between the AM particles (case II) contains few (≤9%) four-branch or higher nodes, resulting in a low average connectivity of Z = 3.11. This contrasts with the CBD (case III), for which the connectivity analysis returns a considerable fraction of four-branch and higher nodes (~23%), yielding an average connectivity of Z = 3.30. These data reveal the CBD as a complex, strongly interconnected pore network that dominates the overall pore space morphology of the electrode.

For those interested in morphological analysis tools, an analysis of the pore tortuousness based on the skeleton lines is provided in the Supporting Information (Section S4). The skeleton-based analysis cannot take constrictivities into account, which is why the resulting geometric tortuosity values for cases I–III do not reflect the transport properties of the respective pore spaces. The accurate characterization of transport properties requires pore-scale diffusion simulations, as shown in the next section.

3.2.4 Pore-scale Diffusion Simulations

Diffusion in the void space of cases I–III was numerically simulated using a random-walk particle tracking technique[58] (see ref. 28 for further details), where passive, point-like tracers are randomly distributed in the void space. All tracers execute random jumps at each time step. The random displacement of each tracer is recorded and a time-dependent diffusion coefficient $D(t)$ calculated from the individual tracer displacements. The transient diffusion coefficient $D(t)$ eventually reaches its asymptotic, long-time limit D_{eff} (Figure 3.S5). The ratio of the bulk diffusion coefficient D_{bulk} and D_{eff} is the diffusive tortuosity, designated as τ_{RS} to indicate its derivation by the RS approach. τ_{RS} reflects the complete morphology, including constrictivities, of the pore space.

The diffusion simulations deliver a value of τ_{RS} = 1.89 for the three-phase reconstruction (case I) compared with only τ_{RS} = 1.47 for case II (Table 3.3). The large tortuosity difference cannot be solely attributed to the ~10% porosity difference between cases I and II. Such a large impact of the porosity on the tortuosity is not supported by tortuosity–porosity correlations for the interstitial pore space in consolidated particulate matter.[59] The large tortuosity of case I is mainly caused by the increased microstructural heterogeneity of the pore space, which comes mostly from the CBD. This becomes clear from considering case III. Although a high porosity of 60% is reached within the CBD, the tortuosity exhibits a high value of τ_{RS} = 1.96. The complex, meandering pore network inside the CBD, including constrictivities, significantly hinders diffusive transport, because the high surface area translates into more wall contacts. The CBD contribution is critical to the overall ionic tortuosity of the electrode as 43.8% of the global porosity are located within the CBD. This analysis demonstrates that transport properties of the electrolyte-filled pore space in battery electrodes cannot be correctly assessed without explicit consideration of the CBD morphology.

3.3 Discussion

The tortuosity obtained for the three-phase reconstruction (case I) from the RS approach (τ_{RS} = 1.89) differs by a factor of 1.2 from the electrochemically determined tortuosity (τ_{EIS} = 2.31). The tortuosity value for case II (τ_{RS} = 1.47) deviates from the electrochemically determined tortuosity by a factor of 1.6. This emphasizes that only three-phase reconstructions with a sufficiently high resolution of the CBD adequately represent the transport properties of the porous electrode. Still, EIS experiments in the framework of the TLM better reflect the actual conditions in the electrode. Since the measurements are conducted under blocking conditions (100% state-of-charge), no charge transfer occurs at the interface between the AM particles and electrolyte. Ions migrate in the electrolyte and a double layer is formed at the surface of the electronically conducting particles; both processes are considered in the TLM. The fact that τ_{EIS} approaches τ_{RS} (case I) quite closely may originate in the actual electrode morphology. A relatively loose packing of the AM particles generates a highly interconnected interparticle void space (cf. Table 3.3). As has been shown by Nguyen et al.,[60] when pore networks are highly percolated and contain a small fraction of dead-end pores (as for the void space between loosely packed particles), the latter have a negligible effect on the tortuosity when EIS measurements are considered, which will provide good agreement with tortuosities from diffusion studies. The remaining difference between τ_{EIS} and τ_{RS} from the three-phase reconstruction can have several origins. One possible source are the different comparison volumes. The RS approach investigates a representative volume taken from the bulk section of the electrode, whereas EIS measurements probe the entire electrode including its edge regions and, therefore, possible porosity gradients across the electrode formed during slurry drying. Another possible source lies in the applicability of the TLM (which assumes straight, cylindrical pores) to the complex pore network found in electrodes. Therefore, RS-derived as well as EIS-derived tortuosity values could reflect the limitations of each method to an extent that is difficult to estimate.

The results of this study show the decisive influence of the CBD morphology on the overall void space distribution in and thus the transport properties of the porous electrode. Commercial battery electrodes have much lower porosities (20–27%) than the investigated cathode sample (40.8%).[7] Assuming the CBD is not much compacted by calendaring, commercial electrodes can thus be expected to contain a larger fraction of the total porosity inside the CBD than the investigated sample. The influence of the CBD morphology on the transport properties of porous electrodes is therefore possibly still underestimated by the investigated sample. Even for electrodes that contain a smaller CBD volume fraction than the investigated sample, a significant influence of the CBD microstructure on overall ion transport is highly probable.

Explicit consideration of the CBD morphology is indispensable to capture the transport-relevant microstructural properties of porous electrodes. The ionic tortuosity of battery electrodes then

should be determined over a wide porosity range by EIS and the RS approach to eventually arrive at a more accurate porosity–tortuosity correlation and quantify how electrode formulation impacts CBD porosity and the overall ionic tortuosity. In a first step, the values found to characterize CBD morphology may serve as input parameters for studies that incorporate the actual electrode manufacturing process[21] and, in a second step, the entire reconstruction could be used as realistic geometrical model in full-cycle simulations, including charge transfer reactions at the electrolyte–AM interface, to investigate the influence of the CBD on the overall battery performance.

3.4 Conclusion

This study contains the first high-resolution, physical reconstruction of a morphologically representative volume of an LCO cathode with resolved porous CBD. The reconstruction shows that the porous CBD spans much of the space between the AM particles. Contact between solid CBD and AM particles blocks 10% of the AM surface, which excludes charge transfer as a limiting factor to battery operation. The porous CBD occupies a much smaller volume fraction than the AM phase (29.0% vs 48.5%, respectively), but contains 43.8% of the total pore space. The presence of the CBD decreases the average pore size and increases tortuosity significantly. This means that Li^+ transport in the electrolyte-filled pore space of the electrode is limited by the morphology of the porous CBD. The tortuosity value obtained from pore-scale diffusion simulations in the three-phase reconstruction of the cathode approaches the tortuosity values determined for comparable cathode samples by EIS experiments in the framework of the TLM. This proves that resolving the porous CDB within a representative reconstructed volume of the electrode is necessary to reproduce experimentally determined tortuosity values and thus to obtain transport-relevant morphological information about porous electrodes by the RS approach.

3.5 Experimental Section

Cathode Materials: $LiCoO_2$ (LCO) was purchased from Alfa Aesar (Kandel, Germany), Super C65 carbon black from Timcal (Bodio, Switzerland), polyvinylidene fluoride (PVDF) binder from Solvay (Hannover, Germany), and *N*-Methyl-2-pyrrolidone (NMP) from Alfa Aesar. Whatman GF/A glass microfiber filters (GE Healthcare, Buckinghamshire, United Kingdom) were used as separators. Lithium metal foil was received from Albemarle (Frankfurt, Germany). The liquid electrolyte EC/EMC 50:50 + 1 M $LiPF_6$ (σ_{bulk} = 7.93 mS cm^{-1}) was purchased from Sigma–Aldrich (Steinheim, Germany).

Cathode Preparation: For a slurry with 60% solid content consisting of 90/5/5 (w/w/w) AM/ carbon black/binder, the binder was first dissolved in NMP at 40 °C before LCO particles and carbon black were added gradually. The slurry was mixed with a T 25 disperser (IKA, Staufen, Germany) and applied to an aluminum foil using a ZAA 2300 automatic film applicator (Zehntner, Sissach, Switzerland). The gap height of the applicator was set to 400 µm. The film was dried over night at 80 °C. The film was calendared at 80 °C using a hot rolling press (MTI, Richmond, CA) to adjust the porosity to 40%. Disc electrodes with a radius of 0.6 cm were cut from the calendared film for EIS measurements, battery cycling, and FIB-SEM tomography.

Electrochemical Impedance Spectroscopy: Electrodes were measured in a symmetrical set-up at 100% state-of-charge using a TSC battery cell (rhd instruments, Darmstadt, Germany). The electrodes were spaced by three separators and soaked with 120 µl electrolyte. The cells were equilibrated over night at room temperature. Measurements were performed in a two-electrode set-up by using a Multi Autolab/M101 equipped with a FRA32M impedance module (Metrohm Autolab BV, Utrecht, The Netherlands) in a range from 10^5 Hz to 10^{-1} Hz with an AC amplitude of 10 mV. The resistance of the liquid electrolyte was subtracted for better comparability of the impedance spectra. The TLM was fitted to the spectra using the analysis software RelaxIS 3.0 (rhd instruments).

Battery Cycling: The battery cycling was performed using a TSC battery cell (rhd instruments). The LCO cathode exhibited a loading of 34.0 mg cm^{-2} and a height of 130 µm. The cell (LCO cathode | separators soaked with electrolyte | Li) was assembled in an argon-filled glove box (UniLab, MBraun, Germany; x_{H2O} < 1 ppm, x_{O2} < 1 ppm). Galvanostatic cycling was performed in a two-electrode setup using a Multi Autolab M101 (Metrohm, Filderstadt, Germany) with a C-rate of 0.1 C between 3.8 V and 4.0 V (Figure 3.S1).

FIB-SEM Serial Sectioning: First, the void space of the cathode was filled by a two-part silicone resin (Elastosil RT 604, Wacker, Munich, Germany). Three drops of the resin were applied to the sample under vacuum (at ~5 mbar) followed by exposure to vacuum for another hour. After curing for 24 h, the sample was embedded in epoxy resin using a 5/2 (w/w) mixture of SpeciFix Resin and SpeciFix-40 Curing Agent (Struers, Ballerup, Denmark) and cured for another 24 h at room temperature. The embedded sample was cut, its cross section polished with sandpaper and then sputtered with gold for 30 s at 30 mA.

A Strata 400S dual-beam FIB-SEM system (FEI/ThermoFisher Scientific, Hilsboro, OR) was used for sample preparation and serial sectioning afterwards. The volume-of-interest was defined in the midsection of the electrode to reconstruct bulk properties and exclude boundary effects in later analyses. A protective platinum layer was deposited on top of the volume-of-interest to reduce curtaining effects. The focused Ga^+ beam was operated at 30 kV with a current

of 21 nA to create a U-shaped trench around the volume-of-interest and a current of 6.5 nA for slicing. The image stack was acquired using the Slice&View package of the instrument software. For this purpose, SEM images were taken at 2 kV collecting backscattered electrons (BSE) with the through-the-lens detector (TLD) in immersion mode (a higher resolution mode of the instrument). The final 8-bit image stack (file size: 5.1 GB) contained 985 slices at a pixel size of 13.9 × 13.9 nm^2 and 20.0 nm spacing in milling direction.

5.6 Computational Methods

Physical Reconstruction: First, the slices were aligned by means of the StackReg[61] plugin in ImageJ Fiji.[62] The inclined SEM viewing angle of 52° was corrected in Fiji by rescaling the voxels. Intensity gradients from shadowing were normalized in the three spatial directions by using Visual C# scripts. Shadowing is caused by the trench around the volume-of-interest and by re-deposited material that accumulates during the experiment and blocks electrons on their way to the detector. Curtaining artifacts were removed using the wavelet-Fourier filter approach proposed in Münch et al.[63] For the wavelet decomposition, a Daubechies 8 wavelet[64] was used. The decomposition level was chosen as $L = 5$ and the damping coefficient was set to $\sigma = 10$. A Gaussian filter was applied for noise removal and the contrast was enhanced using Fiji. As the curtaining was more severe in the bottom part of the image, the image quality in this region remained reduced even after application of the decurtaining filter, resulting in a loss of contrast between the different phases in this area. This made segmentation with global or local color threshold values difficult, so that we relied on a machine learning approach for this critical step of the reconstruction process. We used the software Zeiss ZEN Intellesis (Oberkochen, Germany), which is based on trainable deep-learning algorithms. The segmentation algorithm yielded good results, which were first evaluated by visual comparison. Charging effects within the silicone resin resulted in some void voxels being wrongly assigned to the AM phase, which was corrected semi-manually using the 3D watershed segmentation of the MorphoLibJ plugin[65] to identify these areas. The resulting 8-bit image stack constituted case I. Case II was derived from case I through reassigning solid CBD voxels as void voxels. For case III, we visually identified the largest section of porous CBD in the reconstructed volume and extracted the maximum possible cuboid from this section.

Chord Length Distribution: A statistically significant number of 10^6 seed points was randomly distributed in the void space of cases I–III. From each seed point, 26 vectors that pointed in directions induced by the 26 neighbourhood in the voxel lattice were projected until the vectors hit the solid–void interface. Opposing vectors form a chord. Chords that reached the boundary

of the reconstruction were discarded. Valid chords were collected and sorted by length into a histogram.

Calculation of the Surface Area: The marching cube algorithm[53] considers the surroundings of the voxels and approximates the area at the solid–void interface by triangles. The algorithm assesses a set of eight voxels at a time, whereby each voxel is considered a cube vertex. The color value of the voxel determines whether the vertex belongs to the solid phase or to the void space, resulting in 15 different cube configurations. The cube configuration in turn results in a certain triangle configuration of up to four triangles per cube. The areas of the triangles are summed up into the total area. A C++ implementation[66] of the algorithm was adapted for the analysis. The resulting surface area was divided by the volume of the reconstruction (1.3×10^4 µm^3) to obtain the volume-specific surface area.

Connectivity Analysis: The skeletonization of the void space was executed in Fiji using the "Skeletonize3D" plugin. The average connectivity Z was calculated by determining the number of branches meeting at each node. Dead-end nodes connected to only one branch were not considered. The average connectivity Z was calculated as the sum of the weighted ratios of the number of three-branch nodes n_t, four-branch nodes n_q, and higher-level branch nodes n_x to the total number of nodes n_j:[55]

$$Z = 3\frac{n_\mathrm{t}}{n_\mathrm{j}} + 4\frac{n_\mathrm{q}}{n_\mathrm{j}} + 5\frac{n_\mathrm{x}}{n_\mathrm{j}} \tag{3.4}$$

Diffusion Simulation: Diffusion in the void space of cases I–III was numerically simulated using the random-walk particle-tracking (RWPT) technique.[58,67,68] 10^6 inert (non-reactive and non-adsorbing) tracers were randomly distributed in the void space. The random displacement $\Delta\mathbf{r}$ of all tracers by molecular diffusion was calculated for each time step:

$$\Delta\mathbf{r} = \boldsymbol{\gamma}\sqrt{6D_\mathrm{bulk}\Delta t} \tag{3.5}$$

Here $\boldsymbol{\gamma}$ represents a spatial vector and D_bulk the tracer diffusion coefficient. Orientation and length of $\boldsymbol{\gamma}$ are random, determined by a Gaussian function. The time steps were chosen such that the mean diffusive displacement remained below $\Delta h/10$ (with Δh denoting the pixel resolution of 13.9 nm). Jumps leading out of the reconstruction volume were treated by mirror boundary conditions, whereby tracers continue their path mirrored in the original domain.[68] The interaction with the solid–void interface was simulated by a multiple-rejection boundary condition,[69] whereby when a tracer crosses the boundary during a jump, this jump is discarded and recalculated until a valid jump is made. The time-dependent diffusion coefficient $D(t)$ was calculated as

$$D(t) = \frac{1}{6N}\frac{\mathrm{d}}{\mathrm{d}t}\sum_{i=1}^{N}[\Delta r_i(t)]^2 \tag{3.6}$$

where $\Delta r_i(t)$ is the displacement of the *i*-th tracer at time *t* (Figure 3.S5). The effective diffusion coefficient D_{eff} was taken from the asymptotic, long-time limit of $D(t)$ and the ionic tortuosity τ_{RS} calculated as

$$\tau_{\mathrm{RS}} = \frac{D_{\mathrm{bulk}}}{D_{\mathrm{eff}}} \tag{3.7}$$

The accuracy of this modeling approach has been confirmed by comparing D_{eff}-values simulated in regular (simple cubic and face-centered cubic) arrays of spheres[70,71] with values calculated using the analytical approach.[72] Among the advantages of the employed RWPT technique are conservation of mass, absence of numerical dispersion, simplicity of program realization, and straightforward parallelization. Consequently, the program realization of the RWPT algorithm was implemented as parallel code in C language using the Message Passing Interface (MPI) standard on a supercomputing platform. All numerical codes and their description can be found in the Supporting Information of ref. 68.

3.7 Supporting Information

3.S1 Cycling of the LCO cathode

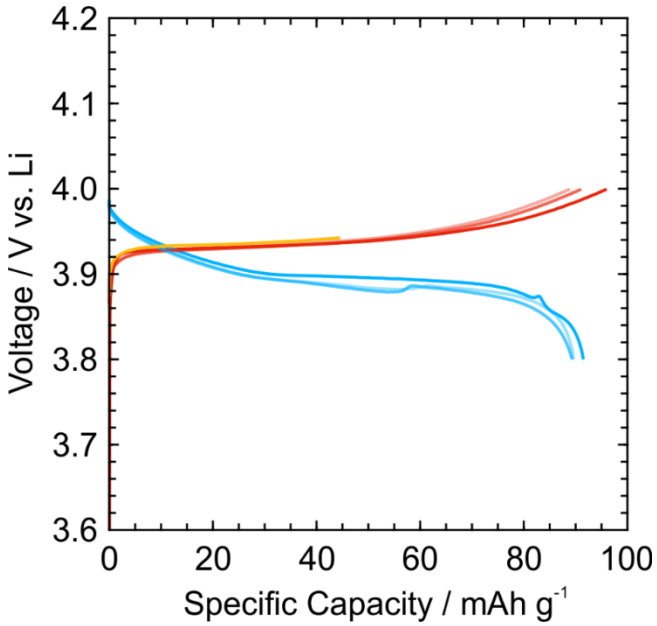

Figure 3.S1: Galvanostatic charge and discharge curves (red and blue, respectively) at a C-rate of 0.1 C. To treat the cathode as gently as possible, a comparatively small voltage window was chosen, resulting in a reduced discharge capacity. After three cycles, the battery was charged to 50% state-of-charge (orange), disassembled, and the cathode prepared for FIB-SEM tomography.

3.S2 SEM images of carbon black

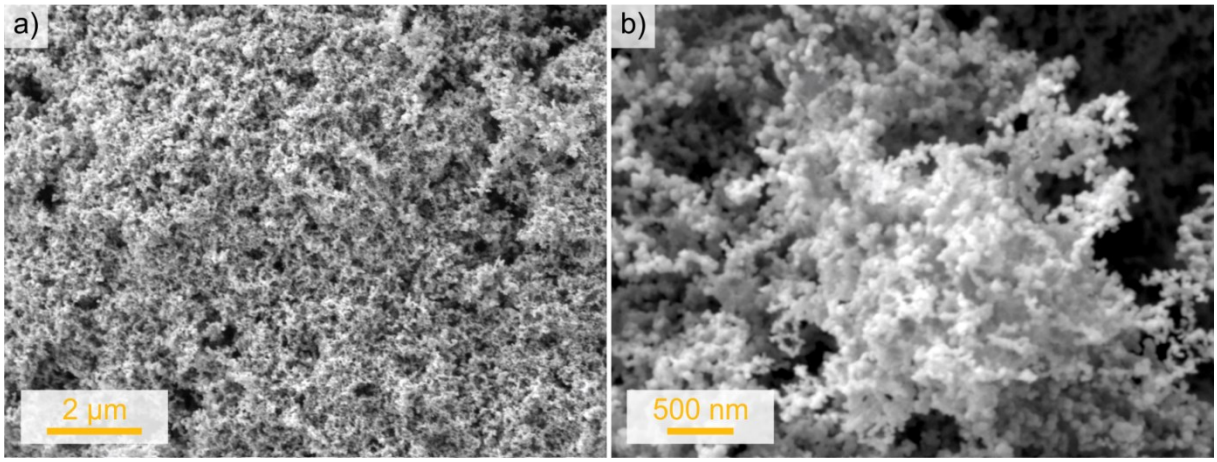

Figure 3.S2: SEM image of carbon black (conductive carbon, without binder). The binder mainly adheres to the high-surface-area carbon, so that the CBD morphology is essentially determined by the morphology of the conductive carbon.

3.S3 Skeletonization of the void space

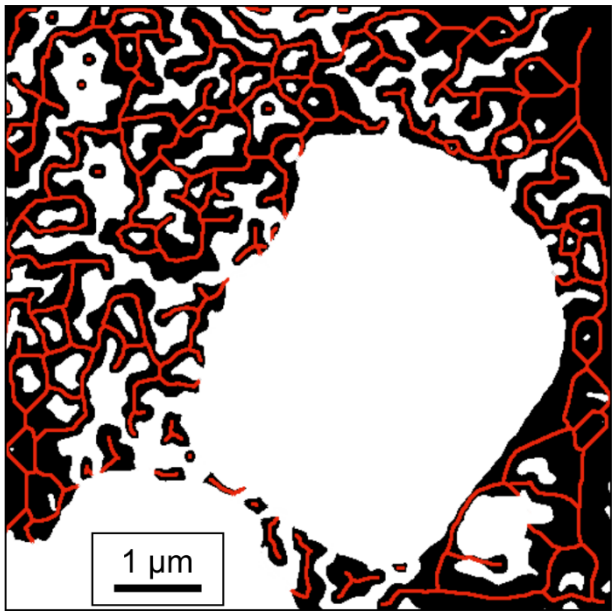

Figure 3.S3: 2D visualization of the skeletonized void space (solid – white, void – black, skeleton – red). The centerlines form a one-voxel wide branch–node network. The connectivity and geometric tortuosity analysis were carried out in 3D.

3.S4 Geometrical tortuosity

The Dijkstra single-source shortest-path algorithm[S1,S2] was implemented to calculate the geometric tortuosity τ_{geom}. The "Branch information" output of the "Analyze Skeleton" plugin was used to import the vertices and edges of the graph. 10^4 vertex pairs were formed, each representing the start and end vertex. The distance value of the start vertex was set to zero, while all remaining vertices were set to infinity. The algorithm determines the distance to all connected vertices beginning at the start vertex. The distance value of the connected vertices is updated. Now the algorithm continues with the unhandled vertex with the smallest distance value managed by a min-priority-queue.[S2] The length to all connected vertices is determined by adding the edge length to the distance value. If the calculated distance is smaller than the previous value, it is overwritten. This is repeated for all remaining vertices until the min-priority-queue returns the end vertex. The shortest path is found. The determined shortest paths of all pairs are plotted against their Euclidean distance. The geometrical tortuosity results from the slope (Figure 3.S4).

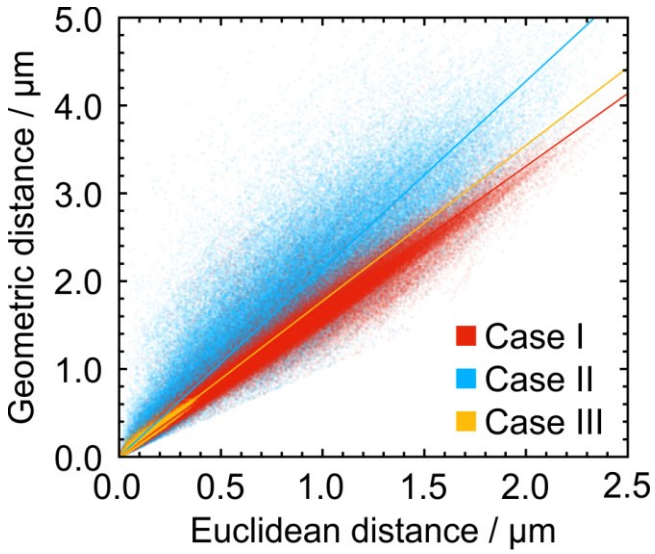

Figure 3.S4: Geometric distance along the skeleton vs the corresponding Euclidean distance. The slope gives the geometric tortuosity τ_{geom}. Cases I–III correspond to different representations of the physical reconstruction describing the void space distribution as defined by solid AM and CBD phases (case I), solid AM phase (case II), and solid CBD phase (case III).

Although mean feature size and porosity for case II are higher than for case I (cf. Table 3.3), the skeletonization returns a much higher geometric tortuosity for case II (τ_{geom} = 2.14) than for the three-phase reconstruction (case I, τ_{geom} = 1.65). In contrast to, for example, the geodesic tortuosity,[S3] the geometric tortuosity follows the centerlines and cannot pass directly along the solid–void boundary. The skeleton branches in case I, which contains the CBD, are shorter and run closer to the large AM particles than the centerlines in the middle of the wide pores in the CBD-free case II. The geometric tortuosity of case I reflects the higher number of shorter paths within the porous CBD. Case I contains a much higher number of bottlenecks and other constrictions than case II, but these are not taken into account for calculation of τ_{geom}, which is why τ_{geom} is unsuitable to estimate the influence of the pore space morphology on diffusive transport. For case III, τ_{geom} is found to be 1.77.

3.S5 Pore-scale diffusion simulations

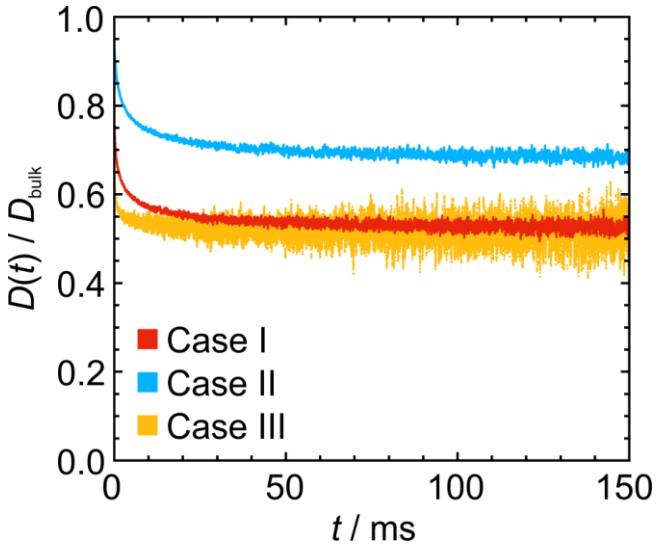

Figure 3.S5: Evolution of the transient diffusion coefficient $D(t)$ normalized by the bulk diffusion coefficient D_{bulk} within the void space. Cases I–III correspond to different representations of the physical reconstruction describing the void space distribution as defined by solid AM and CBD phases (case I), solid AM phase (case II), and solid CBD phase (case III). The tortuosity $\tau_{\mathrm{RS}} = D_{\mathrm{bulk}}/D_{\mathrm{eff}}$ is determined from the asymptotic long-time limit of the curve, which corresponds to $D_{\mathrm{eff}}/D_{\mathrm{bulk}}$.

3.8 References

[1] T. Kim, W. Song, D.-Y. Son, L. K. Ono, Y. Qi, *J. Mater. Chem. A* **2019**, *7*, 2942.

[2] J. B. Goodenough, K.-S. Park, *J. Am. Chem. Soc.* **2013**, *135*, 1167.

[3] H. Sun, J. Zhu, D. Baumann, L. Peng, Y. Xu, I. Shakir, Y. Huang, X. Duan, *Nat. Rev. Mater.* **2019**, *4*, 45.

[4] L. Pfaffmann, S. Jaiser, M. Müller, P. Scharfer, W. Schabel, W. Bauer, F. Scheiba, H. Ehrenberg, *J. Power Sources* **2017**, *363*, 460.

[5] J. Chen, J. Liu, Y. Qi, T. Sun, X. Li, *J. Electrochem. Soc.* **2013**, *160*, A1502.

[6] L. Zielke, T. Hutzenlaub, D. R. Wheeler, I. Manke, T. Arlt, N. Paust, R. Zengerle, S. Thiele, *Adv. Energy Mater.* **2014**, *4*, 1301617.

[7] L. Almar, J. Joos, A. Weber, E. Ivers-Tiffée, *J. Power Sources* **2019**, *427*, 1.

[8] G. Liu, H. Zheng, S. Kim, Y. Deng, A. M. Minor, X. Song, V. S. Battaglia, *J. Electrochem. Soc.* **2008**, *155*, A887.

[9] M. Müller, L. Pfaffmann, S. Jaiser, M. Baunach, V. Trouillet, F. Scheiba, P. Scharfer, W. Schabel, W. Bauer, *J. Power Sources* **2017**, *340*, 1.

[10] G.-W. Lee, J. H. Ryu, W. Han, K. H. Ahn, S. M. Oh, *J. Power Sources* **2010**, *195*, 6049.

[11] S.-L. Chou, Y. Pan, J.-Z. Wang, H.-K. Liu, S.-X. Dou, *Phys. Chem. Chem. Phys.* **2014**, *16*, 20347.

[12] J. Landesfeind, A. Eldiven, H. A. Gasteiger, *J. Electrochem. Soc.* **2018**, *165*, A1122.

[13] R. Dominko, M. Gaberscek, J. Drofenik, M. Bele, S. Pejovnik, J. Jamnik, *J. Power Sources* **2003**, *119-121*, 770.

[14] J. K. Mayer, L. Almar, E. Asylbekov, W. Haselrieder, A. Kwade, A. Weber, H. Nirschl, *Energy Technol.* **2020**, *8*, 1900161.

[15] R. Morasch, J. Landesfeind, B. Suthar, H. A. Gasteiger, *J. Electrochem. Soc.* **2018**, *165*, A3459.

[16] T. Hutzenlaub, A. Asthana, J. Becker, D. R. Wheeler, R. Zengerle, S. Thiele, *Electrochem. Commun.* **2013**, *27*, 77.

[17] Z. Liu, Y.-C. K. Chen-Wiegart, J. Wang, S. A. Barnett, K. T. Faber, *Microsc. Microanal.* **2016**, *22*, 140.

[18] S. Vierrath, L. Zielke, R. Moroni, A. Mondon, D. R. Wheeler, R. Zengerle, S. Thiele, *Electrochem. Commun.* **2015**, *60*, 176.

[19] L. Zielke, T. Hutzenlaub, D. R. Wheeler, C.-W. Chao, I. Manke, A. Hilger, N. Paust, R. Zengerle, S. Thiele, *Adv. Energy Mater.* **2015**, *5*, 1401612.

[20] T. Hutzenlaub, S. Thiele, N. Paust, R. Spotnitz, R. Zengerle, C. Walchshofer, *Electrochim. Acta* **2014**, *115*, 131.

[21] M. Chouchane, A. Rucci, T. Lombardo, A. C. Ngandjong, A. Franco, *J. Power Sources* **2019**, *444*, 227285.

[22] A. Shodiev, E. N. Primo, M. Chouchane, T. Lombardo, A. C. Ngandjong, A. Rucci, A. Franco, *J. Power Sources* **2020**, *454*, 227871.

[23] A. C. Ngandjong, T. Lombardo, E. N. Primo, M. Chouchane, A. Shodiev, O. Arcelus, A. Franco, *J. Power Sources* **2021**, *485*, 229320.

[24] T.-T. Nguyen, J. Villanova, Z. Su, R. Tucoulou, B. Fleutot, B. Delobel, C. Delacourt, A. Demortière, *Adv. Energy Mater.* **2021**, *11*, 2003529.

[25] G. Gaiselmann, M. Neumann, V. Schmidt, O. Pecho, T. Hocker, L. Holzer, *AIChE J.* **2014**, *60*, 1983.

[26] O. Stenzel, O. Pecho, L. Holzer, M. Neumann, V. Schmidt, *AIChE J.* **2016**, *62*, 1834.

[27] D. Hlushkou, A. E. Reising, N. Kaiser, S. Spannenberger, S. Schlabach, Y. Kato, B. Roling, U. Tallarek, *J. Power Sources* **2018**, *396*, 363.

[28] M. Kroll, D. Hlushkou, S. Schlabach, A. Höltzel, B. Roling, U. Tallarek, *J. Electrochem. Soc.* **2018**, *165*, A3156.

[29] A. P. Cocco, G. J. Nelson, W. M. Harris, A. Nakajo, T. D. Myles, A. M. Kiss, J. J. Lombardo, W. K. S. Chiu, *Phys. Chem. Chem. Phys.* **2013**, *15*, 16377.

[30] J. Conder, C. Marino, P. Novák, C. Villevieille, *J. Mater. Chem. A* **2018**, *6*, 3304.

[31] P. R. Munroe, *Mater. Charact.* **2009**, *60*, 2.

[32] G. Möbus, B. J. Inkson, *Mater. Today* **2007**, *10*, 18.

[33] A. Ul-Hamid, *A Beginners' Guide to Scanning Electron Microscopy*, Springer International Publishing, Cham, **2018**.

[34] J. Landesfeind, M. Ebner, A. Eldiven, V. Wood, H. A. Gasteiger, *J. Electrochem. Soc.* **2018**, *165*, A469.

[35] B. L. Trembacki, A. N. Mistry, D. R. Noble, M. E. Ferraro, P. P. Mukherjee, S. A. Roberts, *J. Electrochem. Soc.* **2018**, *165*, E725.

[36] L. S. Kremer, A. Hoffmann, T. Danner, S. Hein, B. Prifling, D. Westhoff, C. Dreer, A. Latz, V. Schmidt, M. Wohlfahrt-Mehrens, *Energy Technol.* **2020**, *8*, 1900167.

[37] S. Hein, T. Danner, D. Westhoff, B. Prifling, R. Scurtu, L. Kremer, A. Hoffmann, A. Hilger, M. Osenberg, I. Manke, M. Wohlfahrt-Mehrens, V. Schmidt, A. Latz, *J. Electrochem. Soc.* **2020**, *167*, 13546.

[38] S. R. Daemi, C. Tan, T. Volkenandt, S. J. Cooper, A. Palacios-Padros, J. Cookson, D. J. L. Brett, P. R. Shearing, *ACS Appl. Energy Mater.* **2018**, *1*, 3702.

[39] T. Hutzenlaub, S. Thiele, R. Zengerle, C. Ziegler, *J. Electrochem. Soc.* **2012**, *15*, A33.

[40] R. de Levie, in *Advances in Electrochemistry and Electrochemical Engineering* (Ed.: P. Delahay), Interscience, New York, **1967**, Vol. 6, pp. 329–397.

[41] A. Lasia, *Electrochemical Impedance Spectroscopy and its Applications*, Springer, New York, **2014**.

[42] N. Ogihara, Y. Itou, T. Sasaki, Y. Takeuchi, *J. Phys. Chem. C* **2015**, *119*, 4612.

[43] J. Landesfeind, J. Hattendorff, A. Ehrl, W. A. Wall, H. A. Gasteiger, *J. Electrochem. Soc.* **2016**, *163*, A1373.

[44] C. Chen, J. Liu, K. Amine, *J. Power Sources* **2001**, *96*, 321.

[45] E. J. Cheng, N. J. Taylor, J. Wolfenstine, J. Sakamoto, *J. Asian Ceram. Soc.* **2017**, *5*, 113.

[46] D. Boudouris, L. Constantinou, C. Panayiotou, *Fluid Phase Equilib.* **2000**, *167*, 1.

[47] T. Prill, K. Schladitz, *Scanning* **2013**, *35*, 189.

[48] T. Müllner, A. Zankel, F. Svec, U. Tallarek, *Mater. Today* **2014**, *17*, 404.

[49] M. D. Uchic, L. Holzer, B. J. Inkson, E. L. Principe, P. Munroe, *MRS Bull.* **2007**, *32*, 408.

[50] A. Çeçen, E. A. Wargo, A. C. Hanna, D. M. Turner, S. R. Kalidindi, E. C. Kumbur, *J. Electrochem. Soc.* **2012**, *159*, B299.

[51] D. Stoeckel, C. Kübel, M. O. Loeh, B. M. Smarsly, U. Tallarek, *Langmuir* **2015**, *31*, 7391.

[52] H. Reinhardt, M. Kroll, S. L. Karstens, S. Schlabach, N. A. Hampp, U. Tallarek, *Adv. Mater. Interfaces* **2021**, *8*, 2000253.

[53] W. E. Lorensen, H. E. Cline, *ACM SIGGRAPH Comput. Graph.* **1987**, *21*, 163.

[54] J. Joos, T. Carraro, M. Ender, B. Rüger, A. Weber, E. Ivers-Tiffée, *ECS Trans.* **2011**, *35*, 2357.

[55] K. Hormann, V. Baranau, D. Hlushkou, A. Höltzel, U. Tallarek, *New J. Chem.* **2016**, *40*, 4187.

[56] D. Enke, R. Gläser, U. Tallarek, *Chem.-Ing.-Tech.* **2016**, *88*, 1561.

[57] T. C. Lee, R. L. Kashyap, C. N. Chu, *CVGIP: Graphical Models and Image Processing* **1994**, *56*, 462.

[58] F. Delay, P. Ackerer, C. Danquigny, *Vadose Zone J.* **2005**, *4*, 360.

[59] B. Ghanbarian, A. G. Hunt, R. P. Ewing, M. Sahimi, *Soil Sci. Soc. Am. J.* **2013**, *77*, 1461.

[60] T.-T. Nguyen, A. Demortière, B. Fleutot, B. Delobel, C. Delacourt, S. J. Cooper, *npj Computational Materials* **2020**, *6*, 123.

[61] P. Thévenaz, U. E. Ruttimann, M. Unser, *IEEE Trans. Image Process.* **1998**, *7*, 27.

[62] J. Schindelin, I. Arganda-Carreras, E. Frise, V. Kaynig, M. Longair, T. Pietzsch, S. Preibisch, C. Rueden, S. Saalfeld, B. Schmid, J.-Y. Tinevez, D.J. White, V. Hartenstein, K. Eliceiri, P. Tomancak, A. Cardona, *Nat. Methods* **2012**, *9*, 676.

[63] B. Münch, P. Trtik, F. Marone, M. Stampanoni, *Opt. Express* **2009**, *17*, 8567.

[64] I. Daubechies, *Ten Lectures on Wavelets*, SIAM, Philadelphia, PA, **1992**.

[65] D. Legland, I. Arganda-Carreras, P. Andrey, *Bioinformatics* **2016**, *32*, 3532.

[66] P. Bourke, "Polygonising a scalar field", http://paulbourke.net/geometry/polygonise/, **1994**.

[67] J. Salles, J.-F. Thovert, R. Delannay, L. Prevors, J.-L. Auriault, P. M. Adler, *Phys. Fluids A* **1993**, *5*, 2348.

[68] D. Hlushkou, A. Svidrytski, U. Tallarek, *J. Phys. Chem. C* **2017**, *121*, 8416.

[69] P. Szymczak, A. J. C. Ladd, *Phys. Rev. E* **2003**, *68*, 036704.

[70] H. Liasneuski, D. Hlushkou, S. Khirevich, A. Höltzel, U. Tallarek, S. Torquato, *J. Appl. Phys.* **2014**, *116*, 034904.

[71] A. Daneyko, D. Hlushkou, V. Baranau, S. Khirevich, A. Seidel-Morgenstern, U. Tallarek, *J. Chromatogr. A* **2015**, *1407*, 139.

[72] M. H. Blees, J. C. Leyte, *J. Colloid Interface Sci.* **1994**, *166*, 118.

[S1] E. W. Dijkstra, Numer. Math. 1959, 1, 269.

[S2] T. H. Cormen, C. E. Leiserson, R. L. Rivest, C. Stein, Introduction to algorithms, MIT Press, Cambridge, Mass., 2009

[S3] K. Hormann, V. Baranau, D. Hlushkou, A. Höltzel, U. Tallarek, *New J. Chem.* **2016**, *40*, 4187.

Chapter 4: Sheet-type all-solid-state batteries with sulfidic electrolytes: Analysis of kinetic limitations based on a cathode morphology study

Authors

Moritz Kroll,[+] Marc Duchardt,[+] Sarah L. Karstens, Sabine Schlabach, Fabio Lange, Janika Hochstrasser, Bernhard Roling,* and Ulrich Tallarek*

[+]These authors contributed equally to this work.

State of publication

Submitted 14 March 2021 to *Journal of Power Sources*, *under review*.

Abstract

All-solid-state batteries (ASSBs) with sulfide-based solid electrolytes (SEs) promise to boost the energy density of future Li-ion batteries. Still little is known about the influence of cathode morphology and charge transport/transfer processes inside the cathode on battery performance. We report on a morphological investigation of two ASSB cathodes prepared by the industrially relevant sheet-type approach. Both employ state-of-the-art NMC 85|05|10 as cathode active material (CAM) and sulfide-based SEs differing in morphology and intrinsic ionic conductivity, i.e., β-Li_3PS_4 (small mesoporous particles, conductivity: 0.2 $mS \cdot cm^{-1}$) and 2 $Li_3PS_4 \cdot LiI$ (large nonporous particles, conductivity: 0.8 $mS \cdot cm^{-1}$). We apply focused ion-beam scanning electron microscopy to obtain high-resolution reconstructions, allowing to differentiate between CAM, SE, and voids and to conduct a morphological analysis of each phase as well as a simulation of ion transport in the SE phase. Based on morphological data, kinetic limitations in the cathodes are analyzed using a transmission-line model, indicating that charge transfer resistance at the CAM–SE interface is the dominating contribution, while resistances due to Li-ion migration in the SE and Li chemical diffusion in the CAM are considerably lower. Reducing charge transfer resistance at the CAM–SE interface is therefore a key to improving ASSB performance.

4.1 Introduction

Currently, the majority of commercial Li-ion batteries is used for mobile devices like phones and laptops. Long gone are the days of phones whose batteries lasted for several days without intermediate recharging. Mobile phones have become smartphones whose performance drastically surpasses that of stationary computers from only 10 years ago. However, whereas computing power soared, Li-ion technology was rather refined. Battery development can hardly keep up with the speed at which computers and their energy consumption evolve. Other possible applications, e.g., electric vehicles, demand even larger energy and power densities. Therefore, a paradigm-shift pushing beyond the current limitations is urgently needed.

Li-ion all-solid-state batteries (Li-ASSBs) promise to do so, potentially leading to a doubling of current volumetric energy densities, if Li metal is utilized on the anode side instead of any kind of host material [1,2]. They are also considered safer than their liquid counterparts due to the absence of flammable organic liquids [3]. Many different solid electrolytes (SEs) exist and can be classified into three main groups: polymeric, oxide-based, and sulfide-based ones. The conductivities of polymeric Li-ion SEs are comparatively low, rendering them inadequate for the application as sole electrolyte in ASSBs at room temperature [1,4]. However, they might promote the stable electrodeposition, effectively impeding lithium from penetrating the SE separator. Thus, polymeric SEs could become suitable as an intermediate layer between a Li anode and the inorganic main SE compound [5,6]. Oxide-based electrolytes, on the other hand, can be quite conductive, but their brittleness and large grain boundary resistances pose serious drawbacks [7,8]. Sulfide-based SEs are softer [9–11] and offer excellent ionic conductivities exceeding 10^{-2} S cm^{-1} [12–17]. Therefore, they are most promising for the commercialization of ASSBs [18]. Unfortunately, sulfide-based SEs synthesizable at acceptable cost and effort (and thus considered potentially marketable) possess lower conductivities, ranging from about 10^{-4} S cm^{-1} to slightly above 10^{-3} S cm^{-1}. These electrolytes are available in different forms, from completely amorphous ones like 2 Li_3PS_4·LiI [19] via glass-ceramics [20] to crystalline ones like $Li_7P_3S_{11}$, Li_6PS_5Cl, and β-Li_3PS_4 [21–23].

2 Li_3PS_4·LiI (LPSI) has been described recently and can be prepared through ball-milling of a stoichiometric mixture of Li_2S, P_2S_5, and LiI [19]. As typically observed for SEs derived from dry ball milling, the average particle size is quite large [19,24]. The resulting ionic conductivity is 0.8 mS cm^{-1}, for which no subsequent high temperature treatment is necessary, rendering this SE an attractive candidate for use in ASSBs. Another and one of the most intensively studied sulfide-based SEs is Li_3PS_4 in its most conductive crystalline modification (β-Li_3PS_4) with a Li-ion conductivity of ~0.2 mS cm^{-1} [23]. It can be synthesized by mechanical milling as well as solvent-mediated from THF, for example [23,25,26]. When β-Li_3PS_4 is synthesized by this approach, Li_3PS_4·3THF is formed as an intermediate compound, which is composed of single

crystalline prisms of ca. 10 to 30 µm size. Upon evaporation of THF followed by evolution of crystalline β-Li_3PS_4, this former crystal habitus is preserved, however, it is accompanied by the generation of a loose assembly of nanosized grains and mesopores in between these nanosized grains [23]. This structure distinguishes it from the typical morphology of virtually all other sulfide-based SEs, including LPSI. Those SEs are usually synthesized by ball-milling or high-temperature solid state reactions, exhibiting large secondary particles whose primary particles cannot be easily differentiated from each other [19,24,27]. Furthermore, the secondary particles form dense blocks without noteworthy porosity.

Due to their favorable plastic properties, sulfide-based SEs can be more readily processed than oxide-based ones. This facilitates a more intimate contact with the cathode active material (CAM) upon pressing. Still – even for sulfide-based SEs – one of the most fundamental issues of Li-ASSBs is the reduced contact area between CAM and SE in the composite cathode compared to liquid electrolyte cells. Usually, only a fraction of the CAM surface is in contact with the SE [28,29].

Today, and particularly in fundamental research, ASSBs are mostly constructed as dry-pressed pellet-type (PT-)ASSBs. This involves building a 3-layer stack of cathode composite, pure SE as separator and (in the simplest case) elementary Li or In as anode. This setup is especially useful for initial performance testing of new materials and examination of their compatibility with others (interface stability). However, these cells can hardly be scaled up, predominantly due to the lack of a polymeric binder that mechanically stabilizes the SE as well as the cathode composite layer [30,31]. Moreover, this type of assembly does not allow for adequately thin SE separator layers that would enable high energy densities. For an eventual mass production of ASSBs, adaptation of the wet-slurry process, giving rise to so-called sheet-type (ST-)ASSBs, is thus advisable [8,32–34]. Furthermore, use of binders may alleviate chemomechanical stress released into the system by the CAM upon repeated charge and discharge cycles [8,35]. In an ideal composite cathode, CAM and SE powders would form coherent phases, interpenetrating each other completely, without creating any intermediate void space. However, the quantitative control of ASSB microstructure is difficult. Neither dry mixing of the respective SE and CAM powders, nor their slurry-casting necessarily result in an optimal packing of the respective materials [36–38].

Most previous studies on morphology of sulfide-based ASSBs shared qualitative information, received from cross-sectional scanning electron microscopy (SEM) images, about shape and size distributions of the respective phases inside a composite cathode [29,39–41]. Only recently, SEM coupled to focused ion beam milling (FIB-SEM) and X-ray tomography were employed to obtain 3D reconstructions that can be used to investigate morphological parameters of ASSBs

quantitatively [38,42–45]. Initial efforts have focused on PT-ASSBs [38,43,44]. Only Choi *et al.* have reported a quantitative FIB-SEM study on ST-ASSBs with NMC-622 and the rarely used Ni-containing electrolyte $(Li_2S)_8(P_2S_5)_2(Ni_3S_2)_1$ [45,46]. However, the probed volume of $5.3 \cdot 10^3$ µm³ (10 µm depth) was too small compared to the CAM particle size of 4–6 µm to obtain representative information. Suppression of finite-size effects requires reconstructions with edge lengths on the order of ~25 times the morphological feature size (in this case, CAM mean particle size) [47]. Furthermore, a C-rate of 0.02 C was realized in the galvanostatic cycling experiments, which is significantly lower than the minimum C-rates used in typical ASSB studies [48–50]. A detailed morphological analysis of a representative volume of state-of-the-art ST-ASSBs is still lacking.

In this work, we present a quantitative comparison of microstructures in two high-performance ST composite cathodes for ASSBs with different SEs, both employing polyisobutene as binder and a small particle-size lithium nickel manganese cobalt oxide (NMC, $LiNi_{0.85}Mn_{0.05}Co_{0.1}O_2$) as CAM. To reduce interfacial decomposition reactions, a typical $LiNbO_3$ coating was applied to the NMC material. As the high-temperature solid state reactions required for many interesting SEs known today (most notably Li_6PS_5Cl) increase production efforts and costs, we decided to use *β*-LPS and LPSI as model-type electrolytes in our study. Those SEs can be synthesized at temperatures <140 °C and at room temperature, respectively. No carbon additives were used, which are known to exacerbate the degradation reactions at the interface between CAM and SE [48,51–53]. Cathode composites were investigated in a ST configuration with polyisobutene as polymeric binder, following an in-house developed tape-casting protocol. Acquisition of FIB-SEM tomographic data and application of image analysis techniques allowed to study in detail the morphological properties of SE phase, CAM, and void space (binder could not be segmented as separate phase due to its poor contrast and small feature size). Large volumes (>$1.2 \cdot 10^5$ µm^3) were probed over the entire thickness of the cathode composite layer. This ensured that the edge length of a reconstruction was 20–25 times the actual CAM feature size and allowed to obtain representative data from both reconstructions [47]. Our analysis features the distribution of void space, connectivity of the CAM particles, CAM–SE contact area, and pore-scale simulations of ion transport in the SE phase. Complementary battery cycling experiments were conducted to characterize the performance of the two ST-ASSBs. The obtained overall battery resistances were combined with the results from the morphological analysis to elucidate kinetic limitations within the composite cathode in the framework of a transmission-line model.

4.2 Experimental

Materials: NMC-85|05|10 powder (d_{50} = 3.5 µm; BASF SE, Ludwigshafen, Germany) and high molecular weight polyisobutene (Oppanol N 150, BASF SE) were dried for 12 h in a vacuum at 300 °C and 60 °C, respectively, and stored in an Ar-filled glovebox (MBraun, Melsungen, Germany; [O_2] and [H_2O] < 0.1 ppm). Indium foil (99.99%) was purchased from Alfa Aesar (Kandel, Germany). 1 M stock solution of LiOEt (99%, Sigma-Aldrich, Taufkirchen, Germany) was prepared by dissolving elementary lithium (Albemarle Germany GmbH, Langelsheim, Germany) in absolute EtOH (99.9%, Sigma Aldrich). Siliconized polyester foil was purchased from PPI Adhesive Products GmbH (Lindlar, Germany).

Synthesis: *β*-Li_3PS_4 *(β*-LPS*)* was synthesized in 3.3 g-batches by slowly adding a thoroughly ground, stoichiometric mixture of Li_2S (99.98% trace metals basis, Alfa-Aesar) and P_2S_5 (99%, Merck-Millipore) to 20 ml THF in an Ar-filled glovebox. The mixture was stirred for 24 h. Then, the suspension was centrifuged and the supernatant removed. The remaining solid was washed with 15 ml of THF and centrifuged again. This procedure was repeated two times (overall three washing steps). The colorless solid was dried in vacuum for 30 min, subsequently heated to 80 °C for 1 h to remove crystal THF from *β*-Li_3PS_4·3 THF and finally heated to 140 °C for 9 h to sinter the material.

The 2 Li_3PS_4·LiI (LPSI) glass was prepared in 2 g-batches by means of mechanical milling using a high-energy planetary ball mill (Pulverisette 7, Fritsch). A stoichiometric mixture of reagent grade Li_2S (99.9%, Alfa Aesar), P_2S_5 (99%, Merck-Millipore), and LiI (99.999%, Alfa Aesar) powders was filled in a zirconia jar (20 ml volume) with 10 zirconia balls (∅ = 10 mm) in an Ar-filled glovebox. A rotational speed of 700 rpm for about 8 h was applied (5 min milling; 15 min rest; 99 cycles). Afterwards, the strongly compacted product was ground in an agate mortar.

$LiNbO_3$-coated NMC-85|05|10: For the coating of NMC-85|05|10, a literature procedure was adapted [54]. First, a 1 M stock solution of LiOEt in EtOH was mixed with pure $Nb(OEt)_5$ in a vial inside a glovebox yielding an equimolar solution of LiOEt and $Nb(OEt)_5$. Then, 6 g of CAM was added to the solution and the vial transferred to an ultrasonic bath preheated to 60 °C outside the glovebox. Under continuous sonication, the bath temperature was increased to 75 °C and a needle put through the cap of the vial to enable the continuous evaporation of EtOH but prevent intrusion of water (and hence the rapid hydrolysis of the sol). After complete evaporation of EtOH, the material was carefully ground in an agate mortar and subsequently calcined in air at 400 °C for 1 h (heating rate: 20 °C h^{-1}), yielding 1 wt%-$LiNbO_3$@NMC-85|05|10 (LNO@NMC).

Preparation of electrode composites: Cathode composite powder consisting of LNO@NMC and β-Li_3PS_4 was prepared by simply mixing the two materials in an agate mortar with pestle and spatula in a weight ratio of 70:30.

Cathode composite powder consisting of LNO@NMC and LPSI was prepared by mixing the two materials in an agate mortar with pestle and spatula in a weight ratio of 68:32, slightly deviating from the typical 70:30 weight ratio used for the β-LPS composite to account for the higher density of LPSI. To reduce the size of the large LPSI particles, the composite was milled at 140 rpm for 30 min under an Ar atmosphere in a planetary ball mill (Fritsch) using 10 zirconia balls (∅ = 10 mm) in a 20 ml jar. The overall amount of material was limited to 1 g to prevent accumulation of composite on the wall of the jar.

Slurry casting: LPSI SE slurry: Polyisobutene (35 mg) was dissolved in *p*-xylene (2 ml) overnight. The solution was then transferred to a mortar and mixed with 1.71 g of LPSI, corresponding to a weight ratio of 98:2 regarding SE and PIB. The overall solid content was 50%. After thorough mixing, the slurry was poured onto siliconized polyester foil as support and doctor-bladed with a gap-size of 600 µm. The silicone layer facilitated the subsequent detachment of the film from the support [30]. After drying, the films were calendared using a hot rolling press (MTI, Richmond, CA) to enhance film stability and reduce voids. The resulting cathode film thickness can be estimated from the physical reconstruction (52 µm for β-LPS and 45 µm for LPSI).

LNO@NMC–β-LPS cathode slurry: Polyisobutene (52 mg) was dissolved in *p*-xylene (4 ml) overnight. The solution was then transferred to a mortar and pre-mixed composite (overall 2.27 g) added stepwise, amounting to a solid content of 40%. The weight ratios of CAM, SE, and binder corresponded to 69:29:2. After thorough mixing, the slurry was doctor-bladed with a gap-size of 420 µm.

LNO@NMC–LPSI cathode slurry: Polyisobutene (59 mg) was dissolved in *p*-xylene (2 ml) overnight. The solution was transferred to a mortar and pre-mixed composite (overall 2.55 g) added stepwise, amounting to a solid content of 60%. The weight ratios of CAM, SE, and binder corresponded to 67:31:2. After thorough mixing, the slurry was doctor-bladed with a gap-size of 320 µm.

Cell assembly and electrochemical testing: For the galvanostatic cycling studies of the ST cells, cathode disks (∅ = 9 mm) were punched out from tape-casted cathode films with a weight of 11 mg. For the SE separator, two LPSI-sheets were punched out (∅ = 10 mm, 20 mg each, Fig. 4.S1). For PT cells, 13.4 mg cathode composite powder were used, accounting for the

difference in cathode surface area compared to the ST cells. For the SE separator, 50 mg LPSI powder were compacted at 98 MPa. Subsequently, an In sheet (25 mg, prepressed at 300 MPa to give homogenous distribution and thickness) and the cathode composite disk or powder were spread on the lower and upper side of the two LPSI-disks or the prepressed LPSI-pellet, respectively, in a polyether ether ketone (PEEK) mold (∅ = 10 mm). For both cell types, to create intimate contact between the respective battery layers, the stacks were densified at a pressure of 294 MPa with two stainless steel pistons. The subsequent cycling experiments were carried out at ambient temperature (25 °C), a pressure of 98 MPa, and between 3.7 V and 2.1 V as upper and lower cutoff potentials, respectively. A current density of 254 μA cm^{-2} (0.1 C) with respect to the area of the cathode layer was used.

X-ray powder diffraction: X-ray powder diffraction data were collected on an STOE StadiMP diffractometer, equipped with a Mythen 1K silicon strip detector and a Cu Kα X-ray source (λ = 1.54056 Å). Samples were measured in transmission mode positioned between Scotch tape.

Impedance spectroscopy: As-prepared SE powders (*β*-Li_3PS_4 and LPSI) were ground in an agate mortar and pressed into pellets with a diameter of 6 mm by applying a pressure of 270 MPa at ambient temperature for approximately 30 min. Sample thicknesses was measured with a micrometer screw gauge from Mitutoyo. Gold was coated on both faces of the pellets using a Cressington 108 auto sputter coater. Alternating current (AC) impedance spectra were recorded using a Novocontrol α-AK impedance analyzer over a frequency range from 1 MHz to 0.01 Hz, with an applied root-mean-square AC voltage of 10 mV. The measurements were carried out at temperatures between −120 and 100 °C, with the sample temperature being controlled by the Novocontrol Quatro Cryosystem. Maximum temperature variation tolerated in the impedance measurements was ±0.1 °C. The impedance spectra were analyzed with the RelaxIS software package (rhd instruments, Darmstadt, Germany).

FIB-SEM tomography: For FIB-SEM tomography, the prepared composite batteries were fixed on a sample holder by means of a conductive carbon pad (Plano, Wetzlar, Germany) with the cathode facing up. Conductive silver paint (ACHESON 1415, Plano) was used to realize direct electrical contact between sample holder and cathode surface. To increase sample conductivity and reduce charging effects, a thin gold layer was deposited at a current of 30 mA for 180 s onto the respective sample surface by sputter coating. The gold also helped protect the sample from air during transfer to the FIB-SEM.

Image acquisition was realized by using a Strata 400S dual-beam FIB-SEM system (FEI/ThermoFisher Scientific, Hillsboro, OR). A platinum layer of 2 μm thickness was deposited on the region of interest (ROI) to mitigate curtaining effects during slicing. A U-shaped trench was milled around the ROI with an ion beam (30 kV voltage, 21 nA current). To

this end, 25 µm were milled on either side of the samples to avoid redeposition and shadowing effects on the cross-section. A stack of images from the ROI was acquired by means of the Slice&View package of the instrument software, applying a Ga^+ ion beam of 30 kV and 6.5 nA to image the cross-section by SEM between slicing. Electron images were taken at a dwell time of 6 µs and a voltage of 5 kV and 10 kV for the *β*-LPS and LPSI sample, respectively, using the Everhart–Thornley detector. Higher voltage for the LPSI cathode was needed to improve contrast between SE and CAM particles. Additionally, instead of the pure secondary electron mode of the detector, in case of the *β*-LPS sample a grid voltage of 95 V was applied allowing backscattered electrons to contribute to material contrast. The final image stacks contained 1157 (*β*-LPS) and 944 (LPSI) slices with 35.7 × 35.7 nm^2 pixel size and 50 nm spacing.

Image processing: An automated, streamlined, largely open-source reconstruction workflow was established for image processing and segmentation utilizing Fiji ImageJ [55]. First, drifts were corrected by aligning the images using the StackReg plugin [56]. Curtaining effects were eliminated by the Stripe Filter [57] (Wavelet FFT dB 20) of the Xlib plugin. To correct the inclined SEM viewing angle (52°) the voxels were rescaled in *y*-direction. The background of each image was subtracted to reduce shadowing (rolling ball radius = 150). Finally, brightness and contrast were adjusted and noise was eliminated by the anisotropic diffusion plugin (30 iterations, edge threshold height = 5). In the last step, the different phases were segmented from the greyscale images. SE separator was detected using the watershed algorithm of the MorphlibJ plugin [58]. CAM particles and subsequently the SE were filtered by means of the Otsu [59] auto local threshold algorithm. Remaining image sections were assigned as void.

Morphological analysis: The physical reconstructions of the two solid state cathodes were used as geometrical models for detailed morphological analyses. To this end, the calculations were implemented in C# and Fiji plugins were used. The volume fractions of the two samples were calculated from their weights to compare them with the volume fractions of the reconstructions. For this purpose, following densities were assumed: 4.43 g cm^{-3} for NMC 85|05|10, 0.92 g cm^{-3} for the polyisobutene binder, 1.90 g cm^{-3} for *β*-LPS [60], and 2.35 g cm^{-3} for LPSI.

Chord length distributions: CLDs were employed to characterize the geometrical properties of the voids and the CAM particles. In this approach, 10^6 seed points were randomly distributed in the phase of interest. 26 vectors pointing in angularly equispaced directions were projected from each seed point until they reached the interface with another phase. Vectors that projected out of the macroscopic reconstruction boundaries were discarded. The absolute lengths of two opposing vectors were then summed up as a chord. Finally, all chords were collected into a histogram (the resulting CLD).

Chemical surrounding of the voids: To better understand the formation of voids, their chemical environment at the interface was examined. Voids are surrounded by SE, CAM, or both phases. All spatially separated voids were first labeled using the 'Connected Component Labeling' [58] plugin in Fiji. Then, the algorithm iterated through all voxels of each void. The six neighboring voxels of each void voxel were noted and other phases identified. Finally, the ratio of CAM to SE environment was formed for each void, weighted by the void size, and transformed into a histogram. A value of zero means that the void is fully surrounded by SE, while a value of unity signifies that the void is located inside a CAM particle.

Calculation of the surface area: To determine the influence of the ball milling process on the surface of the CAM particles and the fraction of their active surface area, the surface was estimated using the marching cube algorithm [61–63]. The reconstruction consists of cuboid voxels whose size is determined by the resolution of the electron microscope and the cutting thickness of the ion beam. A direct calculation of the surface from the voxel areas leads to an overestimation of the real surface by up to 1.5 times [62]. The marching cube algorithm smooths the surface by taking into account the voxel environment, which allows a good estimation of the surface. For this purpose, the algorithm assesses a set of eight voxels at a time. Each voxel can be considered as a vertex of a cube. The color value of the voxel determines if the vertex relates to the examined phase or not. This results in 15 different cube configurations. The surface is approximated with up to four triangles, which follows from the cube configuration. The triangle surfaces are summed up and the algorithm marches on to the next cube. A C++ implementation [64] of the algorithm was adapted for the analysis. The resulting surface is divided by the phase volume calculated from the voxel volume.

The active surface $A_{\mathrm{CAM,active}}$ of the CAM particles is defined as area where SE and CAM are in direct contact. Li-ions intercalate here from the SE into the CAM. Voids block this process so that less surface area is available for the charge transfer reaction. $A_{\mathrm{CAM,active}}$ can be calculated from the CAM surface A_{CAM}, void surface A_{void}, and surface $A_{\mathrm{CAM,void}}$ where CAM particles and voids are seen as one phase:

$$A_{\mathrm{CAM,active}} = A_{\mathrm{CAM}} - \frac{1}{2}\left(A_{\mathrm{CAM}} + A_{\mathrm{void}} - A_{\mathrm{CAM,void}}\right) \tag{4.1}$$

Isolated particles: CAM particles form a large network by direct contact, ensuring electronic conductivity of the cathode towards the current collector. Unconnected particles were detected by the 'Connected Component Labeling' [58] plugin in Fiji. The largest interconnected particle network was cut out, leaving isolated CAM particles.

Diffusion simulations: Diffusive transport of pointlike, passive (nonreacting and nonadsorbing) tracers in the void volume of the reconstructed electrodes was simulated using a random walk particle tracking (RWPT) technique, which is described in detail elsewhere [65–67]. Briefly, a large number ($N = 10^7$) of point tracers was inserted at random positions in the SE phase of the reconstructions. During every time step δt, sufficiently small to ensure that the mean diffusive displacement is below $\Delta h/10$ (where $\Delta h = 35.7$ nm is the spatial resolution of a reconstruction), the tracers were displaced due to molecular diffusion to new positions in the void volume. The tracer displacements $\Delta\mathbf{r}$ were calculated by

$$\Delta \boldsymbol{r} = \boldsymbol{\gamma}\sqrt{6D_{\mathrm{bulk}}\Delta t} \tag{4.2}$$

where D_{bulk} is the bulk diffusivity and $\boldsymbol{\gamma}$ a vector with random orientation in space and a length that follows a Gaussian distribution with zero mean and unity variance. Tracer displacement into space outside a reconstruction was handled through a mirror-boundary condition, that is, tracers crossing the border of a reconstruction continued their walk in the mirror image of the original domain [66]. A multiple-rejection boundary condition [68] was implemented to restrict tracer diffusion to the SE phase within a reconstruction: If a tracer crossed the interface to another phase, this displacement was rejected and recalculated until the tracer position remained in the SE. After each time step, tracer positions were monitored and a time-dependent diffusion coefficient $D(t)$ calculated according to

$$D(t) = \frac{1}{6N} \cdot \frac{\mathrm{d}}{\mathrm{d}t} \sum_{i=1}^{N} [\Delta r_i(t)]^2 \tag{4.3}$$

where $\Delta r_i(t)$ is the displacement of the ith tracer after time t. From the long-time asymptote, the effective diffusion coefficient could be calculated for each reconstruction. The corresponding diffusive tortuosity τ was obtained by

$$\tau = \frac{D_{\mathrm{bulk}}}{D_{\mathrm{eff}}} \tag{4.4}$$

where D_{eff} is the effective (time-independent) diffusion coefficient.

4.3 Results and Discussion

4.3.1 Morphology of the solid electrolyte particles

To investigate the 3D microstructure of ST-ASSB systems relevant for industrial production, preparation protocols for stable films were first established. The choice of binder was based on literature reports, which indicated favorable mechanical characteristics and compatibility with SEs, especially for nitrile butadiene rubber (NBR) and its hydrogenated analogue (H-NBR) and polyisobutene (PIB) [30]. H-NBR for casting SE separator tapes resulted in smooth films that could readily be utilized for the construction of ASSBs. However, in preliminary experiments, we found H-NBR-based slurries for cathode films to be far more difficult to process. They repeatedly thickened instantaneously after complete addition of composite material powders to the binder solution, rendering reproducible casting difficult. We therefore preferred PIB as binder of choice for the subsequent studies.

β-Li_3PS_4 (β-LPS) and 2 Li_3PS_4·LiI (LPSI) were synthesized according to their respective synthesis protocols (see Experimental Section for details) in a phase-pure manner (cf. Fig. 4.S2). They revealed conductivities of 0.2 mS cm^{-1} and 0.8 mS cm^{-1} at 25 °C (Fig. 4.S3), respectively, well in line with literature reports [19,69]. At first sight, β-LPS and LPSI particles do not seem to have very different morphologies (Fig. 4.1a and 4.1b). Both materials are composed of a mixture of larger and smaller particles – the LPSI just shows a slightly larger fraction of particles in the 10 µm-range. However, after closer inspection, the two materials show fundamentally different morphologies. On the one hand, observable upon higher magnification (Fig. 4.1c), the β-LPS is composed of very small primary particles arranged in mostly preserved prism-shaped habitus of the former Li_3PS_4·3THF crystal, forming larger secondary particles [23,70]. Recognizable is the considerable pore space within the secondary particles. In the case of LPSI, on the other hand, primary particles cannot be distinguished at a magnification of 5000x (the particle in Fig. 1d rather constitutes a single large block). This is typical for sulfide-based Li-ion SEs prepared by dry ball-milling, if no special attention is paid to the synthesis of smaller SE particles [24,71]. The large forces acting on the SE material at high rotation frequencies (needed for the desired mechanochemical reaction) lead to strong compression of the material. Therefore, the material sticks in large parts to the inner wall of the milling container. Subsequent manual grinding with mortar and pestle only insufficiently breaks these large chunks apart. Such large SE particles are also obtained when carrying out syntheses of other sulfide-based SEs via conventional solid-state reactions [72]. Fused together at high temperatures, the SE particles are often similarly difficult to separate.

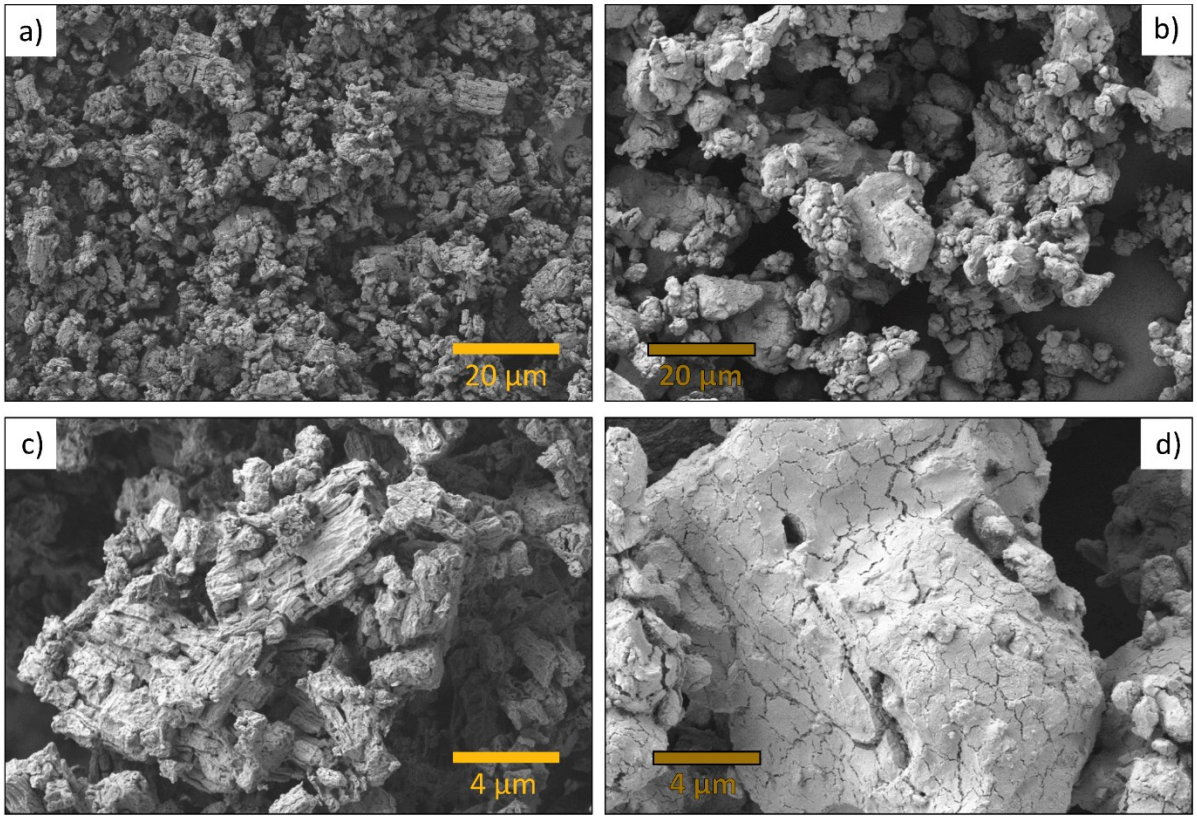

Fig. 4.**1.** Morphology of the as-prepared solid electrolyte powders. Left: β-Li_3PS_4 particles, right: LPSI-particles.

The consequences of the large LPSI particle size (average >10 µm) for the morphologies of the prepared cathode sheets can be recognized in Fig. S4a. If the composite of SE and CAM is only manually ground with mortar and pestle prior to its introduction into the binder solution and subsequent doctor-blading, large particles of LPSI are very inhomogeneously distributed in the cathode sheet. This leads to relatively tortuous paths for the ionic transport and produces large fractions of CAM particles that are completely secluded from the LPSI particles. Thus, to obtain a more homogenous distribution of SE and CAM inside the cathode sheet, the composite was carefully ball-milled prior to its addition to the binder solution. The improved result is shown in Fig. S4b. Clearly, the LPSI particles are significantly smaller (average size <5 µm) and more homogenously distributed within the cathode sheet. β-LPS, on the other hand, with only slightly smaller but very porous secondary particles, is extremely moldable. As a consequence, it is

capable of much more intimately contacting the CAM, even without involving a previous ball-milling step (Fig. 4.S4c).

LPSI sheets served as separator to keep not only the In anode, but also the SE separator identical for both samples. As demonstrated by impedance measurements, the LPSI–*β*-LPS interface in the ASSB with the LPSI-based cathode does not lead to additional interfacial impedances (Fig. 4.S5). The performance differences of the two batteries can therefore be attributed exclusively to the cathodes.

4.3.2 Morphological analysis

4.3.2.1 Physical reconstruction

The differences in the morphology of the SE particles influence the 3D microstructure of the composite electrodes and, therefore, the battery performance. The shape of the SE affects the entire cathode morphology, with a particularly noteworthy impact on Li-ion transport pathways in the SE, the actual contact area between SE and CAM, and the distribution of (undesirable) voids. To investigate more closely the impact of SE morphology on the microstructure of the prepared cathodes, representative sections of both samples were physically reconstructed using FIB-SEM tomography. Fig. 4.2 visualizes the complete volumes reconstructed in the course of our investigations.

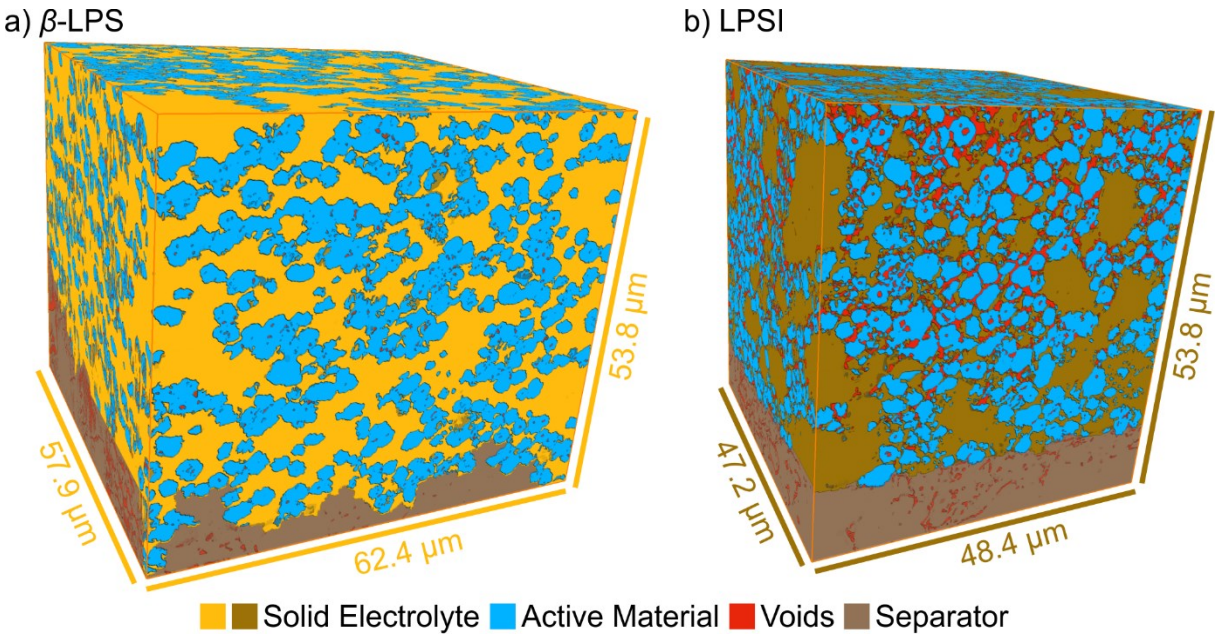

Fig. 4.2. Visualization of the two reconstructed NMC cathodes, with a) β-LPS (volume: $1.9 \cdot 10^5$ µm^3) and b) LPSI (volume: $1.2 \cdot 10^5$ µm^3) as the solid electrolyte.

To assess the accuracy of the reconstructions, the phase volume fractions were compared with values from the synthesis. Both cathodes were reconstructed over the entire cross-section, from the current collector to the separator on the bottom side. About 5 µm were then cut off on the top side, because a particularly large number of voids occurred there – a likely consequence of SE degradation due to the brief air contact during sample transfer to the FIB-SEM. By using the topology-sensitive Everhart–Thornley detector, voids could be detected with high accuracy without compromising the good material contrast between CAM and SE. For LPSI, contrast was further increased by applying a higher acceleration voltage of the scanning electron microscope. All three phases (CAM, SE, voids) could therefore be well segmented. However, the binder could not be identified as separate phase, because the difference in contrast to the SE was too small and thin layers cannot be resolved by SEM due to the chosen voxel resolution of $35.7 \times 35.7 \times 50$ nm^3. Table 4.1 compares the volume fractions of the different phases from the synthesis procedure and after the reconstruction process.

Table 4.1. Comparison of volume fractions in the synthesis and after reconstruction.[a]

	β-LPS		LPSI	
	Synthesis	Reconstruction	Synthesis	Reconstruction
CAM	46.3%	44.0%	49.3%	50.8%
SE	46.3%	55.0%	42.7%	38.5%
Binder	7.3%	–	8.0%	–
Voids	–	1.0%	–	10.7%

[a] The binder generally cannot be resolved due to its small feature size and poor contrast. However, for the nanocrystalline *β*-LPS, the binder and the SE interpenetrate each other and are therefore seen as one phase, overestimating the SE volume fraction.

The binder has no distinct morphology and rather builds a thin layer over available surfaces. It might help to relax mechanical strain due to the volume change of the CAM during cycling [30] and holds the phases together. During the preparation of the cathode films, the binder is first dissolved in the slurry. The average pore size of the mesoporous, secondary *β*-LPS-particles corresponds to ~28 nm [23], and the binder most likely collects predominantly in this extensive network once the slurry dries. As a consequence, both the solid components and the binder form an interpenetrating composite phase. Importantly, this phase cannot be further distinguished in the reconstruction. Thus, *β*-LPS and the binder are seen as one phase, which leads to a distinct overestimation of the SE volume fraction in the reconstruction. It explains the actual differences in SE volume fractions by ~9% between synthesis and reconstruction (Table 4.1). For the LPSI sample, on the other hand, the differences in feature size between SE, CAM, and voids are much smaller. Due to its larger particle size, LPSI offers less surface area to which the binder can adhere. Therefore, binder is most likely distributed equally over all interfaces and within the delimitable void space, where it remains as unresolved phase in the reconstruction. Moreover, a considerably larger fraction of voids is found when using LPSI (Table 4.1). This aspect is further examined below. The mechanical properties of both cathode films corroborate the proposed difference in binder distribution. Even though it contains virtually the same volume fraction of binder as the LPSI-based cathode film, the mechanical stability and elasticity of the *β*-LPS cathode film is considerably lower. A large amount of the binder collects inside the pores of the secondary *β*-LPS particles and therefore cannot support adhesion between SE

and CAM. In addition, larger pores (as for the LPSI-based cathode) might more effectively compensate for the bending of the sheets.

4.3.2.2 Distribution of voids

Void space in ASSBs is necessarily dead space. It makes Li-ion transport pathways in the SE more tortuous, prevents charge transfer reactions at the CAM surface, and lowers the overall volumetric energy density and the performance of the battery. In the literature, void contents of 13–15 vol% are usually reported for ASSBs [38,45], whereas only 3 vol% voids are observed for β-LPS [44]. Under pressure, β-LPS particles show a higher compressibility, which allows to better fill also smaller interstitial gaps at the CAM. Fig. 4.3a and 4.3b visualize the distribution of voids in both materials. It can be seen that the voids are indeed homogeneously distributed over both cathode volumes, without agglomeration in a particular region.

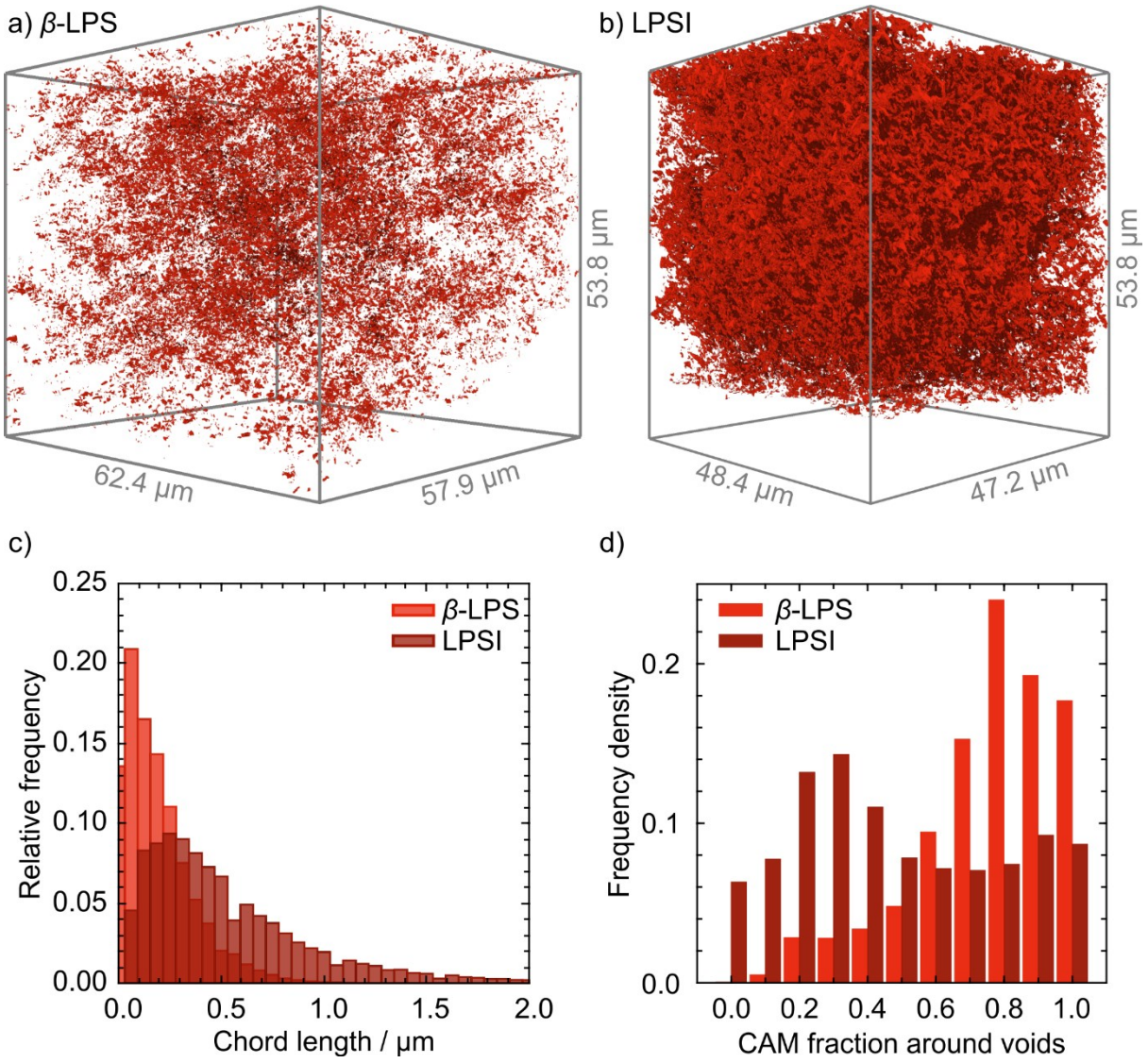

Fig. 4.3. Spatial distribution of voids in the samples with a) *β*-LPS and b) LPSI. The presentation does not include voids in the SE separator at the bottom. Voids are distributed uniformly and randomly over the cathodes. The *β*-LPS sample shows less voids throughout the reconstructed volume. The detection of voids is limited by the SEM resolution. c) Chord length distributions characterizing the voids in the two samples. The narrow distribution for *β*-LPS indicates many smaller, more uniform voids. d) Fraction of CAM around voids weighted by the void size. A fraction of zero indicates that the void is completely surrounded by SE, while unity signifies void within a CAM particle. Voids are mostly found at the interface with (or within) the CAM when using *β*-LPS. For LPSI, voids are mainly seen between secondary SE particles and at the interface to the CAM.

In Fig. 4.3c, we show results from using chord length distribution (CLD) analysis to characterize the size distribution of the voids. In general, chords measure distances between two interfaces, which are set apart by a homogenous phase [73–75]. CLD analysis proceeds along the following steps: First, seed points are randomly placed in the homogeneous phase of interest (here, inside the voids); from each point, vectors are then projected in angularly equispaced directions until they hit an interface (here, with CAM or SE); finally, chord lengths are extracted as the sum of the absolute lengths of a pair of opposed vectors and collected into a histogram (the CLD). This methodology is applicable to all multiphase materials, because no assumptions about size and shape of the analyzed phase are made. Voids in the *β*-LPS cathode are characterized by a mean chord length of 230 nm. In the LPSI electrolyte, the mean value is 518 nm and comes with an overall broader distribution. The dense, secondary LPSI particles are larger and more rigid than the *β*-LPS particles and thus less capable of adapting their shape in order to fill void space, even at the high pressure of 294 MPa applied for compaction.

The location of voids was analyzed to elucidate if they predominantly hinder the electronic transport within the CAM network, the charge transfer at the CAM–SE interface, or Li-ion transport in the SE. For that purpose, the surroundings of the voids were analyzed. The fraction of CAM voxels at the solid–void interface was calculated and collected into a histogram, weighted by void size. A ratio of 0.5 indicates a void surrounded to 50% by CAM and to 50% by SE. Fig. 4.3d compares the fractions for both cathodes. Void surroundings differ significantly for the two cathodes. In the *β*-LPS-based cathode, the fraction tends towards unity. Voids are mostly located in the CAM network or at the interface between CAM and SE (where they are still mostly surrounded by CAM). This likely originates in the preparation of the CAM, which consists of spherically agglomerated primary particles (cf. Fig. 4.S6). The LPSI-based cathode contains the same CAM. The number of closed pores within the CAM should therefore be very similar. In addition to those voids, many voids are observed in the LPSI and at its interface with the CAM. LPSI is therefore more prone to void formation in the SE phase, as also indicated by the higher overall void fraction (Table 4.1).

4.3.2.3 Analysis of the CAM surface area and particle network

The external surface of the CAM (A_{CAM}) defines the potential area for charge transfer reactions. Calculated surface-to-volume ratios ($A_{CAM}\,V_{CAM}^{-1}$) of the cathodes are provided in Table 4.2. A larger surface area is observed for the LPSI-based cathode, which indicates a greater amount of smaller CAM particles. This is due to the fact that this sample was additionally pretreated by ball milling. As a result, the CAM was partially crushed, as reflected by the higher population

of shorter chords in the CLD (Fig. 4.4b). The smaller particles lead to a larger surface area per volume of CAM. However, these small particles are often not connected to the CAM network, which will be shown in the next step. For Li-ion charge transfer, the CAM has to be in direct contact with SE. Therefore, the active surface $A_{CAM,active}$ is of higher relevance. The fraction of active surface to the total CAM surface ($A_{CAM,active}/A_{CAM}$) is lower for the LPSI-based cathode due to the existence of more voids at the CAM–LPSI interface. For β-LPS, $A_{CAM,active}/A_{CAM}$ is 43% larger compared to LPSI, in good agreement with the void analysis.

Table 4.2: Surface-to-volume ratio and ratio of active to overall surface area.

Sample	$A_{CAM}\ V_{CAM}^{-1}$ / µm^{-1}	$A_{CAM,active}\ A_{CAM}^{-1}$
β-LPS	4.16	0.87
LPSI	4.74	0.61

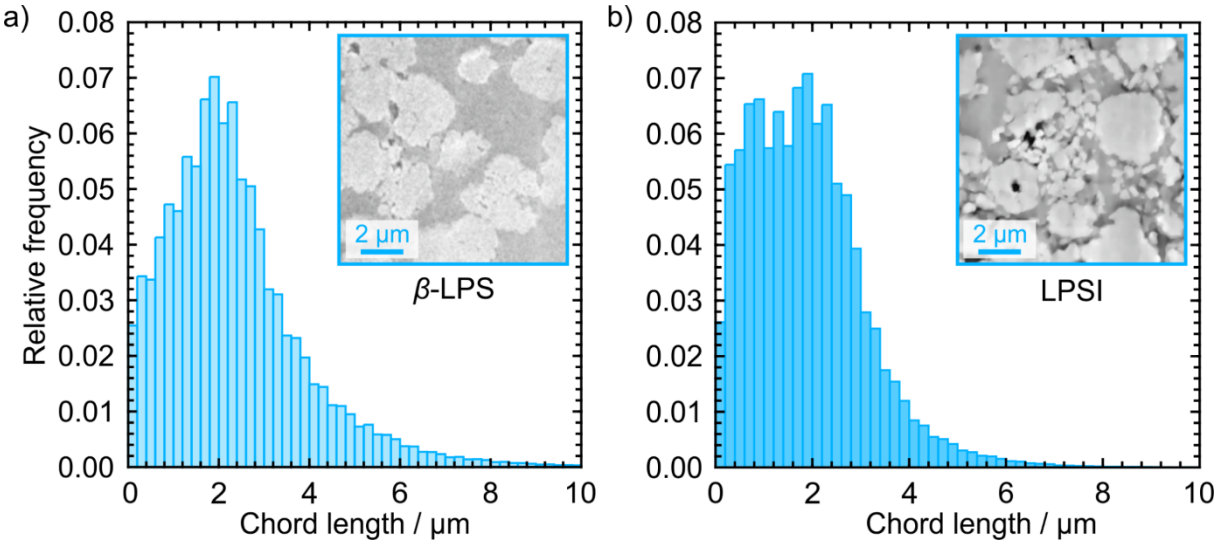

Fig. 4.4. Chord length distributions for the CAM particles in the samples with a) β-LPS and b) LPSI, providing mean chord lengths of 2.20 µm and 1.83 µm, respectively. Insets show parts of the greyscale SEM images of the reconstructed volumes. CAM particles in the LPSI sample are partially crushed due to the additional ball milling step during the preparation process. This leads to a narrower, bimodal distribution.

We now examine closer the connectivity of the CAM particles. Contact between the particles and between particles and the current collector ensures electronic conduction. It is of particular important, because no conductive carbon was added to the cathodes. We found that 99.7 and 99.6 vol% of CAM particles in the *β*-LPS- and LPSI-containing samples, respectively, belong to a single network. The CAM particles thus exhibit a highly interconnected and well-dispersed network that provides both a large surface area for charge transfer and many pathways available for electronic transport. The agglomerates formed by the particles are preserved in the films (cf. Fig. 4.S6). Interestingly, this holds for both investigated SEs. Fig. 4.5 highlights isolated CAM particles that are not part of the network (large particles observed at the edges of a reconstructed volume are still part of the main network through connections with neighboring volumes). The additional ball milling step likely causes the presence of many smaller, unconnected particles in the LPSI based cathode (Fig. 4.5b). However, the high overall degree of connectivity suggests that electronic conduction in the cathodes is guaranteed without limitations.

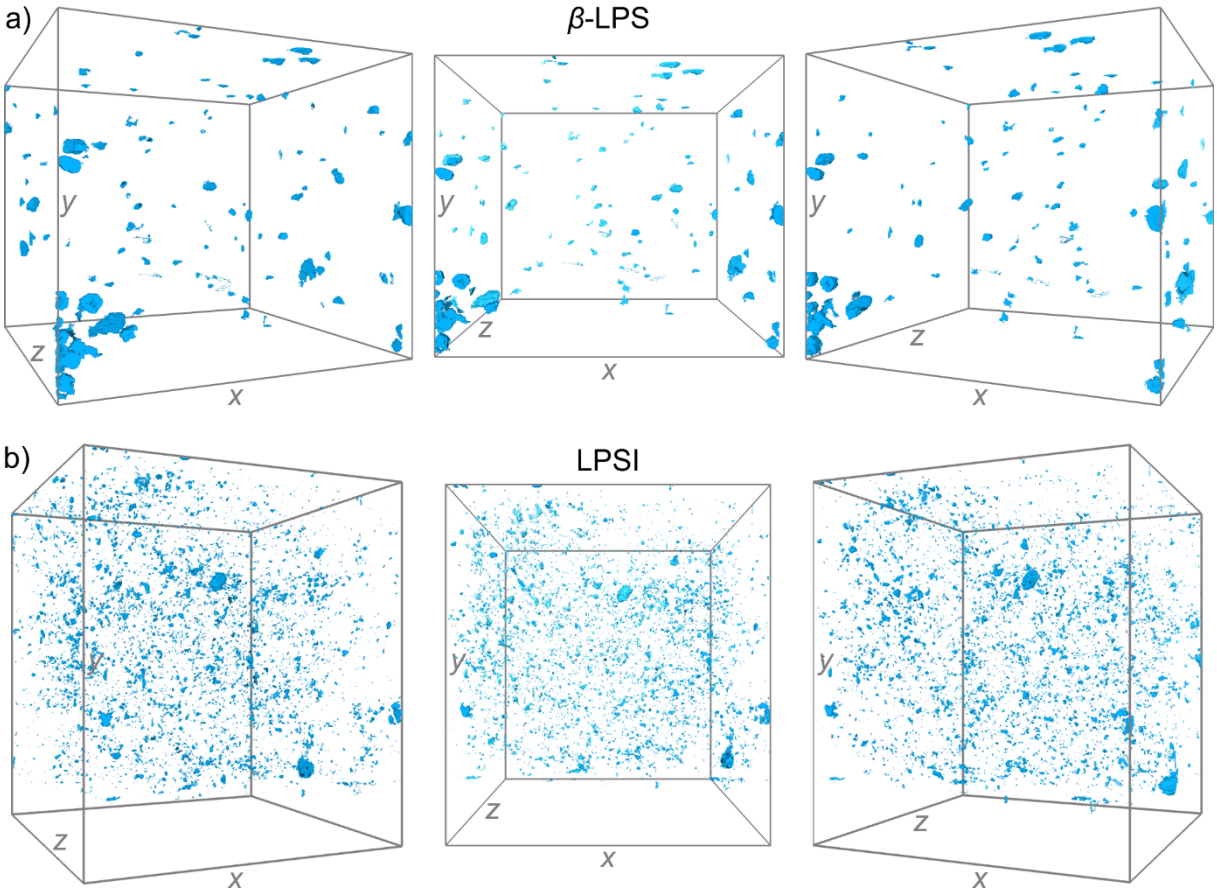

Fig. 4.5. Isolated CAM particles in the a) *β*-LPS and b) LPSI based samples shown from three different perspectives. The LPSI sample exhibits more isolated particles, which are also smaller

due to the secondary ball milling in the preparation procedure. However, unconnected material makes up only 0.3–0.4% of the total network volume of both samples.

4.3.3 Numerical transport simulations

In the next step, potential transport limitations arising from the SE morphology are investigated in more detail. The transport tortuosity for Li-ions τ_{Li^+} (cf. Eq. (4)) represents the impact of the SE morphology on diffusive transport compared to unhindered transport in the bulk electrolyte [76]. Bottlenecks, dead ends, and other constrictions affect Li-ion transport in the SE, causing a decrease of D_{eff} (increase of τ_{Li^+}), because macroscopic transport parameters like the effective diffusion coefficient D_{eff} sensitively depend on the microstructural heterogeneity, in addition to the volume fraction as the main parameter. To determine D_{eff} in the SE of the reconstructions, a RWPT technique [65,77] was employed (see Section 2 for further details). For this purpose, passive, pointlike tracers were randomly distributed in the SE and their random displacement determined at each time step. From that dynamics, a time-dependent diffusion coefficient could be recorded, which approached D_{eff} in the asymptotic (long-time) limit. τ_{Li^+} is then the ratio of the bulk diffusion coefficient D_{bulk} and this D_{eff}-value.

Fig. 4.S7 shows the evolution of the simulated transient diffusion coefficients normalized by D_{bulk} for the two SEs in the cathodes. Asymptotic values are reached, resulting in τ_{Li^+} values of 1.79 and 3.70 for β-LPS and LPSI, respectively. Because SE and binder are seen as one phase in the β-LPS reconstruction (Table 4.1), the SE volume fraction is overestimated in the simulation and the ionic tortuosity therefore driven to lower values. This could be important, as the tortuosity τ depends first and foremost on the porosity ε (here, SE volume fraction). However, based on tortuosity–porosity relationships for particulate materials [78], the actually observed difference in tortuosities (by a factor of more than two) cannot be explained by the overestimated β-LPS volume fraction. In particular, using the Weissberg equation, $\tau = 1 - p\ln(\varepsilon)$, with $p = 0.5$, the error caused by the overestimated porosity of $\varepsilon = 0.55$ in the reconstruction (versus 0.46 in the experiment, Table 4.1) leads to a downshift of the tortuosity by only 0.1. The Weissberg equation has been originally derived with $p = 0.5$ on a theoretical basis as lower bound for the diffusive tortuosity in the space between freely overlapping spheres [79]. This p-value has been closely matched using fixed and fluidized beds of spherical particles [80,81]. Indeed, the morphology of the CAM phase in Fig. 4.2a (with β-LPS as the SE) can be approximated by a model of freely overlapping particles. We conclude that the substantial difference in tortuosities between both cathodes (by a factor of more than two, i.e., 1.79 versus 3.70) can by far not be explained with the porosity error, which causes an upward correction to the τ_{Li^+} value of 1.79 by just ~0.1. The reason for the high tortuosity of the reconstructed LPSI

phase is the less favorable morphology of these SE particles, caused by the larger number of voids in the SE and at the interface to the CAM, a consequence of the poorer deformability of the LPSI particles.

The higher tortuosity for LPSI originates in the shape and size distribution of the SE particles. Even under pressure, the particles show a high mechanical stability and are not able to fill tightly into (especially finer) gaps. This leaves many voids in the cathode, which make Li-ion pathways more tortuous. β-LPS, on the other hand, fills the space around the CAM particles well, giving rise to only a few voids.

The ionic tortuosity values can in turn be used to calculate the ionic resistance R_{ion} of the battery cathodes as

$$R_{\mathrm{ion}} = \frac{\tau_{\mathrm{Li^+}} d}{\varepsilon_{\mathrm{SE}}\, \sigma} \tag{4.5}$$

with the electrode thickness d, the SE volume fraction $\varepsilon_{\mathrm{SE}}$, and the SE bulk conductivity σ [76]. The electrode thickness d is estimated from the physical reconstructions as 52 µm for β-LPS and as 45 µm for LPSI. The calculation leads to R_{ion}-values of 85 and 54 Ω cm^2 for β-LPS and LPSI, respectively. This is a key finding and shows that the actual differences in the individual morphologies (in particular, the difference in transport tortuosities by a factor of more than two) cannot compensate for the intrinsic bulk conductivity differences between LPSI and β-LPS. The higher ionic conductivity of LPSI thus overcompensates the less favorable morphology of the SE phase with respect to Li^+ transport in the SE phase.

4.3.4 Battery cycling

Fig. 4.6 compares the first charge and discharge curves for two ST batteries cycled at a C-rate of 0.1 C, with the CAM's theoretical capacity of 210 mAh g^{-1} as reference. It should be noted that both batteries used LPSI sheets as separator, so that they only differed regarding the composite cathodes. For the ST-type cells, two LPSI-sheets were used to prevent short-circuiting (Fig. 4.S8). The cell with the LPSI-based cathode sheet reached a first discharge capacity of 178 mAh g^{-1} at a mean overpotential of 55 mV. This, in turn, indicates an impeding effect of the added binder compared to the binder-free PT cell using LPSI (Fig. 4.S9), which reached 188 mAh g^{-1} at an overpotential of only 40 mV. On the other hand, the two cells incorporating β-LPS as SE exhibit discharge capacities of 150 and 156 mAh g^{-1}, respectively, at the same overpotential of 80 mV (Fig. 4.6 and Fig. 4.S9). The LPSI-based ST-cell

demonstrates a significantly better performance than the β-LPS-based ST-cell, despite the less favorable morphology of LPSI than β-LPS for its use as the SE phase.

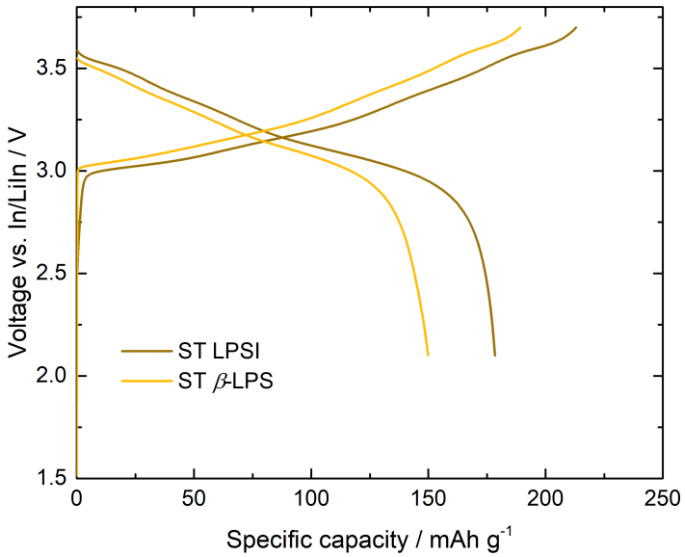

Fig. 4.6. Initial voltage profiles of ST cells (with β-LPS or LPSI as SE in the cathode composite) at a C-rate of 0.1 C.

4.3.5 Analysis of kinetic limitations

The results of the morphological analysis and transport simulations are now used to analyze the contributions of kinetic limitations in the cathode to the overall battery impedance. Electronic transport in the CAM network was shown to be uncritical, because the CAM particles are highly interconnected in both samples, most likely due to the achieved packing density and the small particle size (d_{50} = 3.5 µm), similar to a previous study [41].

In the framework of a transmission-line model (TLM), the impedance of the composite cathode with fast electronic transport can be written as [82]:

$$Z_{\mathrm{cathode}} = \sqrt{\frac{Z_{\mathrm{loc}} R_{\mathrm{ion}}}{a_{\mathrm{v}} l_{\mathrm{SE}}}} \cdot \coth\left(\sqrt{\frac{R_{\mathrm{ion}} a_{\mathrm{v}} l_{\mathrm{SE}}}{Z_{\mathrm{loc}}}}\right) \tag{4.6}$$

with

$$Z_{\mathrm{loc}} = \left(\left(R_{\mathrm{CT}} + \frac{\mathrm{d}U}{\mathrm{d}c_{\mathrm{CAM}}} Y_{\mathrm{CAM}} \right)^{-1} + i\omega C_{\mathrm{DL}} \right)^{-1} \tag{4.7}$$

and

$$Y_{\mathrm{CAM}} = \frac{r_{\mathrm{CAM}}}{F D_{\mathrm{CAM}}} \cdot \frac{\tanh\left(\sqrt{\frac{i\omega {r_{\mathrm{CAM}}}^2}{D_{\mathrm{CAM}}}} \right)}{\tanh\left(\sqrt{\frac{i\omega {r_{\mathrm{CAM}}}^2}{D_{\mathrm{CAM}}}} \right) - \sqrt{\frac{i\omega {r_{\mathrm{CAM}}}^2}{D_{\mathrm{CAM}}}}} \tag{4.8}$$

Here, Z_{loc} denotes the local impedance due to charge transfer at the CAM–SE interface and due to Li chemical diffusion in the CAM particles. $a_{\mathrm{v}} = \varepsilon_{\mathrm{CAM}} A_{\mathrm{CAM,active}} / V_{\mathrm{CAM}}$ is the active area of the CAM particles in contact with SE normalized by the electrode volume ($\varepsilon_{\mathrm{CAM}}$ denotes the volume fraction of the CAM, cf. Tables 4.1 and 4.2) and was found to be 1.59 µm^{-1} for *β*-LPS and 1.47 µm^{-1} for LPSI. $l_{\mathrm{SE}} = \tau_{\mathrm{Li^+}} d$ is the effective diffusion path length in the SE phase, R_{CT} the charge transfer resistance, $\mathrm{d}U/\mathrm{d}c_{\mathrm{CAM}}$ the dependence of electrode potential on Li concentration in the CAM (–26.1 Vcm^3 mol^{-1} for *β*-LPS and –24.7 Vcm^3 mol^{-1} for LPSI, as estimated from the cycling experiments), *i* the imaginary unit, *ω* the angular frequency, C_{DL} the double layer capacitance, r_{CAM} the mean radius of the CAM particles (~2.2 µm for *β*-LPS and ~1.8 µm for LPSI), *F* the Faraday constant, and D_{CAM} the Li chemical diffusion coefficient in the CAM particles. For Ni-rich NMC, D_{CAM} is about $7 \cdot 10^{-11}$ cm^{2}s^{-1} [83,84]. R_{ion} was determined in Section 3.3 as 85 and 54 Ω cm^2 for *β*-LPS and LPSI, respectively.

The total resistance of the batteries R_{bat} can be calculated from the overpotentials (80 mV for *β*-LPS and 55 mV for LPSI) found during the galvanostatic cycling experiments with a current density of 254 µA cm^{-2}. Values of 315 and 217 Ω cm^2 are obtained, respectively, for *β*-LPS and LPSI. The resistance of the interface between the In–Li anode and *β*-LPS has been reported as $R_{\mathrm{anode/SE}} \approx 10$ Ω cm^2 [85]. In the following, we assume that the resistance of the In/Li–LPSI interface exhibits a similar value, because the resistance of the Li–LPSI interface is also in the range of $R_{\mathrm{anode/SE}} \approx 10$ Ω cm^2 [86]. Furthermore, $R_{\mathrm{anode/SE}}$ is identical for both ASSBs. The resistance of the separator R_{sep} can be calculated from the LPSI conductivity and its thickness (~200 µm) as 25 Ω cm^2 for both samples.

Based on these values of resistances, we conclude that R_{ion} is small compared to $R_{\mathrm{cathode}} = R_{\mathrm{bat}} - R_{\mathrm{sep}} - R_{\mathrm{anode/SE}}$, so that we have to consider the limiting case of the TLM with $R_{\mathrm{ion}} < |Z_{\mathrm{loc}}|$. The zero-frequency limit $R^{\mathrm{zf}}_{\mathrm{cathode}}$ of the real part of the cathode impedance can then be expressed by a zero-frequency Taylor expansion of the coth function in Eq. (6) [87,88]:

$$R_{\mathrm{cathode}}^{\mathrm{zf}} = \frac{R_{\mathrm{ion}}}{3} + \frac{R_{\mathrm{CT}}}{a_{\mathrm{v}} l_{\mathrm{SE}}} - \frac{r_{\mathrm{ap}}}{5FD_{\mathrm{CAM}} a_{\mathrm{v}} l_{\mathrm{SE}}} \cdot \frac{\mathrm{d}U}{\mathrm{d}c_{\mathrm{CAM}}} = \frac{R_{\mathrm{ion}}}{3} + \frac{R_{\mathrm{local}}}{a_{\mathrm{v}} l_{\mathrm{SE}}} \tag{4.9}$$

The only unknown in this equation is the charge-transfer resistance R_{CT}. Consequently, we can use the resistance values given above together with Eq. (9) to derive profound estimates for the relative contributions of the different resistances to the overall battery resistance and to estimate the charge-transfer resistance R_{CT} (Table 4.3). Regarding the contributions to the effective local resistance $\frac{R_{\mathrm{local}}}{a_{\mathrm{v}} l_{\mathrm{SE}}}$, we find that the effective diffusive resistance $-\frac{r_{\mathrm{ap}}}{5FD_{\mathrm{CAM}} a_{\mathrm{v}} l_{\mathrm{SE}}} \cdot \frac{\mathrm{d}U}{\mathrm{d}c_{\mathrm{CAM}}}$ ($\approx$ 0.5–1 Ω cm^2) is very small compared to the effective charge transfer resistance $\frac{R_{\mathrm{CT}}}{a_{\mathrm{v}} l_{\mathrm{SE}}}$. The effective charge transfer resistance $\frac{R_{\mathrm{CT}}}{a_{\mathrm{v}} l_{\mathrm{SE}}}$ is clearly the dominating contribution to the overall battery resistance. The charge transfer resistance R_{CT} (normalized to the effective CAM–SE area) is similar for both cathodes and in the range of 40 kΩ cm^2. On the one hand, it is expected due to the similar chemical composition of both SEs. On the other hand, this is a strong indication that the coating of the CAM particles has not been damaged during the additional ball milling step for the CAM–LPSI cathode particle mixture. In the case of a coating damage, the electrolyte would have decomposed, leading to a strong increase of the charge transfer resistance [89]. The lower resistance of the LPSI-based cathode is thus mainly caused by the larger $a_{\mathrm{v}} l_{\mathrm{SE}}$-value, i.e., by the larger effective CAM–SE interfacial area with this cathode.

Table 4.3. Calculated/estimated resistances for the ASSBs obtained by using a transmission-line model for the composite cathodes.

	β-LPS-based cathode	LPSI-based cathode
R_{bat}	315 Ω cm^2	217 Ω cm^2
$R_{\mathrm{anode/SE}}$	≈ 10 Ω cm^2	≈ 10 Ω cm^2
R_{sep}	25 Ω cm^2	25 Ω cm^2
$R_{\mathrm{ion}}/3$	28 Ω cm^2	18 Ω cm^2
$a_{\mathrm{v}} l_{\mathrm{SE}}$	148	245

$-\frac{r_{\mathrm{ap}}}{5FD_{\mathrm{CAM}}}\cdot\frac{\mathrm{d}U}{\mathrm{d}c_{\mathrm{CAM}}}$	170 Ω cm^2	134 Ω cm^2
$-\frac{r_{\mathrm{ap}}}{5FD_{\mathrm{CAM}}a_{\mathrm{v}}l_{\mathrm{SE}}}\cdot\frac{\mathrm{d}U}{\mathrm{d}c_{\mathrm{CAM}}}$	1.1 Ω cm^2	0.5 Ω cm^2
$R_{\mathrm{CT}}/(a_{\mathrm{v}}l_{\mathrm{SE}})$	≈ 250 Ω cm^2	≈ 160 Ω cm^2
R_{CT}	≈ 37 kΩ cm^2	≈ 40 kΩ cm^2

4.4 Conclusions

Detailed morphological analyses of composite cathodes were conducted to elucidate kinetic limitations in two ST-ASSBs containing different sulfide-based SEs. The small NMC-85|05|10 particles form a highly interconnected and well dispersed network, which makes the electronic conduction uncritical and leads to a high discharge capacity of 178 mAh g^{-1} for the LPSI-based ST-ASSB. The larger SE particle size and larger number of voids result in a twofold higher ion transport tortuosity for LPSI. However, the fourfold higher bulk ionic conductivity of LPSI compared to β-LPS overcompensates its less favorable morphology in the cathode. Nonetheless, the use of small, soft, and nonporous SE particles appears promising to minimize ion transport limitations caused by unfavorable morphological features.

The analysis of individual contributions to the overall resistance of the ST-ASSBs provides a strong indication that the charge transfer resistance at the CAM–SE interface is the dominating resistance in the cathodes (and even within the complete batteries), whereas the resistances due to Li-ion transport in the SE phase and Li chemical diffusion in the CAM phase are considerably lower. Remarkably, the charge transfer resistance is similar for the CAM–SE interfaces in both cathodes ($R_{\mathrm{CT}} \approx 40$ kΩ cm^2). However, the larger effective CAM–SE interfacial area $a_{\mathrm{v}}l_{\mathrm{SE}}$ in the LPSI-based cathode leads to a lower effective charge transfer resistance $R_{\mathrm{CT}}/(a_{\mathrm{v}}l_{\mathrm{SE}})$ and thus to a lower overall battery resistance.

This study underscores the importance of quantitative morphological data for understanding kinetic limitations in ST-ASSBs. In particular, the optimization of the CAM–SE interface and a reduction of voids in the SE phase are important prerequisites for improving the performance of future ASSBs.

4.5 Supporting information

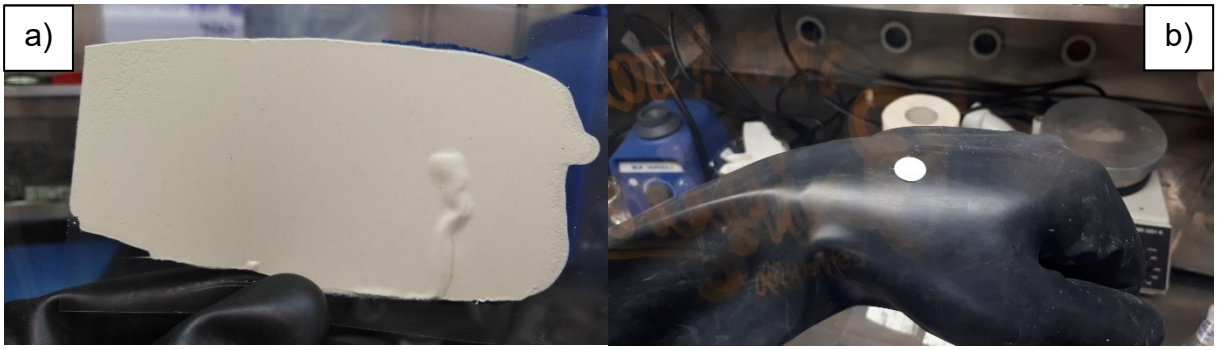

Fig. 4.S1. Images showing a) a slurry-cast and subsequently calendared film of LPSI/PIB and b) a separator disk (∅ = 10 mm) after punching out and delamination from its underlying polyester support.

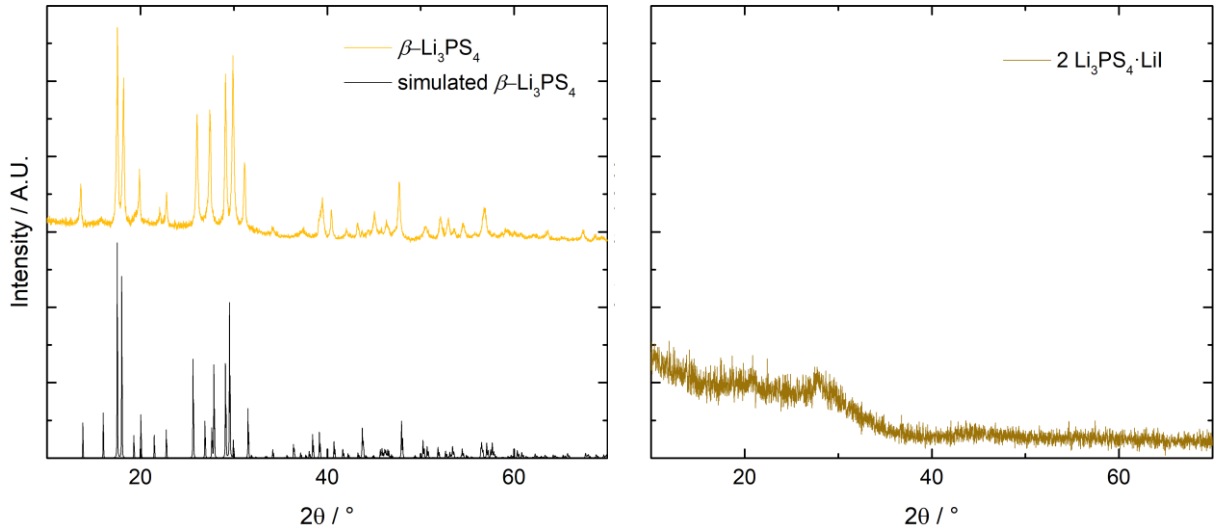

Fig. 4.S2. P-XRD pattern of β-Li_3PS_4 (left, with a simulated pattern) and 2 Li_3PS_4·LiI (right).

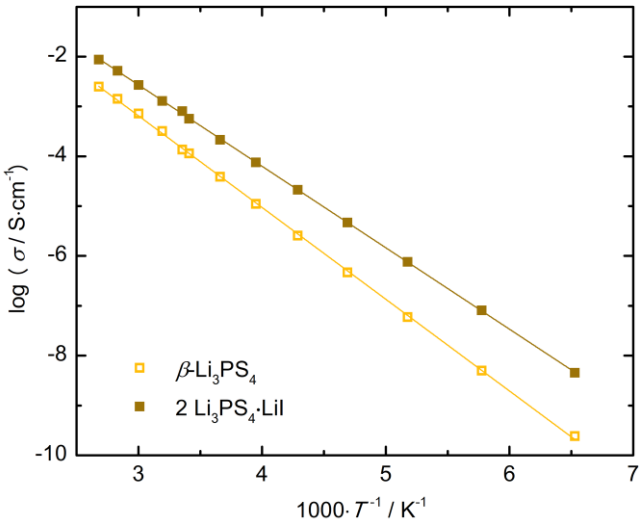

Fig. 4.S3. Arrhenius plots for the β-LPS and LPSI solid electrolyte powders.

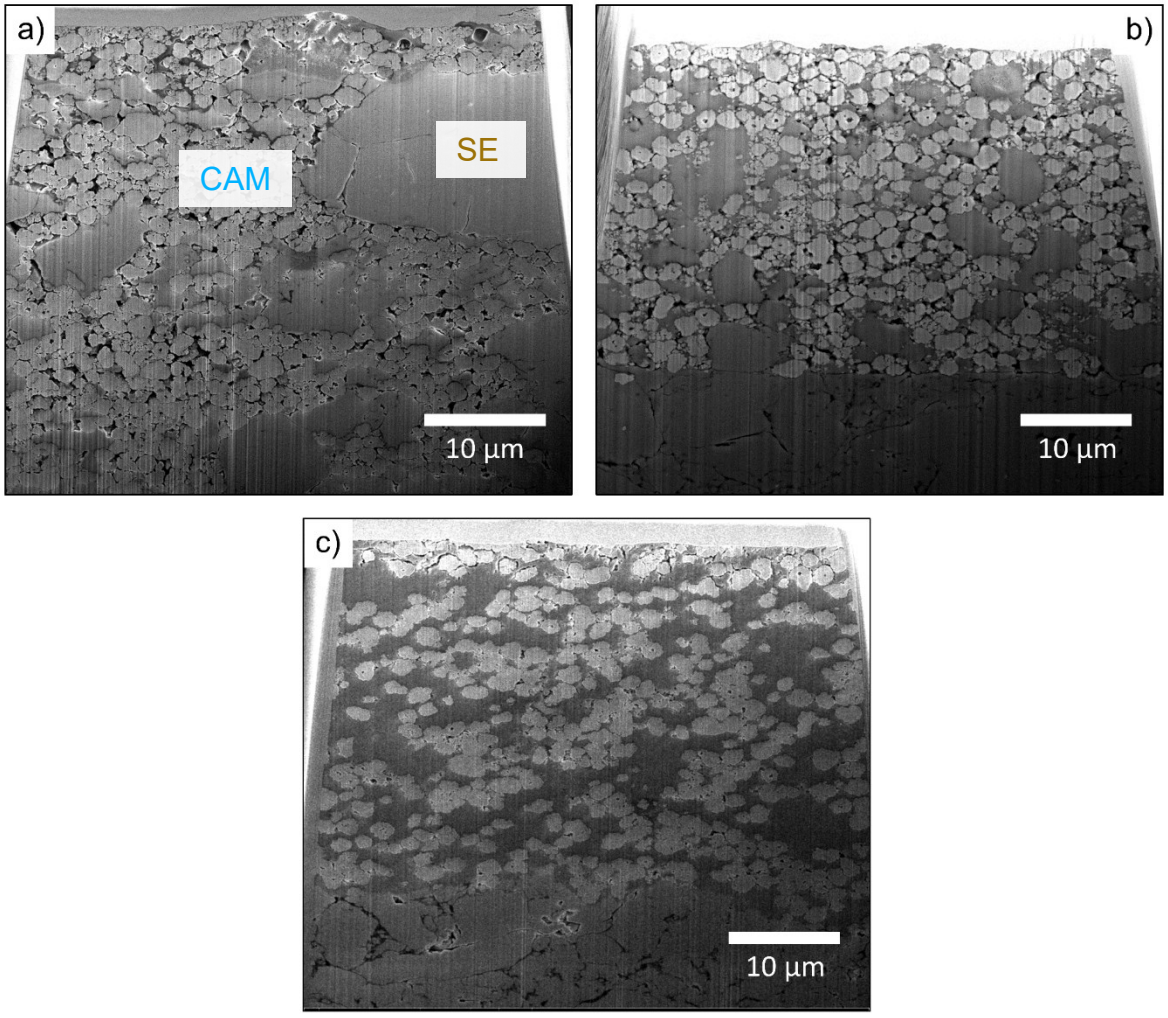

Fig. 4.S4. SEM images of slurry-cast cathode stacks prepared from a dry-mixed blend of LPSI and NMC, a) without previous ball-milling and b) with a previous ball-milling step. c) Slurry-cast cathode stack prepared from a dry-mixed blend of *β*-LPS and NMC.

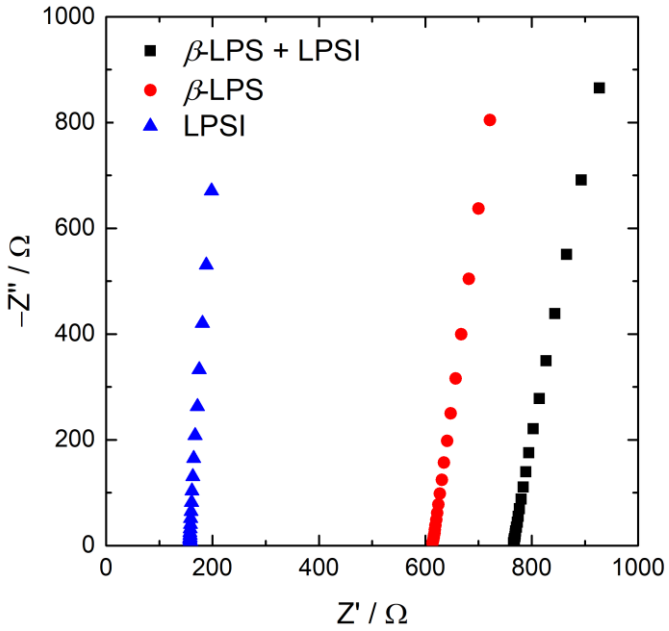

Fig. 4.S5. Nyquist plots of a pure *β*-LPS pellet and of the same pellet combined with an equally thick layer of LPSI. The data show that the LPSI–*β*-LPS interface does not lead to any additional interfacial impedances.

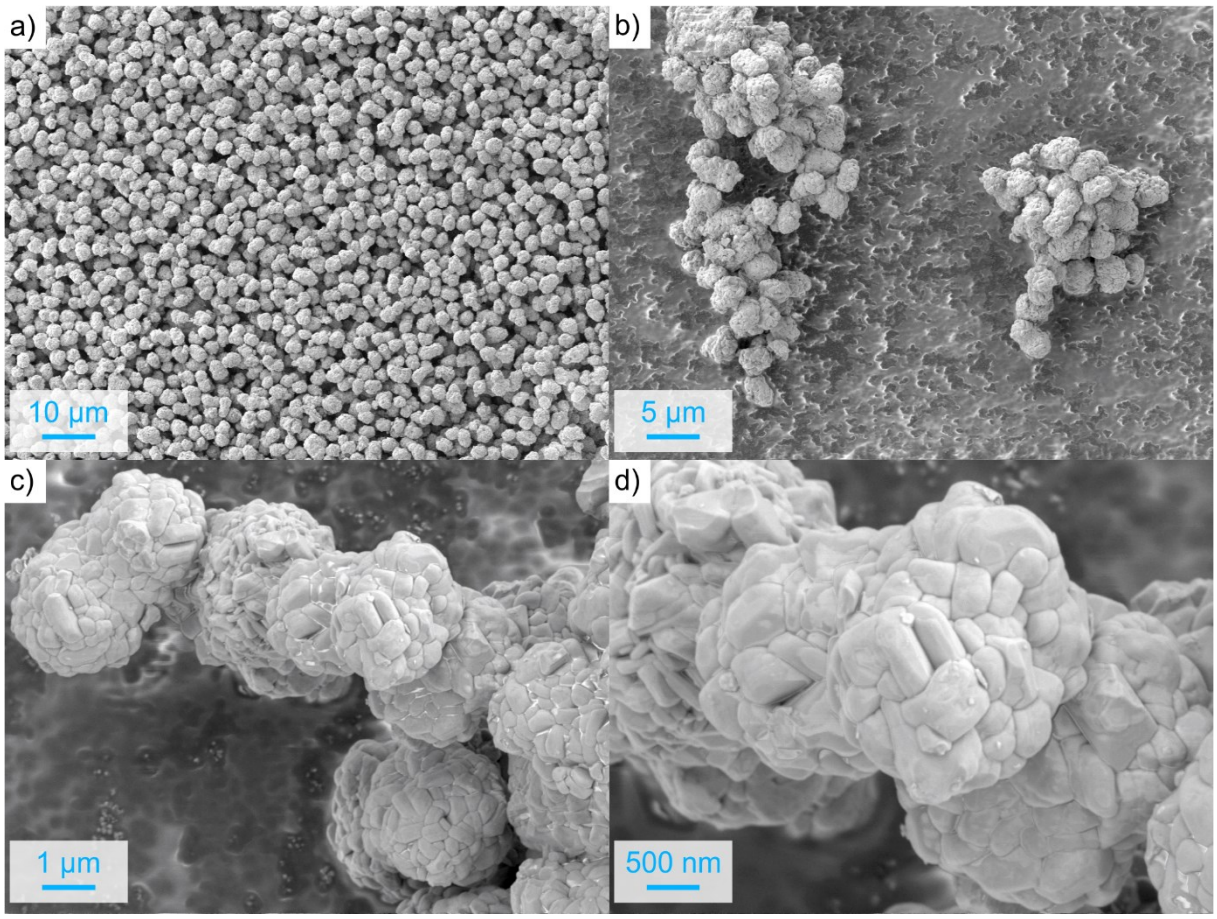

Fig. 4.S5. SEM images at different magnifications of CAM (NMC-85|05|10) used in this study. a, b) Spherical particles agglomerate forming a large network. c, d) Close-up view of the CAM particles, which are composed of small primary particles.

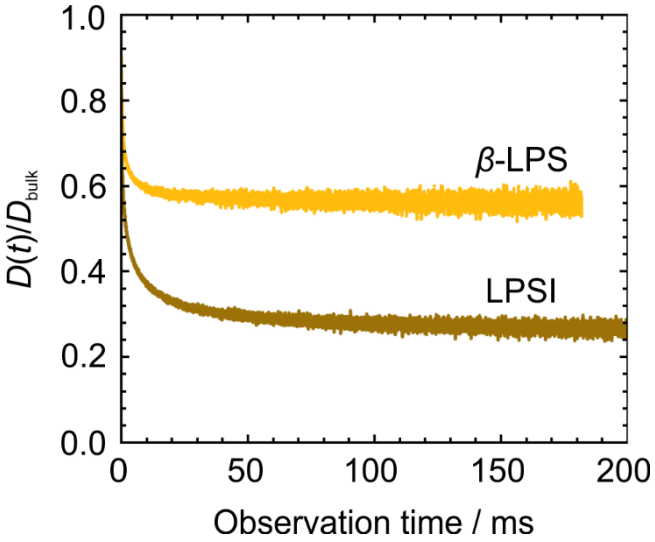

Fig. 4.S6. Transient diffusion coefficients $D(t)$ in the reconstructed SEs normalized by the bulk diffusivity D_{bulk}. Asymptotic (effective) values are reached at D_{eff}/D_{bulk} = 0.56 and 0.27 for □-LPS and LPSI, respectively. Note that the diffusive tortuosity τ discussed in the main text (cf. Eq. (4) and Chapter 3.3) is $\tau = D_{bulk}/D_{eff}$, i.e., the inverse of what is shown in the figure.

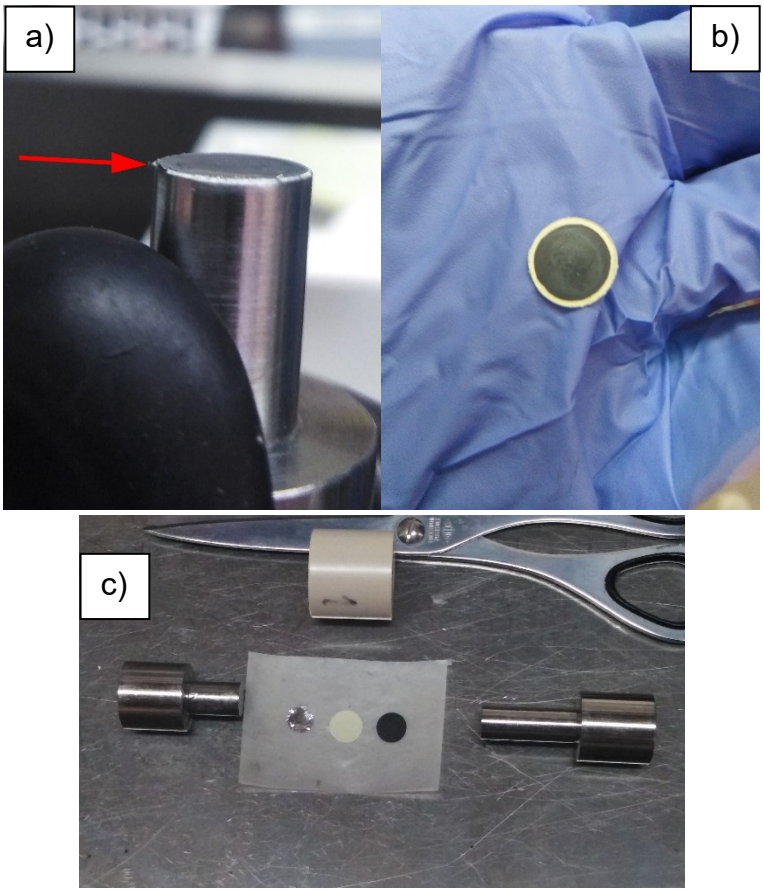

Fig. 4.S7. a) An image depicting the issue of short-circuiting when using equal diameters for the electrolyte separator layer and the cathode disk (∅ = 10 mm). b) Top-view onto a stack of two LPSI-sheet disks (∅ = 10 mm) as separator layer and a cathode disk (∅ = 9 mm) on top (the In anode is located below the LPSI-sheet layer and cannot be seen). c) All parts mentioned in b) before their assembly.

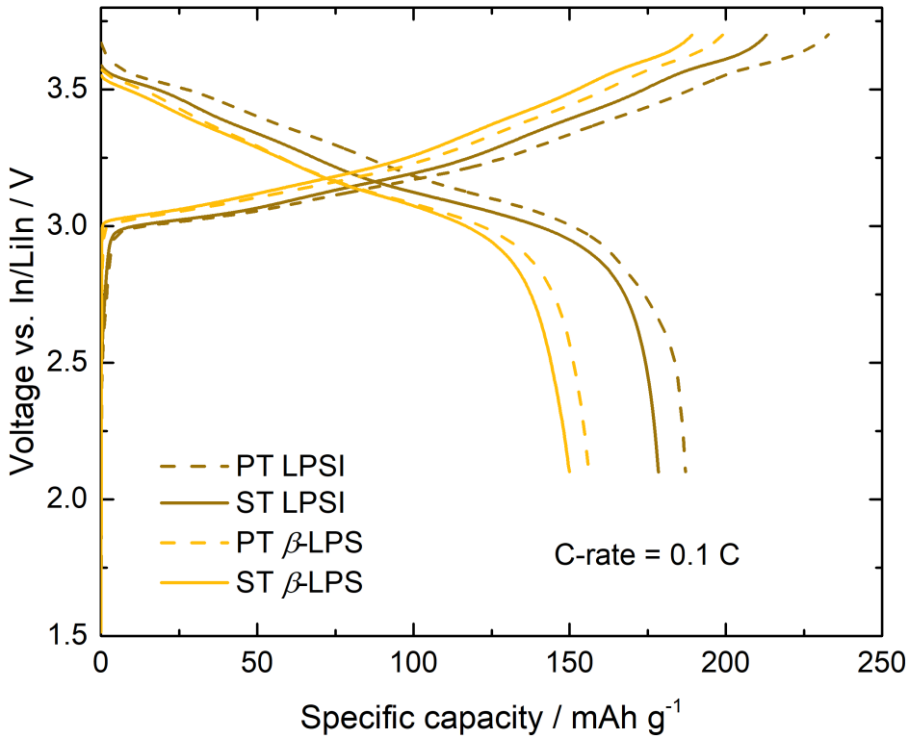

Fig. 4.S8. Initial voltage profiles of PT cells (dashed lines) and ST cells (solid lines – see Fig. 6 in the main text) using β-LPS or LPSI as SE in the cathode composite.

4.6 References

[1] J. Janek, W.G. Zeier, A solid future for battery development, Nat. Energy 1 (2016) 16141. https://doi.org/10.1038/nenergy.2016.141.

[2] J.G. Kim, B. Son, S. Mukherjee, N. Schuppert, A. Bates, O. Kwon, M.J. Choi, H.Y. Chung, S. Park, A review of lithium and non-lithium based solid state batteries, J. Power Sources 282 (2015) 299–322. https://doi.org/10.1016/j.jpowsour.2015.02.054.

[3] Y.-S. Hu, Batteries: Getting solid, Nat. Energy 1 (2016) 16042. https://doi.org/10.1038/nenergy.2016.42.

[4] A. Manthiram, X. Yu, S. Wang, Lithium battery chemistries enabled by solid-state electrolytes, Nat. Rev. Mater. 2 (2017) 16103. https://doi.org/10.1038/natrevmats.2016.103.

[5] C. Monroe, J. Newman, The impact of elastic deformation on deposition kinetics at lithium/polymer interfaces, J. Electrochem. Soc. 152 (2005) A396–A404. https://doi.org/10.1149/1.1850854.

[6] T. Ates, M. Keller, J. Kulisch, T. Adermann, S. Passerini, Development of an all-solid-state lithium battery by slurry-coating procedures using a sulfidic electrolyte, Energy Storage Mater. 17 (2019) 204–210. https://doi.org/10.1016/j.ensm.2018.11.011.

[7] R. Wagner, G.J. Redhammer, D. Rettenwander, A. Senyshyn, W. Schmidt, M. Wilkening, G. Amthauer, Crystal structure of garnet-related Li-ion conductor $Li_{7-3x}Ga_xLa_3Zr_2O_{12}$: Fast Li-ion conduction caused by a different cubic modification?, Chem. Mater. 28 (2016) 1861–1871. https://doi.org/10.1021/acs.chemmater.6b00038.

[8] D.Y. Oh, Y.J. Nam, K.H. Park, S.H. Jung, K.T. Kim, A.R. Ha, Y.S. Jung, Slurry-fabricable Li^+-conductive polymeric binders for practical all-solid-state lithium-ion batteries enabled by solvate ionic liquids, Adv. Energy Mater. (2019) 1802927. https://doi.org/10.1002/aenm.201802927.

[9] T. Famprikis, P. Canepa, J.A. Dawson, M.S. Islam, C. Masquelier, Fundamentals of inorganic solid-state electrolytes for batteries, Nat. Mater. 18 (2019) 1278–1291. https://doi.org/10.1038/s41563-019-0431-3.

[10] L. Zhou, K.H. Park, X. Sun, F. Lalère, T. Adermann, P. Hartmann, L.F. Nazar, Solvent-engineered design of argyrodite Li_6PS_5X (X = Cl, Br, I) solid electrolytes with high ionic

conductivity, ACS Energy Lett. 4 (2019) 265–270. https://doi.org/10.1021/acsenergylett.8b01997.

[11] M. Duchardt, U. Ruschewitz, S. Adams, S. Dehnen, B. Roling, Vacancy-controlled Na^+ superion conduction in $Na_{11}Sn_2PS_{12}$, Angew. Chem. Int. Ed. 57 (2018) 1351–1355. https://doi.org/10.1002/anie.201712769.

[12] M.A. Kraft, S. Ohno, T. Zinkevich, R. Koerver, S.P. Culver, T. Fuchs, A. Senyshyn, S. Indris, B.J. Morgan, W.G. Zeier, Inducing high ionic conductivity in the lithium superionic argyrodites $Li_{6+x}P_{1-x}Ge_xS_5I$ for all-solid-state batteries, J. Am. Chem. Soc. 140 (2018) 16330–16339. https://doi.org/10.1021/jacs.8b10282.

[13] L. Zhou, A. Assoud, Q. Zhang, X. Wu, L.F. Nazar, A new family of argyrodite thioantimonate lithium superionic conductors, J. Am. Chem. Soc. 141 (2019) 19002–19013. https://doi.org/10.1021/jacs.9b08357.

[14] N. Kamaya, K. Homma, Y. Yamakawa, M. Hirayama, R. Kanno, M. Yonemura, T. Kamiyama, Y. Kato, S. Hama, K. Kawamoto, A. Mitsui, A lithium superionic conductor, Nat. Mater. 10 (2011) 682–686. https://doi.org/10.1038/nmat3066.

[15] J. Wu, L. Shen, Z. Zhang, G. Liu, Z. Wang, D. Zhou, H. Wan, X. Xu, X. Yao, All-solid-state lithium batteries with sulfde electrolytes and oxide cathodes, Electrochem. Energy Rev. 4 (2020) 101–135. https://doi.org/10.1007/s41918-020-00081-4.

[16] G. Peng, X. Yao, H. Wan, B. Huang, J. Yin, F. Ding, X. Xu, Insights on the fundamental lithium storage behavior of all-solid-state lithium batteries containing the $LiNi_{0.8}Co_{0.15}Al_{0.05}O_2$ cathode and sulfide electrolyte, J. Power Sources 307 (2016) 724–730. https://doi.org/10.1016/j.jpowsour.2016.01.039.

[17] J. Wu, S. Liu, F. Han, X. Yao, C. Wang, Lithium/sulfide all-solid-state batteries using sulfide electrolytes, Adv. Mater. 33 (2021) 2000751. https://doi.org/10.1002/adma.202000751.

[18] A. Miura, N.C. Rosero-Navarro, A. Sakuda, K. Tadanaga, N.H.H. Phuc, A. Matsuda, N. Machida, A. Hayashi, M. Tatsumisago, Liquid-phase syntheses of sulfide electrolytes for all-solid-state lithium battery, Nat. Rev. Chem. 3 (2019) 189–198. https://doi.org/10.1038/s41570-019-0078-2.

[19] S. Spannenberger, V. Miß, E. Klotz, J. Kettner, M. Cronau, A. Ramanayagam, F. di Capua, M. Elsayed, R. Krause-Rehberg, M. Vogel, B. Roling, Annealing-induced

vacancy formation enables extraordinarily high Li^+ ion conductivity in the amorphous electrolyte 0.33 LiI + 0.67 Li_3PS_4, Solid State Ionics 341 (2019) 115040. https://doi.org/10.1016/j.ssi.2019.115040.

[20] A. Hayashi, K. Noi, A. Sakuda, M. Tatsumisago, Superionic glass-ceramic electrolytes for room-temperature rechargeable sodium batteries, Nat. Commun. 3 (2012) 856. https://doi.org/10.1038/ncomms1843.

[21] M. Wang, J. Sakamoto, Correlating the interface resistance and surface adhesion of the Li metal-solid electrolyte interface, J. Power Sources 377 (2018) 7–11. https://doi.org/10.1016/j.jpowsour.2017.11.078.

[22] H. Deiseroth, S. Kong, H. Eckert, J. Vannahme, C. Reiner, T. Zaiß, M. Schlosser, Li_6PS_5X: A class of crystalline Li-rich solids with an unusually high Li^+ mobility, Angew. Chem. Int. Ed. 47 (2008) 755–758. https://doi.org/10.1002/anie.200703900.

[23] Z. Liu, W. Fu, E.A. Payzant, X. Yu, Z. Wu, N.J. Dudney, J. Kiggans, K. Hong, A.J. Rondinone, C. Liang, Anomalous high ionic conductivity of nanoporous β-Li_3PS_4, J. Am. Chem. Soc. 135 (2013) 975–978. https://doi.org/10.1021/ja3110895.

[24] T. Shi, Q. Tu, Y. Tian, Y. Xiao, L.J. Miara, O. Kononova, G. Ceder, High active material loading in all-solid-state battery electrode via particle size optimization, Adv. Energy Mater. 10 (2020) 1902881. https://doi.org/10.1002/aenm.201902881.

[25] D. Prutsch, B. Gadermaier, H. Brandstätter, V. Pregartner, B. Stanje, Wohlmuth Dominik, V. Epp, D. Rettenwander, I. Hanzu, H.M.R. Wilkening, Nuclear spin relaxation in nanocrystalline β-$L_{i3}PS_4$ reveals low-dimensional Li diffusion in an isotropic matrix, Chem. Mater. 30 (2018) 7575−7586.

[26] M. Duchardt, M. Diels, B. Roling, S. Dehnen, Flow-oriented synthesis of Li_2S and Li_3PS_4·3THF: Opening up a completely solvent-based solid electrolyte value chain, ACS Appl. Energy Mater. 3 (2020) 6937–6945. https://doi.org/10.1021/acsaem.0c01007.

[27] P. Bron, S. Johansson, K. Zick, J. Schmedt auf der Günne, S. Dehnen, B. Roling, $Li_{10}SnP_2S_{12}$: An affordable lithium superionic conductor., J. Am. Chem. Soc. 135 (2013) 15694–15697. https://doi.org/10.1021/ja407393y.

[28] K.H. Park, D.Y. Oh, Y.E. Choi, Y.J. Nam, L. Han, J.Y. Kim, H. Xin, F. Lin, S.M. Oh, Y.S. Jung, Solution-processable glass LiI-Li_4SnS_4 superionic conductors for all-solid-

state Li-ion batteries, Adv. Mater. 28 (2016) 1874–1883. https://doi.org/10.1002/adma.201505008.

[29] D.H. Kim, D.Y. Oh, K.H. Park, Y.E. Choi, Y.J. Nam, H.A. Lee, S.-M. Lee, Y.S. Jung, Infiltration of solution-processable solid electrolytes into conventional Li-ion-battery electrodes for all-solid-state Li-ion batteries, Nano Lett. 17 (2017) 3013−3020. https://doi.org/10.1021/acs.nanolett.7b00330.

[30] N. Riphaus, P. Strobl, B. Stiaszny, T. Zinkevich, M. Yavuz, J. Schnell, S. Indris, H.A. Gasteiger, S.J. Sedlmaier, Slurry-based processing of solid electrolytes: A comparative binder study, J. Electrochem. Soc. 165 (2018) A3993–A3999. https://doi.org/10.1149/2.0961816jes.

[31] N. Riphaus, B. Stiaszny, H. Beyer, S. Indris, H.A. Gasteiger, S.J. Sedlmaier, Understanding chemical stability issues between different solid electrolytes in all-solid-state batteries, J. Electrochem. Soc. 166 (2019) A975–A983. https://doi.org/10.1149/2.0351906jes.

[32] K.H. Park, Q. Bai, D.H. Kim, D.Y. Oh, Y. Zhu, Y. Mo, Y.S. Jung, Design strategies, practical considerations, and new solution processes of sulfide solid electrolytes for all-solid-state batteries, Adv. Energy Mater. 8 (2018) 1800035. https://doi.org/10.1002/aenm.201800035.

[33] J. Schnell, T. Günther, T. Knoche, C. Vieider, L. Köhler, A. Just, M. Keller, S. Passerini, G. Reinhart, All-solid-state lithium-ion and lithium metal batteries – paving the way to large-scale production, J. Power Sources 382 (2018) 160–175. https://doi.org/10.1016/j.jpowsour.2018.02.062.

[34] J. Zhang, H. Zhong, C. Zheng, Y. Xia, C. Liang, H. Huang, Y. Gan, X. Tao, W. Zhang, All-solid-state batteries with slurry coated $LiNi_{0.8}Co_{0.1}Mn_{0.1}O_2$ composite cathode and Li_6PS_5Cl electrolyte: Effect of binder content, J. Power Sources 391 (2018) 73–79. https://doi.org/10.1016/j.jpowsour.2018.04.069.

[35] R. Koerver, W. Zhang, L. de Biasi, S. Schweidler, A.O. Kondrakov, S. Kolling, T. Brezesinski, P. Hartmann, W.G. Zeier, J. Janek, Chemo-mechanical expansion of lithium electrode materials – on the route to mechanically optimized all-solid-state batteries, Energy Environ. Sci. 11 (2018) 2142–2158. https://doi.org/10.1039/C8EE00907D.

[36] A. Bielefeld, D.A. Weber, J. Janek, Microstructural modeling of composite cathodes for all-solid-state batteries, J. Phys. Chem. C 123 (2019) 1626–1634. https://doi.org/10.1021/acs.jpcc.8b11043.

[37] A. Bielefeld, D.A. Weber, J. Janek, Modeling effective ionic conductivity and binder influence in composite cathodes for all-solid-state batteries, ACS Appl. Mater. Interfaces 12 (2020) 12821–12833. https://doi.org/10.1021/acsami.9b22788.

[38] D. Hlushkou, A.E. Reising, N. Kaiser, S. Spannenberger, S. Schlabach, Y. Kato, B. Roling, U. Tallarek, The influence of void space on ion transport in a composite cathode for all-solid-state batteries, J. Power Sources 396 (2018) 363–370. https://doi.org/10.1016/j.jpowsour.2018.06.041.

[39] F. Strauss, D. Stepien, J. Maibach, L. Pfaffmann, S. Indris, P. Hartmann, T. Brezesinski, Influence of electronically conductive additives on the cycling performance of argyrodite-based all-solid-state batteries, RSC Adv. 10 (2019) 1114–1119. https://doi.org/10.1039/c9ra10253a.

[40] A. Sakuda, K. Kuratani, M. Yamamoto, M. Takahashi, All-solid-state battery electrode sheets prepared by a slurry, J. Electrochem. Soc. 164 (2017) A2474–A2478. https://doi.org/10.1149/2.0951712jes.

[41] F. Strauss, T. Bartsch, L. De Biasi, A.Y. Kim, J. Janek, P. Hartmann, T. Brezesinski, Impact of cathode material particle size on the capacity of bulk-type all-solid-state batteries, ACS Energy Lett. 3 (2018) 992–996. https://doi.org/10.1021/acsenergylett.8b00275.

[42] X. Wu, J. Billaud, I. Jerjen, F. Marone, Y. Ishihara, M. Adachi, Y. Adachi, C. Villevieille, Y. Kato, Operando visualization of morphological dynamics in all-solid-state batteries, Adv. Energy Mater. 9 (2019) 1901547. https://doi.org/10.1002/aenm.201901547.

[43] A. Neumann, S. Randau, K. Becker-Steinberger, T. Danner, S. Hein, Z. Ning, J. Marrow, F.H. Richter, J. Janek, A. Latz, Analysis of interfacial effects in all-solid-state batteries with thiophosphate solid electrolytes, ACS Appl. Mater. Interfaces 12 (2020) 9277–9291. https://doi.org/10.1021/acsami.9b21404.

[44] T. Shi, Y. Zhang, G. Ceder, Q. Tu, Y. Wang, M.C. Scott, Characterization of mechanical degradation in an all-solid-state battery cathode, J. Mater. Chem. A 8 (2020) 17399–17404. https://doi.org/10.1039/d0ta06985j.

[45] S. Choi, M. Jeon, J. Ahn, W.D. Jung, S.M. Choi, J.S. Kim, J. Lim, Y.J. Jang, H.G. Jung, J.H. Lee, B.I. Sang, H. Kim, Quantitative analysis of microstructures and reaction Interfaces on composite cathodes in all-solid-state batteries using a three-dimensional reconstruction technique, ACS Appl. Mater. Interfaces 10 (2018) 23740–23747. https://doi.org/10.1021/acsami.8b04204.

[46] M. Park, H.G. Jung, W.D. Jung, S.Y. Cho, B.N. Yun, Y.S. Lee, S. Choi, J. Ahn, J. Lim, J.Y. Sung, Y.J. Jang, J.P. Ahn, J.H. Lee, H. Kim, Chemically evolved composite lithium-ion conductors with lithium thiophosphates and nickel sulfides, ACS Energy Lett. 2 (2017) 1740–1745. https://doi.org/10.1021/acsenergylett.7b00497.

[47] T. Müllner, A. Zankel, F. Svec, U. Tallarek, Finite-size effects in the 3D reconstruction and morphological analysis of porous polymers, Mater. Today 17 (2014) 404–411. https://doi.org/10.1016/j.mattod.2014.07.003.

[48] W. Zhang, T. Leichtweiss, S. Culver, R. Koerver, D. Das, D.A. Weber, W.G. Zeier, J. Janek, The detrimental effects of carbon additives in solid-state batteries using $Li_{10}GeP_2S_{12}$ as solid electrolyte, ACS Appl. Mater. Interfaces 9 (2017) 35888–35896. https://doi.org/10.1021/acsami.7b11530.

[49] W. Zhang, D.A. Weber, H. Weigand, T. Arlt, I. Manke, D. Schröder, R. Koerver, T. Leichtweiss, P. Hartmann, W.G. Zeier, J. Janek, Interfacial processes and influence of composite cathode microstructure controlling the performance of all-solid-state lithium batteries, ACS Appl. Mater. Interfaces 9 (2017) 17835−17845. https://doi.org/10.1021/acsami.7b01137.

[50] R. Koerver, I. Aygün, T. Leichtweiß, C. Dietrich, W. Zhang, J.O. Binder, P. Hartmann, W.G. Zeier, J. Janek, Capacity fade in solid-state batteries: Interphase formation and chemomechanical processes in nickel-rich layered oxide cathodes and lithium thiophosphate solid electrolytes, Chem. Mater. 29 (2017) 5574–5582. https://doi.org/10.1021/acs.chemmater.7b00931.

[51] F. Walther, R. Koerver, T. Fuchs, S. Ohno, J. Sann, M. Rohnke, W.G. Zeier, J. Janek, Visualization of the interfacial decomposition of composite cathodes in argyrodite-based all-solid-state batteries using time-of-flight secondary-ion mass spectrometry, Chem. Mater. 31 (2019) 3745–3755. https://doi.org/10.1021/acs.chemmater.9b00770.

[52] F. Walther, S. Randau, Y. Schneider, J. Sann, M. Rohnke, F.H. Richter, W.G. Zeier, J. Janek, On the influence of carbon additives on the decomposition pathways in

thiophosphate-based all-solid-state batteries, Chem. Mater. 32 (2020) 6123–6136. https://doi.org/10.1021/acs.chemmater.0c01825.

[53] R. Koerver, F. Walther, I. Aygün, J. Sann, C. Dietrich, W. Zeier, J. Janek, Redox-active cathode interphases in solid-state batteries, J. Mater. Chem. A 5 (2017) 22750–22760. https://doi.org/10.1039/C7TA07641J.

[54] A.-Y. Kim, F. Strauss, T. Bartsch, J.H. Teo, T. Hatsukade, A. Mazilkin, J. Janek, P. Hartmann, T. Brezesinski, The stabilizing effect of a hybrid surface coating on Ni-rich NCM cathode material in all-solid-state batteries, Chem. Mater. 31 (2019) 9664–9672. https://doi.org/10.1021/acs.chemmater.9b02947.

[55] J. Schindelin, I. Arganda-Carreras, E. Frise, V. Kaynig, M. Longair, T. Pietzsch, S. Preibisch, C. Rueden, S. Saalfeld, B. Schmid, J.Y. Tinevez, D.J. White, V. Hartenstein, K. Eliceiri, P. Tomancak, A. Cardona, Fiji: An open-source platform for biological-image analysis, Nat. Methods 9 (2012) 676–682. https://doi.org/10.1038/nmeth.2019.

[56] P. Thévenaz, U.E. Ruttimann, M. Unser, A pyramid approach to subpixel registration based on intensity, IEEE Trans. Image Process. 7 (1998) 27–41. https://doi.org/10.1109/83.650848.

[57] B. Münch, P. Trtik, F. Marone, M. Stampanoni, Stripe and ring artifact removal with combined wavelet-Fourier filtering, Opt. Express 17 (2009) 8567–8591. https://doi.org/10.1364/oe.17.008567.

[58] D. Legland, I. Arganda-Carreras, P. Andrey, MorphoLibJ: Integrated library and plugins for mathematical morphology with ImageJ, Bioinformatics 32 (2016) 3532–3534. https://doi.org/10.1093/bioinformatics/btw413.

[59] N. Otsu, A threshold selection method from gray-level histograms, IEEE Trans. Syst. Man Cybern. 9 (1979) 62–66. https://doi.org/10.1109/TSMC.1979.4310076

[60] Y. Chen, L. Cai, Z. Liu, C.R. Dela Cruz, C. Liang, K. An, Correlation of anisotropy and directional conduction in β-Li_3PS_4 fast Li^+ conductor, Appl. Phys. Lett. 107 (2015). https://doi.org/10.1063/1.4926725.

[61] W.E. Lorensen, H.E. Cline, Marching cubes: A high resolution 3D surface construction algorithm, Comput. Graph. (ACM) 21 (1987) 163–169. https://doi.org/10.1145/37402.37422

[62] J. Joos, T. Carraro, M. Ender, B. Rüger, A. Weber, E. Ivers-Tiffée, Detailed microstructure analysis and 3D simulations of porous electrodes, ECS Trans. 35 (2011) 2357–2368. https://doi.org/10.1149/1.3570232.

[63] L. Almar, J. Joos, A. Weber, E. Ivers-Tiffée, Microstructural feature analysis of commercial Li-ion battery cathodes by focused ion beam tomography, J. Power Sources 427 (2019) 1–14. https://doi.org/10.1016/j.jpowsour.2019.04.019.

[64] P. Bourke, Polygonising a scalar field (1994). http://paulbourke.net/geometry/polygonise/ (accessed September 1, 2020).

[65] F. Delay, P. Ackerer, C. Danquigny, Simulating solute transport in porous or fractured formations using random walk particle tracking: A review, Vadose Zone J. 4 (2005) 360–379. https://doi.org/10.2136/vzj2004.0125.

[66] D. Hlushkou, A. Svidrytski, U. Tallarek, Tracer-size-dependent pore space accessibility and long-time diffusion coefficient in amorphous, mesoporous silica, J. Phys. Chem. C 121 (2017) 8416–8426. https://doi.org/10.1021/acs.jpcc.7b00264.

[67] J. Salles, J.F. Thovert, R. Delannay, L. Prevors, J.L. Auriault, P.M. Adler, Taylor dispersion in porous media. Determination of the dispersion tensor, Phys. Fluids A 5 (1993) 2348–2376. https://doi.org/10.1063/1.858751.

[68] P. Szymczak, A.J.C. Ladd, Boundary conditions for stochastic solutions of the convection-diffusion equation, Phys. Rev. E 68 (2003) 036704. https://doi.org/10.1103/PhysRevE.68.036704.

[69] F. Marchini, S. Saha, D. Alves Dalla Corte, J.-M. Tarascon, A Li-rich layered sulfide as cathode active material in all-solid-state Li-metal batteries, ACS Appl. Mater. Interfaces 12 (2020) 15145–15154. https://doi.org/10.1021/acsami.9b22937.

[70] H. Stöffler, T. Zinkevich, M. Yavuz, A. Senyshyn, J. Kulisch, P. Hartmann, T. Adermann, S. Randau, F.H. Richter, J. Janek, S. Indris, H. Ehrenberg, Li-ion dynamics in β-Li_3PS_4 observed by NMR – local hopping and long-range transport, J. Phys. Chem. C 122 (2018) 15954−15965. https://doi.org/10.1021/acs.jpcc.8b05431

[71] S. Choi, J. Ann, J. Do, S. Lim, C. Park, D. Shin, Application of rod-like Li_6PS_5Cl directly synthesized by a liquid phase process to sheet-type electrodes for all-solid-state lithium batteries, J. Electrochem. Soc. 166 (2019) A5193–A5200. https://doi.org/10.1149/2.0301903jes.

[72] S. Wang, Y. Zhang, X. Zhang, T. Liu, Y.H. Lin, Y. Shen, L. Li, C.W. Nan, High-conductivity argyrodite Li_6PS_5Cl solid electrolytes prepared via optimized sintering processes for all-solid-state lithium-sulfur batteries, ACS Appl. Mater. Interfaces 10 (2018) 42279–42285. https://doi.org/10.1021/acsami.8b15121.

[73] S. Torquato, B. Lu, Chord-length distribution function for two-phase random media, Phys. Rev. E 47 (1993) 2950–2953. https://doi.org/10.1103/PhysRevE.47.2950.

[74] K. Hormann, V. Baranau, D. Hlushkou, A. Höltzel, U. Tallarek, Topological analysis of non-granular, disordered porous media: Determination of pore connectivity, pore coordination, and geometric tortuosity in physically reconstructed silica monoliths, New J. Chem. 40 (2016) 4187–4199. https://doi.org/10.1039/c5nj02814k.

[75] M. Kroll, D. Hlushkou, S. Schlabach, A. Höltzel, B. Roling, U. Tallarek, Reconstruction–simulation approach verifies impedance-derived ion transport tortuosity of a graphite battery electrode, J. Electrochem. Soc. 165 (2018) A3156–A3163. https://doi.org/10.1149/2.0711813jes.

[76] J. Landesfeind, J. Hattendorff, A. Ehrl, W.A. Wall, H.A. Gasteiger, Tortuosity determination of battery electrodes and separators by impedance spectroscopy, J. Electrochem. Soc. 163 (2016) A1373–A1387. https://doi.org/10.1149/2.1141607jes.

[77] M. Park, X. Zhang, M. Chung, G.B. Less, A.M. Sastry, A review of conduction phenomena in Li-ion batteries, J. Power Sources 195 (2010) 7904–7929. https://doi.org/10.1016/j.jpowsour.2010.06.060.

[78] B. Ghanbarian, A.G. Hunt, R.P. Ewing, M. Sahimi, Tortuosity in porous media: A critical review, Soil Sci. Soc. Am. J. 77 (2013) 1461–1477. https://doi.org/10.2136/sssaj2012.0435.

[79] H.L. Weissberg, Effective diffusion coefficient in porous media, J. Appl. Phys. 34 (1963) 2636–2639. https://doi.org/10.1063/1.1729783.

[80] M. Barrande, R. Bouchet, R. Denoyel, Tortuosity of porous particles, Anal. Chem. 79 (2007) 9115–9121. https://doi.org/10.1021/ac071377r.

[81] S. Khirevich, A. Höltzel, A. Daneyko, A. Seidel-Morgenstern, U. Tallarek, Structure-transport correlation for the diffusive tortuosity of bulk, monodisperse, random sphere packings, J. Chromatogr. A 1218 (2011) 6489–6497. https://doi.org/10.1016/j.chroma.2011.07.066.

[82] J. Huang, J. Zhang, Theory of impedance response of porous electrodes: Simplifications, inhomogeneities, non-stationarities and applications, J. Electrochem. Soc. 163 (2016) A1983–A2000. https://doi.org/10.1149/2.0901609jes.

[83] S. Cui, Y. Wei, T. Liu, W. Deng, Z. Hu, Y. Su, H. Li, M. Li, H. Guo, Y. Duan, W. Wang, M. Rao, J. Zheng, X. Wang, F. Pan, Optimized temperature effect of Li-ion diffusion with layer distance in $Li(Ni_xMn_yCo_z)O_2$ cathode materials for high performance Li-ion battery, Adv. Energy Mater. 6 (2016) 1501309. https://doi.org/10.1002/aenm.201501309.

[84] Y. Wei, J. Zheng, S. Cui, X. Song, Y. Su, W. Deng, Z. Wu, X. Wang, W. Wang, M. Rao, Y. Lin, C. Wang, K. Amine, F. Pan, Kinetics tuning of Li-ion diffusion in layered $Li(Ni_xMn_yCo_z)O_2$, J. Am. Chem. Soc. 137 (2015) 8364–8367. https://doi.org/10.1021/jacs.5b04040.

[85] A.L. Santhosha, L. Medenbach, J.R. Buchheim, P. Adelhelm, The indium−lithium electrode in solid-state lithium-ion batteries: Phase formation, redox potentials, and interface stability, Batteries & Supercaps 2 (2019) 524–529.

[86] R. Schlenker, D. Stępień, P. Koch, T. Hupfer, S. Indris, B. Roling, V. Miß, A. Fuchs, M. Wilhelmi, H. Ehrenberg, Understanding the lifetime of battery cells based on solid-state Li_6PS_5Cl electrolyte paired with lithium metal electrode, ACS Appl. Mater. Interfaces 12 (2020) 20012–20025. https://doi.org/10.1021/acsami.9b22629.

[87] F. Sälzer, L. Pateras Pescara, F. Franke, C. Müller, J. Winkler, M. Schwalm, B. Roling, Assessing the ion transport properties of highly concentrated non-flammable electrolytes in a commercial Li-ion battery cell, Batteries & Supercaps 3 (2020) 117–125. https://doi.org/10.1002/batt.201900111.

[88] M. Cronau, M. Kroll, M. Szabo, F. Sälzer, B. Roling, Thickness-dependent impedance of composite battery electrodes containing ionic liquid-based electrolytes, Batteries & Supercaps 3 (2020) 611–618. https://doi.org/10.1002/batt.202000023.

[89] H. Kitaura, A. Hayashi, T. Ohtomo, S. Hama, M. Tatsumisago, Fabrication of electrode-electrolyte interfaces in all-solid-state rechargeable lithium batteries by using a supercooled liquid state of the glassy electrolytes, J. Mater. Chem. 21 (2011) 118–124. https://doi.org/10.1039/c0jm01090a.

Chapter 5: Nanoscaled Fractal Superstructures via Laser Patterning – A Versatile Route to Metallic Hierarchical Porous Materials

Authors

Hendrik Reinhardt,[+] Moritz Kroll,[+] Sarah L. Karstens, Sabine Schlabach, Norbert A. Hampp,* and Ulrich Tallarek*

[+]These authors contributed equally to this work.

State of publication

Published 19 February 2021 in *Advanced Materials Interfaces*, Vol. 8, 2000253.
DOI: 10.1002/admi.202000253

Abstract

A laser-based procedure for the preparation of metallic hierarchical porous materials is introduced and exemplified on tin, copper, silicon, titanium, and tungsten surfaces to demonstrate its general applicability. The impact of suitably tuned nanosecond laser pulses triggers a process in which laser-induced metal ablation and instantaneous recondensation of partially oxidized metals lead to cauliflower-like superstructures comprising a hybrid micro-/nanopatterning. Repeated scanning with the intense focused beam over the surface creates microstructures of hierarchically tunable porosity in a layer-by-layer design. The three-dimensional morphology of these superstructures was analyzed using tomographic data based on focused ion-beam scanning electron microscopy to return a fractal dimension of $D_f = 2.79$ – practically identical to a natural cauliflower ($D_f \approx 2.8$), even though the plant is four orders of magnitude larger than the superstructures generated through the laser process. The high D_f value signifies a complex morphology that boasts a huge external surface. The introduced concept enables convenient access to a variety of metallic hierarchical porous materials, which are key to performance in environmentally and technologically relevant areas like energy generation, storage, and conversion, as well as sensing and catalysis.

5.1 Introduction

Hierarchical porous materials (HPMs) attract increasing attention as they combine the benefits of nanomaterials with enhanced mechanical robustness and structural integrity.[1,2] Multilevel porosity on the scale of micro-, meso-, and macropores is a common characteristic of this intriguing class of functional materials.[3] Their interconnected hierarchical porosity provides large specific surface area and huge accessible pore volume, which are favorable in fundamental processes such as light harvesting, charge carrier transport, and mass diffusion.[4] Currently, the applications for HPMs range from (photo)catalysis[5,6] via energy storage[7–9] and conversion[10,11] to separation,[12,13] sensing,[14,15] and pollution remediation.[16] At first glance, nanoparticles appear as ideal candidates for such applications, however, in practice nanoparticles tend to agglomerate, leading to the loss of active surface area and hence reduced performance. This problem can be overcome by materials comprising microstructures that carry nanopatterns such that aggregation is avoided and the active surface preserved.

A natural example that demonstrates the great potential of HPMs is the lotus leaf.[17] Its upper side is covered by micro-sized papillae which secrete nanostructured waxy substances. The self-cleaning ability of the lotus leaf inspired lasting efforts in creating mimicry for technical implementations. Besides water conservation, applications include anti-icing, anti-fogging, and corrosion protection.[18] HPMs in general promise a boost of performance for many applications where a high specific surface area is essential. A major hurdle for rapid progress, however, is the lack of a universal synthesis route for HPMs applicable to a wide range of materials. Established approaches such as templating strategies, solvothermal synthesis, the sol-gel method, and selective leaching are material-specific and thus not generally applicable.[19] With regard to versatility and sustainability, laser-based processes are well suited as they are readily applicable to a multitude of materials, easy to reproduce, solvent-free, and scalable. Although commonly perceived as tools for micropatterning, lasers are increasingly used for nanostructure formation. Examples include laser-induced periodic surface structures,[20,21] pulsed laser-induced dewetting,[22,23] and formation of nanocomposites via laser-stimulated self-organization.[24,25] To enhance the specific surface area of solids, femtosecond lasers are often used, since they facilitate the ablation of almost any material, thus roughening its surface.[26,27]

This study introduces a laser-based concept for the generation of metallic HPMs. Despite the current trend of using femtosecond lasers for surface patterning, the advantage of nanosecond lasers for this field of application is demonstrated. As the names suggest, the primary difference between the two laser types is the pulse duration. Laser pulses in the femtosecond time domain are well suited for pure ablation since the thermalization time of materials scales in the picosecond domain. In addition to ablation, nanosecond lasers induce photothermal heating of the treated materials because their pulse duration surpasses the time required for thermalization.

Concomitant heating during pattern formation offers control over the morphology and composition during the patterning process. The demonstrated technique is based on photothermal heat accumulation on the metallic surfaces beyond the point of evaporation. It facilitates reactions between the affected materials and the surrounding medium (in this case ambient air) into which a recondensation zone is expanding. Rapid quenching leads to the recondensation of reaction products that form highly porous nanostructures on self-organized microstructures. The very interaction of these micro- and nanostructuring effects facilitates formation of HPMs from a variety of metals. The composition of these HPMs may be controlled by specific reactive environments for quenching recondensation. To demonstrate the general applicability of this concept, materials with pronounced differences in their melting and evaporation temperatures (Sn, Cu, Si, Ti, and W) were transformed into HPMs (Figure 5.1). All laser treatments were conducted in ambient air, consequently resulting in oxidic HPMs. Using copper as example, the mechanisms of nanosecond laser-induced HPM generation are disclosed. In order to elucidate the formation process of the laser-generated cauliflower-like superstructures, their three-dimensional (3D) morphology is analyzed using focused ion-beam scanning electron microscopy (FIB-SEM).

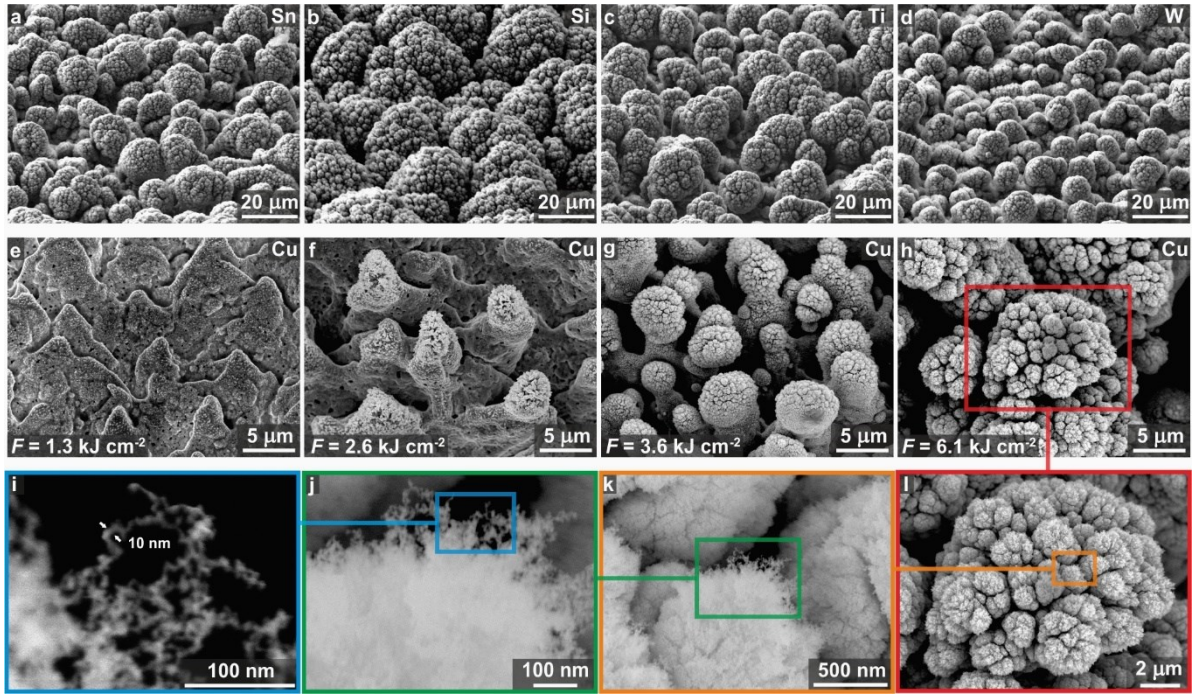

Figure 5.1: Laser-induced formation of HPMs on (a) tin, (b) silicon, (c) titanium, and (d) tungsten. (e–h) Electron micrographs visualizing the pattern formation on copper in dependence of the laser fluence *F*. (i–l) Detailed views on the nanostructure of a copper cauliflower (with increasing magnification from right to left).

5.2 Results and discussion

Laser-generated HPMs on tin (Sn), silicon (Si), titanium (Ti), and tungsten (W) are shown in Figure 5.1a–d. The wide span of melting points underlines the general applicability of nanosecond laser-based HPM formation. The mechanism of hierarchical pattern formation is illustrated in more detail using copper (Cu) as example. Its melting point is right between Sn and Si. Hybrid patterning of copper sheets was conducted with a 532 nm nanosecond pulsed laser having a pulse width of 6 ns. For the modification of extended surface area, the laser beam was focused to a spot diameter of 30 µm and scanned over the copper samples in a meandering motion with a line spacing of 5 µm. Both pulse energy and pulse frequency were kept constant at 90 µJ and 50 kHz, respectively. Depending on the line scan speed of the laser spot, affected surface areas were subjected to a specific energy input per unit area, henceforth indicated as laser fluence F. At a comparably low F of 1.3 kJ cm^{-2}, the copper surface is initially transformed into a scaly texture (Figure 5.1e). When F is doubled, bud-like microstructures with diameters around 5 µm appear (Figure 5.1f). A further increase to F = 3.6 kJ cm^{-2} yields a surface morphology that shares similarities with the lotus leaf (Figure 5.1g). Finally, at a laser fluence of 6.1 kJ cm^{-2}, cauliflower-like structures are generated (Figure 5.1h). These are composed of conically shaped subunits. The most striking feature of these cauliflower-like structures are delicate nanostructures that can hardly be resolved even by high resolution SEM (Figure 5.1i–l). The copper surfaces modified with cauliflowers appear night-black and exhibit broadband absorption in a wavelength range of 200–2500 nm (Supporting Information S1). This is attributed less to the type of material the cauliflowers are made of (Cu_2O and CuO, Supporting Information S2) but rather to light getting trapped in their fuzzy surface architecture. Hence, the question arises how structures of such complexity are actually formed. Investigation of a field of cauliflowers provides insight into the process of hybrid micro-/nanostructure formation (Figure 5.2a). The laser spot was scanned along a meandering path from left to right, as indicated by the superimposed green lines.

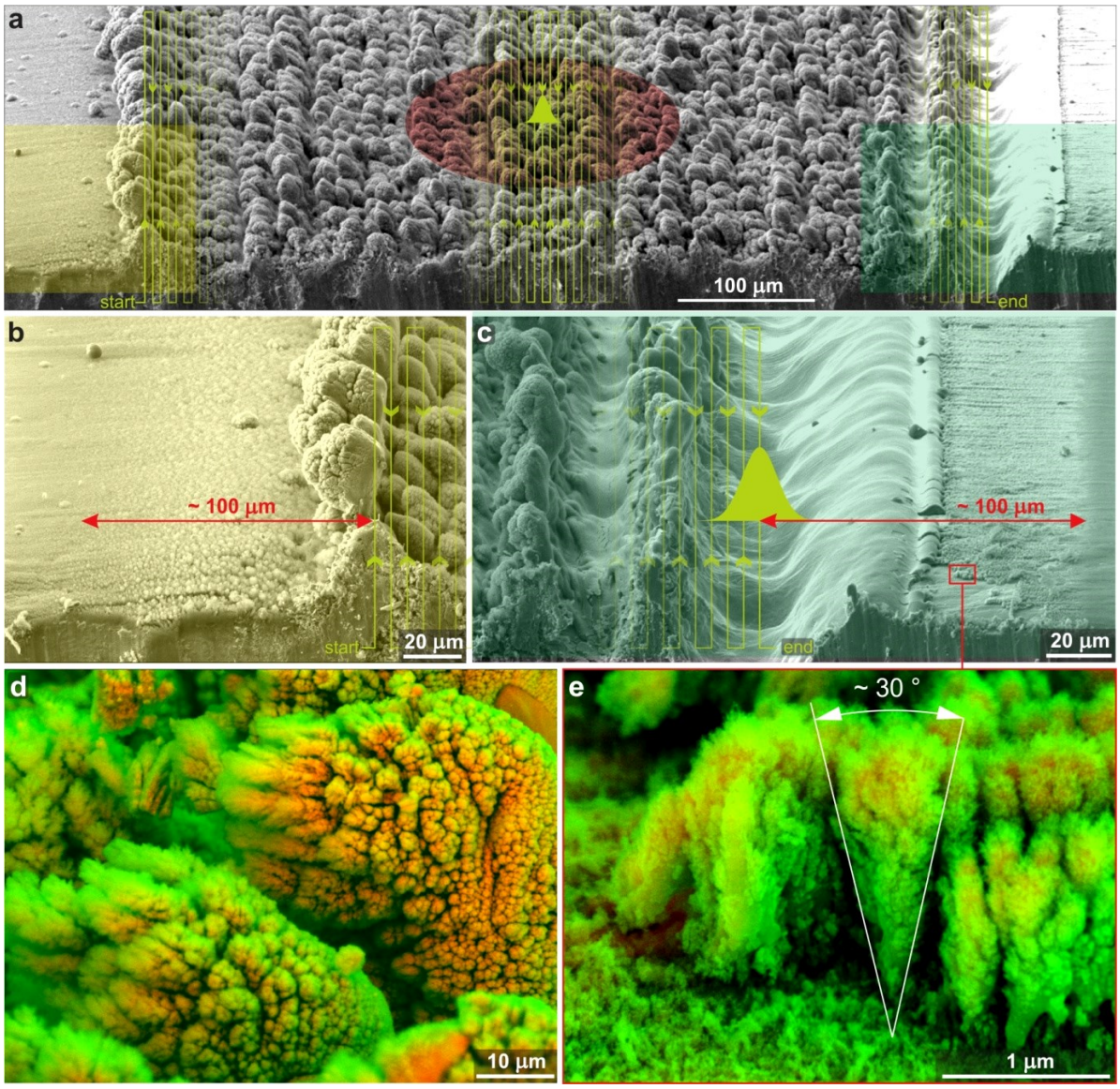

Figure 5.2: Mechanisms of laser-induced hybrid patterning. (a) Perspective view onto a cauliflower field formed with a laser fluence of 7 kJ cm^{-2} on copper. The meandering path of the laser spot is marked by green lines and is true-to-scale (line spacing, 5 µm). In the center, the size of the laser spot is represented by its Gaussian intensity distribution. The surrounding red colored region marks the spatial expansion of the recondensation zone (r = 100 µm). (b,c) Detailed views on the highlighted start and end zones of the cauliflower field. Deposition radius (red arrows), spot path (green lines), and laser intensity profile are superimposed. (d) Cauliflowers in the field visualized by interlacing morphology (green, secondary electron detector) and material contrast (orange, backscattered electron detector). (e) Electron

micrograph of nanomaterial deposits found on the right side of the cauliflower field (end of the laser scan).

Intriguingly, microstructures resulting from the laser treatment are larger than the line spacing of the laser scans, which are displayed true-to-scale (5 µm line spacing). The reason why structures larger than the scan line spacing are created becomes clear at the right edge of the scanned field. At the applied laser fluence (7 kJ cm^{-2} in this case) copper is not ablated homogeneously but is rather transformed into microstructures which, due to their geometry, avoid annihilation under the intense laser irradiation. Besides ablation, nanosecond laser pulses also induce photothermal heating which leads to a softening of the generated microstructures. This enables mass transport away from the heat source, thus causing the observed convergence of microstructures adjacent to already solidified ones. Like surging waves, the microstructures are added row by row. Intense laser irradiation also leads to the evaporation of copper, thereby creating a recondensation zone (cf. Figure 5.2a), out of which reaction products between copper and oxygen (the laser process was conducted in air) recondense in a radius of approximately 100 µm around the laser spot, as the deposition fringes in Figures 5.2b and 5.2c illustrate. It is striking that all microstructures feature an orientation-dependent coverage with copper oxides (Figure 5.2d). Sides facing the laser-induced recondensation zone exhibit fewer deposits compared to sides remaining unaffected by scattered laser light. Hence, the formation of the nanostructures is a process comprising deposition and deterioration, or rather, melting. Lasting nanostructures are deposited over a distance of up to ~50 µm from the recondensation zone center. With increasing distance, mutual shadowing of the hybrid structures provides protection against scattered laser light and radiated heat. The overall course of the structural evolution is recapitulated in Figure 5.3. In the very first laser scan the copper surface is just slightly roughened. As a result, photothermal coupling is improved, promoting distinct morphological transformations to occur upon the second and all subsequent laser scans. Microstructures created in this process accumulate to fields as described above and mature into cauliflowers as soon as nanostructure build-up overcomes nanostructure deterioration inflicted by radiation damage. In the literature, similar SnO_2 structures have been observed for layer deposited gas-born particles synthesized in a microwave plasma process.[28,29] This shows that highly porous structures can be produced by recondensation processes, in general.

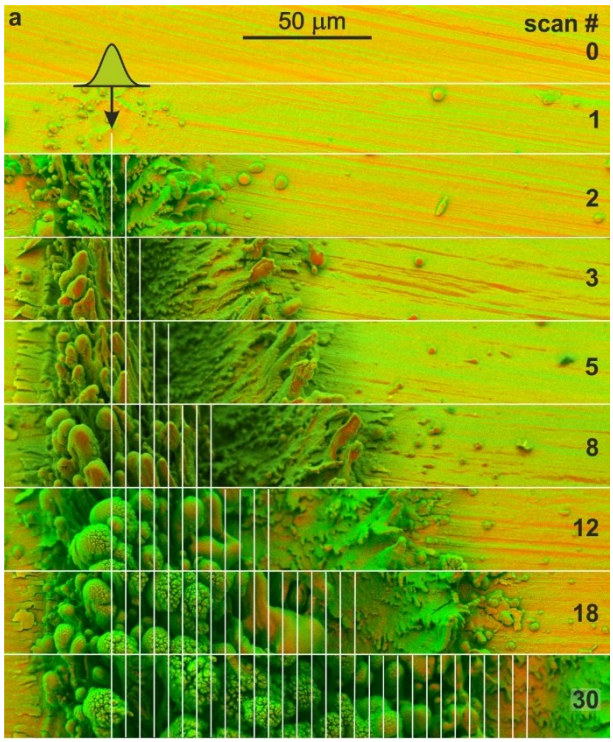

Figure 5.3: Sequential view of hybrid pattern formation. Series of assembled electron micrographs illustrating the course of pattern formation on copper at a laser fluence of 6.1 kJ cm^{-2}. The number of applied scans is indicated on the right (line spacing, 5 µm).

Investigations into the inner structure of resulting cauliflowers substantiate a formation process based on layer-by-layer deposition of reaction products recondensing onto microstructures created by the earlier scan(s) (Figure 5.4a). The studies of Kask et al.,[30] Vlasova et al.,[31] and Aksenov et al.[32] provide detailed insights into fractal pattern formation in and around laser plasmas. The cross-sectional view onto a FIB-sliced cauliflower reveals that early deposits fuse due the close proximity to the recondensation zone center. With increasing distance to this hotspot, the balance is increasingly shifted towards nanostructure build-up. The number of superimposed porous layers can be controlled by the line spacing of the laser scan pattern. Halving the spacing to 2.5 µm, for instance, results in twice the number of deposited layers since the microstructures are passed by the recondensation zone twice as often (Figure 5.4b). Similar to tree rings, the history of structure formation can therefore be traced in detail.

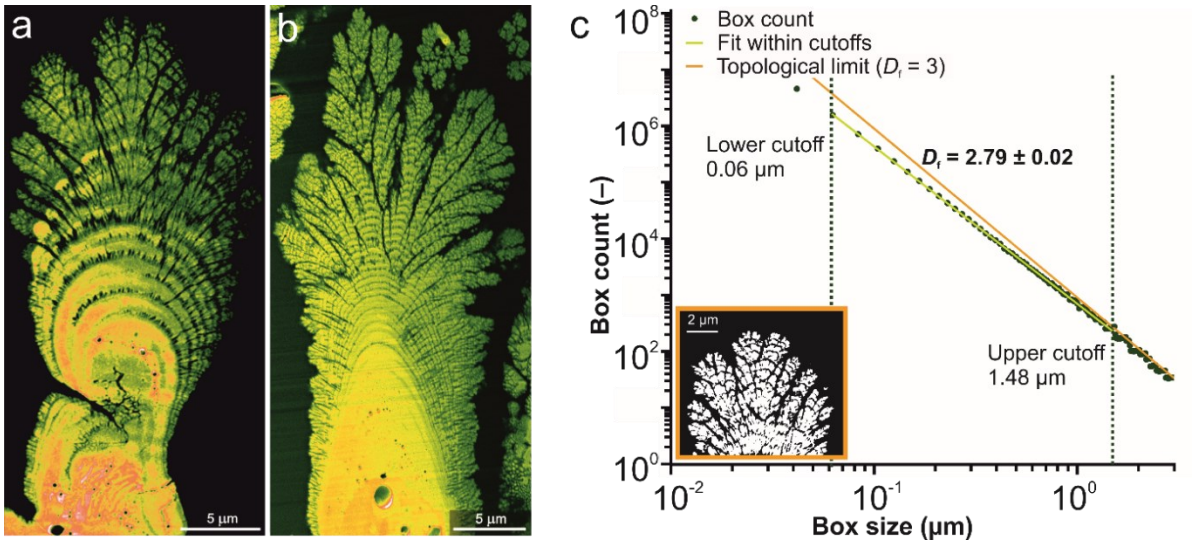

Figure 5.4. Cross-sections of cauliflowers and fractal analysis. (a) Cross-section via FIB slicing of a cauliflower generated with a laser scan line spacing of 5 µm and (b) of 2.5 µm. (c) Determination of the fractal dimension D_f, providing an index of the space-filling capacity and complexity of a fractal. The inset shows a slice of the 3D volume that was used as input for the analysis.

To provide detailed insights into the 3D pore space morphology, the copper cauliflower shown in Figure 5.4a was reconstructed from data obtained by FIB-SEM tomography (Scheme 3.1 and Figure 5.5a). The fractal nature of the solid phase as well as the spatial and size distributions of macroporous void space were analyzed based on the binarized tomographic data. Cauliflower cross-sections in Figures 5.4a and 5.4b suggest that the morphology of solid substructure can be described as fractal with scaling self-similarity. To prove that the laser-generated cauliflowers truly resemble fractals, the box-counting method[33–35] was chosen to determine their fractal dimension D_f (see Supporting Information S3). The box-counting method divides 3D structures into boxes and counts the number of boxes containing solids. The fractal dimension D_f of a structure is determined from the slope of a double-logarithmic plot of the box counts versus the box size. For laser-generated cauliflowers, the plot shows a constant slope of $D_f = 2.79 \pm 0.02$ (Figure 5.4c). Feature sizes from 0.06 to 1.48 µm are contained within the fractal range. The high value of D_f confirms the complex boundary[34] of the laser-generated cauliflowers and indicates a structure becoming increasingly finer from the center outward, thereby unfolding a huge external surface. Intriguingly, natural cauliflowers have a fractal dimension of $D_f = 2.8$,[36] although the plant is about four orders of magnitude larger than the laser-generated cauliflowers.

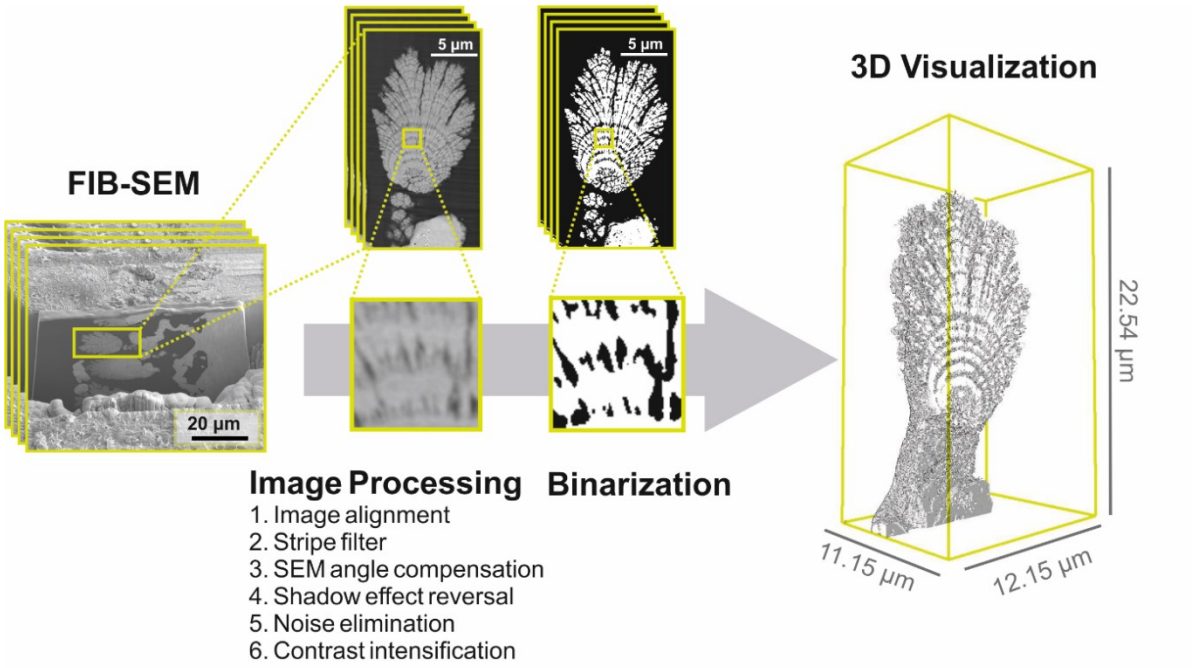

Scheme 5.1: Overview of the 3D reconstruction workflow based on FIB-SEM.

To verify the above-mentioned formation process of cauliflowers, the porosity distribution was analyzed. The porosity is described as the fraction of void space in the porous medium and was determined from the ratio of black voxels to the sum of white and black voxels in the binarized reconstruction. Accordingly, the global porosity of laser-generated cauliflowers is ~34%, whereby the proportion of closed pores (predominantly located in the stem) is about 1% (Figure 5.5b). The closed pores are presumably formed due to the trapping of gas upon rapid solidification of liquid and partially evaporated material as soon as the laser-generated heat zone moves away. With increasing distance to the laser spot, evaporated material recondenses onto the previously generated microstructures. Due to the meandering scan pattern of the laser spot this event is repeated, thus forming layered deposits piling up to a porous network. The resulting superstructure is shown in Figure 5.5c together with a plot determining the porosity ε of the deposited layers (cf. Supporting Information S3). All layer contours can be fitted very well using ellipses that share the same center point. Together with a uniform mean layer height of 0.7 ± 0.1 µm (distance between ellipses along the major direction), this corroborates the layer-based growth model established for laser-generated cauliflowers. Slight deviations from the ideal ellipsoidal geometry are due to mutual shadowing effects of cauliflowers growing next to each other in the recondensation zone. Alternating peak heights in the porosity plot result

from interfaces created by the layer-wise deposition scheme as well as the meandering scan path of the laser spot including changes in direction. Nevertheless, the overall porosity shows a clear increase from the inner elliptical rings to the outer ones, hence the fraction of void space is higher in the outer layers.

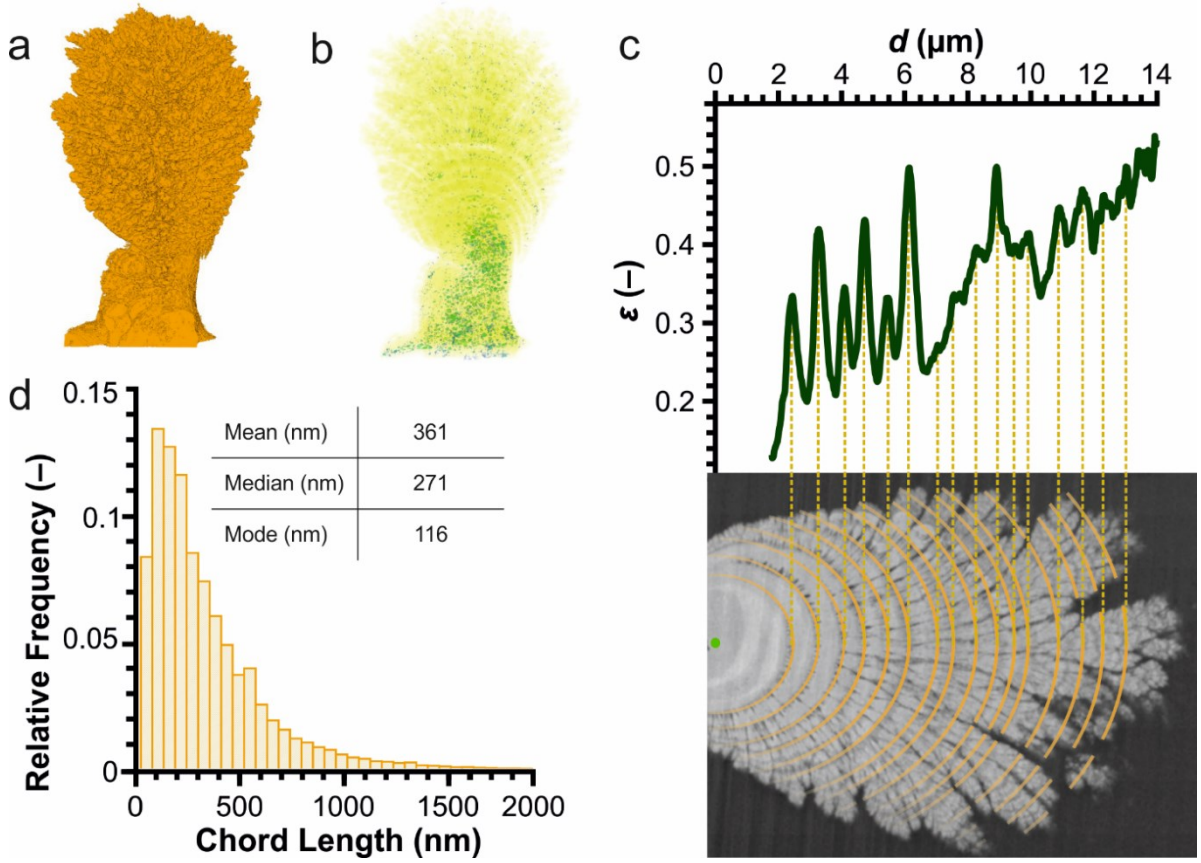

Figure 5.5: Porosity analysis for a cauliflower reconstructed using FIB-SEM tomography. (a) 3D visualization of the reconstructed cauliflower. (b) Closed porosity is highlighted in green. (c) Porosity profile along elliptical rings (orange) fitting the layered structure of the cauliflower. All ellipses have the same center point (green, left side of the image). Porosity increases from inner to outer layers. (d) Characterization of macropore size in the reconstruction by CLD analysis.

To move beyond porosity and characterize the void space regarding its characteristic size, we employed chord length distribution (CLD) analysis (Supporting Information S3).[37–39] In general, the chords collected in a CLD sample the geometry by measuring distances between two interfaces set apart by a homogeneous phase. Since CLD generation does not require any assumptions about the size and shape of the analyzed phase, this methodology is virtually applicable to all multiphase materials. CLD analysis proceeds along the following steps: seed points are randomly placed in the void space of a reconstructed cauliflower; from each point, vectors are projected in angularly equispaced directions until they hit the void–solid interface; finally, chord lengths are extracted as the sum of the absolute lengths of a pair of opposing vectors and stored. The histogram in Figure 5.5d (the CLD) contains the distribution of chords characterizing the void space of laser-generated cauliflowers. It should be noted that meso- and micropores, which are obviously present in the hierarchically structured cauliflowers (see Figure 5.1j–l), are not represented in this analysis as they could not be resolved by FIB-SEM tomography. The CLD shows a median pore size of 0.27 µm and a wide distribution of pore sizes ranging from 50 nm up to 2 µm, underlining the fractal nature of the hierarchical pore network. Besides a wide range of envisioned applications, it makes these laser-generated cauliflowers particularly attractive for catalytic networks[40] and electrochemical processes.[41]

5.3 Conclusion

A universal concept for the generation of metallic HPMs based on a facile nanosecond pulsed laser-treatment of solids is introduced. Using the examples of tin, copper, silicon, titanium, and tungsten the general applicability of the methodology is demonstrated. The process is easy to implement, reproducible, solvent-free, and scalable. The surfaces transformed into HPMs appear deep black, as light is trapped inside the hybrid micro-/nanostructures. The formation process of cauliflower-like superstructures and their morphology was closely investigated. Basically, intense nanosecond laser pulses ablate the surface of solids while at the same time heating it up to the point of evaporation. Microstructures self-organizing in this regime are simultaneously coated with nanostructured materials from the recondensation zone. Due to the meandering path of the laser scan, material deposition occurs in a layer-by-layer scheme. Fractal superstructures result from a scenario comprising nanostructure build-up and deterioration. The shape and morphology of the generated superstructures are tunable by laser process parameters such as the line spacing and energy fluence. A cauliflower-like superstructure was analyzed via physical reconstruction based on FIB-SEM tomography. It features a fractal dimension of 2.79, a value very close to that of natural cauliflowers (2.8). Together with the hybrid micro-/nanostructure patterns, the fractal characteristic of the laser-

generated cauliflowers classifies them as HPMs with highly tunable properties, promising potential for a variety of technical applications.

5.4 Experimental section

5.4.1 Nanosecond Laser Structuring

All laser treatments were carried out in ambient air using a frequency doubled nanosecond pulsed laser (Spectra Physics Explorer XP 5-532, Newport, Santa Clara, CA) emitting at 532 nm. All specimen materials (Sn, Cu, Si, Ti, W) were modified at an average laser power of 4.5 W, a pulse frequency of 50 kHz, a pulse energy of 90 µJ, and a pulse width of 6 ns. The laser beam was focused to a spot diameter of 30 µm ($1/e^2$) by a 163 mm focal length F-Theta lens (Rhodenstock 163-532, Munich, Germany). The focus spot was scanned over the sample surfaces in a meandering pattern using a galvanometer scan head (ScanGine 14, Scanlab, Puchheim, Germany). For the adjustment of laser fluences *F* suitable for HPM generation, the scan speed of the laser spot was varied in a range between 5 and 50 mm s^{-1} while the line spacing was kept constant at 5 µm, unless indicated otherwise.

5.4.2 Scanning Electron Microscopy

Scanning electron microscopy (SEM) was performed on a field emission microscope (JSM-7500F, Jeol, Tokyo, Japan) equipped with a backscattered electron detector for material contrast imaging correlated to the effective atomic number.

5.4.3 Crystal Structure Analysis

Crystal structure analyses were performed on an X'pert PRO MPD (Philips, Eindhoven, The Netherlands) X-ray powder diffractometer equipped with an X'pert tube Co LFF operating at 40 kV and 30 mA. Diffractograms were recorded in a range of $45° \leq 2\Theta \leq 105°$ and with an angular resolution of 0.1° 2Θ at room temperature.

5.4.4 Focused Ion-Beam Scanning Electron Microscopy (FIB-SEM)

The morphology of a copper HPM was investigated using tomographic data obtained by a Strata 400S dual-beam FIB-SEM system (FEI / ThermoFisher Scientific, Hillsboro, OR). For that purpose, the pore space of the sample was filled with epoxy resin to enhance contrast and

prevent shine-through artifacts as well as redeposition in the pores during serial sectioning. In particular, a 5:2 (w/w) mixture of SpeciFix resin and SpeciFix-40 curing agent (Struers, Ballerup, Denmark) was used to infiltrate the porous sample under vacuum (<100 mbar). Prior to sectioning, a protective Pt layer was deposited to reduce curtaining effects. The focused beam of Ga^+ ions was operated at 30 kV with a current of 6.5 nA to create a trench around the region of interest and to acquire an image stack using the Slice&View package of the instrument software. Image acquisition was performed via SEM at 5 kV using an Everhart-Thornley detector. The final image stack contained 202 slices with (20.8 × 20.8) nm^2 pixel size and 50 nm spacing in milling direction.

5.4.5 Physical Reconstruction

Image restoration and processing were realized with Fiji[42] ImageJ in combination with Visual C# scripts. Images were first aligned to correct drifts between slices. Curtaining effects were eliminated by using the Stripes Filter of the Xlib[43] ImageJ plugin. The inclined SEM viewing angle (52°) was corrected by rescaling the voxels in ImageJ. Intensity gradients within the two phases were normalized in all three spatial directions. Noise was removed by applying a Gaussian filter ($\sigma = 1$). Finally, image contrast was enhanced. In the last step, the image stack was binarized by applying a Phansalkar auto local threshold in ImageJ to distinguish between the bright copper HPM substructure and the dark epoxy resin. Scheme 3.1 provides an overview of the reconstruction workflow and shows a 3D visualization of a reconstructed copper HPM.

5.4.6 Morphological Analysis

The binary 8-bit image stack was used as input for the morphological analysis. White voxels are treated as solid phase and black voxels as void space. This allows the characterization of the interstitial void space in terms of porosity distribution, mean feature size, and fractal dimension. The underlying computational procedures are described in the Supporting Information.

5.5 Supporting information

5.5.1 Optical properties of copper cauliflowers

Optical properties of laser-treated copper were analyzed in a wavelength range of 200-2500 nm on a Lambda 1050 UV/VIS/NIR spectrometer (Perkin-Elmer) equipped with integration sphere. Samples were mounted at an angle of 8° (diffuse reflectance) with respect to the optical axis of the spectrometer. Depending on the laser fluence applied, the spectral reflectance of copper could be adjusted in a wide range. Copper sheets subjected to laser fluences exceeding 1.5 kJ cm^{-2} show overall reflectances well below 5 % and a night black visual appearance, as photographs of the corresponding samples indicate. The broadband absorption of light commences as soon as hybrid micro-/nanostructures are formed (cf. Figure 5.1e-h in the main text) and runs into a maximum for cauliflower-like structures (> 6 kJ cm^{-2}).

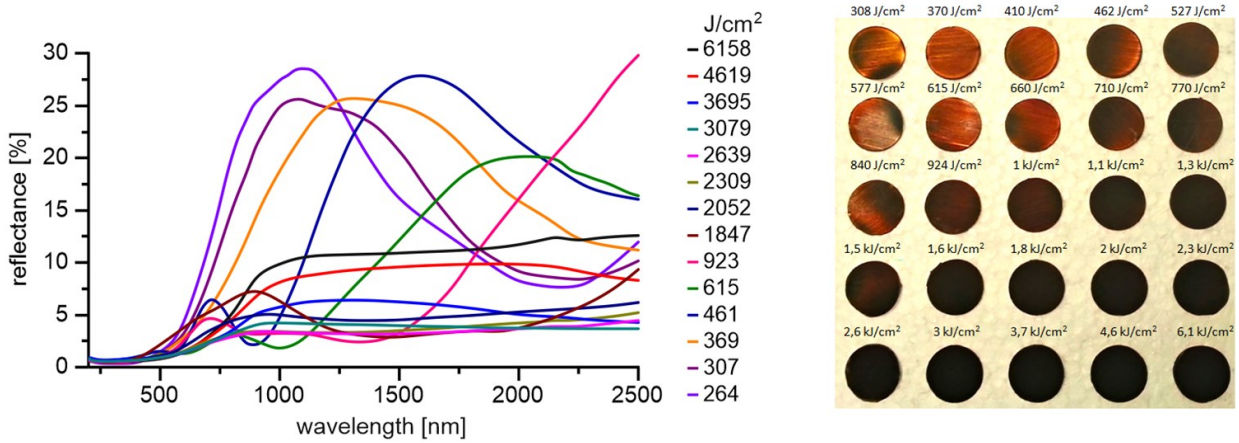

Figure 5.S1. Diffuse optical reflectance of laser treated copper samples (left) and photographs of measured samples (right). Laser fluences applied for surface modification are indicated for each sample.

5.5.2 Structural analysis of cauliflowers generated on copper

Laser-induced formation of cauliflowers on copper was realized in ambient air. Matter evaporating from the copper substrate reacts with oxygen in the plasma. Nanostructures recondensing from the plasma are thus oxygen species of copper. According to X-ray diffraction (Figure 5.S2), Cu_2O was identified as major reaction product; traces of CuO were also detected. The predominant formation of copper(I) oxide can be interpreted as a sign of oxygen deficiency during the formation. It should be noted, however, that copper(I) oxides (Cu_2O) typically form together with copper(II) oxides (CuO) when metallic copper is heated to

red heat in air, since the oxygen affinity of copper is low compared to less noble elements. Copper(I) oxide is formed by the reduction of copper(II) oxide with metallic copper from the substrate and due to the thermal decomposition of copper(II). Most importantly, the analysis shows that the composition of cauliflowers can be defined by the choice of substrate and the reactive environment provided during laser processing. In the given example, oxygen from ambient air is just the most easily accessible reaction environment.

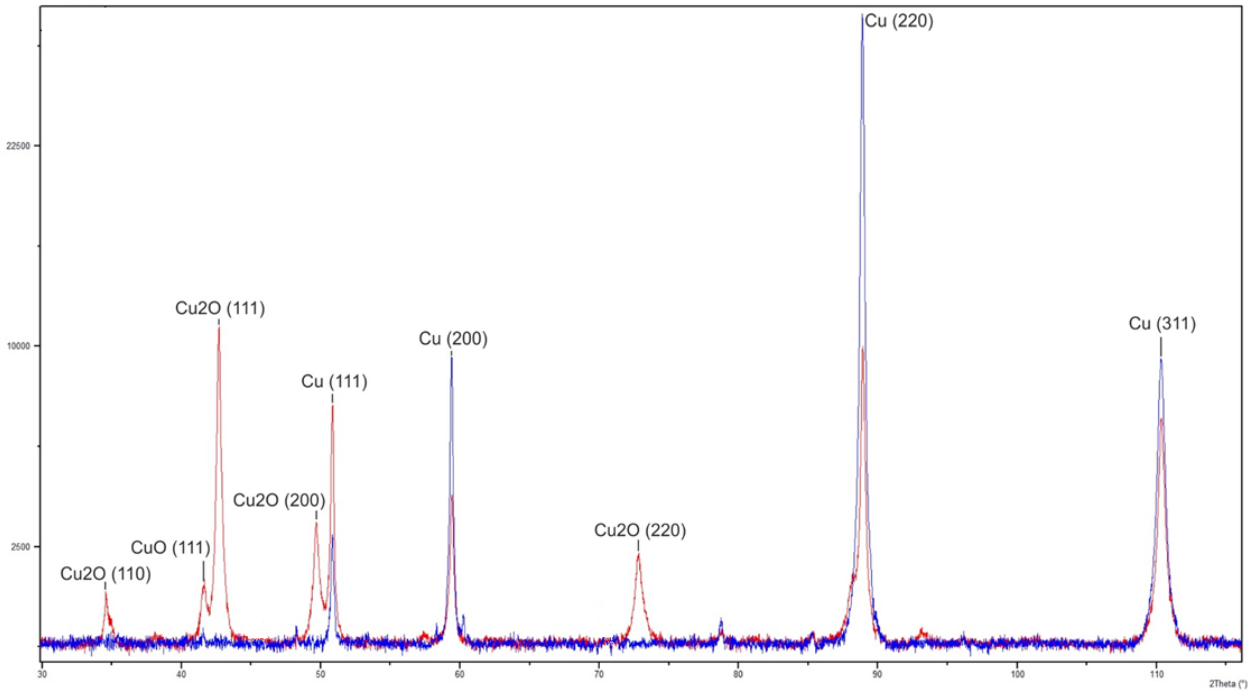

Figure 5.S2. Diffractogram of the copper substrate before (blue) and after (red) laser treatment.

5.5.3 Morphological analysis

Fractal dimension of the reconstructed copper HPM was determined by the box-counting method. This method counts the minimal number of boxes to completely cover the feature depending on box size. For this, the three-dimensional reconstruction is divided into boxes with an edge length of d. The number of boxes that covers any part of the solid phase is counted. In the following steps, d is increased and the number of boxes containing at least one voxel of the solid phase is recorded. Finally, the number of boxes versus d is plotted in a double-logarithmic plot. The fractal range is limited by two cutoffs. The lower cutoff is the minimal box size to cover the smallest structuring unit of the fractal. At the upper cutoff the boxes are large enough to coincide with the topological limit, e.g., 3 for three-dimensional space. The box size becomes too large here to describe the wispy fractal structure. Within the fractal range, the negative

linear slope deviates from the topological dimension and corresponds to the fractal dimension D_f.

The box-counting algorithm was implemented in C# and tested by measuring the fractal dimension of the Menger sponge. This is an ideal three-dimensional fractal structure which is mathematically well-described. Its Hausdorff dimension is $D_H = \log(20)/\log(3) = 2.727$. A binary image stack of a Menger sponge was recursively created with a recursion depth of seven. The algorithm was applied to this ideal structure and gave a fractal dimension of $D_f = 2.72 \pm 0.02$ (Figure 5.S3). This corresponds to the theoretical value and shows that the algorithm works correctly.

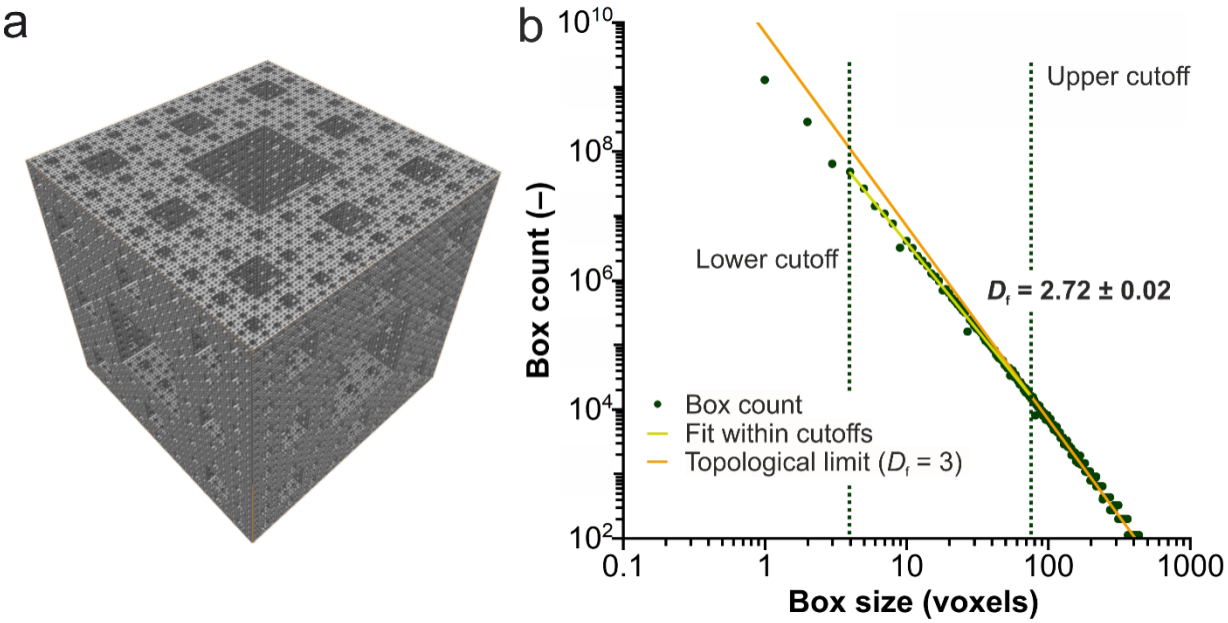

Figure 5.S3. Determination of the fractal dimension of a Menger sponge using the box-counting method. (a) Three-dimensional presentation of a Menger sponge with a recursion depth of seven. (b) Double-logarithmic plot of the number of boxes that cover the structure versus box edge length in voxels. The fractal dimension is $D_f = 2.72 \pm 0.02$, which corresponds to the theoretical value of $D_H = \log(20)/\log(3) = 2.73$.

The porosity of the reconstructed cauliflower-like substructure was determined as the fraction of void voxels (the ratio between black voxels and the sum of black and white voxels). The void space around the substructure was not considered here. The “Find Connected Regions” plugin in ImageJ was used to calculate the fraction of closed porosity. This plugin finds clusters of

voxels that are not connected to the rest and counts the number of voxels. In addition, the porosity was determined along the rings of ellipses to show that the cauliflower-like substructure was uniformly formed as an ellipsoid by the laser. An ellipse can be described by its semi-major axis *a*, its semi-minor axis *b*, and its center point. Ellipses were fit to the cross-section of the cauliflower-like substructure to find good start parameters for *a*, *b*, and the center point. A start ellipse with a fixed center point was then defined and *a* and *b* were increased linearly (with different slope). The C# script measures the porosity along the rings of the ellipses for 20 slices in the center of the reconstruction, where the dimensions of the substructure change only slightly. The resulting plot shows the mean porosity along the semi-major axis (cf. Figure 5.5c).

The chord length distribution was used to characterize the shape and size of the cauliflower's void space. For this, 10^5 seed points were randomly distributed within the void space. From each seed point, 26 angularly equispaced vectors were spread out until they reached the solid-void interface. Pairs of opposing vectors were summed up to one chord. If a vector left the void space within the cauliflower or the image bounds, the corresponding vector pair was discarded. All chords were collected in a histogram (the chord length distribution), describing the size of the pores within the substructure without any assumption about limits of individual pores or their geometry.

5.6 References

[1] M. Hartmann, W. Schwieger, *Chem. Soc. Rev.* **2016**, *45*, 3311.

[2] R. Lakers, *Nature* **1993**, *361*, 511.

[3] W. G. Bae, H. N. Kim, D. Kim, S. H. Park, H. E. Jeong, K.-Y. Suh, *Adv. Mater.* **2014**, *26*, 675.

[4] M.-H. Sun, S.-Z. Huang, L.-H. Chen, Y. Li, X.-Y. Yang, Z.-Y. Yuan, B.-L. Su, *Chem. Soc. Rev.* **2016**, *45*, 3479.

[5] X. Zhao, P. Pachfule, S. Li, T. Langenhahn, M. Ye, C. Schlesiger, S. Praetz, J. Schmidt, A. Thomas, *J. Am. Chem. Soc.* **2019**, *141*, 6623.

[6] H. Wang, M. Qu, S. Wang, X. Liu, L. Li, *Adv. Sustain. Syst.* **2019**, *3*, 1970013.

[7] W. G. Lim, C. Jo, A. Cho, J. Hwang, S. Kim, J. W. Han, J. Lee, *Adv. Mater.* **2019**, *31*, 1806547.

[8] N. P. Sari, D. Dutta, A. Jamaluddin, J.-K. Change, C.-Y. Su, *Phys. Chem. Chem. Phys.* **2017**, *19*, 30381.

[9] S. Jia, Y. Wang, X. Liu, S. Zhao, W. Zhao, Y. Huang, Z. Li, Z. Lin, *Nano Energy* **2019**, *59*, 229.

[10] H.-W. Liang, X. Zhuang, S. Brüller, X. Feng, K. Müllen, *Nat. Commun.* **2014**, *5*, 4973.

[11] Y. Chen, Y. Lin, Y. Zhang, S. Wang, D. Su, Z. Yang, M. Han, F. Chen, *Nano Energy* **2014**, *8*, 25.

[12] R. L. Thankamony, X. Li, X. Fan, G. Sheng, X. Wang, S. Sun, X. Zhang, Z. Lai, *ACS Appl. Mater. Interfaces* **2018**, *10*, 44041.

[13] Y. Guan, F. Cheng, Z. Pan, *Polymers* **2019**, *11*, 806.

[14] Y. Jiao, S. W. Cho, S. Lee, S. H. Kim, S. Y. Jeon, K. Hur, S. M. Yoon, *Adv. Eng. Mater.* **2018**, *20*, 1700608.

[15] Z. Wang, X. Guan, H. Huang, H. Wang, W. Lin, Z. Peng, *Adv. Funct. Mater.* **2019**, *29*, 1807569.

[16] L. S. Zhong, J. S. Hu, H. P. Liang, A. M. Cao, W. G. Song, L. J. Wan, *Adv. Mater.* **2006**, *18*, 2426.

[17] H. J. Ensikat, P. Ditsche-Kuru, C. Neinhuis, W. Barthlott, *Beilstein J. Nanotechnol.* **2011**, *2*, 15.

[18] J. Jeevahan, M. Chandrasekaran, J. G. Britto, R. B. Durairaj, G. Mageshwaran, *J. Coat. Technol. Res.* **2018**, *15*, 231.

[19] X.-Y. Yang, L.-H. Chen, Y. Li, J. C. Rooke, *Chem. Soc. Rev.* **2017**, *46*, 481.

[20] H. M. Reinhardt, K. Bücker, N. A. Hampp, *Opt. Express* **2015**, *23*, 11965.

[21] H. M. Reinhardt, H.-C. Kim, C. Pietzonka, J. Kruempelmann, B. Harbrecht, B. Roling, N. Hampp, *Adv. Mater.* **2013**, *25*, 3313.

[22] H. Oh, J. Lee, M. Seo, I.-U. Baek, J.-Y. Byun, M. Lee, *ACS Appl. Mater. Interfaces* **2018**, *7*, 38368.

[23] H. M. Reinhardt, C. Hellmann, P. Nürnberger, S. Kachel, N. Hampp, *Adv. Mater. Interfaces* **2017**, *4*, 1700508.

[24] H. M. Reinhardt, C. Pietzonka, B. Harbrecht, N. Hampp, *Adv. Mater. Interfaces* **2014**, *1*, 1300060.

[25] Z. Lui, J. Siegel, M. Garcia-Lechuga, T. Epicier, Y. Lefkir, S. Reynaud, M. Bugnet, F. Vocanson, J. Solis, G. Vitrant, N. Destouches, *ACS Nano* **2017**, *11*, 5031.

[26] A. Y. Vorobyev, C. Guo, *Laser Photonics Rev.* **2013**, *7*, 385.

[27] J. Yong, Q. Yang, C. Guo, F. Chen, X. Hou, *RSC Adv.* **2019**, *9*, 12470.

[28] B. Schumacher, R. Ochs, H. Tröße, S. Schlabach, M. Bruns, D. V. Szabó, J. Haußelt, *Plasma Process. Polym.* **2007**, *4*, S865.

[29] R. Ochs, D. V. Szabó, S. Schlabach, S. Becker, S. Indris, *Phys. Status Solidi A* **2011**, *208*, 471.

[30] N. E. Kask, S. V. Michurin, G. M. Fedorov, *Quantum Electronics* **2003**, *33*, 57.

[31] M. Vlasova, P. A. Márquez Aguilar, M. C. Reséndiz-González, M. Kakazey,V. Stetsenko, T. Tomila, A. Ragulya, *Science of Sintering* **2008**, *40*, 69.

[32] V. P. Aksenov, V. V. Voronov, G. N. Mikha lova, N. E. Kask, E. G. Leksina, S. V. Michurin, G. M. Fedorov, *Opticheski Zhurnal* **2008**, *75*, 43.

[33] B. B. Mandelbrot, *The Fractal Geometry of Nature*; Freeman, New York, USA, **1983**.

[34] S. S. Cross, *Micron* **1994**, *25*, 101.

[35] R. Zahn, M. F. Lagadec, V. Wood, *ACS Energy Lett.* **2017**, *2*, 2452.

[36] S.-H. Kim, *J. Korean Phys. Soc.* **2005**, *46*, 474.

[37] S. Torquato, *Annu. Rev. Mater. Res.* **2002**, *32*, 77.

[38] T. Müllner, K. K. Unger, U. Tallarek, *New J. Chem.* **2016**, *40*, 3993.

[39] M. Kroll, D. Hlushkou, S. Schlabach, A. Höltzel, B. Roling, U. Tallarek, *J. Electrochem. Soc.* **2018**, *165*, A3156.

[40] S. Gheorghiu, M.-O. Coppens, *AIChE J.* **2004**, *50*, 812.

[41] B. Y. Park, R. Zaouk, C. Wang, M. J. Madou, *J. Electrochem. Soc.* **2007**, *154*, P1.

[42] J. Schindelin, I. Arganda-Carreras, E. Frise, V. Kaynig, M. Longair, T. Pietzsch, S. Preibisch, C. Rueden, S. Saalfeld, B. Schmid, J.-Y. Tinevez, D. J. White, V. Hartenstein, K. Eliceiri, P. Tomancak, A. Cardona, *Nat. Methods* **2012**, *9*, 676.

[43] B. Münch, P. Trtik, F. Marone, M. Stampanoni, *Opt. Express* **2009**, *17*, 8567.

IV. Conclusions and perspective

IV.1 Conclusions

This thesis comprises five experimental studies which all dealt with the identification of kinetic limitations in porous electrodes or with the morphological characterization of porous media. The use of tomographic methods for a detailed representation of the battery 3D microstructure is becoming ever more common. Morphology-based investigations are best suited to identify microstructure-related kinetic limitations. Focused ion-beam scanning electron microscopy (FIB-SEM) tomography is a very suitable technique to obtain a realistic geometrical model of electrodes of lithium-ion batteries (LIBs), as it covers the relevant feature size range from nm to µm-scale, provides resolutions down to 5–10 nm, and exhibits a high material contrast (even for light elements).

This work provides a broad characterization of battery electrodes in order to detect and describe kinetic limitations. The investigation ranges from slurry-based electrode preparation to electrochemical measurements, FIB-SEM sample preparation and tomography, physical reconstruction, morphological analysis, and interpretation of pore-scale transport simulations. In this manner, a routine for two- and three-phase FIB-SEM-based reconstruction was established. The pore space of the samples was filled with curing agents, which enhance contrast in the SEM images: Osmium-based staining (Chapter 1) and silicone (Chapter 3) or epoxy (Chapter 5) resin. After image processing, a color threshold was defined based on contrast for two-phase segmentation. In Chapters 3 and 4, the routine was upgraded to three phases using advanced segmentation algorithms (local threshold, machine learning). The developed procedure was based on self-written C# scripts and open-source software to acquire large-scale high-resolution reconstructions of the anode, cathode and laser-generated fractal structures (Chapters 1, 3–5). This enabled the representation of a variety of materials: graphite, transition metal oxides, sulfur-based solid electrolytes (SEs), and carbon-binder domain (CBD).

The subsequent morphological analysis enabled the investigation of kinetic limitations: charge transfer at the cathode active material (CAM)–electrolyte interface, electron transport through the AM or CBD, and Li^+ transport in the electrolyte phase. Calculations in the framework of a transmission-line model (TLM) showed that charge transfer at the (CAM)–electrolyte interface is limiting to the battery performance for all-solid-state batteries (ASSBs, see Chapter 4). Electronic conduction was also found to be noncritical if the AM particles form a highly connected network (Chapter 4) or if the CBD ensures electronic conduction between the AM and the current collector (Chapter 3). Chapters 1, 3, and 4 investigated to what extent Li^+ transport in the electrolyte phase is hindered by the electrode microstructure through a combination of morphological analysis and pore-scale simulations. The morphological analysis already provided important indications with small computational effort. Direction-dependent

chord length distribution (CLD) and geometric tortuosity gave first characterizations of the electrolyte phase and detected an anisotropic microstructure of a graphite anode in Chapter 1. Anisotropy may obstruct transport paths in single spatial directions. For a realistic determination of the Li^+ transport properties in the electrolyte phase, however, numerical transport simulations on high-performance computational systems are mandatory. Transport simulations include constrictivities like bottlenecks or dead-end pores. Diffusion simulations using a random-walk particle tracking (RWPT) approach were used to determine the ionic tortuosity (Chapters 1, 3 and 4). Direct imaging of a representative volume in combination with numerical simulations is thus key to elucidate the source of transport limitations.

Taken together, this work has provided new insights into the microstructure of battery electrodes. Comparisons with electrochemical impedance spectroscopy (EIS) experiments within the TLM showed good agreement with simulated values (Chapters 1 and 3) if a reconstruction, based on high-resolution FIB-SEM tomography with actively stained pores, served as input. Moreover, the reconstruction-simulation-based studies showed that the shape of the pore space does not depend only on the choice of CAM. Rather, the CBD was identified to significantly affect Li^+ transport in the liquid electrolyte (Chapter 3). In ASSBs, the shape of the SE particles primarily determines the contact area to the CAM and the fraction of unwanted void space (Chapter 4). Hence, the use of small, soft, highly conductive SE particles offers great potential toward more powerful batteries. The evaluations of the analytical battery model in Chapter 2 also showed a low dependence on the electrode thickness of the impedance, provided that the morphology can be kept constant throughout the electrode. In addition to conventional electrodes formed by CAM particles, fractal hierarchical microstructures with large surface areas (as shown in Chapter 5) may also be of interest to optimize Li^+ transport.

IV.2 Perspective

The presented results provide a good basis for further investigations. The laser structuring procedure shown in Chapter 5 could be applied to transition metals which are more suitable as AM, like cobalt that are more suitable as AM. The cauliflower-like structures provide both an easily accessible pore network for charge transport and a large surface area for charge transfer and can thus serve for energy storage in LIBs. The high surface area of the tunable superstructures also makes them potential candidates for supercapacitors.

The weak thickness dependence of the cathode impedance shown in Chapter 2 should be verified by EIS experiments. Thicker electrodes would increase the overall charge density of the battery as the fraction of passive components such as current collectors or separators decreases proportionally. In practice, electrodes are usually produced with a thickness of only 80–100 µm. While analytical battery models usually assume a homogeneous morphology

across the entire electrode volume, in reality there are likely porosity gradients and other forms of heterogeneity due to the manufacturing process. FIB-SEM cross-sectional imaging or 3D reconstructions would be useful for closer investigation of possible disadvantageous morphological effects at high thicknesses. This way, it may be possible to identify a critical electrode thickness.

In order to reduce the amount of void space in sheet-type ASSBs (Chapter 4), solvent-assisted ball milling could be used to obtain smaller SE particles of highly conducting LSPI. A mixture of both investigated SEs, LPSI with small amounts of nano-scaled β-LPS, is also conceivable. The large void fraction observed for LPSI could thus be filled by β-LPS, making ion transport in the SE phase less tortuous. The reconstruction protocol, which has been developed in Chapter 4, can be used for fast acquisition of further tomographic data sets. A significant reduction of void space in ASSBs offers high potential to tune the SE–CAM interface and therefore battery performance.

A three-phase reconstruction protocol, as developed in Chapters 3 and 4, is indispensable for multiphase systems such as those found in LIBs. It has been shown that a simple color threshold segmentation does not produce adequate results, since the color values of different phases often overlap. Overall, only an integer range of 0–127 is available. The color range of each phase therefore decreases the more different phases have to be segmented. The artificial intelligence (AI) approach used in Chapter 3, which uses supervised learning to train neural networks, has proven to be particularly promising. The trained algorithm also takes features such as shape or size into account, which allows the segmentation of three or more phases. AI approaches should definitely be considered for future reconstructions of multiphase systems.

Chapters 1 and 3 showed that the reconstruction–simulation (RS) approach leads to similar results compared with EIS measurements in the framework of the TLM to determine the ionic tortuosity. However, more reconstruction samples over a wide porosity range are needed for robust validation. The prerequisites for such a study have been set by establishing the lab-scale electrode preparation procedure and by identifying suitable reconstruction parameters (sample preparation, pore staining, reconstruction volume, ion milling parameters etc.). At the same time, such a study is qualified to generally investigate porosity–tortuosity relationships in LIBs. In the battery community, the Bruggeman relationship is usually used to describe this dependence. However, the Bruggeman relationship is defined for two-phase systems with spherical sphere packings. Chapters 3 and 4 showed that the microstructure of batteries using a liquid electrolyte and ASSBs consists of at least three phases with complex morphologies and feature sizes on different size scales (voids or CBD versus AM). The feature sizes of all phases are known from the preliminary work shown here, so the reconstruction volumes can be chosen as small as possible (but still representative). Using EIS measurements, the ionic tortuosity can be determined quickly over a large porosity range. However, a change of porosity may be

accompanied by changing morphological properties of single phases (e.g., distribution and size of void space, porosity, and connectivity of the CBD). This underscores that an observation of such effects is only possible by direct imaging, which makes 3D tomography indispensable for investigating porosity–tortuosity relationships in complex porous media.

In summary, this work has made an important contribution to the development of FIB-SEM reconstruction protocols for LIBs and to their morphological description. Physical reconstructions are an important tool for giving a realistic geometrical model and for elucidating constrictivities and morphological heterogeneity. Nowadays, the largest performance improvements of LIBs are achieved by the development of new AMs and (solid) electrolytes. In the future, the consideration of microstructure will become of increasing importance. Transport in the electrolyte phase, for example, can be further optimized by using spherical CAM particles or monolithic microstructures so that transport resistances can be further minimized. A similar development towards optimal spherical packing has also occurred in chromatography over the past decades. However, processes such as volume expansion of the AM, solid electrolyte interface (SEI) formation, dendrite growth, or degradation of the electrolyte make LIBs highly complex. Therefore, morphological studies still remain of enormous relevance on this journey.

V. Appendix

V.1 Curriculum Vitae

Der Lebenslauf wurde aus der elektronisch publizierten Version der Arbeit zum Schutz personenbezogener Daten entfernt.

V.2 Erklärungen

Erklärung zum Eigenanteil

Die vorliegende Dissertation mit dem Titel „Characterization and Morphological Analysis of Porous Electrodes for Lithium-Ion Batteries“ habe ich selbstständig verfasst. Der kumulative Teil dieser Arbeit (Chapter 1–5) beinhaltet veröffentlichte Fachartikel, die in Kooperation mit Koautoren verfasst wurden. Die Beiträge der einzelnen Koautoren werden im Folgenden in Anlehnung an die CRediT Terminologie (siehe www.casrai.org/credit/) dargestellt.

Kapitel 1: Reconstruction–Simulation Approach Verifies Impedance-Derived Ion Transport Tortuosity of a Graphite Battery Electrode

M. Kroll, D. Hlushkou, S. Schlabach, A. Höltzel, B. Roling,* U. Tallarek*
J. Electrochem. Soc., **2018**, *165*, A3156–A3163. DOI: 10.1149/2.0711813jes

M. Kroll wirkte an der Methodologie, an der Softwareentwicklung, der wissenschaftlichen Datenerhebung, der Visualisierung sowie am Schreiben des Entwurfs mit. Die Rekonstruktion wurde im Rahmen der Masterarbeit angefertigt, wobei die übrige Auswertung und schlussendliche Interpretation in die Promotionszeit fiel. D. Hlushkou übernahm die Simulationsanalyse. S. Schlabach trug durch die Aufnahme der FIB-SEM-Tomographie zur wissenschaftlichen Datenerhebung bei. A. Höltzel wirkte am Schreiben des Entwurfs und der Editierung des Manuskripts mit. B. Roling und U. Tallarek übernahmen die Supervision, Konzeptualisierung, Bereitstellung von wissenschaftlichen Materialien und Ressourcen sowie die Editierung des Textes.

Kapitel 2: Thickness-Dependent Impedance of Composite Battery Electrodes Containing Ionic Liquid-Based Electrolytes

M. Cronau,[+] M. Kroll,[+] M. Szabo, F. Sälzer, B. Roling*
Batteries & Supercaps, **2020**, *3*, 1–9. DOI: 10.1002/batt.202000023

M. Cronau trug zur Methodologie, zur wissenschaftlichen Datenerhebung (EIS-Messungen) und zur Visualisierung bei und steuerte Text zum Entwurf bei. M. Kroll trug im selben Maße durch Mitarbeit an der Methodologie, wissenschaftlichen Datenerhebung, Softwareentwicklung, Visualisierung und Textproduktion bei. M. Szabo unterstützte die wissenschaftliche Datenerhebung. F. Sälzer steuerte Software bei. B. Roling übernahm die Supervision, Konzeptualisierung, das Schreiben des ersten Entwurfs sowie dessen Editierung und die Bereitstellung von wissenschaftlichen Materialien und Ressourcen.

Kapitel 3: Three-Phase Reconstruction Reveals How the Microscopic Structure of the Carbon-Binder Domain Affects Ion Transport in Lithium-Ion Batteries

M. Kroll, S. L. Karstens, M. Cronau, A. Höltzel, S. Schlabach, N. Nobel, C. Redenbach, B. Roling,* U. Tallarek*

Batteries & Supercaps **2021**, *accepted*. DOI: 10.1002/batt.202100057R1

M. Kroll wirkte an der Konzeptualisierung, der Methodologie, der Entwicklung von Software, der wissenschaftlichen Datenerhebung, der Visualisierung sowie dem Schreiben des Entwurfs mit. Die wissenschaftlichen Untersuchungen wurden von S. L. Karstens (Bildentwicklung) und M. Cronau (Probenvorbereitung und EIS-Messungen) unterstützt. S. Schlabach trug durch die Aufnahme der FIB-SEM-Tomographie zur wissenschaftlichen Datenerhebung bei. A. Höltzel wirkte an der Konzeptionierung und Editierung des Textes mit. N. Nobel und C. Redenbach unterstützten die wissenschaftliche Datenerhebung durch das Aufarbeiten der FIB-SEM-Daten. B. Roling und U. Tallarek übernahmen die Supervision und wirkten an der Konzeptualisierung, der Bereitstellung von wissenschaftlichen Materialien und Ressourcen und an der Editierung des Textes mit.

Kapitel 4: Sheet-type all-solid-state batteries with sulfidic electrolytes: Analysis of kinetic limitations based on a cathode morphology study

M. Kroll,[+] M. Duchardt,[+] S. L. Karstens, S. Schlabach, F. Lange, J. Hochstrasser, B. Roling,* U. Tallarek*
Journal of Power Sources **2021**, *under review*.

M. Kroll und M. Duchardt wirkten im gleichen Maße an der Konzeptualisierung, der Methodologie, der wissenschaftlichen Datenerhebung, der Visualisierung sowie dem Schreiben des Entwurfs mit. M. Kroll arbeitete an der Entwicklung des Herstellungsprotokolls der ST-ASSB mit und war für die FIB-SEM-basierte Rekonstruktion und morphologische Analyse verantwortlich. L. Karstens trug zur wissenschaftlichen Datenerhebung bei (Rekonstruktion und morphologische Analyse). S. Schlabach trug durch die Aufnahme der FIB-SEM-Tomographie ebenfalls zur wissenschaftlichen Datenerhebung bei. F. Lange unterstützte die wissenschaftlichen Untersuchungen. J. Hochstrasser übernahm die Simulationsanalyse. B. Roling und U. Tallarek übernahmen die Supervision und wirkten an der Konzeptualisierung, der Bereitstellung von wissenschaftlichen Materialien und Ressourcen und an der Editierung des Textes mit.

Kapitel 5: Nanoscaled Fractal Superstructures via Laser Patterning—A Versatile Route to Metallic Hierarchical Porous Materials

H. Reinhardt,[+] M. Kroll,[+] S. L. Karstens, S. Schlabach, N. Hampp,* U. Tallarek*
Adv. Mater. Interfaces, **2021**, *8*, 2000253. DOI: 10.1002/admi.202000253

H. Reinhardt und M. Kroll wirkten im gleichen Maße an der Konzeptualisierung, der Methodologie, der wissenschaftlichen Datenerhebung, der Visualisierung sowie dem Schreiben des Entwurfs mit. H. Reinhardt übernahm die Laserstrukturierung und die Aufnahme von SEM-Bildern während M. Kroll die FIB-SEM-basierte Rekonstruktion und morphologische Analyse durchführte. S. L. Karstens unterstützte die wissenschaftlichen Untersuchungen und die Visualisierung. S. Schlabach trug durch die Aufnahme der FIB-SEM-Tomographie zur wissenschaftlichen Datenerhebung bei. N. Hampp und U. Tallarek wirkten an der Konzeptualisierung, der Bereitstellung von wissenschaftlichen Materialien und Ressourcen, der Editierung des Textes sowie der Supervision mit.

(Ort, Datum, Unterschrift Promovierender) (Ort, Datum, Unterschrift der Betreuer)

Erklärung zum selbständigen Verfassen

Ich erkläre, dass eine Promotion noch an keiner anderen Hochschule als der Philipps-Universität Marburg, Fachbereich Chemie, versucht wurde.

Ich versichere, dass ich die beigefügte Dissertation mit dem Titel

"Characterization and Morphological Analysis of Porous Electrodes for Lithium-Ion Batteries"

selbstständig, ohne unerlaubte Hilfe Dritter angefertigt und andere als die in der Dissertation angegebenen Hilfsmittel nicht benutzt habe. Alle Stellen, die wörtlich oder sinngemäß aus veröffentlichten oder unveröffentlichten Schriften entnommen sind, habe ich als solche kenntlich gemacht. Dritte waren an der inhaltlich-materiellen Erstellung der Dissertation nicht beteiligt; insbesondere habe ich hierfür nicht die Hilfe eines Promotionsberaters in Anspruch genommen. Kein Teil dieser Arbeit ist in einem anderen Promotions- oder Habilitationsverfahren verwendet worden. Mit dem Einsatz von Software zur Erkennung von Plagiaten bin ich einverstanden.

Ort/Datum	Moritz Kroll